Multi-nuclear magnetic resonance imaging and spectroscopy of lithium in the brain

Dissertation

for the award of the degree

"*Doctor rerum naturalium*" (*Dr. rer. nat.*)

of the Georg-August-Universität Göttingen

within the doctoral program IMPRS Neurosciences

of the Georg-August University School of Science (GAUSS)

submitted by

Tor Rasmus Memhave

from Ganløse, Denmark

Göttingen, 2023

Thesis Advisory Committee:

Prof. Dr. Susann Boretius
Functional Imaging Laboratory, German Primate Center (DPZ), Göttingen

Prof. Dr. Dr. Hannelore Ehrenreich
Professor of Neurology & Psychiatry, Georg-August University of Göttingen

Prof. Dr. Silvio Rizzoli
Neuro- and Sensory Physiology, University Medical Center Göttingen

Members of the Examination Board:

Referee: Prof. Dr. Susann Boretius
Functional Imaging Laboratory, German Primate Center (DPZ), Göttingen

2nd Referee: Prof. Dr. Dr. Hannelore Ehrenreich
Professor of Neurology & Psychiatry, Georg-August University of Göttingen

Further members of the Examination Board:

Prof. Dr. Silvio Rizzoli
Department of Neuro- and Sensory Physiology, University Medical Center Göttingen

PD Dr. Peter Dechent
Department of Cognitive Neurology, University Medical Center Göttingen

Prof. Dr. Ralf Heinrich
Department of Cellular Neurobiology, Georg-August University of Göttingen

Prof. Dr. Christian Griesinger
Department of NMR-based Structural Biology, Max Planck Institute for Multidisciplinary Sciences, Göttingen

Date of oral examination: December 8th, 2023

"Vel tør jeg maaske haabe, at De, naar jeg er kommet til Ende med min Fremstilling, ville indrømme, at Manglerne ikke udelukkende have deres Oprindelse fra mine egne Ufuldkommenheder […], men at de ganske væsenligt ligge i Æmnets Beskaffenhed"

– Carl Lange (1886) "Om periodiske Depressionstilstande og deres Patogenese"

"I may dare to hope that you, when I reach my conclusion, will admit that the limitations do not entirely originate from my own imperfections […], but that they fundamentally lie in the nature of the subject."

– Carl Lange (1886) on "On Periodical Depressions and their Pathogenesis"

ABSTRACT

Equipped with only three protons, lithium stands as one of the most unexpected drug discoveries in history. Despite its initial FDA approval in 1970, lithium's precise mechanism for regulating mood remains largely elusive. Lithium is generally considered a modulator of neurotransmission, an inhibitor of enzymes in the signaling cascade of inositol (1,4,5)-triphosphate and diacylglycerol, and neuroprotective. Yet, the true challenge lies in understanding how lithium effectively treats patients with bipolar disorder. Bipolar disorder is a psychiatric illness that is characterized by recurrent periods of mania and depression, often accompanied by a high suicide rate (12-fold higher than the population average) and various comorbidities. While lithium is an effective drug for some bipolar patients (between 30-50%), it also carries an increased risk of renal disease. It is therefore essential to understand the early stages of lithium treatment and find a way to predict whether a treatment is successful. However, despite extensive research, biomarkers for lithium treatment response have largely eluded scientists.

In this thesis, I aim to tackle a part of this problem, focusing on the effect of lithium on the healthy brain. By isolating the drug from its pathological context, I have focused on characterizing lithium treatment in mice during the first four weeks of treatment. My investigation encompasses three key aspects: lithium distribution in the brain, brain metabolism, and changes in water diffusivity in the brain.

Employing magnetic resonance imaging and spectroscopy, I have looked for biomarkers with a translational perspective. The primary isotope of lithium, lithium-7, is a spin-3/2 nucleus with a nuclear receptivity of 0.29 compared to 1 of protons. Lithium-7 is therefore magnetically active making it possible to detect lithium directly in the brain. Previous studies in humans and animals have revealed an inhomogeneous distribution of lithium in the brain. However, no *in vivo* imaging of lithium in mice has previously been performed. Through optimizing the magnetic resonance sequence and hardware, I successfully performed the first *in vivo* lithium-7 magnetic resonance imaging of the mouse brain (Chapters 2-3). I found lower lithium concentrations in the olfactory bulb and cerebellum compared to the rest of the brain. Furthermore, I successfully estimated the lithium concentration in the brain of mice.

To investigate brain metabolism, I employed magnetic resonance spectroscopy – a technique that relies on the principle of chemical shift. The conventional approach to analyze spectroscopy data is to fit it with a linear combination of basis spectra (model functions of different metabolites). I performed this analysis using a software package called LCModel, which is currently considered the gold standard for *in vivo* spectroscopy. I could show that this software has non-ideal behavior when adding noise to spectra (Chapter 4). To better characterize the impact of adding noise on the quality of the fit, I incorporated data from five different species: mice, rats, marmosets, macaques, and humans. I also developed an open-source toolbox for simulating cortical spectra from these species at various noise levels.

To analyze 3D astrocyte cell cultures within an MRI scanner I developed a magnetic resonance-compatible bioreactor linked to a compact incubator, enabling precise control of

gas mixing and exchange (Chapter 5). Using the bioreactor, I investigated the metabolic response of astrocytes to lithium-enriched media. I found that astrocytes exposed to therapeutic concentrations of lithium (0.78 mM) exhibited reduced levels of myo-inositol and glutamate plus glutamine, while these levels increased at higher lithium concentrations (4.38 mM).

Finally, I established a magnetic resonance-based characterization of the effects of lithium treatment in mice, incorporating structural analysis, metabolic assessments, and diffusion-related changes. I found that mice on a lithium-enriched diet showed elevated levels of myo-inositol, decreased N-acetylaspartate, and reduced diffusivity. At first glance these changes looked bleak – considering that these suggest increased glial content, decreased neuronal health, and inflammation. However, upon further investigation, I found that these were accompanied by a change in the glutamate-to-glutamine ratio and increased neurite density index – changes associated with a potential shift in cell population rather than neurotoxicity.

This thesis starts by developing methods enabling the study of lithium treatment in mice *in vivo*. The second half demonstrates the application of these methodologies and presents evidence for a shift in cell population following lithium treatment. While I obviously cannot claim to have solved the mechanism of lithium action, I have succeeded in delineating a magnetic resonance-based profile of lithium treatment in both astrocytes and mice.

Table of Contents

LIST OF FIGURES

LIST OF TABLES

LIST OF ABBREVIATIONS

^{1}H	hydrogen-1, proton
^{7}Li	lithium-7
^{31}P	phopshorus-31
ADC	apparent diffusion coefficient
Akt	protein kinase B
ANTs	Advanced Normalization Tools
ATP	adenosine triphosphate
AUC	area under the curve
Bcl-2	B-cell lymphoma 2
BDNF	brain-derived neurotrophic factor
bSSFP	balanced steady-state free precession
CHESS	chemical shift selective
Cho	choline
Cr	creatine
CREB	cAMP response element binding protein
DAG	diacyl glycerol
dkntmn	baseline flexibility
DMEM	Dulbecco's modified Eagle's medium
DSURQE	Dorr-Steadman-Ulman-Richards-Qiu-Egan
DTI	diffusion tensor imaging
EPI	echo-planar imaging
FA	fractional anisotropy
FBS	fetal bovine serum
FID	free induction decay
FLASH	fast low-angle shot
FWHM	full-width at half maximum
GABA	γ-aminobutyric acid
Glc	glucose
Gln	glutamine
Glu	glutamate
GSK-3	glycogen synthase kinase 3
IMPase	inositol-1 monophosphatase
Ins	myo-inositol
IP$_3$	inositol 1,4,5-triphosphate
ISIS	image-selected *in vivo* spectroscopy
ISMRM	the international society for magnetic resonance in medicine
LDH	lactate dehydrogenase
MAE	mean absolute error
MEM	minimal essential medium
MR	magnetic resonance
MRI	magnetic resonance imaging
MRS	magnetic resonance spectroscopy
MT	magnetization transfer
mTOR	mammalian target of rapamycin
NA	number of averages
NAA	N-acetylaspartate
NDI	neurite density index
NMR	nuclear magnetic resonance

NODDI	neurite orientation dispersion and density
PCh	phosphocholine
PCr	phopshocreatine
PDE	phosphodiesters
PFA	paraformaldehyde
P_i	inorganic phosphate
PKC	protein kinase C
PLA	polylactic acid
PME	phosphomonoesters
pMg	concentration of free magnesium
ppm	parts per million (unit of chemical shift)
ppmend	end of chemical shift range
ppmst	start of chemical shift range
PRESS	point-resolved spectroscopy
R^2	coefficient of determination
RARE	rapid acquisition with relaxation enhancement
RF	radiofrequency
ROI	region of interest
sddegz	standard deviation of the zero-order phase correction
sddegp	standard deviation of the first-order phase correction
SNR	signal-to-noise ratio
STEAM	stimulated echo acquisition mode
T1 relaxation	longitudinal relaxation
T1 time	longitudinal relaxation time
T2 relaxation	transverse relaxation
T2 time	transverse relaxation time
Tau	taurine
tCr	total creatine
TE	echo time
TMS	tetramethylsilane
tNAA	total N-acetylaspartate
TORC	transducer of regulated CREB
tPCh	total phosphocholine
TR	repetition time
Tx/Rx	transmit-receive
X-nuclei	nonproton nucleus with nonzero spin

1

GENERAL INTRODUCTION

The ancient Romans knew it, so did the Greeks… lithium may be used to alleviate mood imbalance. Well to be more precise, they realized that drinking water from specific alkaline springs could lessen symptoms of mania and melancholia (depression) – thanks to the insights of Soranus of Ephesus[1]. Sadly most of the writings of Soranus of Ephesus were lost to time, while the remainder went largely unnoticed – despite him distinguishing mania and depression as separate, but interconnected illnesses[2] as well as encouraging gentle handling of psychiatric patients with a focus of therapy through speaking to the patients[3]. The notion of alkaline healing waters faded and was replaced by other hypotheses. It should of course be noted that – lithium was first discovered in 1817 after all[4] – Soranus of Ephesus was not aware that lithium was the working element in his treatment.

Almost 1800 years after Soranus of Ephesus discovery, a second discovery of lithium as a therapeutic was made[5]. The brothers Carl and Frederik Lange used lithium to treat patients with periodic[5] and acute[6] depression. This was the first modern usage of lithium carbonate, rather than lithium bromide[7]. However, it required a third discovery, before lithium treatment against "psychotic excitement" caught on[8]. John F. Cade showed that bipolar patients could be brought from the manic to euthymic phase with the help of lithium treatment[8]. It is worth noting that lithium carbonate was first approved in the United States of America in 1970.

Lithium is regarded as the frontline and recommended treatment of bipolar disorder[9] with recent numbers from Sweden indicating that over half of bipolar patients were prescribed lithium[10]. Bipolar disorder is an affective illness characterized by periods of (hypo)mania (elevated mood) and depression – in some cases occurring simultaneously[11–13]. Manic episodes are characterized by an elevation in mood and increased energy, but are often accompanied by psychotic symptoms (e.g. delusion)[14]. In depressive episodes, bipolar patients exhibit only minor differences to patients with unipolar or major depression[14]. Affection approximately 3% of the population in their lifetime, bipolar disorder is among the leading causes of disability in young adults[10,15–18]. Due to its high prevalence, onset in early adulthood, and 12-fold elevated risk of suicide[16], the societal impact of bipolar disorder can hardly be overstated. The direct and indirect societal cost of bipolar disorder have been estimated to be about €28000 per patient (in Sweden) with indirect costs constituting 75%[18]. German estimates from 2004 showed a similar tendency with a combined direct and indirect cost of €5.6 billion[16], while the number for direct costs in 2020 of all affective disorders (ICD-10-F30-39) was €10 billion[19].

On the behavioral level, lithium treatment has shown decreased suicidal behavior and reduction in both manic and depressive episodes[20]. Despite the success of lithium treatment in patients with bipolar disorder, only about 30% of patients respond optimally[21]. Furthermore, lithium treatment can cause nephrogenic diabetes insipidus, a kidney disease characterized by polyuria as the kidneys are no longer able to concentrate urine[22,23]. Long-term treatment (especially at higher doses) can lead to a six-fold increased risk of end-stage renal disease[22]. Despite the usage of lithium salts in treating bipolar disorder patients for almost 75 years[8], lithium treatment is not fully understood. It is therefore of concern that no clear biomarkers exist to indicate the success of lithium treatment in bipolar disorder patients. Furthermore, monitoring treatment efficacy and response in patients is often difficult as clinical symptoms first start to subside after 1-3 weeks of treatment[24], meanwhile frequent blood samples are taken to control lithium dosage and avoid toxicity. Lithium has a low therapeutic index of ~2 and narrow therapeutic window, 0.4-1.2 mM recommend serum concentrations[9].

In this thesis, I have attempted to tackle the main problem associated with lithium treatment – the absence of detectable biomarkers. However, I have approached this from an alternative perspective by using magnetic resonance imaging (MRI) and spectroscopy (MRS) to examine the effect of lithium on astrocyte cell cultures (chapter 5) and the healthy mouse brain (chapter 6), thereby generating an MR-based profile of lithium treatment in the healthy mouse. A challenged of lithium treatment is that there are many brain regions that may be potential targets. I therefore started by developing the tools to study the lithium distribution and characterize MR-detectable biomarkers in the mouse brain. We developed lithium-7 MRI and MRS from the *in vivo* mouse brain for the first time (chapter 2) along with a low-cost radiofrequency (RF) coil with comparable signal quality to commercially available alternatives (chapter 3). In doing so, I was able to show the first *in vivo* lithium-7 images of the mouse brain. In order to reliably analyze MR spectra *in vitro* and *in vivo*, I explored the limitations of LCModel[25] – a fitting software for MRS analysis – and provided an open-source toolbox for simulation of *in vivo* spectra for five different species: mice, rats, marmosets, macaques, and humans (chapter 4). A more detailed overview of the studies included in this thesis is given in section 1.4.

1.1 MAGNETIC RESONANCE

MRI and MRS are essential tools used in both clinical diagnostics and preclinical research. They exploit the principle of nuclear magnetic resonance (NMR). In short, protons in magnetic field exist in two energetically distinct states that are unequally populated. A second small field can be used to excite protons in the low energy state. The excited protons can be detected using a small antenna. The signal may then be transformed into either images (MRI) or spectra (MRS). The following sections will elaborate on the principle of NMR, spectroscopy, and imaging.

1.1.1 Principles of nuclear magnetic resonance

All nuclei have a total angular momentum, which we will refer to as spin. This is a property of the nucleus arising from the constituent nucleons (protons and neutrons). Protons and neutrons are both spin-1/2 particles that consist of quarks and gluons; however, why this results in the intrinsic property that we refer to as spin is well beyond the scope (and interest)

of this thesis. We will simply consider spin an intrinsic property of nucleons. However, it is important that protons and neutrons are not elemental particles, because despite an absence of net charge, neutrons – like protons – have a magnetic moment (although the magnetic moment of a proton and neutron is not equal). We may therefore treat protons and neutrons jointly for the ensuing discussion. Since the proton is the most abundant nucleus in the human body, it will be used for the description of NMR.

As protons have spin, they have a nonzero net angular momentum and therefore a nonzero magnetic moment. Consequently, in the presence of an external magnetic field, these spins may align with (also referred to as parallel or spin-up) or against (also referred to as antiparallel or spin-down) to the external magnetic field. As the magnetic moment is placed in a magnetic field, it will experience a torque, which will make it precess about the axis of the external magnetic field. The rate of precession is known as the Larmor frequency (ω_L), which depends on the gyromagnetic ratio, γ, – the ratio of the magnetic moment and the angular momentum – and the field strength of the external magnetic field, B_0.

$$\omega_L = \gamma \cdot B_0$$

In the two quantized states, parallel alignment is energetically favorable compared to antiparallel alignment. The energy difference (ΔE) between two neighboring energy levels may be expressed in terms of Planck's constant (h) and Larmor frequency – thereby increasing as a function of field strength.

$$\Delta E = h\omega_L$$

While NMR may be observed on the single proton level, it is the behavior of an ensemble of protons that makes this technique interesting for biomedical research. By considering a population of protons, we can describe how many align parallel and antiparallel to the field. The distribution of spins (N_{down}/N_{up}) at equilibrium is described by Boltzmann statistics (k is Boltzmann's constant and T is temperature).

$$\frac{N_{down}}{N_{up}} = e^{-\frac{\Delta E}{kT}} = e^{-\frac{h\omega_L}{kT}}$$

For a proton at 37°C in a standard clinical MRI system with a field strength of 3T, the difference between parallel and antiparallel alignment is a few spins per million. However, this difference in distribution between the two energy levels results in a net magnetization. Using an excitation that fulfills the resonance criterion, one can manipulate this equilibrium.

Prior to explaining how a simplified MR experiment works, the above explanation must be extended to include X-nuclei (nonproton nucleus with nonzero spin). Calculating the spin of a nucleus is not trivial; however, using a nuclear shell model, it is possible. For the sake of brevity, we will not discuss this in detail, but rather focus on the general rules. If both the number of protons and neutrons are even, then the nucleus will have a spin of 0. Carbon-12 is an example of a spin-0 nucleus. If the mass number is odd, then the spin will be half-integer. If both the number of protons and neutrons are odd, then the nucleus will have a positive integer spin – deuterium (spin-1) is the simplest example with one proton and one neutron.

At this point, we can describe the simplest MR experiment. We want to disrupt our equilibrium and observe the system as it reverts. The way we disturb – or more correctly

perturb – the system is through a secondary electromagnetic field. This field is only applied for a short time and needs to match the Larmor frequency in order to meet the resonance criterion. As the Larmor frequency is in the order of megahertz, we will refer to this field as a RF pulse. Following the RF pulse, the net magnetization vector has been rotated by 90° and is now orthogonal to the external magnetic field, we refer to this step as the excitation. The excitation angle is referred to as the flip angle, in this example 90° is chosen for conceptual simplicity. The net magnetization vector continues to precess about the external magnetic field; however, as it is now perpendicular to the external magnetic field it can be observed. As the protons are now in an excited state and precessing in the same phase, there are two types of relaxation that can occur: longitudinal and transversal. Longitudinal relaxation – also known as T1 relaxation or spin-lattice relaxation – is the process by which spins return from the excited state back to thermal equilibrium. This process is described by one minus an exponential decay with the time constant T1 (T1 time). The longitudinal relaxation therefore describes the relaxation along the axis of the external magnetic field, commonly referred to as the z-axis. The transverse relaxation – also known as T2 relaxation or spin-spin relaxation – arises from the dephasing of the individual spins. The transverse relaxation is also governed by an exponential decay with the time constant T2 (T2 time); however, since the transverse relaxation is about the dephasing of spins, it describes relaxation orthogonal to the external magnetic field, commonly referred to as the xy-plan. For most biological tissues, the T2 time is shorter than the T1 time or in other words the transverse relaxation is faster than the longitudinal relaxation. Following an excitation, the signal will therefore decay in amplitude, which is called the free induction decay (FID). This free induction decay is usually what is detected in MR experiments, if it is Fourier transformed it will give a spectrum, which shows the signal intensity at different frequency components – indicating the different chemical environments present in the solution/tissue, the foundation of NMR spectroscopy.

Having discussed X-nuclei and the simplified NMR experiment, we will conclude the theory section by looking at the maximum signal intensity and relaxation properties. The nuclear receptivity, P_X – relative to proton, which is assigned 1 – is a measure of the potential signal intensity that can be achieved for a given nucleus – it depends on dependent on the gyromagnetic ratio and spin.

$$P_X = \left| \frac{\gamma_X^3}{\gamma_{^1H}^3} \right| \cdot \frac{I(I+1)}{\frac{1}{2}\left(\frac{1}{2}+1\right)}$$

The nuclear receptivity is used to approximate the signal-to-noise ratio (SNR) of a nucleus at thermal equilibrium or *in vivo*. It is worth noting that using techniques such as hyperpolarization (to change the equilibrium) or isotopic labelling (to change the abundance) one can achieve higher SNR than predicted by the nuclear receptivity. However, as neither of these techniques are relevant for hydrogen-1 (proton), lithium-7, or phosphorus-31, they will not be discussed. Protons are spin-1/2 with a natural abundance of 99.99% and a gyromagnetic ratio of 42.58 MHz T^{-1}. Lithium-7 is a spin-3/2 nucleus with a natural abundance of 92.7% and a gyromagnetic ratio of 16.55 MHz T^{-1}. The nuclear receptivity of lithium-7 is therefore 0.29; however, the concentration of lithium in the brain – even after therapy – is less than 2 mM. Phophorus-31 is a spin-1/2 nucleus with a natural abundance of 100% and a gyromagnetic ratio of 17.24 MHz T^{-1}, which means that nuclear

receptivity is 0.06. However, since phosphorus-containing metabolites are common, the *in vivo* concentration of (detectable) phosphorus in the brain is roughly 10 mM. The SNR is proportional to the nuclear receptivity, concentration [X], and isotopic abundance (A_X) of the nucleus.

$$SNR \propto A_X \cdot [X] \cdot P_X$$

We can therefore see that the anticipated signal for a proton experiment is roughly 10^5 times larger than lithium-7 (after treatment) and phosphorus-31. As a result, X-nuclei experiments require longer acquisition durations and more efficient MR sequences.

1.1.2 Spectroscopy

MRS is an extension of the classic NMR experiment described in section 1.1.1. However, for *in vivo* measurements, we would like to detect signal from only specific regions – to determine metabolism in cortex, we do not want to observe signal from subcutaneous fat outside the brain. In other words, the signal must come from a specific region of interest or voxel (volume element). A voxel may be localized using a variety of different methods – in MR research we call them sequences, example in Fig. 1-1; however, the main prerequisite is that only signal inside the voxel is detected. In this thesis, I used three different sequences for single-voxel spectroscopy – stimulated echo acquisition mode (STEAM), point-resolved spectroscopy (PRESS), and image-selected *in vivo* spectroscopy (ISIS). I used STEAM and PRESS for proton MRS and ISIS for lithium-7 and phosphorus-31 MRS.

STEAM[26] and PRESS[27] are commonly used MR spectroscopy sequence that use three RF pulses with orthogonal gradients to produces an echo arising only from the desired voxel, Fig. 1-1. However, STEAM achieves this using a stimulated echo approach – three consecutive 90˚ pulses – whereas PRESS generates a double spin echo – with 90˚-180˚-180˚ RF pulses. This means that STEAM can be acquired using shorted echo times allowing for better visualization of metabolites with short T2 relaxation times. However, as a stimulated echo decays faster than a spin-echo, the expected signal of a STEAM sequences is half that of a PRESS sequence[28]. PRESS is the conventional sequence of choice at clinical field strengths (0.5-3T), but at ultrahigh field (>7T) STEAM is the preferred method due to the possibility of short echo times.

Most metabolites in the brain are present at concentrations less than 10 mM, which is significantly less than the ~40000 mM of water (depending on brain region)[29]. As a result, if one acquires a spectrum of the brain, one will only see water. Spectra are therefore always acquired with water suppression, which in this thesis was performed using chemical shift selective (CHESS) water suppression[30,31]. CHESS water suppression uses three long RF pulses – with a narrow frequency range – to suppress only the water signal at 4.7 ppm. Each RF pulse is followed by a spoiler gradient, which dephases any residual signal to prevent accidental coherences. This allows for the detection metabolites that are present at concentrations of at least 0.5 mM. The effect of water suppression on proton spectra is visualized in Fig. 1-1.

Contrary to proton spectroscopy, lithium-7 and phosphorus-31 spectroscopy is commonly acquired using an ISIS sequence[32]. An ISIS sequences uses four RF pulses, as opposed to three in both STEAM and PRESS. The first three pulses of an ISIS sequence are slice-
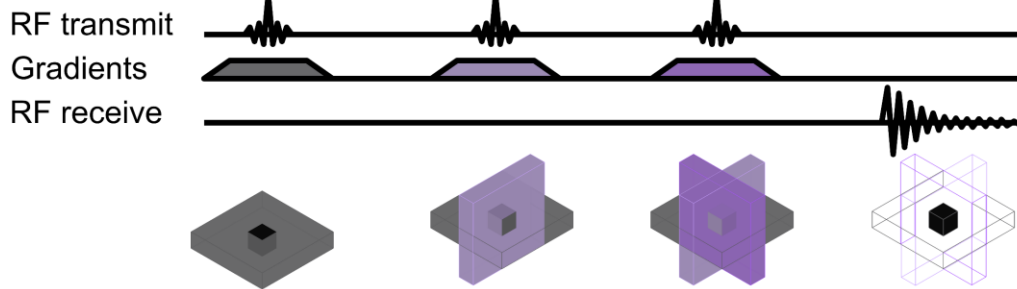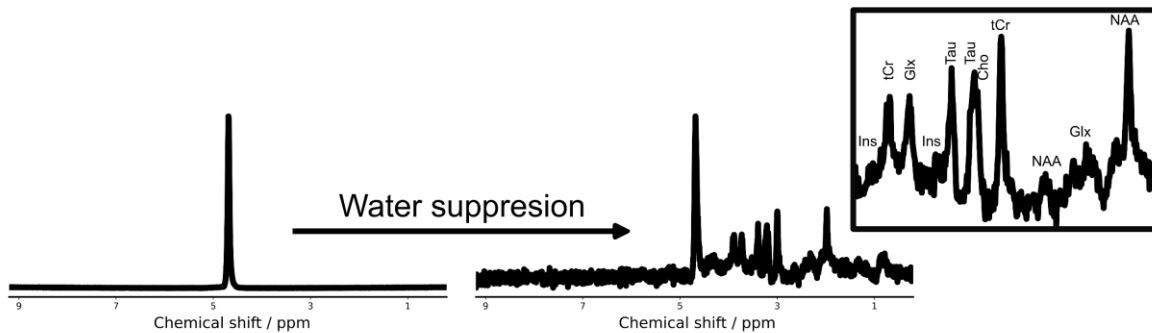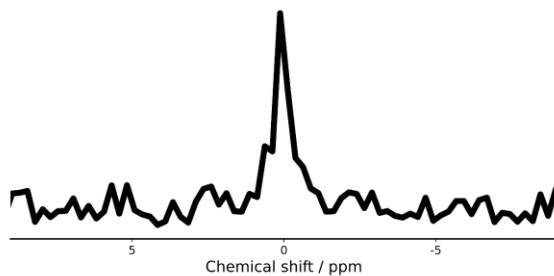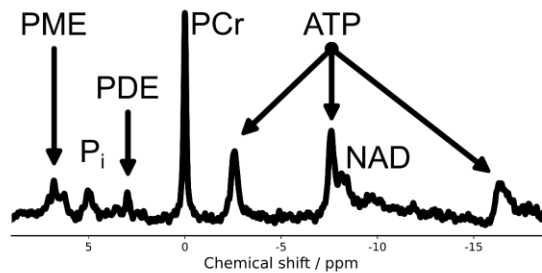
*Figure 1-1: **Magnetic resonance spectroscopy**. Spectroscopy localization is performed using at least three different localization pulses. For proton spectroscopy water suppression is a necessity as the concentration of metabolites are about 10000-fold lower than water. Lithium-7 spectra have a single resonance at 0 ppm. Phosphorus-31 spectra are characterized by phosphocreatine at 0 ppm, ATP upfield of phosphocreatine, and inorganic phosphate as well as phosphoesters downfield of phopsphocreatine.*

selective inversion pulses (180°), similar to those in Fig. 1-1. These pulses are followed by a non-localized excitation RF pulse (90°) followed by the signal acquisition. As the localization is performed prior to the excitation, this sequence can acquire signal with an echo time close to 0 ms, thereby detecting almost all the signal. However, the ISIS sequence has one major drawback, namely that because the excitation is non-localized, the signal will arise from the whole imaging volume and thereby also outside the desired voxel. As each of the three inversion pulses will have an associated gradient, one can solve this problem by varying whether the inversion pulse is with or without a gradient. If one acquires 8 ISIS spectra, then every iteration of gradient on and off can be acquired. One can show using a matrix to describe the phase of the spins that if one pairs these into four groups differing only by one gradient (e.g. on|off|off and off|off|off), then the sum of the difference between groups will give signal only from the central voxel[32]. Moreover, the signal intensity will be eight times greater than the intensity in a single spectrum, thus resulting in no signal penalty from combining the spectra. However, the ISIS sequence is especially

prone to motion related artifacts, as movement within this block of eight spectra will lead to errors during the subtraction. For this reason, ISIS spectroscopy is not commonly used for proton spectroscopy; however, as the signal can be acquired with short repetition times, it is a well-suited MR sequence for most X-nuclei.

Spectroscopy is analyzed in the frequency domain. However, since the operational frequency is field strength dependent, the location of two peaks will be field strength dependent. In spectroscopy, the chemical shift, δ, is plotted along the x-axis and has the unit parts per million (ppm). The main advantage of the chemical shift is that it is field independent, because it is defined relative to a reference – tetramethylsilane (TMS). The chemical shift of compound X (δ_X) can therefore be calculated based on the frequency of X (v_X) and TMS (v_{TMS}).

$$\delta_X = \frac{v_X - v_{TMS}}{v_{TMS}} \cdot 10^6$$

This allows spectra to be compared at different field strengths and systems. However, it should be noted that the coupling constants are also field independent; however, as they are measured in Hz, they do visually change due to the definition of the chemical shift. The area under the curve of a peak in the spectrum depends on the concentration and number of protons. We note that for spectra with a nonzero echo time and/or short repetition time (less than five times the T1 time) the area under the curve will also depend on the transverse and longitudinal relaxation rates.

The proton spectrum of the mouse brain is characterized by the N-acetylaspartate peak at 2 ppm. Between N-acetylaspartate and creatine/phosphocreatine (~3 ppm), glutamate, glutamine, and GABA contribute to the signal – glutamate and glutamine also give rise to signal at 3.8 ppm. Creatine and phosphocreatine can be distinguished by their peak at 3.9 ppm, where phosphocreatine (due to the phosphate) is shifted further downfield – towards water. Choline and the two taurine peaks are in the range between 3.2-3.4 ppm. Myo-inositol has peaks at 3.5-3.6 ppm, but more easily noticeable at 4.05 ppm, labelled proton spectrum in Fig. 1-1. Lithium-7 shows a single peak. Phosphorus-31 is characterized by a larger phosphocreatine peak defined as 0 ppm. Upfield of phosphocreatine (towards negative numbers) there are the three peaks arising from the three phosphates on ATP – (in order γ, α, β). Downfield of phosphocreatine (higher values) there are peaks arising from phosphodiesters (~3 ppm), inorganic phosphate (~5 ppm), and phosphomonesters (~8 ppm) – labelled phosphorus-31 spectrum in Fig. 1-1.

1.1.3 Imaging

In this thesis, I employed three main MRI techniques – structural, diffusion, and X-nuclei. I will discuss each of these techniques in brief with a focus on how they are acquired as well as their application.

Structural MRI was performed using fast-low angle shot (FLASH) sequence with a magnetization transfer (MT) pulse added. This sequence allows for fast three-dimensional imaging of the mouse brain with a 100-μm isotropic resolution. MT relies on using off-resonance RF pulses that saturate the signal in the exchangeable protons of macromolecules[33], fig 1-2. These protons are exchanged between the macromolecules and the surroundings, which results in a partial saturation of the water signal. However, the
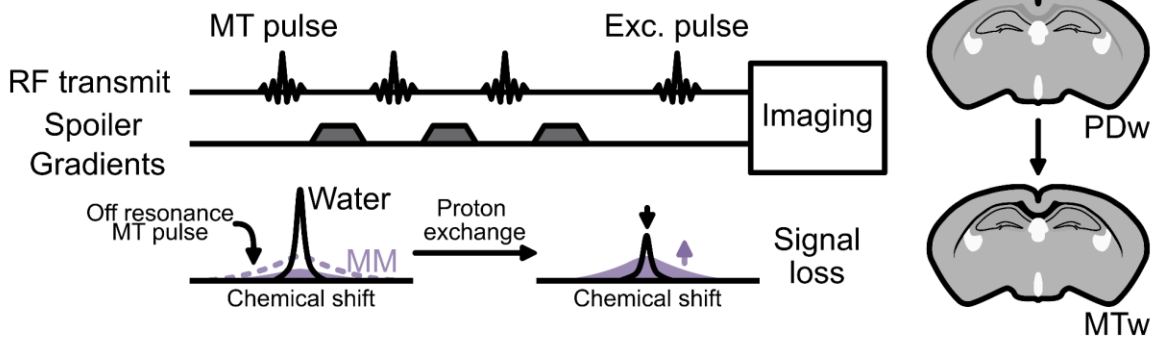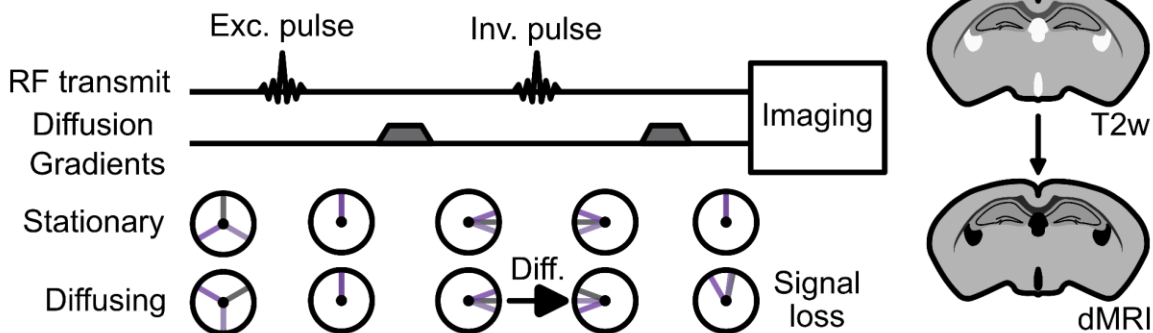
Figure 1-2: **Magnetic resonance imaging contrasts.** *Magnetization transfer (MT) uses one (or more) off resonance radiofrequency pulses to saturate the macromolecular protons (MM). The exchangeable protons from the macromolecules will then exchange with free water protons, which leads to signal loss. Diffusion MRI (dMRI) uses diffusion gradients to dephase the spins, then using an inversion pulse and the same diffusion gradient re-phases the spins. However, diffusing spins – like in the ventricles – are not re-phased correctly, leading to signal loss. PDw – proton density weighted; T2w – T2-weighted MRI.*

saturation of the water signal is dependent on the macromolecular content of the tissue, so the effect is larger in brain regions that have higher amounts of macromolecules – such as myelin. Using MT MRI, we get a good grey-to-white matter content in mice with high spatial resolution and fast acquisition times, Fig. 1-2.

A diffusion MRI sequence is built-up in five different phases – excitation, diffusion gradient, inversion, diffusion gradient, acquisition, Fig. 1-2. In this thesis, I focused on diffusion tensor imaging (DTI)[34,35] and neurite orientation dispersion and density imaging (NODDI)[36], I will therefore describe diffusion sequences that use multiple gradient strengths and directions. This is an extension of the conventional diffusion-weighted imaging. The excitation and acquisition phases are standard for MRI sequences; however, it should be noted that for *in vivo* experiments the acquisition is usually done with either echo-planar imaging (EPI) or spiral read-out, both of which allow for faster acquisition of the k-space than conventional line-by-line cartesian MRI, Fig. 1-3. EPI is commonly used for functional MRI, because it allows for the acquisition of the whole k-space in a single repetition time – for diffusion it is common to acquire this in multiple shots (or segments). However, EPI sequences are prone to distortion artifacts due to rapid switching of gradients. Spiral read-out gradients are sinusoidal switching of the gradients allowing for a fast read-out with low gradient usage – however, due to non-ideal gradients and potential movement, spiral read-outs often have blurring leading to lower effective spatial resolution than what was originally encoded. In this thesis, diffusion MRI was acquired with EPI. The diffusion gradients are directional and
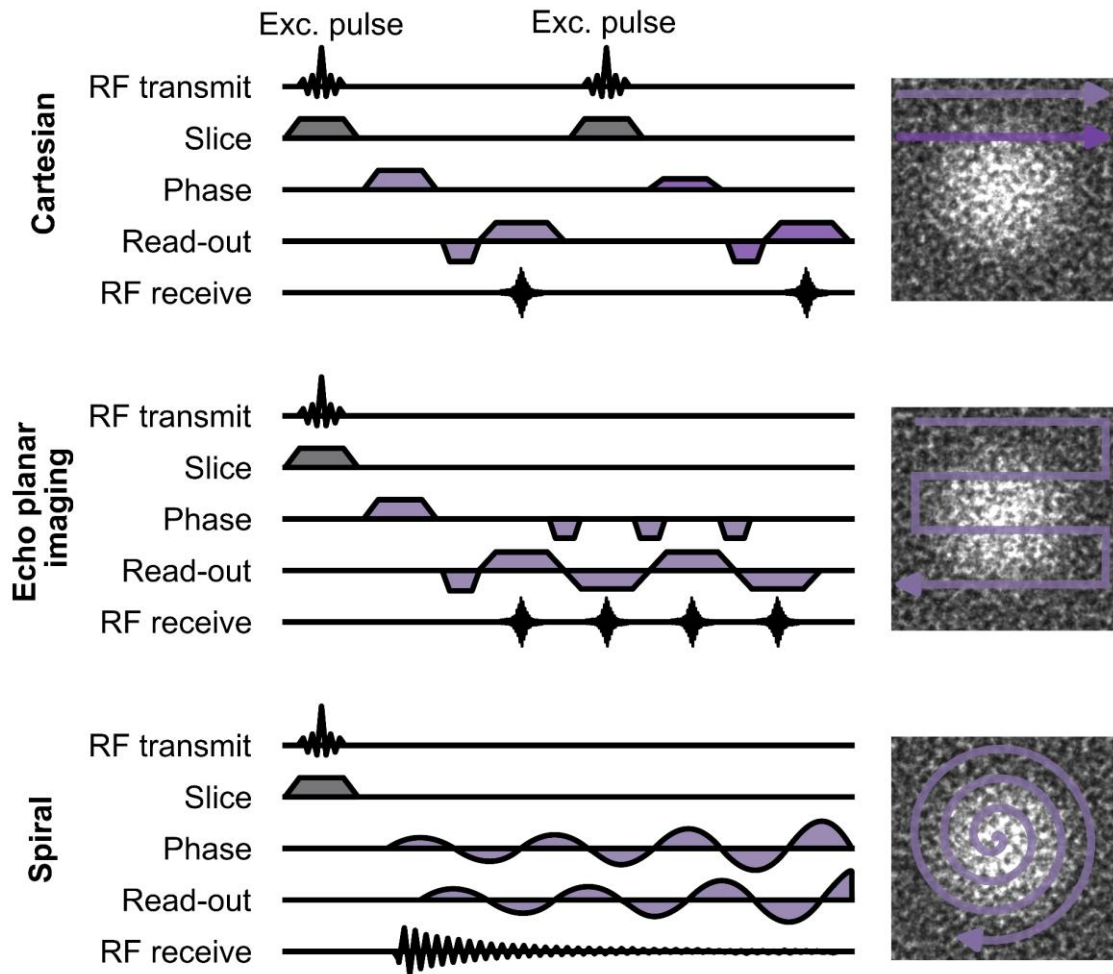
*Figure 1-3: **Magnetic resonance imaging sequences.** Simple Cartesian sequences allow for reliable imaging with high spatial resolution; however, they are comparatively slow as they only acquire one k-space line per repetition time. Echo planar imaging is a faster sequence, which acquires multiple k-space lines simultaneously. However, it is prone to distortion artifacts, due to the high rate of gradient switching. Spiral-encoding uses sinusoidal gradient switches to allow for fast imaging of the whole k-space in a single repetition time, but with comparatively low gradient usage. However, due to the relatively long sampling time of a spiral read-out and gradient imperfections, spiral read-out leads to smoothing at high spatial resolution.*

serve to dephase the spins. The time between the diffusion gradients and the inversion is called the diffusion time. The inversion pulse is placed exactly in the center of the two diffusion gradients, just as the two diffusion gradients are identical. As a result, any spin that is stationary will rephase during the second diffusion gradient. However, for spins that are moving (or diffusing) they will not rephase, which will lead to signal loss, Fig. 1-2. Diffusion MRI may be used to image tissue microstructure, as the diffusion gradients are directional thus allow for the characterization of both the directionality and amount of diffusivity in a voxel. The diffusivity will depend on the diffusion time, gradient amplitude, and gradient duration. These three values are combined to define a factor – called a b-value – that allows for describing the diffusion experiment in a comparable manner between field strengths and scanner types. In short, the b-value is proportional to the square of gyromagnetic ratio, diffusion time, gradient amplitude, and gradient duration[37]. For the sake of completion, it should be said that the b-value is proportional to the square of twice the diffusion time, which is the time between the centers of the two diffusion gradients.

Diffusion tensor imaging uses different directions and b-values to determine the direction and strength of diffusion[38]. Diffusion along the main diffusion direction is called axial

diffusion and diffusion orthogonal to the main diffusion direction is called radial diffusivity. The average diffusion in all directions is referred to as the mean diffusivity or the apparent diffusion coefficient. The square root of the ratio of sum of squared differences between the three directions to twice the sum of squares of the three directions is referred to as the fractional anisotropy (FA). If the diffusion is equal in every direction (spherical diffusion) then FA=0, whereas if the diffusion is only along one direction (radial diffusivity of zero) then FA=1.

NODDI is a more advanced diffusion model, which uses a three-compartment model: intra-neurite, extra-neurite, and free water[36,39]. The method is useful for distinguishing the diffusion inside and outside of neurite bundles; however, it is a model and only works for well-defined cases. In this thesis, I use this model to support my conclusions, but not as the main explanation for them.

X-nuclei MRI – as with spectroscopy – suffers from low SNR. Phosphorus-31 is possible to image; however, due to the contribution of signal from many different metabolites it is not meaningful. However, lithium-7 MRI – although still in its early stages – offers an opportunity to directly image the drug. The historical usage and approaches toward lithium-7 MRI will be discussed in detail in chapter 1.3, in this section I will focus on the prerequisites for performing X-nuclei MRI. X-nuclei MRI requires fast acquisition with a high number of averages to get sufficient signal for meaningful interpretation. In this thesis, I explored two main approaches: SPIRAL MRI and balanced steady-state free precession (bSSFP) MRI. SPIRAL MRI has been discussed for diffusion; however, due to the low spatial resolution of X-nuclei MRI blurring is not as prominent. This means that spiral read-outs are ideal for sampling X-nuclei combining fast acquisition and short echo times. bSSFP relies on creating a steady state and maintaining it during the acquisition. The key to bSSFP is that the gradient moments are balanced and the excitation pulses flip the magnetization to the other side, thus creating a steady state for the excitation – this allows for multiple k-space lines to be read-out in succession without having relaxation effects. However, bSSFP suffers from larger artifacts due to inhomogeneities, because in these areas a proper steady state cannot be maintained leading to signal loss and "black band" artifacts. As such, although theoretically the ideal sequence for X-nuclei MRI, in practice bSSFP is difficult to execute on a preclinical MRI system.

1.2 LITHIUM AND THE BRAIN

The molecular weight of lithium is 6.94 with the primary isotope (92.7% natural abundance) being lithium-7. It has been shown that lithium-6 and lithium-7 have different diffusivities[40] and induce different behaviors in rodents[41–44]; however, as this thesis is only concerned with lithium food without isotopic enrichment, these differences will be left for the general discussion(chapter 7). With only three protons, lithium is the third smallest element, yet it is a frontline treatment of bipolar disorder[45]. However, the mechanism of action that leads to the mood-regulatory effect of lithium still remains unclear[20]. In the following sections, I will explore the three main effects of lithium on the brain: modulation of neurotransmission, cellular signaling pathways, and neuroprotective effects. It is worth noting that the division of the mode of action of lithium into these three classes is largely artificial. In the final section, I will briefly discuss which effects are believed to be most prominent at therapeutic concentrations and thereby likely to provide the mood-regulatory effect.

1.2.1 Modulation of neurotransmission

Lithium is known to modulate multiple different neurotransmission systems[20,46]: glutamatergic, dopaminergic, serotoninergic, GABAergic (γ-aminobutyric acid). Glutamatergic signaling is excitatory and mediated by four different families of receptors: AMPA, kainate, NMDA, and metabotropic. It has been shown that glutamate levels are elevated in mania[47] and that lithium inhibits NMDA receptors, reducing the calcium response[48]. Furthermore, lithium is known to inhibit glutamate reuptake in the acute application on brain slices; however, it increases glutamate uptake in chronic treatment, in mice[49]. Lithium protection against glutamate-mediated excitotoxicity was found in rat neurons that were pretreated with lithium[50]. In humans, it has been shown that the glutamate concentration in bipolar patients with therapeutic concentration of lithium (>0.5 mM in plasma) was increased, on the contrary bipolar patients with lithium levels below this have decreased glutamate[51]. It has been theorized that the inhibition of the glutamatergic system is a driving force for the anti-manic action of lithium[46,52]. As with glutamate, it is known that dopamine neurotransmission is increased during mania[53]. While dopamine levels do not appear to decrease, dopaminergic activity decreases under chronic lithium administration in rats[54,55]. Serotonin is increased extracellularly following lithium administration[56] as a result of the inhibition of serotonin autoreceptors[57]. The GABAergic system is known to be activated by acute high doses of lithium[58]. GABA is increased in the cerebrospinal fluid following lithium treatment[59,60]. It may therefore be said that the effect of lithium on neurotransmission is a down regulation of excitatory circuits and an up regulation of inhibitory systems. However, one must be careful with this claim as many of the processes are dose-dependent and disease-state dependent.

1.2.2 Cellular signaling pathways

I will focus on three proteins that are inhibited by lithium: inositol-1 monophosphatase (IMPase), protein kinase C (PKC), and glycogen synthase kinase 3 (GSK-3). As these proteins are involved in processes that may (in part) be visualized by MRS.

The phosphoinositide cycle is known for its production of two secondary messengers IP_3 (inositol 1,4,5-triphosphate) and DAG (diacyl glycerol)[61]. This leads to PKC activation via IP_3 induced calcium release and DAG directly interacting with PKC[62]. PKC regulates the phosphorylation of GSK-3[63] – a threonine/serine kinase that is involved in a myriad of cell processes including metabolism and apoptosis[64]. The IMPase and GSK-3 magnesium sites are vulnerable to exchange with lithium ions[65]. Furthermore, in rats, myo-inositol is depleted and myo-inositol 1-phosphate is increased following lithium treatment[66,67]. This hypothesis of lithium treatment – although studies in humans have produced mixed results[68–71] – became known as the inositol depletion hypothesis[61]. Lithium decreased the PKC activity in the rat brain following four weeks of treatment, but not after five days[72]. The regulation of PKC by lithium has led to the hypothesis that regulation of this signaling cascade is important for the anti-manic effect of lithium treatment[73]. Through direct inhibition of GSK-3[74], lithium activates the neuroprotective Akt (or protein kinase B) signaling pathway[46,75]. It is clear that lithium alters cellular signaling pathways, which now allows us to focus on how these alterations are neuroprotective.

1.2.3 Neuroprotective effects

Having briefly mentioned the Akt signaling pathway in the previous section, I will focus on some of the neuroprotective effects of lithium. Lithium inhibits autophagy indirectly, as the inhibition of GSK-3 – contrary to IMPase – is known to activate mTOR (mammalian target of rapamycin) leading to decreased autophagy[76]. Another major pathway that is altered by lithium, thus leading to neuroprotective effects is through the transcription factor CREB (cAMP response element binding protein). CREB activity is increased when exposed to lithium; however, only when there is no modification to the TORC (transducer of regulated CREB) binding site[77]. CREB facilitates the expression of both brain-derived neurotrophic factor (BDNF) and B-cell lymphoma-2 (Bcl-2)[78]. BDNF is a neurotrophin – a group of proteins involved sustaining neuronal health and growth[79,80]. Decreased BDNF has been observed in mood disorders[80–82]; lithium and antidepressants have been shown to increase BDNF, which may promote neurogenesis[83,84]. Bcl-2 is an apoptosis regulator[85–87], increasing the expression Bcl-2 has an anti-apoptotic effect[88,89]. It may be said that lithium has a general neuroprotective effect; however, this effect is likely the result of these pathways being down-regulated in bipolar disorder (and other mood disorders). This fact highlights the general difficulty in discerning the molecular effect of lithium from the function of the lithium during treatment for bipolar disorder.

1.2.4 The combined effect

The combination of decreased excitatory neurotransmission, altered secondary messenger signaling, and increased neuroprotection may explain both the anti-manic and stabilizing effect of lithium. However, as these processes are difficult to study *in vivo*, researchers have looked for signs of their presence in bipolar patients using MRI and MRS. N-acetylaspartate – considered a marker of neuronal health and integrity – has been found to be increased following lithium treatment in bipolar patients[90,91]. These findings correlate well with the increased grey matter volume and density of lithium treated bipolar patients, but not in lithium-naïve patients[92,93]. Although it should be mentioned that lithium treatment does not always lead to increased N-acetyl aspartate in bipolar patients[68]. Furthermore, in Canavan disease, which is characterized by elevated concentrations of N-acetylaspartate, lithium treatment yielded decreased N-acetylaspartate[94]. Myo-inositol changes associated with lithium have showed a variety of effects from the anticipated decrease[67,95,96] to no change[68,97,98] and even an increase of myo-inositol following lithium treatment[99,100].

However, as ideal lithium responders make up only about 30% of bipolar patients[21], it is fair to wonder whether lithium response in itself may be a diagnostic tool for subtype of bipolar disorder[20]. This hypothesis is supported by lithium-responders having low rates of comorbidities[20], longitudinal stability, family history suggesting positive response, and shortage of biomarkers predicting lithium-response.

1.3 VISUALIZING LITHIUM IN THE BRAIN

Lithium is a treatment for bipolar disorder, first described in the 1940s, it has been the clinical standard since its FDA approval in 1970. As a drug, it has garnered much fascination for its simplicity. Lithium-7, the primary isotope, is an MR visible nucleus. ^{7}Li MRI and MRS was first acquired in the 1980s[101,102]; however, developments have been hindered by the low SNR and *in vivo* concentration. The average ^{7}Li T1 time in the brain across known

studies is 3.6±1.3 s; however, larger variability in T1 time measurements have been observed[101,103–116]. Most studies found a two-component T2 time[101,103,111,114,116] equal to 43±25 ms for the short and 355±154 ms for the long T2 component, where the short component made up the majority. The relatively long T1 time and a short T2 time is an unfavorable combination for MR measurements. Consequently, sequence choice is essential to optimize the low SNR.

1.3.1 MR Spectroscopy: lithium pharmacokinetics

Lithium uptake in the rat brain has been studied following an intraperitoneal injection[103], which showed a maximum lithium concentration after 8 hours in the brain. The blood concentration peaked within a maximum of 30 minutes. It was observed that both uptake and elimination of lithium was faster in serum than the brain. While the uptake kinetics of lithium following an intraperitoneal injection are of some interest, they were tested on lithium-naïve rats. The concentration of lithium (intraperitoneal injection twice a day) in the rat brain at 6.6 days and 16.1 days showed that the average lithium brain concentration was correlated and, in over half the animals, lower after 16.1 days compared to 6.6 days of treatment[117].

Human studies on the pharmacokinetics have primarily involved psychiatric patients; however, the first ^{7}Li MRS study on lithium uptake kinetics was conducted on healthy volunteers[118]. Unsurprisingly, lithium uptake following oral administration was faster in serum than muscle and brain, but neither serum nor brain concentrations reached equilibrium in the seven days of treatment[118]. Similar to the experiments performed on rats, lithium in humans was eliminated slower from the brain than serum[104,118–121].

The lithium brain-to-serum ratio has often been viewed as a crucial marker for treatment efficacy, due to the narrow therapeutic window of lithium. As the elimination in the brain is slower than serum, lithium brain concentrations may exceed serum concentrations during washout periods[119,121]. We note that in most older studies, as reviewed by Komoroski[122], the human brain-to-serum ratio of lithium was in the range of 0.4-0.8, lower than the rat brain-to-serum of roughly 0.9. The mouse lithium brain-to-blood ratio has been estimated to be 1.2 for C57BL mice[123]. More recent data have showed similarly large variability in brain-to-serum concentrations ranging from 0.33-0.78 with most studies finding ratios close to 0.4[112,113,115,124]. Intriguingly, a somewhat recent *ex vivo* study in rats found a brain-to-serum ratio of 0.4, which is significantly lower than expected[116]. It is worth noting that the brain-to-serum ratio varies between illness state (euthymic vs. manic)[125], with age[126], and between responders and non-responders[127], which makes the assessment and understanding difficult. Due to the large variations between mood states and with age, serum lithium concentrations remain a poor marker for treatment efficacy.

1.3.2 MR Imaging: lithium distribution in the brain

Lithium distribution in the brain is heterogeneous. This fact has been reiterated across species using different techniques[109,115,116,124,128–134]. Since lithium treatment in humans has side effects, few MR experiments have been conducted in healthy adults and none of these have included imaging[113,118,119,121]. Increased lithium has been found in the brain stem, subcortical areas, and white matter in humans[115,128]. However, large inter-subject variation was present, suggesting that distribution and clinical response may be linked. As lithium-7

MRI is still in the early stages of development, despite first measurements in 1985[102], the *in vivo* distribution of lithium is not well established. Imaging has been further complicated by low SNR and long acquisition times. In rodents, where acquisition time is less problematic, studies on chronic lithium administration have not reached consensus on the distribution in the brain, although low concentrations in the cerebellum have been reported[116,132].

1.3.3 Non magnetic resonance methods

Multiple methods that do not rely on MRS and MRI have been proposed over the years. I will look at three main techniques: flame photometry, neutron irradiation, and ion imaging. While these techniques are useful for determination of the concentration of lithium ions, they may not be performed on tissue *in vivo*. Ion selective electrodes, a common technique used to determine serum lithium concentrations in the clinical setting, will not be discussed as it is not useful for the examination of tissue[135].

For flame photometry, we will split this into two different developments namely atomic emission spectroscopy and atomic absorption spectrometry. As the names suggest, the former measures the emission of radiation from the sample, whereas the latter measures the light absorption of the sample. Atomic emission spectroscopy was initially performed on for the measurement of lithium in fluids and dissolved tissue[136,137]. It has been shown that atomic absorption spectroscopy performs at a comparable level to atomic emission spectroscopy[138]. However, the major limitation of both methods is that only dissolved, homogenized tissue may be measured. While useful for fluids – e.g. serum and cerebrospinal fluid, these methods serve as endpoints for the animal when performed on tissue. Furthermore, they are not imaging techniques and brain regions have to be dissected to achieve region specificity.

The neutron irradiation studies of lithium rely on a (n,α) nuclear reaction – specifically ^{6}Li (n, α) ^{3}H – that produces alpha particles, which can be detected[139]. In short, fresh tissue is frozen in liquid nitrogen and sliced into ~10 µm thick slices. For the measurement, a slice is placed on a detector – cellulose nitrate on plastic – and irradiated with neutrons. Usually, the detector is treated with sodium hydroxide following the experiment to improve the size of the newly generated particles (from the irradiation). These studies have shown that in rodents grey matter has higher lithium concentrations than white matter[139,140]. While this technique allows for high spatial resolution, 3-5 µm, it may only be performed *ex vivo* on frozen brain samples. Furthermore, the experiments require a neutron source – comparatively rare – and as the quantification is an image of the detector, it is not trivial.

Ion imaging has been performed using time-of-flight secondary ion mass spectrometry imaging on mouse brains[132]. In short, secondary ion mass spectrometry uses an ion beam – bismuth(III) ions for example – that generates secondary ions in the sample, which are observed. Using the information about the time between irradiation and detection (time-of-flight) allows for the discrimination of different masses. The ions will have different velocities as they have the same kinetic energy. This technique allows for both high spatial resolution and a good separation of masses, which makes it suitable for the detection of lithium in the brain with a pixel size of ~5 µm. It should be noted that similar to the neutron irradiation techniques, time-of-flight secondary ion mass spectrometry also requires the tissue to be frozen, sliced thinly, and then dried[132]. The usage of secondary ion mass spectrometry for examination of biological tissue is an interesting research tool; however, as it does not allow

for *in vivo* examination and requires extensive preparation, it is a difficult technique to implement for large scale studies on lithium in the brain.

1.4 OVERVIEW OF STUDIES

The aim of this thesis is to identify biomarkers predicting lithium response. To this end, I chose to investigate astrocytes and wild-type mice with MR-based techniques to observe the structural, diffusive, and metabolic changes associated with lithium treatment without the interference of an illness. In doing so, I conducted five different studies: the first two with the aim of improving lithium-7 MRI – developing the technique for mice (chapter 2) and providing a cost-efficient lithium-7 RF coil (chapter 3), the third with a focus on optimizing MRS analysis with LCModel across five species (chapter 4), the fourth on measuring changes in diffusion and metabolism in astrocyte hydrogels exposed to lithium (chapter 5), and finally utilizing all of this to establish an MR-based profile of lithium treatment in wild-type mice (chapter 6).

1.4.1 Chapter 2: ^{7}Li MRI in mice

SPIRAL MRI for *in vivo* Lithium-7 Imaging – A feasibility study in mice after oral lithium treatment. In my master thesis, I improved lithium-7 MRI to allow for imaging of *ex vivo* mouse brains that had been suspended in 10 mM LiCl solution (10-fold greater than the therapeutic concentration); however, I needed to prove that it was possible to perform lithium-7 MRI at physiological concentrations *in vivo.* This study comprises the first pilot experiments performed on lithium-fed mice. I was motivated by wanting to describe the distribution of lithium in the *in vivo* mouse brain and see if mice, like humans, showed a non-homogeneous distribution of lithium. Prior to these experiments, lithium-7 MRI had never been performed in mice and the highest resolution lithium-7 MRI had been performed at was 2×2×4 mm^3 in rats[116]. I was able to show *in vitro* that SPIRAL lithium-7 MRI provided improved SNR compared to conventional FLASH and rapid acquisition with relaxation enhancement (RARE) sequences. I found that while bSSFP performed well *in vitro*, due to inhomogeneity of the main magnetic field, it was significantly worse than SPIRAL *in vivo*. I found that lithium was detectable after one week on a lithium-enriched diet. In this study, I showed that lithium-7 MRI is feasible *in vivo* in four hours of measurement time at a resolution of 2×2×3 mm^3. Using SPIRAL lithium-7 MRI, I found that lithium was found in lower concentration in the olfactory bulb and cerebellum and higher concentrations in the center of the brain.

1.4.2 Chapter 3: Home-built ^{7}Li radiofrequency coil

A home-built, cost-efficient lithium-7 Tx/Rx coil for in vivo ^{7}Li magnetic resonance imaging and spectroscopy. Since every nucleus has a different resonance frequency, each nucleus will usually require a different RF coil that is tuned and matched to that specific frequency. Purchasing these RF coils for multiple nuclei is a cost-intensive endeavor, which has limited the development of X-nuclei MRI in preclinical and clinical research. In this study, I provide a comprehensive overview of how to build a single-resonance surface RF coil with cost-efficient components. I developed an open-source, 3D-printable circuit board (with a protective cover) with circuits made from adhesive copper wire and soldered-on components (capacitor and inductor). The circuit board design was made in a flexible manner allowing for the creation of multiple configurations, which makes the development

of RF coils for other X-nuclei feasible. I found that the optimal number of segmentation capacitors for a single-resonance lithium-7 mouse brain RF coil operating at 155 MHz was two. I compared the home-built coil to a commerical dual-tuned (proton/lithium-7) mouse RF coil and found that we were able to acquire MRS with comparable quality. I was able to show that with a cost-efficient, home-built RF coil *in vivo* lithium-7 MRI of the mouse brain is possible. Additionally, the design of the RF coil allows for easy adaptation to other nuclei and/or shapes and sizes.

1.4.3 Chapter 4: Cross-species LCModel analysis

Cross-species quantification of ¹H magnetic resonance spectra - Lessons learned from simulation and in vivo data. MRS allows for the quantification of brain metabolites. In this thesis, I have used MRS to detect metabolic changes in brain of mice on a lithium-enriched diet. This study was motivated by an age-old problem in the field of MRS, namely that the quality of the fit determines the concentration of the metabolites. I was by no means the first to realize this issue and at its root, it seems relatively intuitive – if the spectrum has a low SNR, then a metabolite will be fit with a lower accuracy. However, the assumption is that if the noise is random then the average concentration in a group will remain constant and the standard deviation will increase as a function of noise. In this study, I illustrated that this is not the case for LCModel analysis – considered the gold-standard, which new software are tested against. First, I looked at the extent to which the start parameters of LCModel altered the quantification of simulated spectra – simulated from the mean and covariance of *in vivo* human and mouse spectra. Thereafter, I created a small open-source toolbox for simulating spectra from basis sets at either "random" concentrations or species specific concentrations. I confirmed that these *in silico* spectra were visually similar to the *in vivo* spectra. I found that specific metabolites correlated in concentration with each other. A part of this project was to provide reference values for cortical MRS for various species, as I have data from mice, rats, marmosets, macaques, and humans – the mean and average metabolite concentrations are shared to allow others to simulate spectra with comparable quality. I looked at the noise behavior of both *in silico* and *in vivo* spectra for all five species and found metabolite and species specific noise behavior was present. I found that using optimized LCModel start parameters led to better fit quality than was achieved by default LCModel, TARQUIN, and FSL-MRS (two other analysis software). TARQUIN and FSL-MRS showed similar tendencies for cross-species comparisons and more ideal (constant average value) noise behavior than the two LCModel approaches. However, at the expected SNR of *in vivo* spectra, LCModel remains the preferred analysis approach, due to its higher fit accuracy.

1.4.4 Chapter 5: Cell culture MRI/S

Magnetic resonance imaging and spectroscopy on 3D astrocyte cell cultures: a feasibility study. In this explorative project, I looked at the effect of lithium on immortalized human astrocytes. Given the ever-changing landscape of animal experimentation, there has been a push towards alternative methods. However, 2D cell cultures do not capture the complexity necessary for understanding many *in vivo* functions. In this project, I have established longitudinal MRI and MRS measurements of 3D cell cultures (astrocytes in a collagen hydrogel). To this end, I have created an open-source, MR-compatible bioreactor and incubator, which allow for the measurement of 3D cell cultures under constant

temperature, with medium exchange and gas-mixing to keep the pH constant. This project showed that measuring 3D cell cultures is feasible in an MRI system. Furthermore, I observed decreased myo-inositol and glutamine plus glutamate at physiological concentrations of lithium (0.78 mM), but increased myo-inositol and glutamine plus glutamate at high lithium (4.38 mM). I likewise showed that longitudinal measurements are feasible with a tendency towards increased lactate over the course of a 1-hour measurement. In conclusion, I was able to measure 3D cell cultures in an MRI system, which may create an avenue for future experimentation on cell cultures and/or organoids. In doing so, I hope to illustrate that preclinical MRI and MRS of 3D cell cultures may, in part, be used as a translational tool to study the impact of lithium on individual cell types.

1.4.5 Chapter 6: Lithium treatment in mice

Establishing a magnetic resonance-based profile of lithium treatment in healthy, wild-type mice. As outlined in section 1.3, there are many hypotheses for the mechanism of action of lithium treatment; however, disentangling the disease progression from the lithium treatment remains a challenge. Furthermore, due to the many potentially serious side effects, detecting ideal responders from non-responders at an early stage would be beneficial for treatment and due to the elevated risk of suicide in bipolar patients, potentially life-saving. As such, I started with the simple question: "what happens to the wild-type mouse brain when a mouse is fed a lithium-enriched diet?" I chose to investigate this question with MR-based techniques to increase the translational potential of any biomarkers found. Before summarizing my findings, I should clarify that lithium-enriched means 0.2% or 0.3% Li_2CO_3 (w/w), which led to brain concentrations of either 0.4 mM or 0.9 mM – giving comparable blood and brain concentrations to human bipolar patients. In mice on a high lithium diet (0.3% Li_2CO_3), I observed a tendency towards increased phosphocreatine with phosphorus-31 MRS, which was significant in proton MRS. Contrary to the myo-inositol depletion hypothesis, myo-inositol was not decreased, but rather increased in cortex. N-acetylaspartate was decreased in both corpus callosum and hippocampus. The glutamate-to-glutamine ratio was likewise decreased in cortex. Combined with the observation of decreased apparent diffusion coefficient and increased neurite density index in cortex, corpus callosum, and hippocampus, these changes suggest a change in cell activity and/or population. A cautious interpretation of this data may be that we have a higher activity or concentration of glial cells following lithium treatment. As I did not observe total brain volume changes or changes in the cerebrospinal fluid volume, my results could suggest that this change was driven by astrocytes.

2

[7]LI MRI IN MICE

SPIRAL MRI for in vivo Lithium-7 Imaging – A feasibility study in mice after oral lithium treatment

Tor Rasmus Memhave[1,2,3], Amir Moussavi[1], Susann Boretius[1,2,3]

[1]Functional Imaging Laboratory, German Primate Center, Leibniz Institute for Primate Research, Göttingen, Germany

[2]Georg-August Universität Göttingen, Göttingen, Germany

[3]International Max Planck Research School for Neurosciences, Göttingen, Germany

Own contributions:

- Conceptualization
- Data acquisition
    - o Mouse handling
    - o Mouse scoring
    - o *In vivo* magnetic resonance imaging and spectroscopy
- Data analysis
- Data interpretation
- Data visualization
- Writing

In Review (Scientific Reports)

2.1 ABSTRACT:

Lithium has been the frontline treatment for bipolar disorder for over 60 years. However, its mode of action and distribution in the brain is still incompletely understood. The primary isotope of lithium, lithium-7 ([7]Li), is a magnetic resonance (MR) active, spin-3/2 nucleus. However, its low MR sensitivity and the small brain size of mice make [7]Li MR imaging (MRI) difficult in preclinical research.

We tested four MRI sequences (FLASH, RARE, bSSFP, and SPIRAL) on lithium-containing phantoms, and bSSFP and SPIRAL on orally lithium-treated adult C57BL/6 mice. [7]Li MR spectroscopy was acquired weekly at 9.4T to monitor the lithium uptake. The *in vivo* T1 relaxation time of [7]Li was estimated in four mice. 4-hour SPIRAL [7]Li MRI was acquired in ten mice at a resolution of 2×2×3 mm^3.

SPIRAL MRI provided the highest signal-to-noise ratio (SNR) per unit acquisition time and the best image quality. We observed a non-homogeneous distribution of lithium in the mouse brain, with the highest concentrations in the cortex, ventricles, and basal brain regions. Almost no lithium signal was detected in the olfactory bulb and the cerebellum. We showed that *in vivo* [7]Li MRI in mice is feasible, although with limited spatial resolution and SNR.

2.2 INTRODUCTION:

Lithium is a frontline treatment for bipolar disorder that has been used clinically for over 60 years[20]. It has been shown that lithium decreases excitatory neurotransmission and inhibits NMDA receptors[48]. It alters secondary messenger signalling[61–63] and increases neuroprotection via increased activity of the transcription factor CREB[77,78]. Despite its
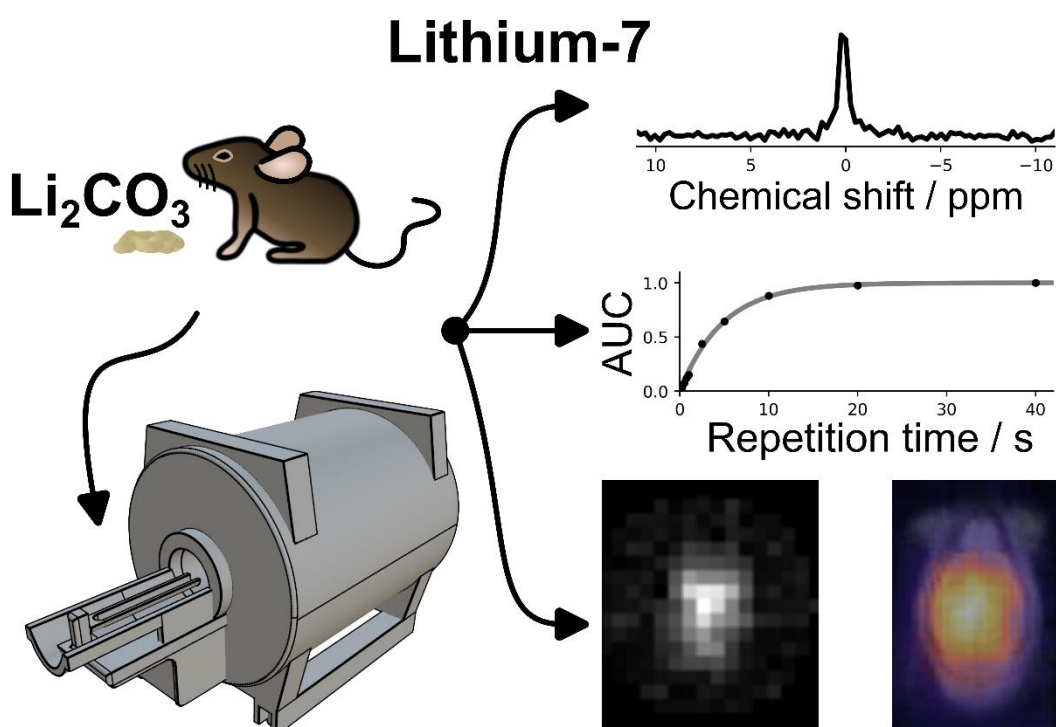
Figure 2-1: **Graphical abstract of the study.** In vivo ^{7}Li MRI and MRS were acquired from 13 wild-type mice on a lithium-enriched diet (0.3% Li$_2$CO$_3$ w/w). Weekly ^{7}Li MRS was performed to monitor the uptake of lithium. [7]Li T1 relaxation time was estimated based on four mice. [7]Li MRI was acquired using a SPIRAL sequence at a resolution of 2×2×3 mm^3 with a 4-hour acquisition time.

therapeutic successes on mood disorders, lithium's potentially complex mode of action in the brain is still not well understood. Of particular interest in this context is that lithium appears to affect individual brain regions differently[21]. This local selectivity may be related to a heterogeneous lithium distribution across the brain, varying enormously between individuals[115,128]. For example, a recent high-field MRI study reported significant clustering of the lithium signal in the left hippocampus in patients with bipolar disorder[115]. In addition, human studies have found increased lithium in the brainstem, white matter, and the limbic system[115,124,128]. Moreover, *post-mortem* studies on three human brains reported a higher lithium concentration in white matter than in grey matter in non-lithium-medicated, non-suicidal individuals[141].

[7]Li is an MR active nucleus with a spin of 3/2 and a relative sensitivity of 0.29 compared to 1 of protons. Due to this low MRI sensitivity *in vivo* lithium imaging has proven difficult. Moreover, lithium is a trace element with daily consumption estimates ranging from ~10 to 3000 µg per day[142,143]. So, the brain concentration in non-lithium-treated healthy humans is in the nano-to-micromolar range[142,144], undetectable for currently available MRI methods. Since the therapeutic window of lithium is narrow[9] and renal failure is a feared side effect, brain concentration cannot readily be increased. Exploring the physiological brain distribution of lithium in healthy humans *in vivo* is, therefore, almost impossible.

Several studies exploring the effect of lithium on the brain have used rodent models where lithium has been administered parenterally (mostly intraperitoneally) or orally (via food and drinking water) to achieve brain concentrations high enough for *in vivo* imaging. The significantly smaller brains, however, place high demands on spatial resolution. So far, the highest reported resolution of [7]Li MRI in rodents is $2{\times}2{\times}4$ mm^3 and was acquired over 36 hours using a turbo-spin echo sequence on *ex vivo* rat brains[116]. In contrast, *in vivo* [7]Li MRI in rats was performed with a resolution of $4{\times}4{\times}7$ mm^3 (single slice)[103], resulting in about 12 voxels per brain (volume of a rat brain: ~$20{\times}10{\times}15$ mm^3). No *in vivo* [7]Li MRI studies on mice have been reported so far.

This study aims to find an MRI sequence suitable for *in vivo* [7]Li MRI in mice. The protocol should provide a sufficient SNR in a measurement time still applicable *in vivo*. To be feasible in mice, we considered an SNR of more than five and an acquisition time of no longer than four hours. To that end, we first tested different MR sequences on lithium-containing phantoms. We explored the following four MR sequences: fast low-angle shot (FLASH), rapid acquisition with relaxation enhancement (RARE), balanced steady-state free precession (bSSFP), and SPIRAL. While FLASH and RARE sequences are commonly used in proton MRI, the efficient data acquisition of bSSFP and SPIRAL sequences make them promising candidates for *in vivo* [7]Li MRI. In addition, bSSFP yields a high SNR, which depends on the ratio of transverse relaxation time (T2 relaxation) to the longitudinal relaxation time (T1 relaxation). The non-cartesian SPIRAL sequence uses a sinusoidal gradient switching, allowing a whole k-space acquisition in a single shot. Based on our results in phantoms, we then conducted an *in vivo* study in mice where we could show for the first time that *in vivo* [7]Li MRI is feasible when using a SPIRAL sequence. A graphical summary of the study is shown in Fig. 2-1.
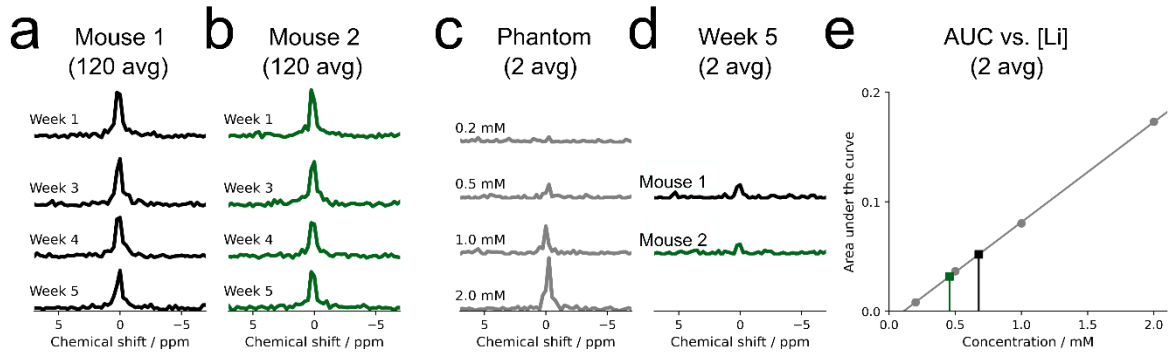
Figure 2-2: **Lithium concentration in the brain.** *Follow-up localized ⁷Li MR spectra of two mice (a, b) were obtained weekly after the onset of oral lithium treatment. Using ⁷Li MR spectra of lithium-containing agarose phantoms (c) as a reference, the estimated brain concentration at weak 5 was 0.68 mM for Mouse 1 and 0.46 mM for Mouse 2 (d). The linear relationship between the area under the curve and the known lithium concentrations of the phantom, together with the estimated brain concentration of Mouse 1 (black) and Mouse 2 (green) are shown in (e).*

2.3 RESULTS:

2.3.1 ⁷Li MR spectroscopy (MRS)

Lithium was reliably detectable in the brain already one week after treatment onset.

Feeding a lithium-enriched diet (0.3% w/w Li_2CO_3) resulted in a significant increase of brain lithium, observable at the first of the weekly acquired localized ⁷Li MR spectra, one week after the treatment started (Fig. 2-2a-b). The brain lithium did not change significantly over the following four weeks. To estimate the concentration, we compared the mice spectra with spectra acquired from agarose phantoms of different lithium concentrations (0.2 to 2.0 mM) using the same coil, identical acquisition parameters, and comparable object geometry and coil loading. In this way, we obtained an average brain lithium concentration of 0.6 mM (0.68 mM brain lithium for mouse 1 and 0.46 mM for mouse 2 at week five; Fig. 2-2c-e).

The average in vivo T1 relaxation time of ⁷Li at 9.4T was about 4.8s.

We acquired non-localized ⁷Li spectra from the mouse head with varying repetition times (Fig. 2-3). The exponential fitting to estimate T1 relaxation time was approached in two different ways, which led to comparable results: first, we used the area under the curve (AUC) of the averaged spectrum of four mice (T1 = 4.85s, Fig. 2-3a), and second, the signal
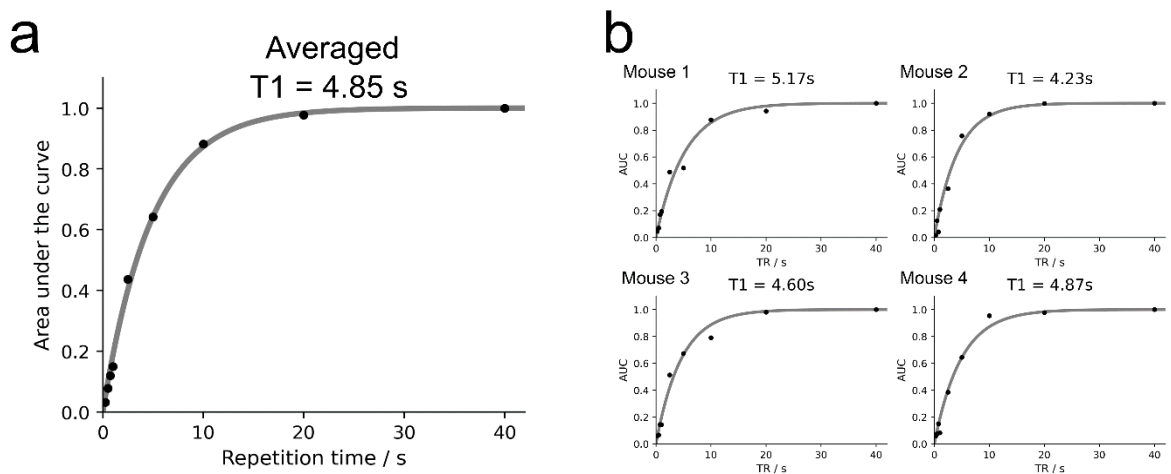
Figure 2-3: **T1 relaxation time of brain lithium in vivo at 9.4T.** *(a) The averaged area under the curve (AUC) obtained from ⁷Li MR spectra of four mice at different repetition times reveals a T1 relaxation time of 4.85 s. The individual results of each mouse are shown in (b).*

Axial	Coronal	Sagittal
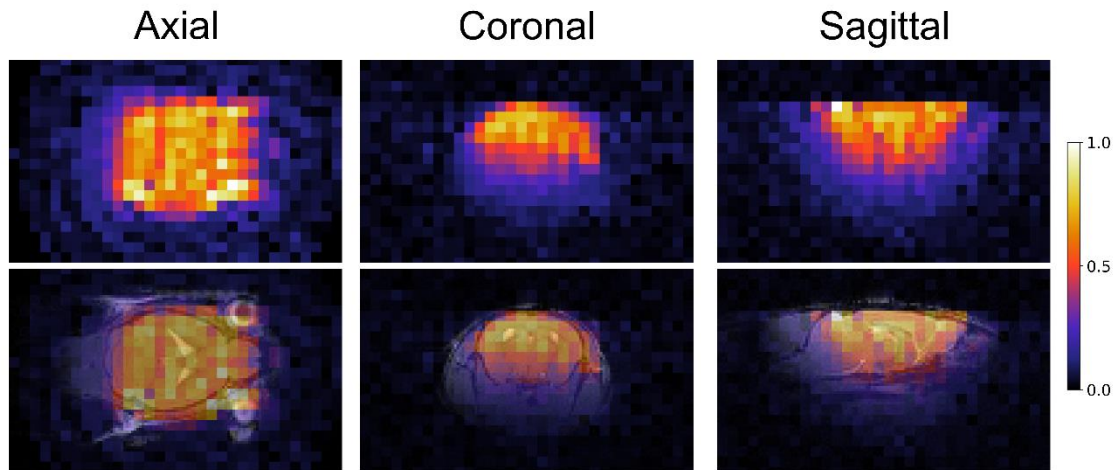
*Figure 2-4: **Sensitivity profile of the 7Li coil.** A SPIRAL [7]Li MRI was acquired on an agarose phantom containing 10 mM LiCl (top row). The bottom row shows the [7]Li image of the phantom overlaid on a ^{1}H image of a mouse head to illustrate the coverage of the brain.*

curve of each mouse was processed individually, resulting in a T1 relaxation time of 4.72 ± 0.35s (Fig. 2-3b).

Ex vivo ^{7}Li MRS revealed significant lithium wash-out within 27 hours after PFA fixation.

Taking advantage of the possibility of longer acquisition time, we performed *post-mortem* lithium measurements of the isolated brain. Following the recommendation of Stout et al.[116], we excised the brain directly after transcardial perfusion fixation and placed it in 5 ml PFA to limit lithium efflux. However, ^{7}Li MRS acquired in intervals over 74 hours, showed a substantial signal reduction, reaching the detection limit of lithium in the brain after about 27 hours (Fig. S-1). Logistic curve fitting revealed a half-maximum at 12.7 hours and a decay rate of 0.21. A steady state (95% decay) was reached after 27 hours.

2.3.2   [7]Li MR imaging

Sensitivity profile of the [7]Li radiofrequency coil

The coil sensitivity profile of the single-loop transmit-receive coil (inner diameter 17 mm) was acquired on an agarose phantom (10 mM LiCl) and overlaid on a T2-weighted anatomical image of a mouse brain, Fig. 2-4. The profile covered almost completely the rostrocaudal and left-right dimensions of the brain. In the anteroposterior direction, the surface coil showed the typical sensitivity loss with increasing distance. However, the predominant brain parts were within the coil's best sensitivity region.

SPIRAL [7]Li MRI had the highest SNR per unit acquisition time.

A protocol feasible for *in vivo* [7]Li MRI in mice should be able to detect lithium at a therapeutic relevant brain concentration (~1 mM), a spatial resolution of at least $2 \times 2 \times 3$ mm^3, and within a measurement time, being still achievable *in vivo*. We compared the SNR of four different sequences (SPIRAL, RARE, bSSFP, and FLASH) using a structured phantom that contained 1 mM LiCl in agarose in its center, Fig. 2-5b. We acquired two coronal slices to obtain a field of view that covers the entire mouse brain. Under these conditions, the SPIRAL sequence achieved the highest SNR (8.2), followed by bSSFP (SNR = 6.8), FLASH (SNR = 3.2), and in the last place, the RARE sequence (SNR = 1.8) (Fig. 2-5a).
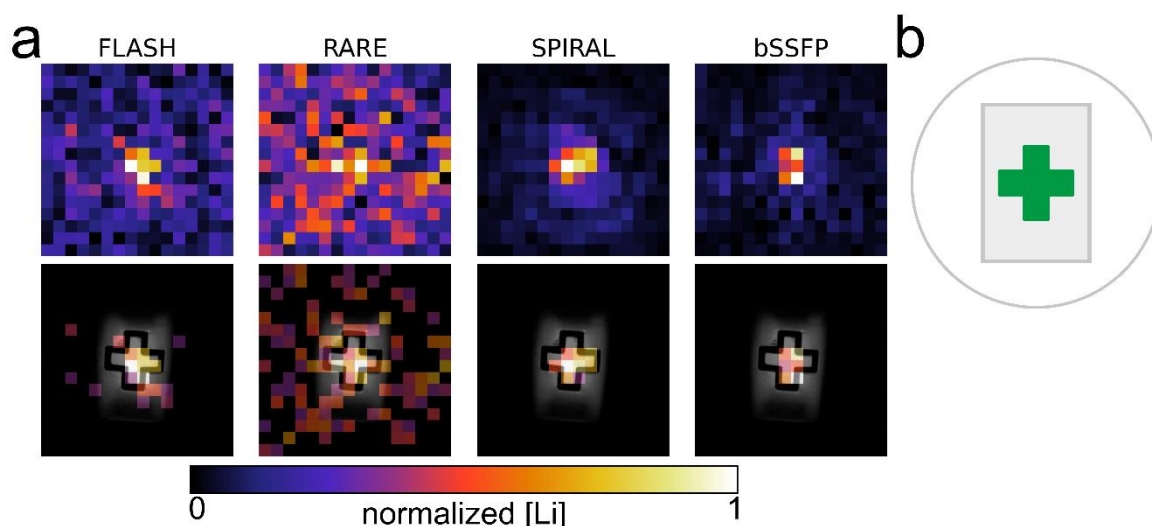
Figure 2-5: ^{7}Li MR images acquired within 4 hours using either FLASH, RARE, SPIRAL or a bSSFP sequence. The top row shows the phantom's ^{7}Li images, and the bottom shows them thresholded and overlaid on a ^{1}H reference image (a). A sketch of the phantom (b), illustrates the circular field of view of the SPIRAL sequence. The green plus sign contained 1.0 mM LiCl. The threshold of the ^{7}Li images was set to one-third the maximum intensity of the ^{7}Li image. The FLASH and RARE sequences performed significantly worse than the SPIRAL and bSSFP sequences. However, the signal from the FLASH images still originated primarily from the lithium-containing plus-shaped center as also shown for SPIRAL and bSSFP. The highest SNR was obtained with the SPIRAL sequence (SNR = 8.2) followed by bSSFP (SNR = 6.8).

SPIRAL ^{7}Li MRI provided the best SNR in vivo

Next, we applied the two sequences with the highest *in vitro* SNR, SPIRAL and bSSFP, each on a lithium-treated mouse *in vivo*. Although the two mice did not show differences in their brain lithium level, as revealed by ^{7}Li MRS in the same session (Fig. 2-6c), bSSFP exhibited a noticeably lower SNR than SPIRAL (2.3 vs. 6.7, Fig. 2-6a-b).
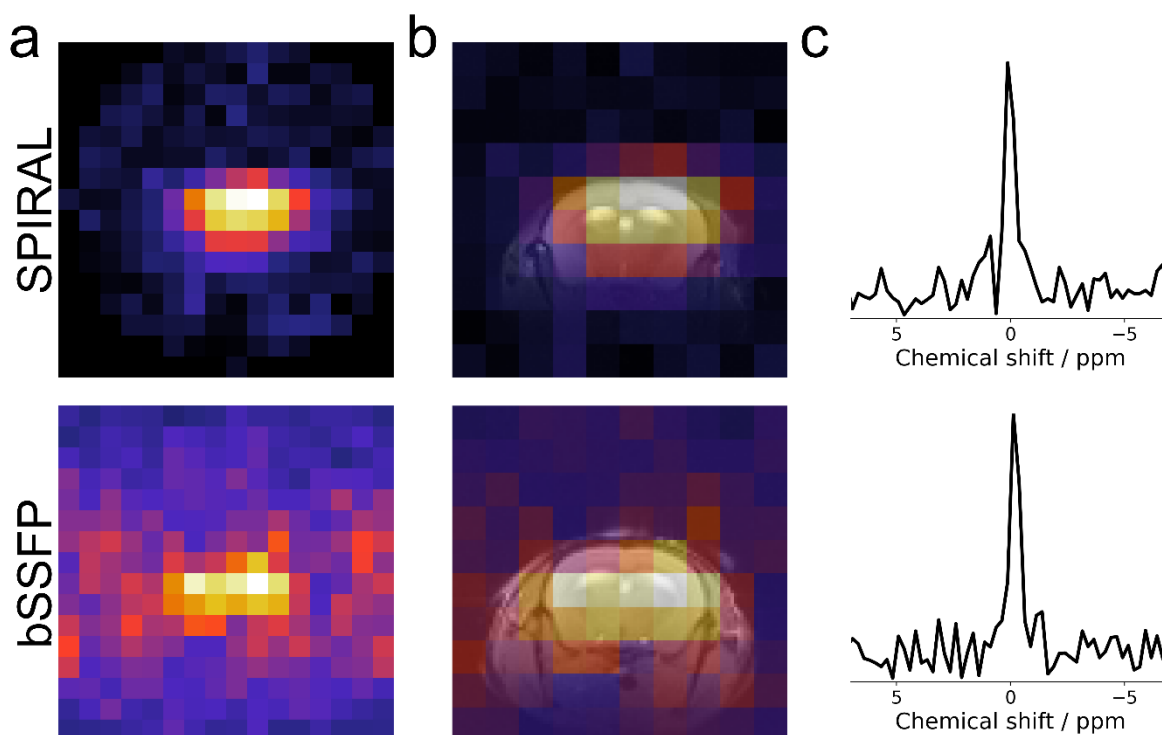
Figure 2-6: SPIRAL ^{7}Li MRI had higher SNR than bSSFP ^{7}Li MRI in vivo. The raw (a) and overlaid (b) ^{7}Li images show lithium signals originating mainly from the brain. The ^{7}Li image acquired with a SPIRAL sequence had higher SNR than the bSSFP (6.7 vs. 2.3) despite the same acquisition time and comparable brain lithium concentration as shown by the respective localized ^{7}Li spectra (c).

In vivo [7]Li SPIRAL MRI is feasible at a resolution of 2×2×3 mm[3].
Having SPIRAL identified as, in our hands, the most suited sequence, we acquired *in vivo* [7]Li SPIRAL MRI in 10 mice after 4-5 weeks of lithium treatment. In one-half of the mice, the images were obtained in two coronal slices (visualized in Fig. 2-7c); for the other half, an axial orientation was chosen. Lithium was detectable in the brains of all mice (Fig. 2-7a-b and 2-8a). We calculated the average [7]Li image for the two slice orientations separately, using the centroid alignment of the respective five mouse brains. The group average [7]Li images showed a prominent lithium signal in the center of the brain, including the lateral ventricles and deep grey matter nuclei (Fig. 2-7d and 2-8b). Interestingly, the olfactory bulb exhibited almost no lithium signal. This fact remained when correcting for the sensitivity profile of the coil and voxel proportions exceeding the head of the mouse (Fig. 2-7d and 2-8c). Compared to the cerebrum, the cerebellum showed a notably lower lithium signal.

2.4 DISCUSSION:

^{7}Li MRS and MRI can provide valuable information about the pharmacokinetics and distribution of lithium in the brain. Combined with the vast number of available genetically modified mouse lines, these *in vivo* techniques may further help to unravel its mood regulation mechanisms. To enable [7]Li MRI in the tiny mouse brain, we tested four MR sequences, namely FLASH, RARE, bSSFP, and SPIRAL, on lithium-containing phantoms, followed by *in vivo* experiments in mice using the two best sequences bSSFP and SPIRAL. We could show for the first time that *in vivo* [7]Li MRI in mice is feasible, although with a limited spatial resolution and SNR. In this context, the fast non-Cartesian sampling of the SPIRAL sequence significantly improved the SNR and image quality.

Feeding mice with a lithium-enriched diet led to a detectable lithium concentration in the brain one week after the treatment started. The estimated brain concentration of 0.6 mM aligns with a previous *post-mortem* study reporting a brain concentration of about 0.8 mM after lithium treatment using time-of-flight secondary ion mass spectrometry on juvenile mice[132]. Assuming a brain-to-blood ratio of roughly 1.2 in C57BL mice[123], the lithium treatment used in this study corresponds to a lithium serum concentration within the upper therapeutic window of 0.4-1.2 mM in patients[9,132,145].

Our estimated T1 relaxation of brain lithium at 9.4T (4.85s) is comparable to previous reports in humans at 7T (3.95s) and 4T (4.12s) and also aligns with measurements obtained in rats at 4.7T (2.5-5.1s)[110,115,146]. This T1 relaxation time was considered when comparing the four MR sequences. *In vitro* and *in vivo*, SPIRAL provided the highest SNR per unit acquisition time. Its single-shot, center-out encoding allowed for a short echo time (TE), low bandwidth per pixel, and efficient k-space sampling. Using the SPIRAL sequence, we could achieve a spatial resolution of 2×2×3 mm[3] within an acquisition time of four hours. Given a mouse brain size of about ~10×6×12 mm[3] this resolution means approximately 15 voxels per coronal brain slice.

We corrected the signal intensity for the tissue percentage in each voxel to compensate for partial volume effects at the brain edges caused by the relatively thick coronal slices. Another limitation was the sensitivity profile of the circular surface coil. We took this into consideration by weighting the obtained images with the sensitivity profile of the receiver
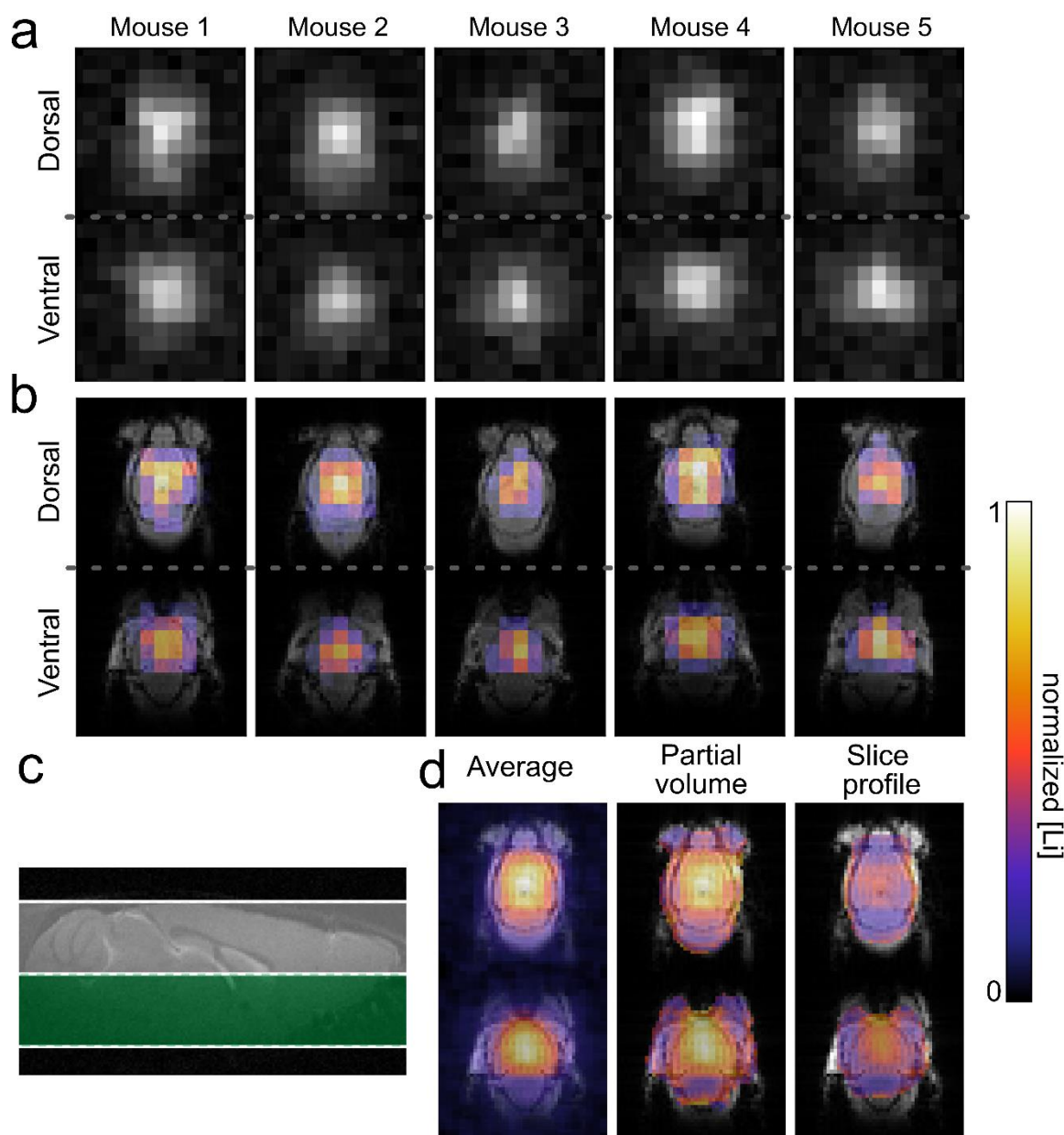
Figure 2-7: *In vivo* *[7]Li MRI of lithium-fed, wild-type mice.* [7]Li MRI was acquired in five mice using a 4-hour SPIRAL sequence (a-b). The position of the two coronal slices is visualized in c. The brains were segmented, and the [7]Li images were overlaid on ^{1}H reference images (b). The average [7]Li image (d, left) showed the highest lithium signal in the brain's center. After partial volume correction (d, center), we also observed a lithium signal at the brain's edges. The [7]Li image, additionally corrected for the signal intensity profile of the coil (d right), shows the highest lithium signal in the main parts of the cerebrum and less in the olfactory bulb and cerebellum.

acquired on a homogeneous lithium-containing phantom resembling the size and shape of a mouse head.

The [7]Li images corrected this way indicated a non-homogeneous distribution of lithium in the healthy mouse brain. The highest concentration was found in the brain center, including large parts of the cortex, lateral ventricles, and basal ganglia. We observed significantly lower concentrations in the cerebellum and olfactory bulb. The former contrasts a *post-mortem* study in juvenile mice[132], where the authors reported an accumulation of lithium in neurogenic regions such as the hippocampus and the olfactory bulb. Although low levels remain in the hippocampus and olfactory bulb of the adult brain, neurogenesis peaks during
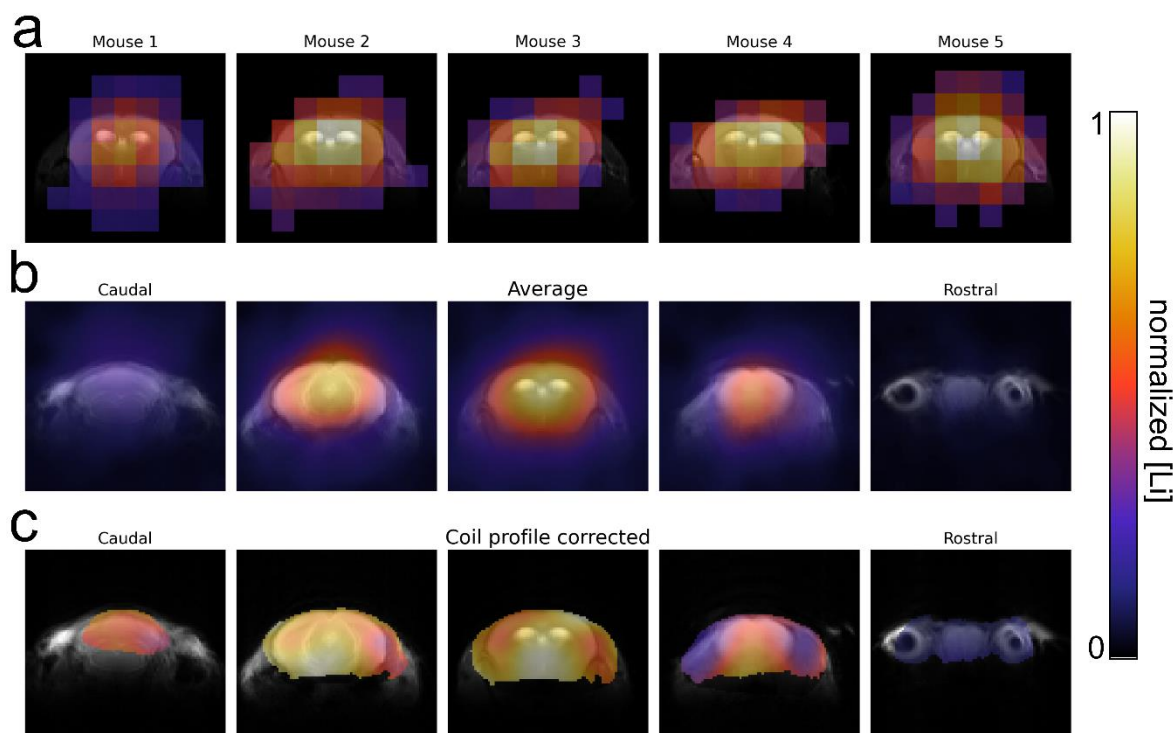
Figure 2-8: **Axial ^{7}Li MRI showed high lithium signal in main parts of the cerebrum and low signal in the cerebellum and olfactory bulb.** *In vivo ^{7}Li MRI of five mice, performed in the axial orientation (a), showed a clear lithium signal originating from the brain. The averaged ^{7}Li image of the five mice revealed the highest lithium concentration in the brain center and only shallow signals in the cerebellum and olfactory bulb (b). These findings remained after correcting for the coil profile (c).*

early development. It is hitherto undescribed whether juvenile and adult mice have different lithium distributions. However, our observation indicates that the neurogenesis level may be responsible for potential age-related differences. Moreover, *ex vivo* rat ^{7}Li MRI found higher lithium levels in the cortex and lower in the brainstem[116]. In addition, the rodent cerebellum, especially in white matter, has been shown to have lower lithium concentrations, per our findings[116,140].

Post-mortem ^{7}Li MRI theoretically reveals the possibility of spatially higher resolved images. However, in contrast to an *ex vivo* rat study[116], we observed a significant wash-out of lithium from the paraformaldehyde (PFA) fixed brain into the solution. In the future, other fixation techniques need to be found to profit from the possible prolonged measurement time in *post-mortem* studies.

In conclusion, to our knowledge, we have acquired the first ^{7}Li MRS and ^{7}Li MRI of a mouse brain *in vivo*. ^{7}Li MRI of mice was feasible within 4 hours at a resolution of $2{\times}2{\times}3$ mm^3. Although restricted in anatomical precision, we found indications that the *in vivo* distribution of lithium in the brain may not be homogeneous. SPIRAL ^{7}Li MRI provides a new tool for studying lithium treatment and response in mice. It may link regional lithium concentrations and structural or metabolic changes. While still in its infancy, murine *in vivo* ^{7}Li MRI may help to increase our understanding of lithium's mode of action.

2.5 MATERIALS AND METHODS:

Animals: 13 adult C57BL/6N mice (8 female, 5 male) were enrolled in the study, which was approved by the local ethics committee (Animal Welfare Service, Lower Saxony State Office

for Consumer Protection and Food Safety, license-number 33.19-42502-04-20/3365). The study design complies with the ARRIVE guidelines and experiments were performed in accordance with the relevant guidelines and regulations. The mice were kept on a 12-hour light-dark cycle. Food (ssniff Spezialdiäten GmbH) and water were provided *ad libitum*. Water consumption was monitored daily. A saline solution was additionally provided when water consumption increased by 300% (B. Braun Medical Inc., Bethlehem, Pennsylvania, USA). All mice received a lithium-enriched diet containing 0.3% Li_2CO_3 (w/w).

For each MR session, the mice were initially anaesthetized with ketamine (MEDISTAR, Serumwerk Bernburg Tiergesundheit GmbH, Bernburg, Germany) and medetomidine (Dorbene Vet, Zoetis Inc., Parsippany, New Jersey, USA), intubated and subsequently artificially ventilated (animal respirator, advanced 4601-2, TSE Systems GmbH, Bad Homburg, Germany). Anesthesia was maintained by 0.5-1.5% isoflurane (Isofluran CP, CP-Pharma Handelsgesellschaft mbH, Burgdorf, Germany) in oxygen-enriched air. Breathing rate and rectal temperature were continuously monitored. At the end of the measurement, medetomidine was antagonized by atipamezole (Atipzole, Provident Pharmaceuticals, Prodivet Pharmaceuticals sa/nv, Eynatten, Belgium). After the final MR session, the mice were transcardially perfused with phosphate-buffered saline solution and 4% PFA (Carl Roth GmbH, Karlsruhe, Germany) and the brains were collected for *post-mortem* analyses.

MRI system: MR data was acquired on a 9.4T MRI system (BioSpec, 30 cm horizontal bore, BGA12 gradient system, ParaVision 6.0.1; Bruker BioSpin MRI GmbH, Ettlingen, Germany). A dual-tuned (^{1}H/^{7}Li) transmit-receive surface coil (RAPID Biomedical GmbH, Rimpar, Germany) was used for both ^{1}H and ^{7}Li measurements. The ^{7}Li channel had a single-loop design with a diameter of 17 mm. The optimal reference power was determined manually by acquiring multiple non-localized ^{7}Li spectra with increasing reference power and a long repetition time (TR = 40s) to eliminate T1 relaxation effects.

Chemicals: Agarose and LiCl used for phantom experiments were acquired from Carl Roth (Carl Roth GmbH + Co. KG, Karlsruhe, Germany).

Magnetic resonance spectroscopy: Axial and sagittal T2-weighted ^{1}H images were acquired to help position the spectroscopy voxel (2D RARE sequence, TR = 2800 ms, TE = 33 ms, RARE-factor = 8, $0.1×0.1$ mm^2 resolution, $19.2×19.2$ mm^2 field of view, 0.5 mm slice thickness, 0.3 mm slice gap, 24 slices, 2 averages, and 2:14 min acquisition time). Localized ^{7}Li MR spectra were obtained using an image-selected *in vivo* spectroscopy (ISIS) sequence[32] with a spectral width of 10 kHz, a voxel size of $6×5×8$ mm^3, and 256 data points. *In vivo* ^{7}Li MR spectra (TR = 2.5 ms, number of averages (NA) 120 resulting in a total acquisition time of 40 min) were acquired weekly from two mice starting at age 146 days, one week after the lithium treatment onset, and continuing for the following four weeks to monitor the brain lithium uptake. No data could be obtained in week two due to technical problems with the MRI system. Subsequent to the *in vivo* experiments, one mouse brain was analyzed in a 4% PFA solution using the same ISIS protocol to investigate the *ex vivo* lithium wash-out. The spectra were acquired over 74 hours with interleaved ^{1}H reference images to ensure an unchanged voxel position.

To estimate the *in vivo* lithium concentration in the brain, ^{7}Li MR spectra from phantoms with a comparable size to mouse heads (2 ml, Sarstedt AG & Co. KG, Nümbrecht, Germany) containing lithium concentrations in the range 0.2-2 mM ([LiCl] in mM/agarose in

%: 0.2/3.00, 0.5/2.99, 1/2.98, 2/2.95) were acquired as a reference and compared with those spectra additionally obtained from the mice in week five using identical acquisition parameters (TR = 40 s, NA = 2, total acquisition time = 10.7 min). The long TR was chosen to minimize the effect of the different T1 relaxation times between the phantom and the brain.

In addition, we acquired non-localized spectra (spectral width 16026 Hz, 256 data points, NA = 10) in four mice to estimate the T1 relaxation time of [7]Li in the brain. The spectra were obtained with nine different TRs (0.25 s to 40 s) from longest to shortest TR with 80s of dummy scans to ensure a steady state during the acquisition.

Magnetic resonance imaging: To find a suitable sequence for *in vivo* [7]Li MRI in mice, four different MR sequences, i.e. 2D FLASH, 2D RARE, 2D bSSFP, and single-shot 2D SPIRAL, were tested on a phantom containing 1 mM aqueous LiCl solution in its cross-shaped center surrounded by lithium-free agarose (2.94%). Two coronally oriented slices were obtained with a resolution of 2×2×3 mm^3. The total acquisition time was 4 hours for each of the four sequences. The respective MR parameters are shown in Table 2-1. For FLASH, RARE, and SPIRAL, the flip angle was calculated using the Ernst angle formula and an estimated T1 of 11s for [7]Li in an aqueous solution[147]. For SPIRAL [7]Li MRI, a bandwidth of 7500 Hz was found to be optimal to balance the effects of sampling time and T2* decay, yielding both good SNR and spatial acuity. [1]H reference images were acquired with a FLASH sequence, 125 µm isotropic in-plane resolution and 3 mm slice thickness.

Table 2-1: MR parameters used for sequence comparison on the lithium-containing phantom shown in Fig. 2-5.

	RARE	FLASH	bSSFP	SPIRAL
TR / ms	2500	2500	5	2500
TE / ms	6.73	1.52	2.5	1.58
Flip angle	36.1°	36.1°	20°	36.1°
N$_{avg}$	60	15	35018	5760
Matrix size	32×32	32×32	16×16	16×16
Slices	2	2	2	2
Voxel size / mm^3	2×2×3	2×2×3	2×2×3	2×2×3
FOV / mm^2	64 x 64	64 x 64	32 x 32	32 x 32
t$_{acq}$ / hr	4	4	4	4
Sequence-specific parameters	RARE-factor: 4			Bandwidth: 7500 Hz

The signal intensity profile of the ^{7}Li coil was measured on a phantom with a volume of 5 ml (ClearLine CLEAR-LOCK, Kisker Biotech GmbH & Co. KG, Steinfurt, Germany) containing 10 mM aqueous LiCl solution. To cover a sufficiently large volume, 20 slices with a spatial resolution of 1×1×1 mm^3 (matrix size 32×32) were acquired within 18 hours (NA = 25920) using a SPIRAL sequence with the same TE, TR and flip angle used *in vivo*.

Eleven of the thirteen mice underwent ^{1}H and ^{7}Li MRI. Axial and coronal ^{1}H reference images were acquired using either a 2D RARE sequence (TR = 2800 ms, TE = 33 ms, 0.2 mm isotropic in-plane resolution, 32×32 mm^2 field of view, 1 mm slice thickness, 21 slices, 5 averages, and 4:40 min acquisition time, Fig. 2-6 and 2-8), a 2D FLASH sequence (TR = 100 ms, TE= 2 ms, 0.5×0.5 mm^2 resolution, 32×32 mm^2 field of view, 0.5 mm slice thickness, 12 slices, 2 averages, 6 dummy scans, and 2:34 min acquisition time, Fig. 2-7) or 3D SSFP sequence (TR = 5 ms, TE= 2.5 ms, 0.25×0.25×0.25 mm^3 resolution, 36×36×36 mm^3 field of view, 2 averages, and 4:47 min acquisition time, Fig. 2-6 – bottom). For *in vivo* sequence comparisons, one axial-oriented ^{7}Li MR images was obtained using a SPIRAL (five mice) or a bSSFP (one mouse) sequence. The respective MR parameters are summarized in Table 2-2. Finally, using ^{7}Li SPIRAL MRI seven axial-oriented or two coronal-oriented slices were acquired from five mice each.

Data processing and analysis: MRI and MRS data were processed and analyzed using MATLAB (The MathWorks, Inc., Natick, Massachusetts, USA) and Python (version 3.7.9, Python Software Foundation). The final figures were assembled in Inkscape (The Inkscape Project).

^{7}Li magnitude spectra were subtracted by the mean of the noise, defined as the mean of the 100 data points furthest from the ^{7}Li resonance. The AUC of each spectrum was calculated using three-parameter Lorentzian fitting (AUC, chemical shift, and full-width at half maximum [FWHM]) with the help of *curve_fit* from the *SciPy* toolbox *optimize*. The following boundary conditions were applied: chemical shift = [-5, 5 ppm], FWHM = [0.2, 1.0 ppm] for the localized spectra and FWHM = [0.2, 1.5 ppm] for non-localized spectra, and AUC = [0, 100]. The fit parameters for the weekly ^{7}Li spectra are given in Table S-1.

Table 2-2: MR parameters used for in vivo sequence comparison – Fig. 2-6.

	SPIRAL	bSSFP
TR / ms	2500	5
TE / ms	1.58	2.5
Flip angle	53.3°	20°
N_{avg}	5760	4800
Matrix size	16×16	24×24×24
Slices	7	3D sequence
Voxel size / mm^3	2×2×3	1.5×1.5×1.5
t_{acq} / hr	4	4

The *in vivo* concentration of lithium in the brain was estimated by comparing the AUC of the *in vivo* 7Li spectra with those obtained from phantoms of known 7Li concentrations, assuming a linear relationship between AUC and 7Li concentration.

To estimate the *in vivo* T1 relaxation time of 7Li, we averaged the spectra across the four mice. All AUCs were normalized to the AUC for the longest TR (40s). The normalized data was fitted to the T1 relaxation equation (equation 2-1, *S* is relative signal intensity). In addition, similar fits were performed for each mouse spectrum individually. Here spectra with a TR<1s had to be excluded due to poor SNR. The fit parameters for the estimation of the T1 relaxation time are shown in Table S-2 (visualized in Fig. S-2).

$$S = 1 - \exp\left(-\frac{TR}{T1}\right)$$

<div align="right">equation 2-1</div>

Moreover, to quantify the *ex vivo* lithium wash-out, the normalized AUC as a function of time was fitted with a logistic curve and the following parameters: amplitude, inflexion point, and steady-state signal intensity.

To compare the four MR sequences explored for 7Li MRI, the field of view of the FLASH and RARE images was reduced to 32×32 mm^2. The SNR of each image was measured as the mean intensity of the signal inside the region of interest (ROI), (in green Fig. 2-5b), divided by the mean intensity of the noise. The ROI was defined based on 1H reference image, down-sampled to an in-plane resolution of 2×2 mm^2 and binarized.

To take the signal intensity profile of a surface coil into account the 7Li image obtained from a homogeneous phantom was down-sampled to a resolution of 2×2×3 mm^3, smoothed with a Gaussian filter (σ=0.5), and normalized between 0 and 1. This mask was then used to weight the pixels of the *in vivo* 7Li MR images, respectively. In addition, 7Li images were corrected for partial volume effects. The percentage of tissue in each voxel of the 7Li image was calculated from the binarized 1H reference images (tissue vs no tissue). To minimize over-correction, we excluded voxels with low tissue content (Otsu threshold; tissue content > 38%).

The 7Li images were overlayed on a 1H reference image for better visualization. To that end, the 7Li images were resized to the resolution of the 1H reference images using nearest neighbour interpolation. The threshold for the 7Li signal was computed by maximizing the inter-class variance using either MATLAB or the *scikit-image* library in Python, both based on Otsu's method[148]. Finally, the 7Li images of five mice were first corrected for partial volume (coronal images only) and the coil profile and then averaged using centroid alignment.

2.6 ACKNOWLEDGEMENTS:

2.7 AUTHOR CONTRIBUTIONS:

All authors contributed to the conceptualization and design of the study. S.B. supervised the study. T.R.M. and S.B. performed data acquisition. T.R.M. conducted the formal

analysis, data visualization, and wrote the first draft of the manuscript. All authors commented on previous versions of the manuscript and have read and approved its final version.

2.8 DATA AVAILABILITY:

The datasets generated during and analyzed during the current study are available from the corresponding author on reasonable request.

2.9 COMPETING INTERESTS:

3

HOME-BUILT ^{7}LI RADIOFREQUENCY COIL

A home-built, cost-efficient lithium-7 Tx/Rx coil for in vivo ^{7}Li magnetic resonance imaging and spectroscopy

Tor Rasmus Memhave[1,2,3], Marco Deckers[1,4], Susann Boretius[1,2,3], Jens Gröbner[4], Amir Moussavi[1]

[1]Functional Imaging Laboratory, German Primate Center, Leibniz Institute for Primate Research, Göttingen, Germany

[2]Georg-August Universität Göttingen, Göttingen, Germany

[3]International Max Planck Research School for Neurosciences, Göttingen, Germany

[4]Fachhochschule Südwestfalen, Iserlohn, Germany

Own contributions:

- Conceptualization
- 3D model creation
- Data acquisition
    - Magnetic resonance imaging and spectroscopy
- Data analysis
- Data interpretation
- Data visualization
- Writing

3.1 ABSTRACT:

X-nuclei magnetic resonance imaging (MRI) and spectroscopy (MRS) is a powerful tool for the *in vivo* investigation of metabolism. However, most nuclei require a dedicated radiofrequency (RF) coil for signal detection, which is often expensive. Coupled with the need for experts to create RF coils, X-nuclei MR measurements are often inaccessible to the general user. In this paper, we present cost-efficient and easy to assemble ^{7}Li RF coils that achieved comparable signal-to-noise ratios (SNRs) to their commercial counterpart. Our coils were created as single resonance, transmit-receive coils. We found that for a mouse surface coil the optimal number of segmentation capacitors was 2, which gave a 75% signal increase *in vitro* and 42% *in vivo* compared to our commercial dual-tuned surface coil. The home-built, 2-segment surface coil had sufficiently high SNR to allow for *in vivo* ^{7}Li MRI in mice.

3.2 INTRODUCTION:

Advancement in the field of MR have increased interest in X-nuclei MRI and MRS. X-nuclei are defined as nonproton nuclei that have nonzero spin (e.g. lithium-7 (^{7}Li), spin-3/2). Due to their specificity they have been used for the *in vivo* investigation of metabolic pathways[149] and energy turnover[150]. As X-nuclei require dedicated RF coils, it becomes a costly affair that often requires specialists and/or commercial partners.

Lithium is a frontline drug used in the treatment of bipolar disorder and depression[20]. Lithium's primary isotope, ^{7}Li, is an MR active nucleus with a high receptivity, 0.29 compared to 1 of protons. However, the therapeutic concentrations of lithium is low with 0.4-1.2 mM being the recommended blood serum concentration[20]. We have previously shown that *in vivo* neuroimaging of ^{7}Li in mice is feasible at 9.4T within 4 hours using a commercial RF coil (chapter 2). Even with an optimized sequence and long acquisition time, we were limited by low SNR.

We created four home-built, single-resonance surface coils and compared them to a commercially available dual-tuned (^{1}H/^{7}Li) RF coil. The quality factor of an RF coil can be increased by adding capacitors that segment the RF coil (referred to as segmentation capacitors) and thereby minimizes electrical losses[151]. We illustrate that with the correct application of segmentation capacitors, we could increase the SNR of ^{7}Li MRI/S.

We illustrated that our home-built coil was able to acquire *in vivo* ^{7}Li MRI/S in mice with comparable SNR to commercially available coils, while also being cost-efficient and easy to assemble.

3.3 MATERIALS AND METHODS

3.3.1 Coil segmentation:

Segmenting a wire reduces its dielectric loss by dividing the power between the capacitors[151]. For each segmentation, the resistance of the sample will increase due to the solder joint between the wire and capacitor. As resistance of the sample increases with the number of segmentation capacitors, the coil will eventually be unable to adapt to the required 50Ω. The resistance of the coil and sample are sufficiently large to ignore other dielectric and radiation losses.
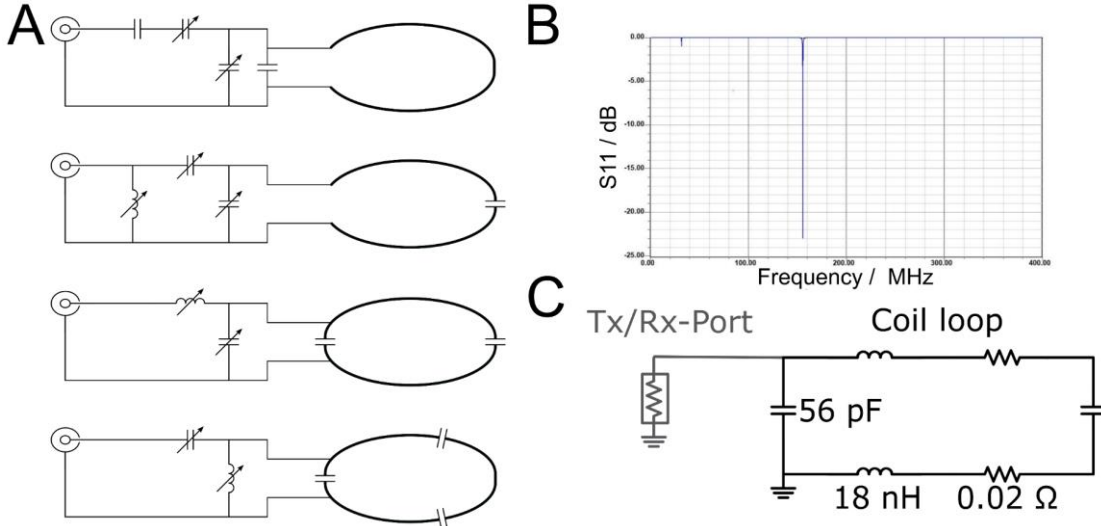
*Figure 3-1: **Coil diagrams.** The four home-built coils (A) are shown with a simplified adjustment network. The matching and tuning (B) were performed to minimize the self-reflection parameter, S11, at 155 MHz (Larmor frequency of ^{7}Li at 9.4T). The coil-loop of the 2-segment coil (C) is shown with the two 56 pF segmentation capacitors as well as the calculated inductance and resistance of the wire.*

The capacitance, C, increases linearly with the number of segmentations, N, equation 3-1. It is inversely related to the coil inductance, L, and Larmor frequency, ω (155 MHz at 9.4T for ^{7}Li).

$$C = \frac{N}{L \cdot (2\pi\omega)^2}$$

<div align="right">equation 3-1</div>

The RF coils were designed in an oval shape with dimensions 18 mm by 14 mm (length (a) × width (b)) to fit the head of an adult mouse. The coil inductance was calculated using the diameter of the coil, d_{coil}, and wire, d_{wire}, using equation 3-2. The total capacitance of each segment was 36.5 pF, as the segments were in series the capacitance is additive.

$$L(nH) = \frac{\pi}{5} \cdot d_{Coil} \left(ln \left(\frac{8d_{Coil}}{d_{Wire}} \right) - 2 \right)$$

<div align="right">equation 3-2</div>

We created four coils with 0-3 segments. Each coil had a matching and tuning network that allowed for manual adjustment of the operation frequency.

3.3.2 Simulation:

We calculated the coil inductance, segmentation capacitances, and coil resistance with Ansoft Designer (Gunthard Kraus, Tettnang). We used the Ramanujan approximation[152], equation 3-3, to calculate the length of the wire, l_{Appr}. The length of the wire was needed to calculate the resistance of the coil, R_{coil}, equation 3-4.

$$l_{Appr} = \pi \cdot (a + b) \cdot \left(1 + \frac{3\lambda^2}{10 + \sqrt{4 - 3\lambda^2}} \right), where \; \lambda = \frac{a - b}{a + b}$$

<div align="right">equation 3-3</div>

$$R_{coil} = \frac{\rho \cdot l}{A} \rightarrow R_{coil} = \frac{4 \cdot \rho \cdot l_{Appr}}{\pi \cdot \left(\frac{d_{Wire}}{2} \right)^2}$$

<div align="right">equation 3-4</div>

A is the cross-sectional area of the wire and ρ is the resistivity of the wire – $1.7 \cdot 10^{-8}$ Ω/m for copper[153]. Using these values, the simulation program Ansoft Designer and Smith Chart (V4.1, Fritz Dellsperger) was used to calculate the impedance and adjustment network.

We designed transmit-receive (Tx/Rx) ^{7}Li RF coils, so we used a 1-port measuring system for simulations. In the Smith chart, only the self-reflection parameter S11 was taken into account. The difference in resonance frequency between ^{1}H and ^{7}Li (245 MHz at 9.4T) meant that the impedance was sufficiently high to render a passive filter network unnecessary.

Each coil was simulated using Ansoft Designer. In Fig. 3-1C, the two-segment coil loop is shown with coil inductance, coil resistance, and segmentation capacitors; the adjustment network is referred to as Tx/Rx-Port. The adjustment network was determined by the Smith chart in Ansoft Designer. After calculating the values of the components in the adjustment network, we ensured that the impedance was 50 Ω at the resonance frequency of ^{7}Li.

Including the adaption network in the Ansoft Designer software, allowed for a simulation of the S11 response. The network had a minimum at 155 MHz corresponding to the resonance frequency of ^{7}Li, Fig. 3-1B.

To account for variations in coil loading, we added a matching and tuning network with variable capacitors and/or inductors, Fig. 3-1A. Small deviations between the measuring bench and MRI system were compensated by home-built variable inductors. The inductance could be changed by simply stretching or compressing the inductors.

3.3.3 Bench evaluation:
The matching and tuning process adapts the coil from its starting impedance to the required 50 Ω using a Smith chart. Non-magnetic capacitors (Johanson Technology, Camarillo, California, USA) were used for the segmentations. The fixed capacitor deviated by a few pF from the simulations.

The coil loop was created from a silver-plated, 1-mm copper wire. The circuit board (Fig. 3-2A-B, Fig. 3-2D) was 3D-printed and fitted with 6-mm adhesive copper tape with a thickness of 0.05 mm, Fig. 3-2. Adhesive copper tape distributes electrical conduction over a larger area than a cable, counteracting the skin effect.

Fixed capacitors allowed for better utilization of the variable capacitors (Bürklin, Oberhaching, Germany). For some networks, we used self-built inductors, Ø1.2 mm copper wire. The variable inductors measured 10 mm in outer diameter and 15-20 mm in length.

The segmentation capacitors, adaption network, and BNC Tx/Rx-port are visualized on the finished coil, Fig. 3-2E. The final adaption network varied slightly from the simulation, but the components were the same type.

We note that soldering the wires and components on the 3D-printed board may cause minor complications due to heating. In rare cases this may cause melting of the 3D model. Furthermore, the adhesive wires were prone to breaking off the board when care was not taken, Fig. 3-2C.

3.3.4 Coat wave barrier:
Sheath currents arise unintentionally when the cable and coil behave as capacitors resulting in unwanted, imbalanced currents. The voltage induced by the system causes a disturbance of the Tx/Rx signal preventing optimal coil performance. We used a braid-breaker with a capacitive coupler to suppress sheath currents with frequencies near the resonance
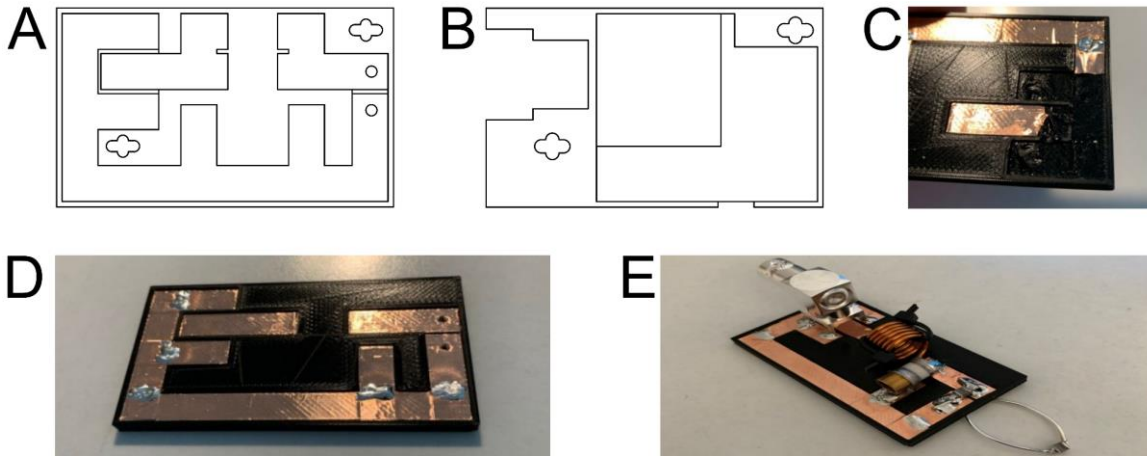
Figure 3-2: ^{7}Li single-resonance RF coil assembly. The layout of the board (A) and lid (B) were made so that all four coils could be assembled on the same board file. The copper tape should be handled with care as it would come off the board if too much force was used (C). The board was assembled first with copper wires (D) and then the adjustment network (E).

frequency of ^{7}Li. The capacitive coupler was realized as a resonant circuit using a coaxial cable with three turns and two parallel capacitances. The sheath current filter was tuned to the resonance frequency of ^{7}Li and positioned in front of the circuit network using BNC adapters at about λ/4. The sheath current filter prevented interference during movement of the cable[154]. The sheath current filter was built from an RG174 c/u coaxial cable and had a capacitance of 62 pF. We created a 3D model to stabilize the sheath current filter and fix the BNC adapters.

An RG223 coaxial cable with an impedance of 50Ω was used to connect the sheath current filter and MRI system. The sheath current filter was connected to the RG223 coaxial cable and RF coil via BNC adapters.

3.3.5 Construction:

The RF coil was connected to the sheath current filter with BNC connectors. The sheath current filter was connected to the MRI system with a Tx/Rx connector. The RF coil was enclosed by a 3D-printed case to protect against damage while still allowing manipulation of the variable inductors and capacitors.

The 3D models were printed with polylactic acid (PLA, standard). The 3D-printed circuit board had a surface area of 40 x 25 mm^2 and thickness of 5 mm. The RF coil was compact to enable versatile positioning in the MRI system.

Depending on the number of segments in the coil ring, the adjustment networks varied slightly, but each configuration could be realized on the 3D-printed circuit board.

3.3.6 Probes:

A realistic mouse head phantom was made based on previously acquired MRI data. The phantom was shaped like the top of a mouse head with a hollow cavity for the brain. The phantom was filled with 100 mM LiCl in 3% agarose solution. We compared the SNR and B1 map of each coil using similar acquisition parameters to the *in vivo* experiments.

3.3.7 MR hardware and acquisition:

MR data was acquired on a 9.4T Bruker MRI system with a 30-cm horizontal bore. The four homemade coils were compared to a commercial, 17-mm, dual-channel surface coil (RAPID Biomedical, Rimpar, Germany). As the home-built coils were single channeled, we used an 86-mm ^{1}H resonator for positioning the animal or phantom as well as acquiring structural images.

The reference power was optimized using non-localized spectroscopy with a flip angle of 90° and repetition time of 40s. The reference power was varied from 0.001-0.030W with increments of 0.001W. The optimal reference power was calculated by finding the maximum area under the curve (AUC), Fig. 3-3A.

We calculated the B1 map of each RF coil using the double angle method[155] using a 2D fast low angle shot (FLASH) sequence with the parameters: 40s repetition time, 2.4 ms echo time, 45°/90° flip angle, 32×32 matrix size, 5 slices, $2{\times}2{\times}3$ mm^3 voxel size, and 21:20 min acquisition time.

To compare the SNR between the RF coils, we acquired ^{7}Li MRS using an image-select *in vivo* spectroscopy sequence[32] with parameters: 2.5s repetition time, 10000 Hz acquisition bandwidth, 256 data points, $6{\times}5{\times}8$ mm^3 voxel size, 120 averages, and 40 min acquisition time. The AUC was calculated using Lorentzian fitting of the magnitude spectra.

[7]Li MRI was acquired using the 2D SPIRAL sequence we have previously described. The SNR was calculated by taking the mean intensity of the region of interest and dividing by the mean intensity of the noise. The parameters of 2D SPIRAL [7]Li MRI were: 2.5s repetition time, 90° flip angle, 7500 Hz acquisition bandwidth, 16×16 matrix size, 2 slices, $2{\times}2{\times}3$ mm^3 voxel size, 5760 averages, and 4 hr acquisition time.

[1]H reference images were acquired with a FLASH sequence: 350 ms repetition time, 3 ms echo time, 30° flip angle, 32×32 matrix, 12 slices, 0.5-mm isotropic voxel size, 12 averages, and 4:29 min acquisition time.

3.3.8 Animal experiments:

Two female C57BL6/N mice were fed a lithium-enriched diet (0.3% Li_2CO_3 w/w) for 5 weeks. We have previously reported the lithium uptake kinetics and imaging from mice undergoing this treatment (chapter 2). The study was approved by the local authorities (TVA: 33.19-42502-04-20/3365).

3.4 RESULTS:

The home-built coils, with the exception of the 1-segment coil, had lower reference power than the commercial coil, Fig. 3-3A. As expected, the reference power was negatively correlated with the AUC (Pearson's R=-0.80) and SNR (Pearson's R=-0.85) of the localized [7]Li spectra. The AUC curve has a local minimum which corresponds to an RF pulse with a flip-angle of 180° or four times the optimal reference power. The home-built 2-segment coil had the highest AUC and lowest reference power.

Having determined the optimal reference power for each coil, we acquired B1 maps with the double-angle method. There were only minor differences in homogeneity between home-built coils and the commercial coil, Fig. 3-3B.
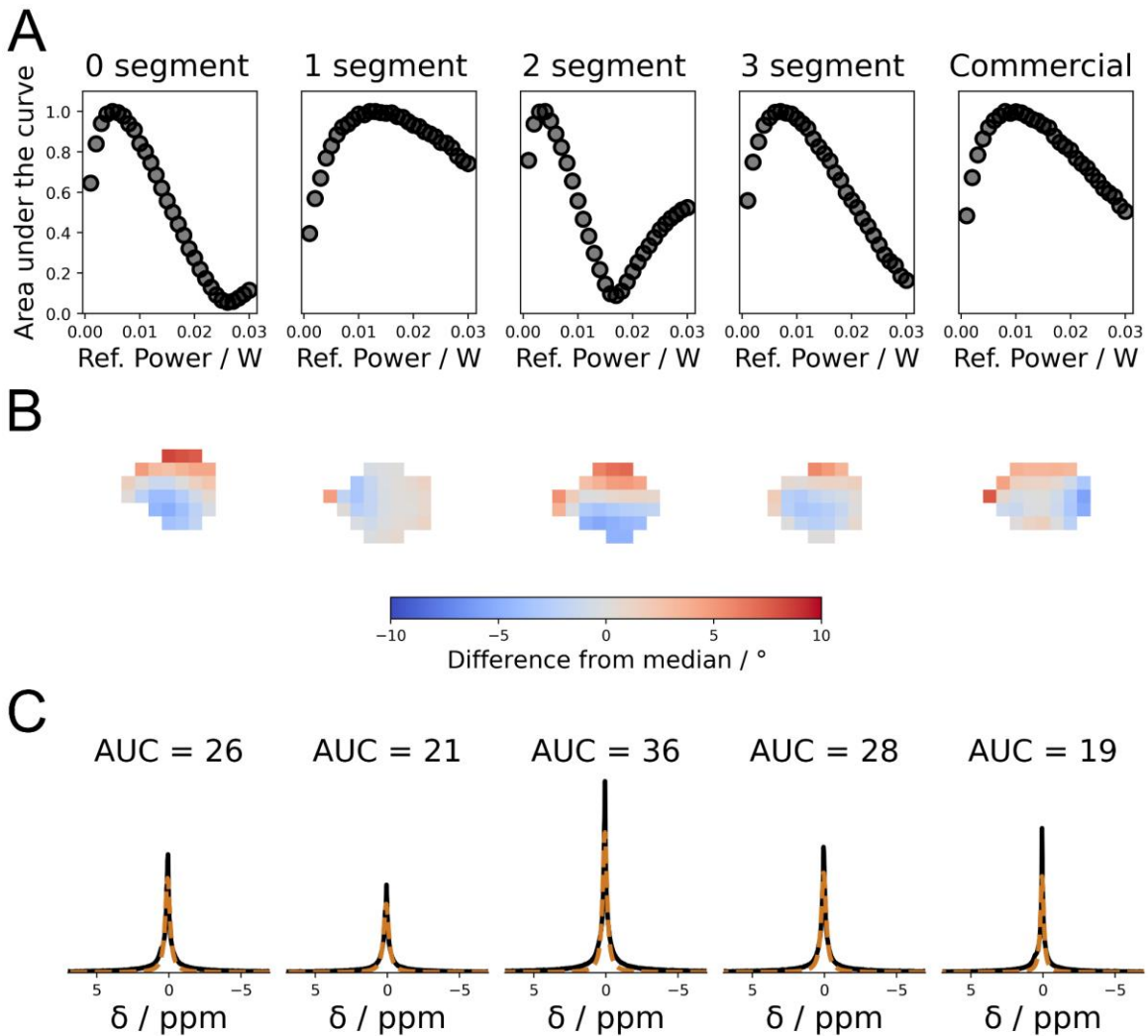
*Figure 3-3: **In vitro RF coil performance test.** The reference power was optimized by calculating the area under the curve at each reference power (A). A minimum was reached at four times the reference power, corresponding to the 180° flip angle. The 0-segment and 2-segment coils show left-right differences in their B1 maps (B). Similarly, the commercial coil showed a similar front-back gradient (B). These are likely the result of the probe lying crooked in the scanner. The 2-segment coil had the largest area under the curve of the five tested coil (C).*

Due to higher SNR and low discrepancies amongst B1 maps, we decided to use the 2-segment coil for the *in vivo* measurements, Fig. 3-3B-C.

In vivo ^{7}Li MRS were acquired from mice in their fifth week of a lithium-enriched diet, Fig. 3-4A. The AUC of the two-segment coil was on average higher than the commercial coil (animal 0: 4.7 vs 3.6; animal 1: 4.7 vs 3.0). We did not observe different AUC between animal 0 and 1 with our home-built coil. In contrast, we observed higher AUC in animal 0 than animal 1 with the commercial coil.

In vivo ^{7}Li images were overlaid on ^{1}H reference image, Fig. 3-4B-C. The lithium signal originated primarily in the brain. The SNR was higher in the dorsal than ventral slice (4.7 vs. 4.0); notably, the SNR of the ^{7}Li images acquired with the home-built coil were lower than those reported in our previous study (chapter 2). Consistent with our previous findings, the signal intensity of both the olfactory bulb and cerebellum were low, whereas the center of the brain had high lithium signal.
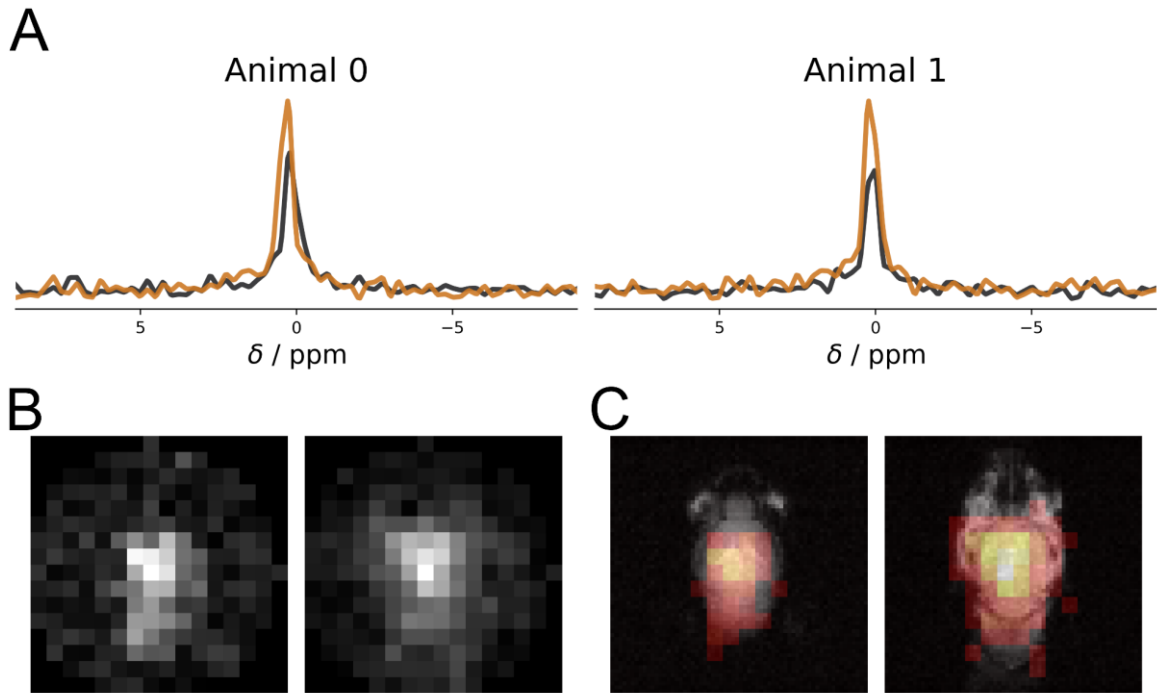
*Figure 3-4: **In vivo ⁷Li MRI/S using a home-built RF coil.** The area under the curve of the 2-segment coil (A in orange), was higher than that of the commercial coil (A in black). The 2-segment coil allowed for in vivo ⁷Li MRI of mice (B) with the signal primarily originating from the brain (C).*

3.5 DISCUSSION:

As ^{1}H imaging was performed with a large volume coil, the ^{1}H image quality was worse than for the dual-tuned commercial surface coil. Reducing the size of the coil, specifically the components of adjustment network, would allow a decrease in the diameter of the volume coil, thereby improving the quality of ^{1}H images.

The minimalist structure of our coil allows for easy implementation of adjustment networks for different nuclei and coil segmentations. The coils may be improved by the addition of a sheath shaft filter, directly integrated on the board, or an implementation of the Tx/Rx coaxial cable on the board without the use of a BNC adapter. Increasing the wire diameter would further reduce the coil impedance and minimize electrical losses. Here, we present a guide to coil building that can also be applied to other nuclei. We note that optimal number of segmentation on a coil will vary with the size of the coil, as over-segmentation would lead to a loss rather than gain in coil quality factor.

The B1 field maps showed only minor differences between the different coils. We do note that the left-right differences seen primarily in 0-segment and 2-segment coil as well as front-back in the commercial coil may be a result of the probe lying askew in the MRI system, which may lead to the observed B1 map gradients across the probe, Fig. 3-3B.

^{7}Li MRI and MRS showed that our coils work at a comparable level to conventional commercial coils. We note that especially in X-nuclei MRI/S, the observed SNR gain may be significant due to the low signal environment. *In vivo* ^{7}Li MRS had increased SNR and ^{7}Li MRI had a slight reduction in SNR compared to the commercial coil. We note that the SNR calculation for imaging is based on the ^{7}Li images. As our coil is longer than the commercial coil, the field of view will increase, thereby increasing signal in low lithium areas,

ultimately affecting the SNR calculation. Finally, the coil was positioned directly on the mouse head at a brain depth of about 3 mm, thereby increasing signal compared to a traditional surface coil.

3.6 CONCLUSION:

We have showed that a home-built, cost effective ^{7}Li coil gave comparable signal quality to commercially available alternatives. Our 3D-printed board allows for high versatility and can be used for other nuclei. We aimed to make the development and building of X-nuclei surface coils a feasible and economically viable option for laboratories. Further improvements could increase the specificity and sensitivity of the coils, such as the usage of components with larger value ranges and the integration of filter systems. Ultimately, we have shown that a home-built ^{7}Li coil can achieve sufficient SNR for *in vivo* ^{7}Li MRI in mice.

3.7 AUTHOR CONTRIBUTIONS:

All authors contributed to the conceptualization and design of the study. S.B., A.M., and J.G. supervised the study. M.D. performed the benchwork. M.D. and T.R.M. performed data acquisition. T.R.M. conducted the formal analysis and data visualization. M.D. and T.R.M. wrote the first draft of the manuscript. All authors commented on previous versions of the manuscript and have read and approved its final version.

4

CROSS-SPECIES LCMODEL ANALYSIS

Cross-species quantification of ^{1}H magnetic resonance spectra - Lessons learned from simulation and in vivo data

Tor Rasmus Memhave[1,2,3], Susann Boretius[1,2,3]

[1]Functional Imaging Laboratory, German Primate Center, Leibniz Institute for Primate Research, Göttingen, Germany

[2]Georg-August Universität Göttingen, Göttingen, Germany

[3]International Max Planck Research School for Neurosciences, Göttingen, Germany

Own contributions:

- Conceptualization
- Data analysis
- Data interpretation
- Data visualization
- Writing

Submitted

4.1 ABSTRACT:

LCModel is considered the gold-standard in magnetic resonance spectroscopy (MRS) analysis. Despite this, accurate quantification of MRS data is still challenging and LCModel is known to behave non-ideally on noisy data. In recent years new, open-source MRS analysis software have been created with the aim of improving MRS quantification. We investigated the quantification accuracy of LCModel on cortical MRS data from two different field strengths and five different species – using a combination of *in vivo* and *in silico* data. MRS data from mice, rats, and marmosets were acquired at 9.4T with a stimulated echo acquisition mode (STEAM) sequence. Human and macaque MRS data was acquired at 3T with a point-resolved spectroscopy (PRESS) sequence. The starting parameters of LCModel (e.g. chemical shift range) had a large impact on metabolite quantification. Spectra simulated from basis sets (*in silico*) and from *in vivo* spectra had similar quantification noise-dependence. We compared LCModel with default and optimized start parameters to TARQUIN and FSL-MRS. We observed improved spectral fitting for LCModel analysis of preclinical data compared with the other two methods. However, both TARQUIN and FSL-MRS showed more ideal noise behavior – increased variance at higher noise, but low drift of the average concentration. We analyzed and simulated MRS data from the cortex of five different species – mouse, rat, marmoset, macaque, and human – showing evidence for species and metabolite specific noise fluctuations.

4.2 INTRODUCTION:

Quantification of MRS is commonly done using a linear combination of model spectra. We designed this study to illuminate a problem that is well-known amongst preclinical scientist working extensively with MRS; however, it is ill-defined. The problem of systematic quantification errors that change with the noise intensity. When comparing groups of spectra with different quality, the assumption is that the uncertainty of metabolite concentrations will be higher in low quality spectra, but that at the group level the average concentration will remain constant. However, in many cases non-ideal behavior leads to increased and/or decreased metabolite concentrations as a function of the signal quality.

MRS allows researchers and clinicians to study *in vivo* brain metabolism across multiple species and field strengths. The acquisition of single voxel spectroscopy is routine in preclinical research; however, a challenging analysis limits widespread clinical implementation. To ameliorate the MRS analysis, best practice guidelines exist for humans[156] and rodents[157] along with expert recommendations for terminology[158] and minimal reporting standards[159]. For preprocessing and analysis of single-voxel spectroscopy there is likewise an experts recommendation on the ideal handling of spectra[160]. Although these recommendations have come a long way toward standardizing analysis and reporting practices, they often deal primarily with human spectra that have an inherent higher signal-to-noise ratio (SNR) than most preclinical data.

Conventional, and recommended, MRS analysis is done through fitting a linear combination of model spectra[160]. The model spectra may be either measured or simulated. The group of model spectra used is collectively referred to as a basis set. A measured basis set will have to be acquired for each sequence and with the exact same parameters as the *in vivo*
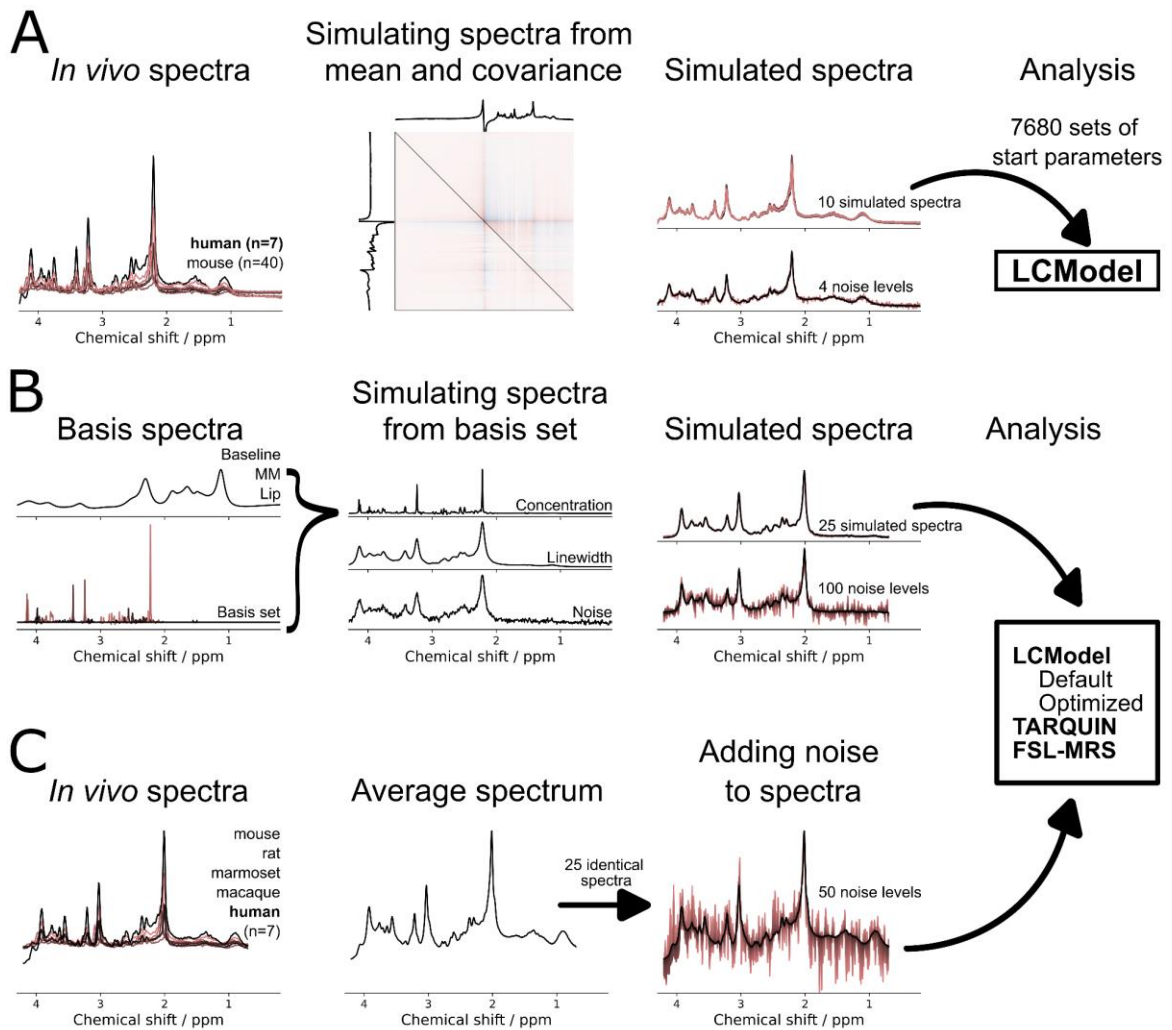
Figure 4-1: **Simulation overview.** *Three different spectral simulation techniques were used. For the optimization of the LCModel start parameters (A) we simulated data using representative spectra from humans (for 3T, depicted as an example) and mice (for 9.4T). The simulated spectra were created using a real and imaginary component multivariate normal distribution using the mean and covariance. The covariance matrix shows both the real and imaginary component (black triangle), the color map is adjusted to improve visualization. The species-specific simulated spectra (B) was created using a linear combination of basis spectra as well as macromolecules, lipids, and Gaussian baseline. The species-specific noise fluctuations (C, human spectra depicted) were simulated on the average spectrum of each species with random noise progressively added.*

spectra, which is time consuming; however, it will take into account specific spin-spin relaxation parameters that are difficult to implement in a simulated basis set[161].

LCModel was the first software to quantify *in vivo* MRS using full *in vitro* model spectra of the metabolites[25]. Prior to LCModel, quantification was performed by curve fitting using prior knowledge[162]. Despite being an older software, original publication in 1993, LCModel is still commonly considered the gold standard for benchmarking new fitting software. The main advantage of LCModel compared with other software is its relative ease-of-use. LCModel requires three files – metabolite free induction decay (FID), unsuppressed water (reference) FID, and a control file – to calculate the concentration of metabolites in the spectrum. The output of LCModel is a graphical summary, table, and coordinate file. These files allow for a quick overview of fit quality parameters such as SNR and linewidth.

However, as LCModel is limited by relying on its own file format and started as a proprietary software, it is difficult to alter and apply in a larger context. This has led to the development

of a wide-variety of different fitting software: FSL-MRS[163], jMRUI[164], TARQUIN[165], and VESPA[166] (non-exhaustive list). These software vary in style from pipeline-based python packages (FSL-MRS and VESPA) to standalone software (jMRUI and TARQUIN). In the last part of this study, we will compared LCModel to FSL-MRS and TARQUIN. FSL-MRS uses NIfTI files and is written in python[163]. TARQUIN allows for the direct usage of files from different operators as well as LCModel raw and is written in C++[165]. In both software a small script may be used to analyze the data without user interaction. Furthermore, the software are open-source, which means user-specific implementations are possible.

Recently developments in the field of MRS have focused on improving spectral quantification. A recent challenge from the international society for magnetic resonance in medicine (ISMRM) showed that despite similar pipelines and software choices there was substantial variability in the results achieved by different groups[167]. The ISMRM challenge was, however, limited to simulated spectra at 3T.

In this study, we analyze cross-species MRS data and provide a pipeline for simulating spectra that are visually similar to *in vivo* spectra at two field strengths. We show metabolite specific fluctuation profiles, compare grey matter MRS of five different species, and show differences between LCModel, TARQUIN, and FSL-MRS quantification for each of these species. The simulation of *in vivo* MRS spectra from basis sets will allow for better benchmarking of new analysis software. The cross-correlation of specific metabolites in uncorrelated spectra as well as species specific metabolite fluctuations give indications of some of the pitfalls of *in vivo* MRS quantification. Finally, comparing LCModel, TARQUIN, and FSL-MRS, we showed the advantages and disadvantages associated with each of these software for *in vivo* quantification of MRS at two field strengths in five species.

4.3 RESULTS:

4.3.1 Simulation of MR spectra

We employed three different types of spectral simulation (Fig. 4-1). First, we generated spectra based on *in vivo* MRS data, creating ample representative datasets to optimize the start parameters for LCModel (Fig. 4-1A). These spectra were simulated using the mean and covariance of *in vivo* data obtained from either humans (n=7, 3T) or mice (n=40, 9.4T). Second, we used basis sets provided by TARQUIN to simulate spectra, including macromolecules, lipids, and a Gaussian baseline (Fig. 4-1B). This approach allowed us to generate spectra with metabolite concentrations specific to each species while avoiding potential bias due to differences in the quality of *in vivo* spectra. Third, we added progressively increasing noise levels to *in vivo* spectra obtained in rodents, non-human primates, and humans (Fig. 4-1C). These spectra were used to explore the quantification accuracy and noise bias of LCModel with default and optimized start parameters and in comparison to TARQUIN and FSL-MRS.

4.3.2 Optimal LCModel start parameters varied across field strengths.

To find the optimal LCModel start parameters, we utilized ten simulated spectra derived from the mean and covariance of *in vivo* spectra from humans (3T) and mice (9.4T), respectively (Figure 4-1A). We tested 7680 different start parameters – each possible iteration of column 2 in Table 4-1. To evaluate the metabolite concentration estimation by

LCModel for each of the 7680 cases, we focused on a group of eight metabolites that are prominent in both mice and humans: myo-inositol, taurine, γ-aminobutyric acid (GABA), glucose, total N-acetylaspartate, total phosphocholine, glutamate plus glutamine, and total creatine.

To identify the optimal LCModel start parameter, we first explored their robustness against noise. We added three different noise levels to each of the simulated spectra (0.33, 0.66, and 1.00 times the standard deviation of the spectrum, Fig. 4-2A-B left column). We then selected all those sets of start parameters leading to metabolite concentrations within a specific cumulative bias range (Fig 4-2A-B, in red). The cumulative bias was defined as the sum of the differences in the metabolite concentrations of each of the three noise-level spectra to those concentrations received from the spectra with no added noise. We found an absolute bias limit of 25 divided by the respective spectral SNR (provided by LCModel) most suited, Fig. 4-2A-B top right. Secondly, the non-noise-added spectra were analyzed with the above identified parameter sets (Fig. 4-2C-D) and the metabolic SNR was calculated. To calculate the metabolic SNR, we calculated the average and standard deviation of each metabolite for every parameter set. The metabolic SNR was defined as the sum of the eight average metabolite concentrations divided by the sum of the eight standard deviations of the metabolite concentrations; see equation 4-1 in the method section. Finally, the parameter set with the highest metabolite SNR was chosen for further analyses. The optimized and default start parameters are given in table 4-1.

At 3T, we observed that increasing the parameter "dkntmn" (baseline flexibility) from 0.15 to 0.25 yields a more rigid baseline, which led to higher metabolite SNR, Fig. 4-2C. A mild line broadening by 0.5 Hz also improved the metabolite SNR. In general, line broadening is not recommended for LCModel as it will alter the program statistics[25,160]. However, we did not use the Cramer-Rao bounds for uncertainty here, as the spectra are all drawn from the same distribution. Changing the downfield and upfield limit of the chemical shift range from 4.2-0.7 ppm also improved metabolite SNR. This is especially noteworthy since 0.7 ppm is further downfield than the recommendation for short echo time spectroscopy[25]. The standard deviation of the phase correction did not have a significant systematic impact on the metabolite SNR.

At 9.4T, we found that a slight increase in baseline flexibility to 0.20 gave the optimal metabolic SNR, Fig. 4-2D. In contrast to the 3T data, a line broadening of 2 Hz improved the metabolite SNR, most likely due to the noisier nature of the mouse spectra. Increasing

Table 4-1: Six parameters were changed during the optimization of LCModel start parameters. The default and optimized LCModel start parameters at both 3T and 9.4T are given.

Start parameter (unit)	Values	Default	Optimized (at 3T)	Optimized (at 9.4T)
Line broadening (Hz)	0, 0.5, 1, 2, 3, 5	0	0.5	2
dkntmn	0.09, 0.12, 0.15, 0.20, 0.25	0.15	0.25	0.20
sddegz	5, 25, 45, 999	999	45	25
sddegp	5, 8, 11, 20	20	11	11
ppmst (ppm)	4.3, 4.2, 4.1, 4.0	4.0	4.2	4.3
ppmend (ppm)	0.2, 0.3, 0.5, 0.7	0.2	0.7	0.2

the chemical shift range to cover the entire spectrum improved the metabolite SNR further, likely due to the downfield myo-inositol peak at 4.05 ppm and the significant macromolecule contribution seen at 0.7 ppm. Similar to the optimization at 3T, we did not observe systematic influences of the phase correction terms on the metabolite SNR.

4.3.3 Optimized LCModel parameters improved robustness against noise at 9.4T.

We then investigated the robustness of LCModel quantification against noise when using the identified optimal start parameters compared to the default set. Here, we focused our analysis on the two most abundant metabolites: total N-acetyl aspartate and total creatine. The results are shown in Fig. 4-2E in grey for the default and in red for the optimized set of parameters.

We found no noticeable improvement with the optimized parameters for the simulated 3T human data, Fig. 4-2E. In contrast, at 9.4T, the metabolite concentration of total N-acetylaspartate and total creatine showed marked improvement when analyzed with the optimized compared to default LCModel start parameters, Fig. 4-2F. While the default start parameters showed an increase in the average total N-acetylaspartate concentration with increasing noise, its mean value became almost noise-independent when using the optimized start parameters. Most noticeable is the effect of the parameter choice on the total creatine concentration. The use of the default LCModel start parameters resulted in substantial variations in total creatine concentration, which could be significantly reduced by applying the optimized LCModel start parameters. Moreover, no systematic changes with added noise were observed when using the optimized start parameter.

4.3.4 Simulation of MR spectra from basis data sets requires calibration for concentration and linewidth.

Low SNR often compromises preclinical data, and the linewidth may be broader than in human spectra. Simulating spectra from basis sets can help to distinguish potential species specific effects on the estimated metabolite concentration from those associated with spectral quality. For that purpose, the basis sets need to be calibrated to ensure that the input concentration aligns with the output concentration of the LCModel analysis. To establish the calibration factor for the basis sets utilized in this study, we simulated spectra in which the concentration of each individual metabolite was systematically altered (Fig. 4-3A-B, left column).

We observed the expected behavior for the 3T data. Here, the resulting fitted concentration increased linearly with the simulated concentration, as shown for myo-inositol in Fig. 4-3A. However, the 9.4T spectra exhibited a slight deviation from the linear relationship for myo-inositol concentrations exceeding 10 mM, Fig. 4-3B.

Importantly, the linewidth of the simulated spectrum had a notable impact on the metabolite concentration determined by LCModel. In the simulated 3T spectra, we noted the highest myo-inositol concentration at a line broadening of 1.66 Hz (Fig. 4-3C, right) and of 1.5 Hz on average for all metabolites. For the 9.4T spectra, the peak myo-inositol concentration was obtained at a line broadening of 2.41 Hz (Fig. 4-3D, right), and the highest concentration for all metabolites was, on average, seen at a line broadening of 2.6 Hz.

4.3.5 LCModel exhibited inherent fitting correlations in independent data.

Some metabolites in a basis set, such as creatine and phosphocreatine, have a high spectral similarity. Other metabolites, such as creatine and myo-inositol, have almost no overlapping resonances. We examined the spectral similarity within LCModel's chemical shift range by correlating the real parts of the spectra for each metabolite in the basis set (see Fig. 4-3E-F, left side). This served as a reference point for investigating potential correlations in the concentrations estimated by LCModel for spectra composed of multiple metabolites.
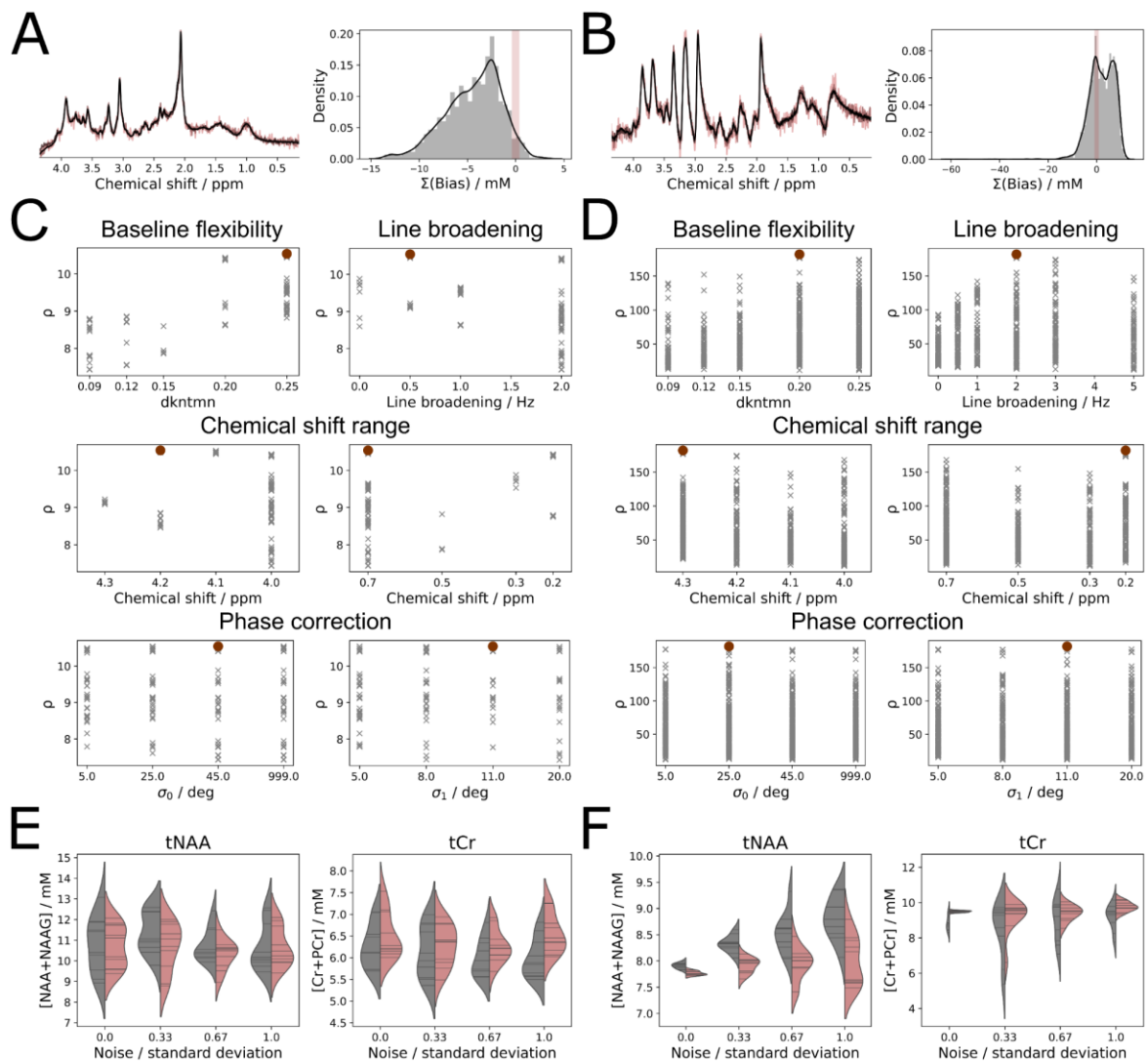
*Figure 4-2: **Finding the optimal start parameters for LCModel**. An example spectrum at 3T (A) and 9.4T (B) with added noise (left). The cumulative bias, Σ(Bias), for each set of start parameters was plotted as a histogram (A-B, right). The bias limit, defined as the acceptable cumulative bias, is highlighted in red. The start parameters within the bias limit were used to find the optimal metabolite SNR, ρ (C-D). The optimal start parameter (red dot) for the baseline flexibility and linewidth (top row), chemical shift range (middle row), as well as phase correction standard deviations (bottom row) showed substantial variation within each group of parameters (C-D). At 3T (C), the optimal start parameters were lower baseline flexibility (0.25) and higher upfield limit (0.7 ppm). At 9.4T (D), the largest chemical shift range gave the optimal fit parameters. Across both field strengths the standard deviation of the phase correction had little impact. The optimized starting parameters (E-F, in red) showed minor improvements in the bias at 3T (E), but marked improvements at 9.4T (F).*

We generated 10,000 spectra from the basis sets, applying the calibration terms for concentration and linewidth that were calculated as explained in the preceding paragraph. To prevent any inherent correlations in the spectra, we opted for a uniform distribution of concentrations. The concentration ranges were determined based on the maximum and minimum concentrations observed across all the *in vivo* spectra used in the subsequent multispecies analysis. The correlation matrixes of the metabolite concentrations estimated by LCModel are shown in Fig. 4-3E-F.

At 3T, we observed that despite spectral similarities (Fig. 4-3E, left), most metabolites showed low correlation in their estimated concentrations (Fig. 4-3E, right). The real parts of the spectra for creatine and –CrCH2 (negative spectrum of the downfield creatine peak) revealed the expected negative correlation, although this was hardly observable for the estimated concentrations. Despite a lack of spectral similarity, a modest concentration correlation was observed for taurine and scyllo-inositol. Glucose concentration showed a moderate positive correlation with phosphocreatine and –CrCH2 and a modest correlation with phosphocholine. A negative correlation with glucose was observed for creatine and glycerophosphocholine. Glucose only shares spectral similarity with myo-inositol; however, the estimated concentrations of myo-inositol and glucose did not correlate.

At 9.4T (Fig. 4-3F), the negative correlation between the real-part spectra of –CrCH2 and creatine was also present in their estimated concentrations. Furthermore, we noted a negative correlation between the concentrations of creatine and phosphocreatine at 9.4T, despite their spectra showing a positive correlation similar to those of the 3T basis set. Likewise, we observed a negative correlation between glycerophosphocholine and phosphocholine. This suggests that the software tends to adjust metabolites with higher spectral similarity. This adjustment can be crucial in maintaining a relatively constant total metabolite concentration and avoiding overfitting. However, it is important to bear this in mind when interpreting results from preclinical MRS studies.

The correlation of metabolites that have high spectral similarity – such as creatine and phosphocreatine – having negative concentration correlation indicates that the software preferentially regulates them. For this reason, glycerophosphocholine and phosphocholine – especially at 9.4T – show strong negative correlation in concentration. These fitting anti-correlations may be important for keeping the total metabolite concentration relatively constant and prevent overfitting; however, their presence means data analysis should be performed carefully.

4.3.6 Pipeline for the simulation of species specific ¹H spectra

Using the results above, we developed a simulation pipeline that allows for the simulation of species specific spectra based on the chosen basis data set, Fig. 4-3G. The tool uses a list of metabolite concentrations with mean and standard deviation of the desired metabolite concentration based on actual measured data. The simulation takes the global concentration and linewidth correction into account. The spectra can be simulated with macromolecules, lipids, and baseline, as well as various levels of noise. The noise is added to the free induction decay after line broadening. A noise level of 1 is defined as 7.5% of the standard deviation over the whole free induction decay. The source code is available on GitHub (https://github.com/Tor-R-Memhave/preppingLCModel).

We used the pipeline to simulate spectra for mice, rats, marmosets, macaques, and humans (Fig. 4-3G) using the following noise levels: 1.5 for mice, rats, and marmosets, 1.25 for
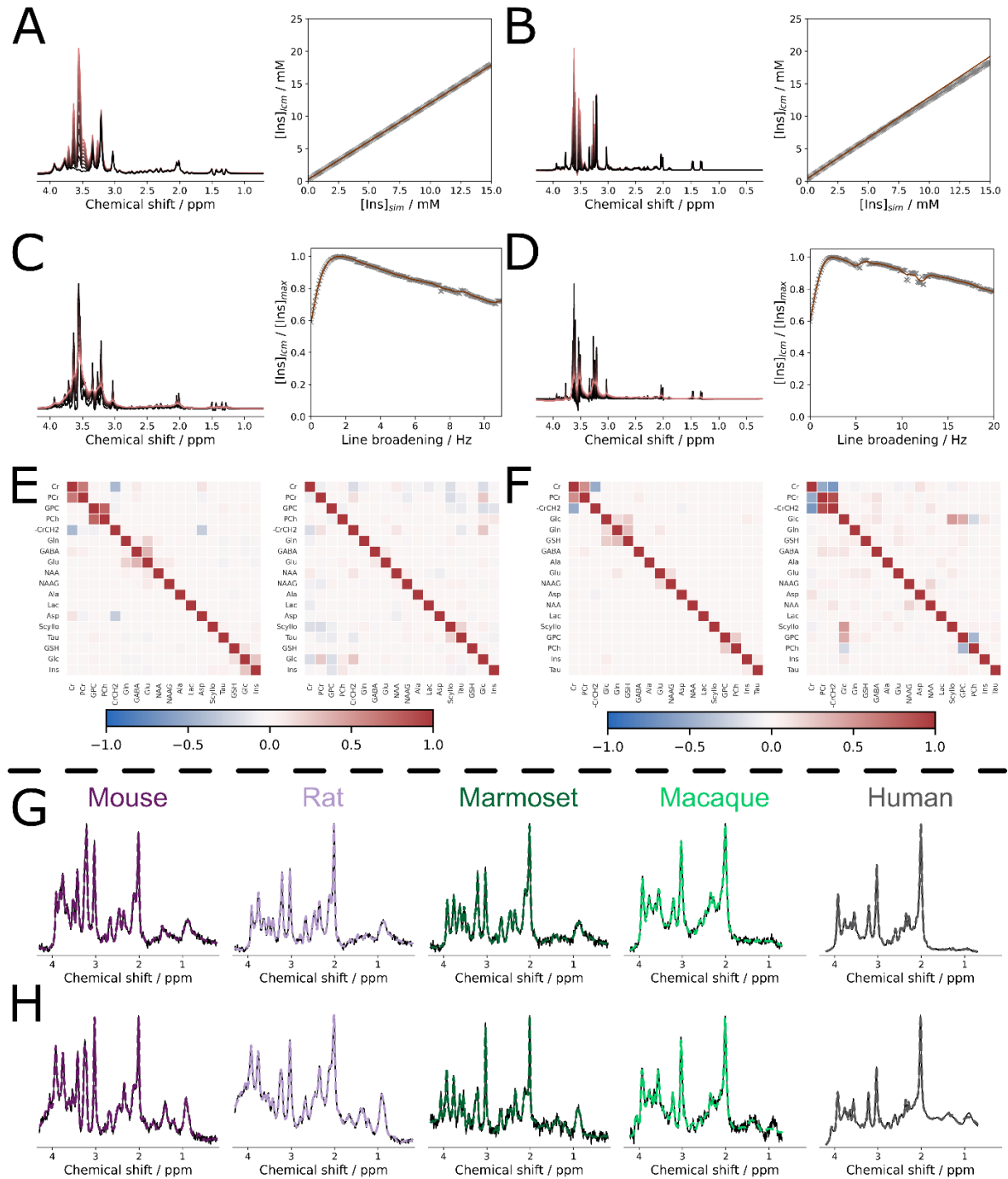
*Figure 4-3: **Species-specific spectral simulation from basis sets.** The spectra (A-D) were simulated using a simulated basis set from TARQUIN at 3T (A,C) and 9.4T (B,D). The black spectrum shows the start condition of the simulation (low concentration (A,B) and narrow linewidth (C,D)) and the red lines show the progressive increase in either concentration or linewidth. The concentration showed linear increase (A-B) and the linewidth (C-D) had a maximum estimated concentration between 1-3 Hz at both field strengths. We compared the correlation matrix of the spectral similarity of metabolites in the basis set (E-F, left) to the correlation between metabolite concentrations fit by LCModel (E-F, right) in 10000 simulated spectra. At 3T (E), only weak correlations are observed between metabolites. However, at 9.4T (F), we observed negative correlation between creatine and phosphocreatine as well as glycerophosphocholine and phosphocholine – the opposite of the spectral analysis. We simulated spectra to look like in vivo spectra (G) for a mouse (purple), rat (pink), marmoset (dark green), macaque (neon green), and human (grey) and compared then with their in vivo counterpart (H). The color for each species will be kept constant for all remaining figures.*

macaques, and 0.25 for humans. The spectra simulated this way did not visually differ from those acquired *in vivo* (Fig. 4-3H).

4.3.7 Cross-species MRS comparisons:

Seven *in vivo* spectra from mice, rats, marmosets, macaques, and humans were acquired at two field strengths. Macaque and human spectra were acquired on a 3T clinical MRI system with a PRESS sequence. Mouse, rat, and marmoset spectra were acquired on a 9.4T preclinical MRI system with a STEAM sequence. All acquisition parameters can be found in table 4-2.

Myo-inositol, a common osmolyte and glial marker[168,169], was increased in nonhuman primates compared with rodents and to a lesser extent humans, Fig. 4-4A. The total N-acetylaspartate increased steadily from rodents to nonhuman primates and humans, Fig. 4-4B. N-acetylaspartate is regarded as a neuronal marker, due to its high concentration in neurons and decrease in many degenerative brain diseases[170]. The most characteristic peaks of the mouse spectrum are the two taurine peaks at 3.25 and 3.4 ppm, which set the spectrum apart from most other species. It is therefore unsurprising that the taurine concentration was highest in mice, Fig. 4-4C. Taurine was higher in rats and marmosets than macaques and humans. Although this effect may be true, it is likely that this difference in part can be explained by taurine being easier to discern from neighboring metabolites at

Table 4-2: Seven animals/subjects were measure for each of the five species. The animal/subject information in the top half. The bottom half of the table shows the spectroscopy sequence parameters.

Parameter	Mouse	Rat	Marmoset	Macaque	Human
Age ($\mu\pm\sigma$)	4.7±0.2 mo	5.1±3.1 mo	9.1±1.6 yr	9.3±3.1 yr	24±3 yr
Sex (male:female)	7:0	0:7	3:4	0:7	3:4
Anesthetized	yes	yes	yes	yes	no
Field strength	9.4T	9.4T	9.4T	3T	3T
Sequence	STEAM	STEAM	STEAM	PRESS	PRESS
Flip angles (˚)	83:83:83	73:73:73	47:47:47	90:180:180	90:180:180
Repetition time (ms)	6000	6000	6000	2000	2000
Echo time (ms)	10	10	10	30	30
Mixing time (ms)	10	10	10	-	-
Data points	2048	2048	2048	1024	1024
Bandwidth (Hz)	5000	5000	5000	1200	1200
Voxel size (mm^3)	8.7	72	75	512	9000
Averages	128	128	128	128	64
Acquisition time (min)	12.8	12.8	12.8	4.3	2.1
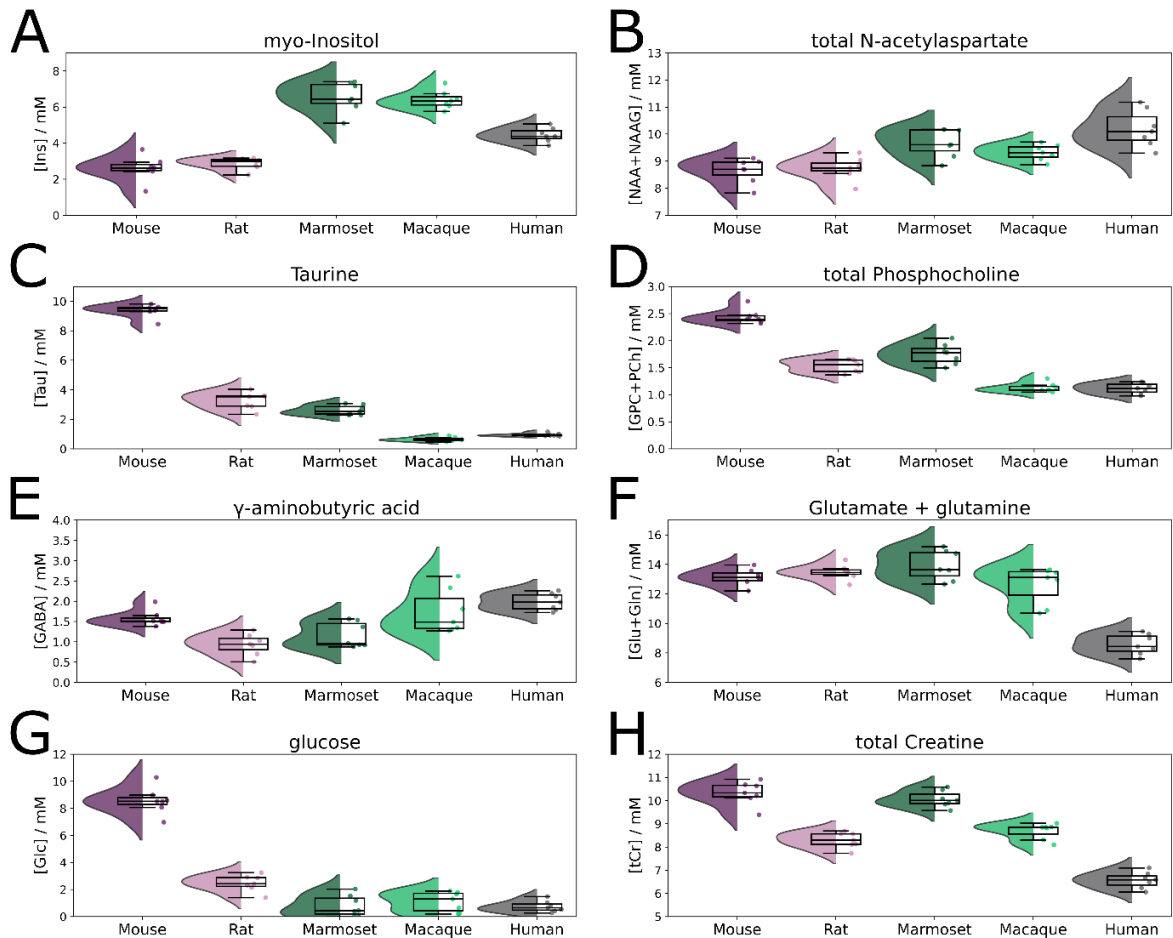
Figure 4-4: **Cross-species comparisons of key brain metabolites.** *The left column shows individual metabolites, whereas the right column shows commonly combined metabolites. The eight metabolites were significantly different across the species (One-way ANOVA p<0.001). Myo-inositol was increased in humans and non-human primates compared to rodents (A). There was a weak increase in total N-acetyl aspartate from mice to humans (B). Taurine was significantly higher in mice than all other animals (C). The total phosphocholine decreased from mice to humans (D). GABA varied across species with rats and marmosets having the lowest concentrations (E). The total glutamate and glutamine concentration was higher in all animals, due to anesthesia, compared with humans. Glucose was elevated in mice (G). Total creatine varied by species, but appears to decrease from mice to rodents and marmosets to humans (H).*

9.4T than at 3T. An interesting pattern in the total phosphocholine concentrations was observed as mice had higher phosphocholine than rats, whereas marmosets had higher concentration than macaques and humans, Fig. 4-4D. However, it should be noted that total phosphocholine concentration in the brain are relatively low in all species (for mice <3 mM). γ-aminobutyric acid (GABA), an inhibitory neurotransmitter, was found to be generally increasing from rats to humans with mice being a slight outlier in this trend, Fig. 4-4E. It is likely that the position of the voxel within grey matter and thereby concentration of inhibitory neurons is the deciding for the GABA concentration[171]. The glutamate plus glutamine concentration was higher in all anesthetized animals than healthy human subjects, Fig. 4-4F. This was anticipated as the concentration of glutamate is known to increase during anesthesia[172]. The glucose concentration in mice was found to be much higher than rats, nonhuman primates, and humans, Fig. 4-4G. We found a similar tendency with total creatine, Fig. 4-4H, as we observed for total phosphocholine, Fig. 4-4D. A marked increase in mice compared with rats and then marmosets compared with macaques and humans. Interestingly, there appears to be a steady decrease in total creatine concentration from marmosets to humans with macaques falling in between. All metabolite concentrations from

the five species can be found in table S-3. For the metabolites discussed in this section statistical tests: one-way ANOVA and post-hoc t-tests are given in table S-4.

4.3.8 The susceptibility to noise is metabolite specific.

As the SNR varies between measurements, studies, and laboratories – it is essential to understand the noise behavior of an analysis method. An ideal fitting algorithm maintains a consistent average even with added noise, although it may exhibit higher variance. However, as most MRS analysis tools rely on optimization procedures with predefined priors, they are likely to behave non-ideally. To test the noise behavior of LCModel, we simulated spectra using two different approaches – from basis sets and from *in vivo* spectra – and progressively added noise, Fig. 4-5A-E left and right side, respectively. We have previously described that LCModel has intrinsic concentration correlations, as such we will look at the noise behavior of all five species. While this behavior is unique for every metabolite, we chose two metabolites with different types of non-ideal behavior: glutamate plus glutamine, Fig. 4-5A-E column 2, and glucose, Fig. 4-5A-E column 3.

We observed an almost ideal noise behavior of glutamate plus glutamine in the spectra simulated from basis set for mice, rats, and marmosets, Fig. 4-5A-C left, with slightly higher noise variation in the spectra simulated from *in vivo* spectra, Fig. 4-5A-C right. However, the glutamate plus glutamine concentration for macaque and humans showed a steady increase prior to the maximum SNR of the spectra simulated from *in vivo* spectra, Fig. 4-5D-E left. Furthermore, the spectra simulated from *in vivo* spectra showed almost 100% increase in glutamate plus glutamine for humans at low SNR. These simulations highlight that glutamate plus glutamine fitting was more robust at 9.4T, Fig. 4-5A-C, than 3T, leading to more ideal noise behavior. Furthermore, we observe that the lower concentration of glutamate plus glutamine in humans led to large overfitting at low SNR, Fig. 4-5E right.

Glucose noise-behavior varies from species-to-species likely due to the concentration variation between species. Most notably in mice the concentration of glucose drops with decreasing SNR, Fig. 4-5A. The behavior is comparable between the two simulations – although the effect is increased in spectra simulated from *in vivo* spectra. The concentration of glucose in rats fluctuated with SNR; however, the average was relatively constant, Fig. 4-5B. Due to the low concentration of glucose in marmosets, the noise behavior was predictably unstable, Fig. 4-4C. However, it is of concern that the glucose concentration showed a stable increase as the SNR decreased. Both macaque and human glucose concentrations were low, which meant their noise behavior was unstable, Fig. 4-4D-E. However, it is particularly problematic that at *in vivo* SNR there is an initial increase in glucose with decreasing SNR followed by a large drop.

The noise behavior of glutamate plus glutamine and glucose were drastically different. However, the metabolite specific noise behavior was partially anticipated. The fact that metabolites at different concentrations behave differently when noise is added was likewise anticipated. However, that metabolites of similar concentration showed different noise behavior across species is previously undescribed. This suggests that the calculated concentration will vary between species not just from concentration differences, but also from fitting uncertainties due to neighboring metabolites.
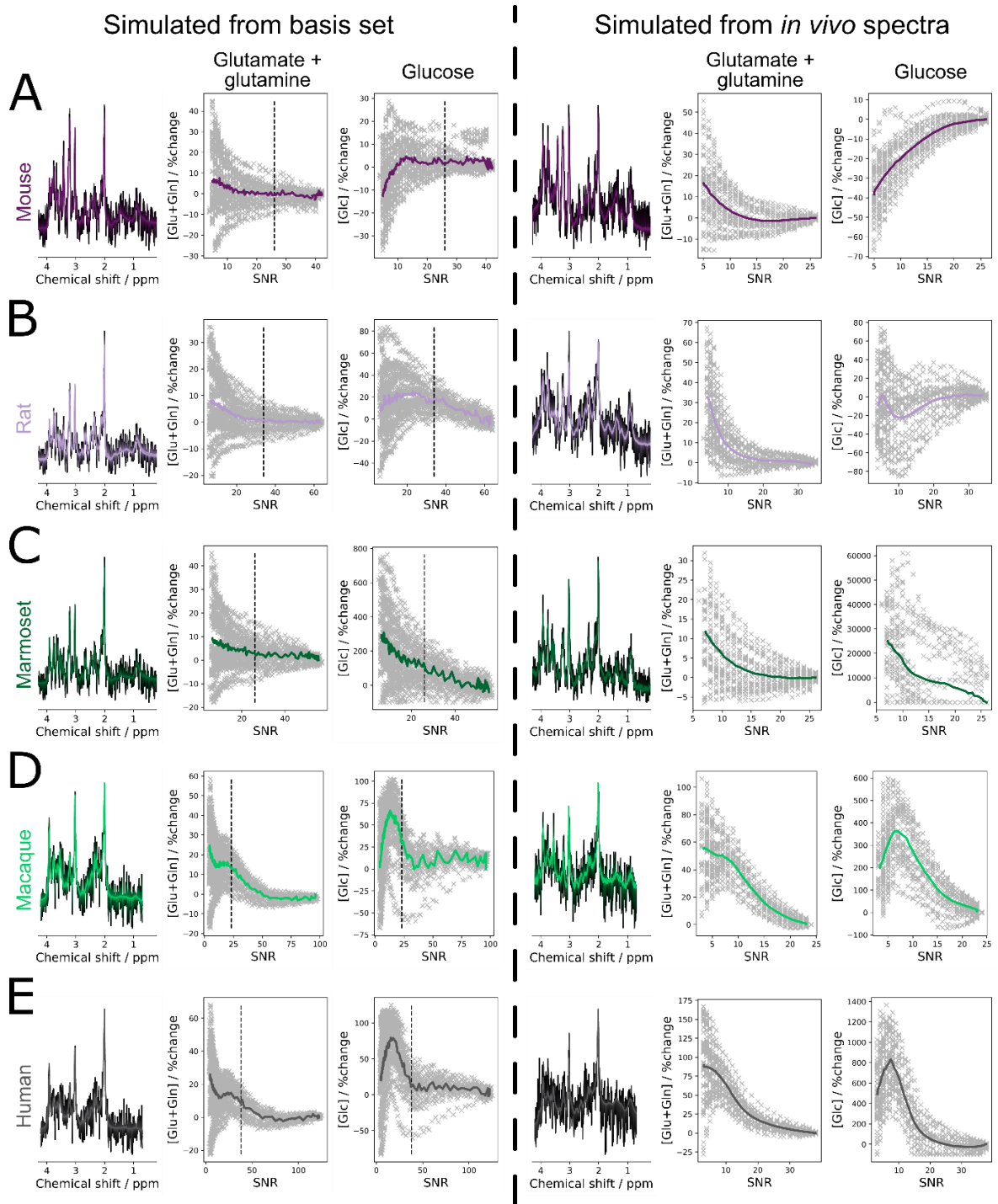
*Figure 4-5: **Species and metabolite-specific concentration changes as a function of SNR.** We looked at the noise behavior of two metabolites (glutamate plus glutamine [Glu+Gln] and glucose [Glc]) across the five species. Noise was progressively added to simulated spectra from basis sets (left side) and from in vivo spectra (right). The black line in column two and three indicate the highest SNR of the in vivo data. Ideal concentration changes with noise are increased variance, but unchanged mean concentration. This type of behavior is observed for glutamate plus glutamine in mice (A), rats (B), and marmosets (C), but not for macaques (D) and humans (E). Glucose behaves in non-ideal manner across all five species – although to a lesser extend in rats.*

4.3.9 LCModel analyses had higher fit quality than TARQUIN and FSL-MRS

While LCModel is still the go-to reference software for benchmarking new analysis software, many other software have been developed for analyzing spectroscopy data. In this study,

we chose to look at two popular software for automated spectroscopy analysis: TARQUIN and FSL-MRS.

We found that optimizing the LCModel start parameters led to an increased coefficient of determination and decreased the mean absolute error compared with the default start parameters, Fig. 4-6A, likely due to line broadening. Looking at the five species, default LCModel analysis generally had a higher coefficient of determination and lower mean absolute error than FSL-MRS and TARQUIN, except for in marmosets where TARQUIN performed better.

4.3.10 LCModel, TARQUIN, and FSL-MRS showed comparable concentration trends across species

To have a more direct comparison of the fitting software, we looked at the concentration of metabolites. We ignored T1-effects for the analysis and normalized the concentrations to total creatine.

We observed comparable metabolite patterns across species for all four analyses, Fig. 4-6B. The optimized start parameters for LCModel led to lower variation within a species compared with the default start parameters, except for myo-inositol in mice, Fig. 4-6B left. We note that a few differences were observed amongst the different software. TARQUIN had a lower spread in myo-inositol values between the groups – most notably with higher concentrations in rodents and decreased concentrations in non-human primates. FSL-MRS had increased variance across all myo-inositol fits. Taurine estimates showed similar tendencies amongst the four software with mice having higher taurine than rats and marmosets and almost no taurine in macaques and humans. However, the taurine concentration is likely overestimated for mice by TARQUIN and FSL-MRS.

The four different analyses showed comparable relative concentration estimates for the species. While LCModel showed a lower variance for most species, the other software performed as expected with only a slight bias toward overestimating taurine. TARQUIN and FSL-MRS were created, primarily, for human data, which has a higher intrinsic SNR. As such, it was reassuring to see relatively high agreement between the four analyses for the human data.

4.3.11 LCModel, TARQUIN, and FSL-MRS showed comparable noise-dependence for at in vivo SNR

We chose to compare the SNR of the four different methods using human spectra simulated from basis sets with procedurally added noise. We have previously shown the non-ideal behavior of glucose in humans with the optimized LCModel start parameters, Fig. 4-5E. It is therefore relevant to explore the noise behavior of all four analyses, Fig. 4-6C.

All four analyses showed ideal noise behavior for myo-inositol at SNR>25, Fig. 4-6C. However, only TARQUIN and FSL-MRS showed ideal noise behavior at SNR<25. The standard deviation of the myo-inositol concentration was lower for FSL-MRS analysis than TARQUIN. The two LCModel approaches were prone to overfitting the concentration at low SNR. The default LCModel start parameters led to increasing and then decreasing myo-inositol concentrations, whereas the optimized LCModel start parameters found steadily increasing myo-inositol concentrations with decreasing SNR.

4.4 DISCUSSION:

We developed three different simulation techniques for creating artificial data that were used for three different aims: finding the optimal LCModel start parameters, simulating spectra from basis set that looked like *in vivo* spectra from different species, and adding noise to a mean spectrum to understand *in vivo* noise behavior. Spectral simulation using the mean and covariance generated spectra that were visually similar to *in vivo* spectra with comparable properties, but they were not identical. This may be of particular use for data augmentation purposes or as presented here for optimizing parameters for the original data without directly using the original data. Our simulation pipeline simulates spectra from basis sets using the mean and standard deviation of the metabolites of a species. We found that calibration these spectra for concentration and linewidth biases was important for accurate quantification. As the data can be simulated at various noise levels, it is our hope that the simulation pipeline may be used for statistical planning related to animal experimentation, thus reducing the number of animals used in research. Adding noise to the mean spectrum for each species gave the simplest simulation paradigm. It was ideal for testing the concentration as a function of SNR with a constant ground truth.

The noise and linewidth behavior of LCModel has previously been reported[173–181]. Our discussion of noise will deal with spectra simulated from basis sets and *in vivo* spectra. While it was reassuring that the noise behavior of the spectra simulated from basis sets was comparable to the spectra simulated from *in vivo* spectra, it is more important to understand how they were different. First and foremost, when simulating spectra from basis sets, we used the same basis set for fitting, which means that the noise behavior was as ideal as possible. For the spectra simulated using *in vivo* spectra, we used our standard analysis pipeline with different basis sets; however, since the spectra also contain information from metabolites not in the basis set, the uncertainty increased at low SNR.

Non-ideal noise behavior is common and should be expected for all *in vivo* spectra of varying quality. In this study, we provide direct evidence of this fact and we can only reiterate that reporting SNR, linewidth, and exact fitting parameters is paramount for both interpretation and reproducibility. The reporting of analysis method, SNR, and quality control parameters is recommended[159]; however, we would like to extend this recommendation to include a few more measures. Most analysis software have default start parameters, which are used for fitting. Even if these default parameters are used, it would be beneficial to explicitly report the chemical shift range and the baseline type. In the optimization of LCModel start parameters, we observed that these two parameters led to large fluctuations in the metabolite SNR. For LCModel, in lieu of reporting all start parameters, a copy of the control file can be included. The spectral SNR and linewidth range should be reported for all groups and if significant differences are observed, the potential impact of SNR and/or linewidth on the conclusions drawn by the study should be discussed. Two types of quality control measures should be provided: metabolite concentrations and fit quality. It is our recommendation that the coefficient of determination and/or the mean absolute error are reported for all groups. The coefficient of determination and mean absolute error are complementary and negatively correlated, meaning that reporting one may be sufficient.
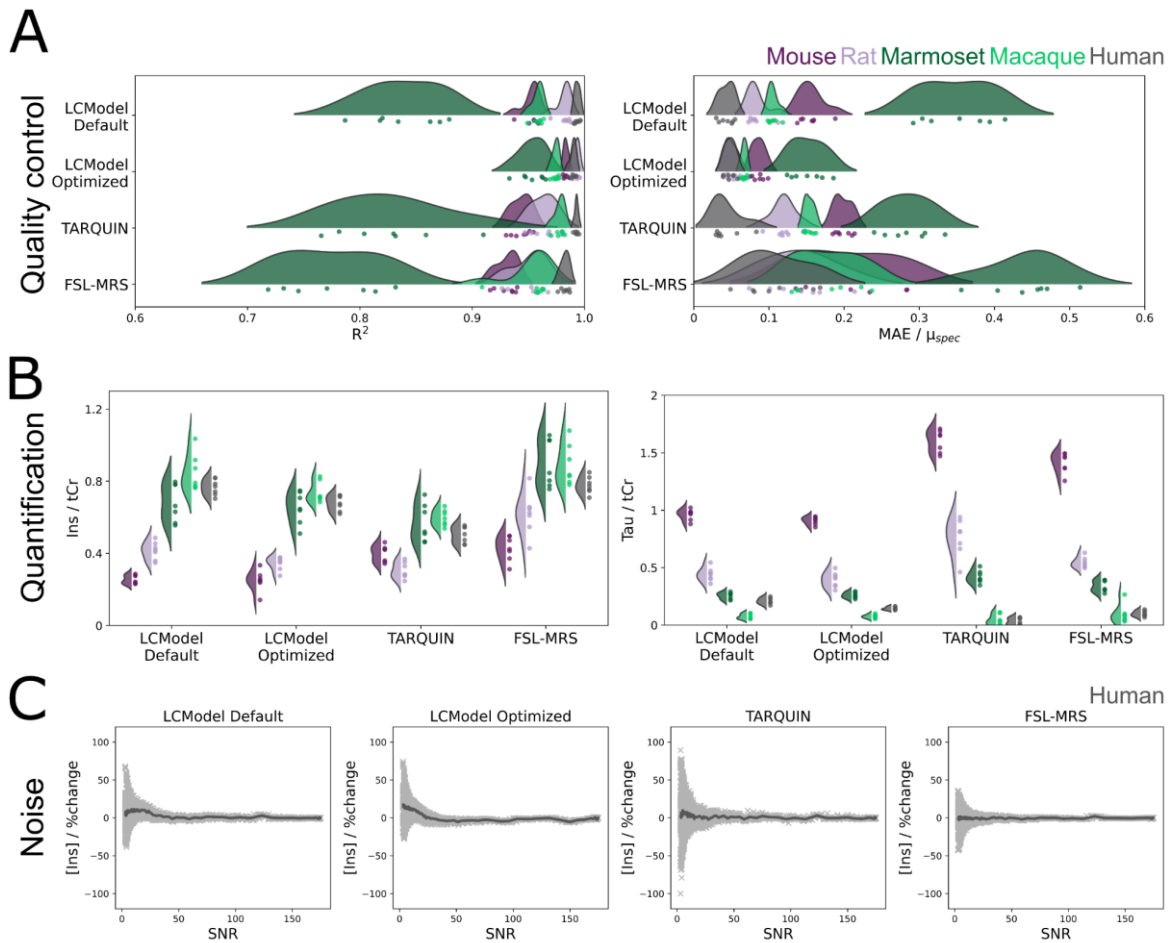
*Figure 4-6: **Comparing different analysis software across species**. The coefficient of determination (R^2) was generally higher and the mean absolute error (MAE) lower when using optimized LCModel model parameters compared with LCModel with default start parameters, TARQUIN, and FSL-MRS (A). All four analyses showed comparable trends for the myo-inositol and taurine concentrations across species although there was slight tendency for TARQUIN and FSL-MRS to over-fit taurine in mice (B). The average concentration of myo-inositol when adding noise was the most robust for FSL-MRS and TARQUIN (C). LCModel with default and optimized start parameters showed noise stability down to an SNR of 25 after which they start overestimating.*

LCModel was more likely to incorrectly estimate concentrations at low SNR than TARQUIN and FSL-MRS. However, the uncertainty of TARQUIN at low SNR was higher than LCModel and FSL-MRS. Ultimately, the choice of fitting tool largely depends on the question at hand. We note that especially for human data only minor differences were observed; however, LCModel generally performed better on preclinical data. It should be noted that LCModel fits data from RAW-files, which we generated from text files of the spectra. TARQUIN was able to use both Bruker and Siemens file formats. FSL-MRS requires a conversion of files into a standardized NIfTI-MRS format, which can be done using *spec2nii*[163].

The optimized LCModel start parameters had a different noise behavior than the default LCModel start parameters. This leads to the direct question of what is defined as optimal start parameters. We chose eight metabolites that differed between species to find start parameters that ensured their accurate quantification. The spectra used in this study had sufficient water suppression to allow for a downfield limit close to the water peak. If this is not the case, a downfield limit closer to 4.0 ppm would be preferable. Furthermore, the upfield limit at 3T (0.7 ppm), was further downfield than recommended by the software – likely a testament to the low macromolecular content of the spectra and macromolecules

not being included in metabolite SNR formula. This illustrates that the optimal start parameters for LCModel may depend on the question. Our general recommendation is to have a chemical shift range of 4.2-0.2 ppm (comparable to FSL-MRS), if the spectra in the study have too much water signal or reduced macromolecular content, then it can be narrowed as necessary. The baseline flexibility term yielded higher spectral SNR at lower values (higher flexibility), but for most metabolites the concentration is largely constant. However, for metabolites with multiplets that are difficult to disentangle, e.g. glucose – a flexible baseline may decrease the fit concentration. For most spectra and species, the effect will be largely negligible and values between the 0.15 (default) and 0.25 provide comparable results. Changing the standard deviation of phase correction performed by LCModel did not provide clear advantages, as the spectra did not have large phase correction errors. Line broadening the spectra led to improved metabolite SNR; however, this is generally not recommended. For noisy data, line broadening will improve the spectral quality, which may improve the accuracy; however, it may also lead to undesired effects and will artificially lower the Cramer-Rao bounds. In this study, we only applied line broadening of less than 75% of the linewidth, which meant a limit of 2 Hz for humans. As a result, the line broadening applied was mild and below the linewidth of the spectra. Regardless, line broadening – if used – should always be reported and best practice would be to ensure that quantification without line broadening produces similar average values. Finally, we illustrated that the start parameters for LCModel led to large variations in cumulative bias and metabolite SNR. Reporting the LCModel start parameters is therefore important for improving reproducibility. We do not offer strict recommendations and the optimal LCModel start parameters provided in this study should be seen as an example of how optimizing start parameters may alter metabolite quantification.

Having compared three different analysis software, LCModel offered comparable results to its contemporary counterparts. It is therefore likely that LCModel will remain the benchmark for new software developments. However, LCModel is less complete than modern analysis tools – TARQUIN and FSL-MRS – that allow basis set simulation and include processing tools. In recent years, multiple software tools have been developed for a plethora of spectroscopy applications such as (but not limited to): FID-A[182], INSPECTOR[183], nmrglue[184], Osprey[185], jMRUI[164], and VESPA[166]. FID-A and nmrglue are useful tools for simulating and preprocessing spectra, whereas INSPECTOR, Osprey, jMRUI, and VESPA also allow for MRS analysis. However, a comparisons of all the spectroscopy analysis software currently available was beyond the scope of this project. In a recent fitting challenge in the MRS study group of ISMRM addressed this question[167]. Notably, almost half the submissions used LCModel for the analysis, suggesting that this is still the preferred analysis software. The fitting challenge found, similar to our results, that LCModel fits are SNR dependent – although to a lesser extent when constraints are removed (default for field strengths greater than 4.7T). We have shown that LCModel is capable of quantification at different field strengths and species with high fit accuracy, making it a useful benchmark for new spectroscopy analyses. However, LCModel is prone to non-ideal noise behavior.

The mean and standard deviation of all metabolites quantified in this study are available in both the supplementary material, table S-3, and on GitHub. While the study primarily explores the behavior of LCModel and to a lesser extend TARQUIN and FSL-MRS, the quantification of healthy adult animals of five different species should provide a

representative reference work for future studies. As the data used was not acquired for this study, the brain regions are not perfectly matched across species. The seven spectra from healthy specimens of each species are insufficient to describe the physiological range of the population. The concentration ranges provided should therefore be seen as a reference guide rather than the ground truth. Furthermore, for the *in vivo* analysis and the optimization of LCModel start parameters, the ground truth was unknown, so optimization meant maximizing metabolite SNR. The spectra simulated from basis sets were created as representative spectra from different species. Since the spectra are simulated and fit by the same basis set – the estimated noise behavior is the lower bound of the true noise behavior, Fig. 4-5. Finally, in the comparisons of the different software, we only optimized the start parameters of LCModel and used both TARQUIN and FSL-MRS without changing parameters. This means that better fit quality and quantification of both software are likely possible through thorough optimization of their changeable parameters.

While this study covers many aspects of LCModel fitting, it does not include changes to every possible parameter. Notably, we did not change the soft constraints of the analysis or the number of simulated peaks – both known to effect the quality and accuracy of the software[167,186]. Future work may delve deeper into these and other changeable parameters of LCModel.

We started this study by looking for a way to explain and describe the noise behavior of LCModel. While this is relatively easy to explain, we found few resources meticulously and systematically testing the software at hand. We have illustrated that the inherent noise-related fluctuations in metabolites can be simulated using spectra simulated from basis sets and from *in vivo* spectra with comparable outcomes. The need for understanding the limitations of software is growing, especially with the new developments in MRS analysis tools in mind. We have illustrated the extremities of noise behavior and shown that it is both metabolite and species specific. However, in doing so, we also do not offer any strict recommendations for software analysis – only that all spectra are inspected visually and analysis parameters are reported.

4.5 METHODS:

4.5.1 Optimizing LCModel start parameters:

LCModel start parameters were optimized by testing all combinations of six different parameters: line broadening, baseline flexibility (dkntmn), standard deviation of the zero (sddegz) and first order (sddegp) phase correction, and the start (ppmst) and end (ppmend) point of the chemical shift range. The 7680 combinations, derived from the aforementioned parameters as well as the default and optimized start parameters are depicted in table 4-1.

4.5.1.1 Simulating spectra using real data for optimizing LCModel start parameters at 3T and 9.4T:

The noise level alters the concentration of metabolites determined by LCModel on the level of a single spectrum. However, as most studies contain multiple animals, we were interested in whether the mean and median concentrations were stable against more modest noise levels.

4.5.1.2 Human (3T):

Human spectra were simulated using data from 7 subjects. We simulated 10 spectra per noise level using a multivariate distribution (mean and covariance). To reduce the variation between the 10 simulated spectra, we multiplied the covariance by 0.01. We applied noise levels of 0.00, 0.33, 0.66, and 1 time the intrinsic noise. The noise was defined as the standard deviation of the spectrum at the 2 ppm furthest downfield.

4.5.1.3 Mouse (9.4T):

Mouse spectra were simulated using 40 cortical spectra from 20 mice (2 time points). The spectra were phase-corrected. Using the average and covariance matrix, we simulated 10 spectra using a multivariate distribution. To reduce the variation between the 10 simulated spectra, we multiplied the covariance by 0.001. We applied noise ranging from 0.00, 0.33, 0.66, and 1 time the intrinsic noise. The noise was defined as the standard deviation of the spectrum at the 2 ppm furthest downfield.

4.5.2 Simulating data from basis sets:

Spectra were simulated directly from the basis set at 3T and 9.4T. In order to ensure that the final concentration could be simulated reliably from the basis set, we calibrated the simulation for concentration, linewidth, and created macromolecules that could be added to the simulation. An example of a simulated spectrum for each species is shown in Fig. 4-3. All simulated data relied on TARQUIN for creating LCModel basis sets. The basis sets at both 3T and 9.4T were simulated at 1 mM. LCModel requires an unsuppressed water reference spectrum to calculate the concentrations. We simulated unsuppressed water reference spectra based on the assumption that the water peak had a Lorentzian shape. We scaled the spectrum to be 43700 (assumed water concentration in mM) time larger than one-third the area under the curve of the creatine singlet at 3.05 ppm (integrates 3). We note that this scaling factor was halved at 3T for our current basis set.

4.5.2.1 Concentration:

In order to ensure that the output concentration from LCModel matched the desired input concentration, we calculated a concentration correction term. The concentration correction of each metabolite was calculated by simulating a linear increase in the metabolite concentration from 0.25-15 mM and keeping the concentration of all other metabolites fixed at 0.5 mM. The relationship between simulation and LCModel concentration is assumed to be linear. The slope and intercept may be used to improve the simulation of metabolites outside physiological concentrations.

4.5.2.2 Linewidth:

While the concentration scales linearly in most cases, the fit of a metabolite may vary based on the linewidth of the data – especially for metabolites that are multiplets. We note that LCModel – by default – adjust the linewidth of the basis set to the spectrum that it is trying to fit. However, it is unclear if the estimated concentration of LCModel depends on the linewidth of the simulated spectrum. We therefore simulated (for each metabolite in the basis set) a spectrum where a metabolite had a concentration of 15 mM (uncorrected) and the remaining metabolites had a concentration of 0.5 mM. The spectrum was then line broadened by 0-11 Hz at 3T and 0-20 Hz at 9.4T in 200 steps. Once these spectra were fit by LCModel, we looked at the variation of the concentration of the metabolite with the

linewidth of the spectrum. The linewidth correction was calculated by smoothing the normalized concentration curves for each metabolite. Due to the maximum concentration being found at linewidths between 1-3 Hz for both field strengths, simulations using a linewidth between 1-3 Hz are corrected using a linewidth correction term of 1. Additionally, the linewidth correction term was capped at 1.33 to avoid overcorrection.

4.5.2.3 Macromolecules:

Macromolecules, lipids, and baseline may be simulated using Gaussian functions. They were defined using the known lipids and macromolecules from the LCModel manual. Macromolecules were simulated at 0.9, 1.2, 1.4, 1.7, and 2.0 ppm. Lipids were simulated at 0.9, 1.3, and 2.0 ppm. Finally, the baseline can be added to the spectrum using a linear combination of Gaussian functions.

4.5.2.4 Comparing basis set similarity with LCModel fitting:

Testing the specificity of a fitting algorithm is important for understanding the limitations of the approach. We simulated 10000 spectra from simulated basis sets and investigated the correlation of the LCModel metabolite concentrations. The dataset was simulated with no intrinsic correlation – concentrations were simulated using a uniform distribution of physiological concentrations. The average concentration and linewidth correction term were used for the simulation. Macromolecules, lipids, and baseline was added for increased similarity to *in vivo* spectra. We compared this correlation to the correlation between metabolite spectra – i.e. the spectral similarity of the real component within the chemical shift range of investigation (4.2-0.7 ppm at 3T and 4.3-0.2 ppm at 9.4T).

4.5.3 Comparing interspecies spectra from cortical grey matter:

Seven animals/subjects were analyzed for five different species. We acquired spectra from two rodent species: mice (C57BL/6N) and rats (Wistar), two nonhuman primate species: the common marmoset (*Callithrix jacchus*) and cynomolgus macaques (*Macaca fascicularis*), and humans. Spectra were acquired from cortical grey matter.

4.5.3.1 Mouse, rat, and marmoset spectra at 9.4 T

Mouse, rat, and marmoset spectra were acquired on a 9.4 T MR scanner with 30-cm horizontal bore (Bruker Biospin, Ettlingen, Germany). Mouse experiments were performed under anesthesia with a BGA12 gradient insert. Rat and marmoset experiments were performed under anesthesia using a BGA20 gradient system. Spectroscopy data was acquired using a STEAM sequence.

Sequence parameters and subject information is given in table 4-2.

4.5.3.2 Macaque and human spectra at 3T

Macaque and human spectra were acquired using a 3T Siemens PRISMA MRI system (Siemens Healthcare GmbH, Erlangen, Germany). Macaque data were acquired under anesthesia and human data were acquired awake. Spectroscopy data was acquired using a PRESS sequence.

Sequence parameters and subject information is given in table 4-2.

4.5.4 In vivo spectroscopy analysis

Spectra were fitted and using three different software: LCModel, TARQUIN, and FSL-MRS. Bruker data were preprocessed by removing the digital filter using the python package nmrglue. Scripts for preprocessing spectra, writing LCModel RAW-files (and control files), and running (as well as batching) LCModel, TARQUIN, and FSL-MRS are available on GitHub (https://github.com/Tor-R-Memhave/preppingLCModel) – in addition to all scripts for simulating data.

4.5.4.1 LCModel

Data were opened as free induction decays using MATLAB and converted to txt-files. Bruker data was opened using an in-house developed script. Siemens macaque spectra were opened using mapVBVD in the rawData format and human spectra were opened in ima-format using FID-A. The data were preprocessed in python using nmrglue. The data was written into RAW-files and analyzed using LCModel. LCModel was performed using the 3 T PRESS dataset accompanying LCModel and a measured 9.4T STEAM basis set.

4.5.4.2 TARQUIN

TARQUIN read both Bruker and Siemens data files. For the mouse, rat, and marmoset spectra, Bruker fid, fid.refscan, and acqus files were input into TARQUIN. The macaque and human spectra were analyzed in Siemens DICOM format ('.ima') using both a water reference and a water suppressed scan. Data was analyzed using simulated basis sets.

4.5.4.3 FSL-MRS

Macaque and human data were converted into NIfTI MRS Files for FSL-MRS analysis from Siemens DICOM format. FSL-MRS was not able to fit our Bruker data or convert it to NIfTI, due to a mismatch between data files and basis set.

4.5.5 Simulating spectra with varying noise for different species:

4.5.5.1 Spectra simulated from basis set:

Data with concentrations comparable to each species was simulated from basis sets. Noise was added in the range from 0-10 in 100 noise levels. At each of the 100 noise levels, 25 spectra were simulated.

The noise levels were defined such that a noise level of 0.25 is comparable to *in vivo* human data and a noise level of 2 is comparable to *in vivo* marmoset data. Therefore, the noise (at noise level 1) is defined as 0.075 times the standard deviation of the free induction decay. The noise was added as random noise to the free induction decay.

4.5.5.2 Spectra simulated from in vivo spectra:

Data for each species was simulated by adding noise to the mean spectrum. At each of the 50 noise levels, 25 spectra were simulated. The intrinsic standard deviation is defined the mean of the standard deviation of each spectrum (calculated as the standard deviation of 2 ppm furthest downfield). The maximum noise level was defined as the ratio of the mean of the magnitude spectrum upfield of 4.65 ppm to the absolute value of the noise, S_N.

4.5.6 Comparing different analysis methods:

For the data acquired at 9.4T, we analyzed the data using LCModel and TARQUIN. For the data acquired at 3T, we analyzed the data using LCModel, TARQUIN, and FSL-MRS.

The direct comparisons was performed on metabolite concentrations normalized to total creatine – to eliminate differences in assumed water concentration and fitting biases. The *in vivo* spectra was analyzed using the software's preferred file formats. For LCModel, the data was converted to RAW files. For TARQUIN, Bruker data was analyzed directly from fid and fid.refscan formats, whereas Siemens data was analyzed in dicom format. For FSL-MRS, the spec2nii conversion did not work for Bruker data acquired with a multi-channel coil, so we resorted to fitting data from RAW files using spec2nii conversion. For FSL-MRS analysis of data acquired on the 3T MRI system (macaque and human) –we used spec2nii to convert Siemens dicom to NIfTI-MRS format. The data was phase-corrected using "fsl_mrs_proc phase" and analyzed using the same basis set as TARQUIN.

4.5.7 Quantification parameters for each analysis:

The fit quality was assessed using the mean absolute error (MAE) and coefficient of determination (R^2). The reported SNRs were calculated by LCModel. LCModel defines the spectral SNR as the ratio of the maximum value (spectrum minus baseline) divided by the root-mean-square of the residual.

The optimal start parameters of LCModel were determined based on the bias and metabolite SNR (ρ). The cumulative bias was calculated for a group of eight metabolites: myo-inositol, taurine, γ-amino butyric acid (GABA), glucose, total N-acetylaspartate, total phosphocholine, glutamate plus glutamine, and total creatine. Only analyses with start parameters that gave a cumulative bias within the bias limit were considered. The bias limit was defined as 25 divided by the mean SNR of the spectra without added noise. For analyses with start parameters fulfilling the bias criterion, we calculated the metabolite SNR. For each of the eight metabolites, we found the average and standard deviation across the 10 simulated spectra. We defined the metabolite SNR (ρ) for the ratio of the sum of the mean concentration (μ) to the sum of standard deviations (σ), equation 4-1. The optimal start parameters of LCModel were found by finding the conditions that gave the maximum value of ρ.

$$\rho = \frac{\sum_i \mu_i}{\sum_i \sigma_i}$$

equation 4-1

4.5.8 Statistical Analysis

Metabolite differences between species were compared using one-way ANOVA test with post-hoc testing performed using two-way, independent t-tests with Bonferroni correction for number of tests between species (10) for each metabolite. Significance was set to $p < 0.05$.

4.6 AUTHOR CONTRIBUTIONS:

S.B. and T.R.M. contributed to the conceptualization and design of the study. S.B. supervised the study. S.B. and T.R.M. performed the initial investigation. T.R.M. conducted the formal analysis and data visualization. T.R.M. wrote the first draft of the manuscript.

5

CELL CULTURE MRI/S

Magnetic resonance imaging and spectroscopy on 3D astrocyte cell cultures: a feasibility study

Tor Rasmus Memhave[1,2,3], Krathika Bhat[4], Lisa Hanke[5], Eckhard Quandt[5], Regine Willumeit-Römer[4], Susann Boretius[1,2,3]

[1]Functional Imaging Laboratory, German Primate Center, Leibniz Institute for Primate Research, Göttingen, Germany

[2]Georg-August Universität Göttingen, Göttingen, Germany

[3]International Max Planck Research School for Neurosciences, Göttingen, Germany

[4]Institute of Metallic Biomaterials, Helmholtz Centre Hereon, Geesthacht, Germany

[5]Inorganic Functional Materials, Institute for Materials Science, Faculty of Engineering, Kiel University, Kiel, Germany

Own contributions:

- Conceptualization
- 3D model creation
- Data acquisition
    - Incubator sensor data
    - Magnetic resonance imaging and spectroscopy
- Data analysis
- Data interpretation
- Data visualization
- Writing

5.1 ABSTRACT:

Astrocytes are believed to be an *in vivo* cellular target of lithium treatment. However, studying the impact of lithium on astrocytes metabolism and function *in vivo* is complicated by the presence of other cells and difficulties with lithium detection. Understanding the impact of lithium on astrocytes in traditional cell cultures suffers from poor translation into clinically detectable biomarkers. In contrast, 3D cell cultures offer a middle ground that allows studying with conventional and translational analysis methods, while removing some of the biological complexity. In this study, we acquired magnetic resonance imaging (MRI) and spectroscopy (MRS) data from immortalized human astrocytes seeded in collagen hydrogels. The data was acquired on a 9.4T MRI system in a home-built bioreactor connected to an incubator allowing for gas-mixing and humidification. The astrocytes were placed in four different medium types that were derived from lithium-magnesium thin films. The media varied in magnesium and lithium concentrations. We found, using diffusion MRI, that astrocytes in low lithium medium (0.78 mM) had increased diffusivity relative to astrocytes in other media, whereas astrocytes in high lithium (4.38 mM) medium had decreased diffusivity. Astrocytes in low lithium medium, as revealed by MRS, had increased glycine and decreased myo-inositol and glutamate-to-glutamine ratio. We illustrate that measuring cell cultures in an MRI system is feasible with home-built components and standard coils. Furthermore, our MRI and MRS results provide evidence for lithium-induced changes in astrocyte metabolism.

5.2 INTRODUCTION:

Studying metabolism using MRS offers direct comparisons between cell cultures, animal models, and humans. As MRS allows for the detection of multiple different compounds simultaneously, it is ideally suited for characterization of cell cultures, fluid samples, and tissue samples[187–189]. In recent years, there has been a shift away from animal experiments towards *in vitro* cell culture experiments. Although MRS allows for measuring cell culture extracts, MRS studies conducted on traditional nuclear magnetic resonance (NMR)
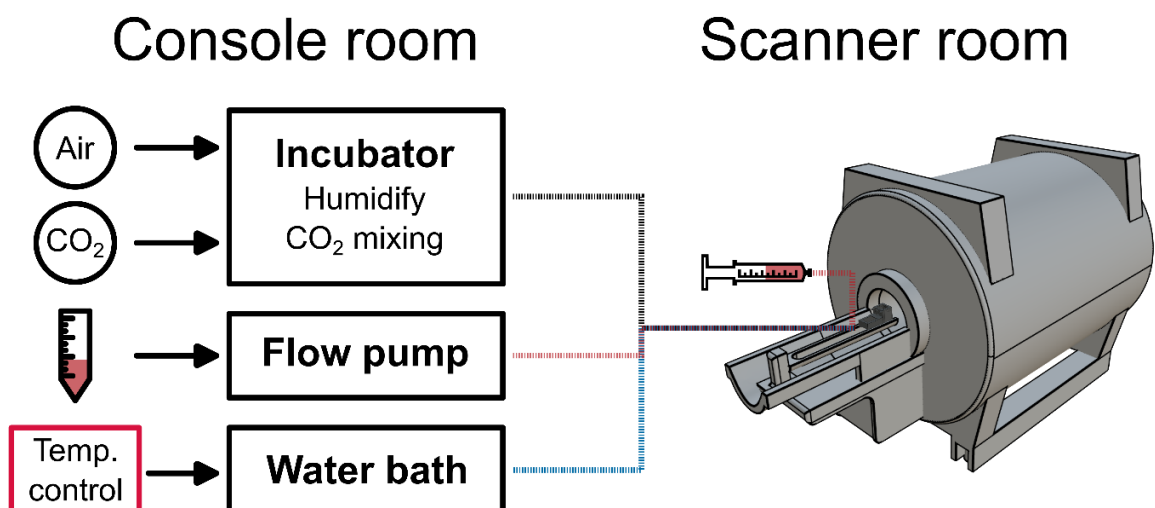
*Figure 5-1: **Experimental overview.** The console room contained the incubator used for gas-mixing, flow pump (not used aside from preliminary testing), and water bath for temperature regulation. The components in the console room were connected via tubes to the bioreactor in the scanner room (where the MRI system is located). The medium exchange was performed following the first 1-hour time series using a syringe directly connected to the bioreactor via Luer taper.*

instruments have often been limited to sampling at individual time points making sample preparation a requirement prior to each acquisition[187,190,191], leading to labor intensive workflows. On the contrary, measuring the cell cultures longitudinally allows for detection of metabolic changes over time. Different longitudinal approaches have been performed using NMR tubes[192], flow systems[193–196], and bioreactors[197,198].

NMR instruments provide higher field strengths and narrower linewidths than MRI systems and in addition have commercially available flow cells for studying 3D cell cultures[197]. However, a traditional NMR tube is 5-10 mm wide, which may be insufficient for larger organoids and 3D cell cultures. Furthermore, for more advanced substance application and longer experiments a bioreactor with a larger volume and easier access would be preferable to an NMR tube.

As translational research tools, MRI and MRS span from single molecule spectra to images used for clinical diagnostics. MRI and MRS is frequently used to study metabolism in preclinical animal research. For *in vitro* experiments performed on 2D cell cultures, the advantages of MRI systems – localization and larger space – are irrelevant, and such experiments have been and continue to be performed on an NMR instrument. While 2D cell cultures are still commonly used in preclinical research, they are often too simplistic[199,200]. The development of 3D cell cultures in hydrogels and organoids potentially allows for investigation of metabolic changes in living tissue with a reduced need for animal experiments. 3D cell cultures are closer to living tissue than 2D cultures[199–203] and provide a volume that can be imaged and acquired spectra from in an MRI system.

Despite clinical usage for over 50 years, lithium's mode of action as a treatment for bipolar disorder is still not thoroughly understood[20]. However, astrocytes – glial support cells, which are omnipresent in the mammalian brain[204] – are believed to be a cellular target of lithium treatment[205]. It has been shown that lithium is able to exchange magnesium in specific magnesium-dependent enzymes[65]. An example is the myo-inositol depletion hypothesis, which relies on the inhibition of inositol monophosphatase (IMPase) by lithium[67,95] and yields altered phosphatidylinositol signaling[206,207]. The inhibition of IMPase leads to decreased myo-inositol in rats[67] and bovine extracts from brain and testes[95]; however, in mice, we have previously shown the opposite effect (chapter 6). Understanding the effect of lithium at different concentrations on astrocytes may provide insight into the findings seen *in vivo*.

In this study, we utilize the preclinical 9.4T MRI system with a 30-cm horizontal bore to study 3D astrocyte cell cultures in a home-built bioreactor. The bioreactor was connected to an incubator, used for gas-mixing, providing a constant gas flow. We acquired diffusion MRI and time-resolved MRS data to investigate the effect of lithium at two concentrations on the metabolism of astrocytes. This is to the best of our knowledge the first MRI and MRS study assessing the feasibility of measuring 3D cell cultures in a preclinical MRI system.

5.3 RESULTS:

5.3.1 Acquiring cell culture experiments in a preclinical MRI system using a home-built bioreactor and incubator

Acquiring cell culture measurements on a preclinical MRI system requires solving two main problems. First, the setup is inaccessible during measurements. This means that whenever

repositioning of the setup is needed, either due to handling the setup or incorrect position, a new set of localization images and field map must be acquired. The field map allows for map-shimming of the system, a process that makes the magnetic field as homogeneous as possible within the region of interest. This process allows for spectra with narrow linewidths of <10 Hz to be acquired. Second, the incubator, flow pump, and water bath are separated from the bioreactor by roughly five meters, Fig. 5-1. As a result, changing the conditions in the setup is a slow process to avoid overshooting the ideal conditions. In test experiments, we used a flow pump; however, we found that due to the long leading line, this was difficult to control at low flow rates. We therefore opted for exchanging the medium using a syringe with Luer taper.

The bioreactor, Fig. 5-2A-B, and incubator, Fig. 5-2C-D, were designed to allow for flexibility in the setup and monitoring of the conditions. The bioreactor was created with valves allowing for gas and medium perfusion of the system as well as heating with water, Fig. 5-2B. The temperature inside the bioreactor was measured using an electrical thermometer at the back of setup, Fig. 5-2B. The gas line was connected to the incubator, which was used to monitor the CO_2, O_2, humidity, and gas temperature. The incubator was constructed using a standard 3-liter plastic box with an airtight lid. The electronic components – fan, sensors, and Arduino holder – were glued to the lid, Fig. 5-2C. The Arduino was connected to the sensors using both analog and digital, circuit diagram in Fig. 5-2D, and was powered
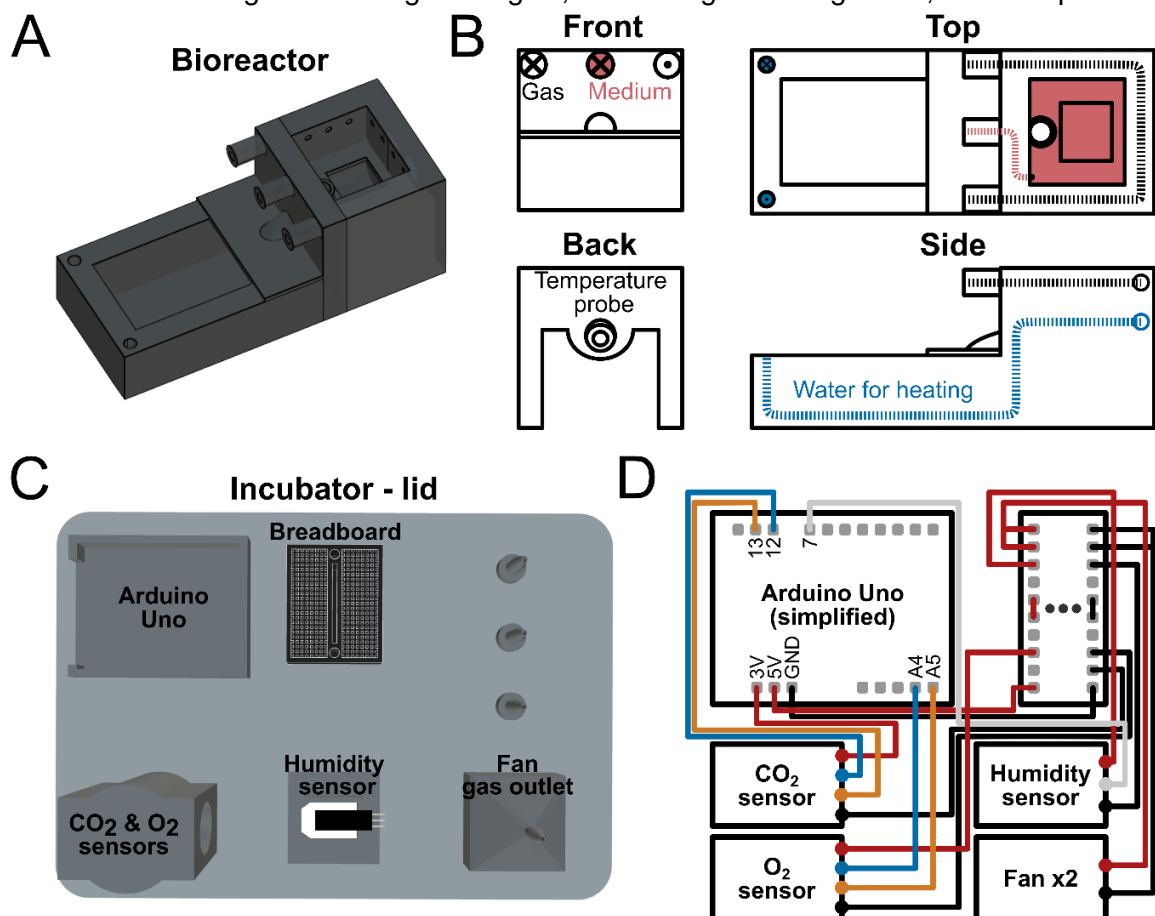
Figure 5-2: **Custom-built bioreactor and incubator**. *The bioreactor (A) was 3D printed on a stereolithography printer with connection sites for gas-lines, medium exchange, and water heating (B). On the back of the bioreactor, a pocket was created to ensure that the thermometer was near the cells. The incubator lid was used as a base for the different sensors needed for gas-mixing (C). The circuit diagram of the Arduino-controlled sensors and fans (D) was implemented using simple jumper-wires to allow for fast assembly and disassembly.*

by a 9V socket. The sensor measurements were plotted real-time using python and were written into a CSV-file for later usage.

5.3.2 Astrocyte preparation and imaging

10 million astrocytes were seeded into collagen hydrogels one-day prior to MR examination. Six hours after seeding the medium of the hydrogels was exchanged to either DMEM with 10% fetal bovine serum (normal medium) or normal medium with Mg-extract (Mg), Mg1.6wt%Li-extract (low lithium), or Mg-9.5wt%Li-extract (high lithium). The low lithium medium had 0.78 mM lithium and the high lithium medium had 4.38 mM lithium, the magnesium concentration of the three extracts was 10 mM. A sample gel of astrocytes was imaged using confocal laser scanning microscope, Fig. 5-3A, showing good homogeneity in the distribution of astrocytes in the gel. Lactate dehydrogenase (LDH) measurements showed no major differences between the hydrogel in a standard incubator and our bioreactor.

5.3.3 Diffusion MRI showed variable changes in apparent diffusion coefficient (ADC) depending on lithium concentration

Diffusion MRI was acquired at the end of the measurement, due to the large heating effects of the sequence compared with spectroscopy. Diffusion MRI showed good SNR and a clear delineation between the hydrogel and medium, Fig. 5-3B. Using the diffusion MRI images, we created manually segmentation of a region of interest in the hydrogel and medium. These regions of interest were used to analyze diffusivity changes between astrocyte hydrogels in different media. We observed increased ADC in the astrocytes in the low lithium medium compared with astrocytes in the high lithium medium (p=0.03), Fig. 5-3C. Although t-tests showed a significant decrease in the ADC of astrocytes in high lithium medium compared to astrocytes normal and low lithium medium, we note that a one-way
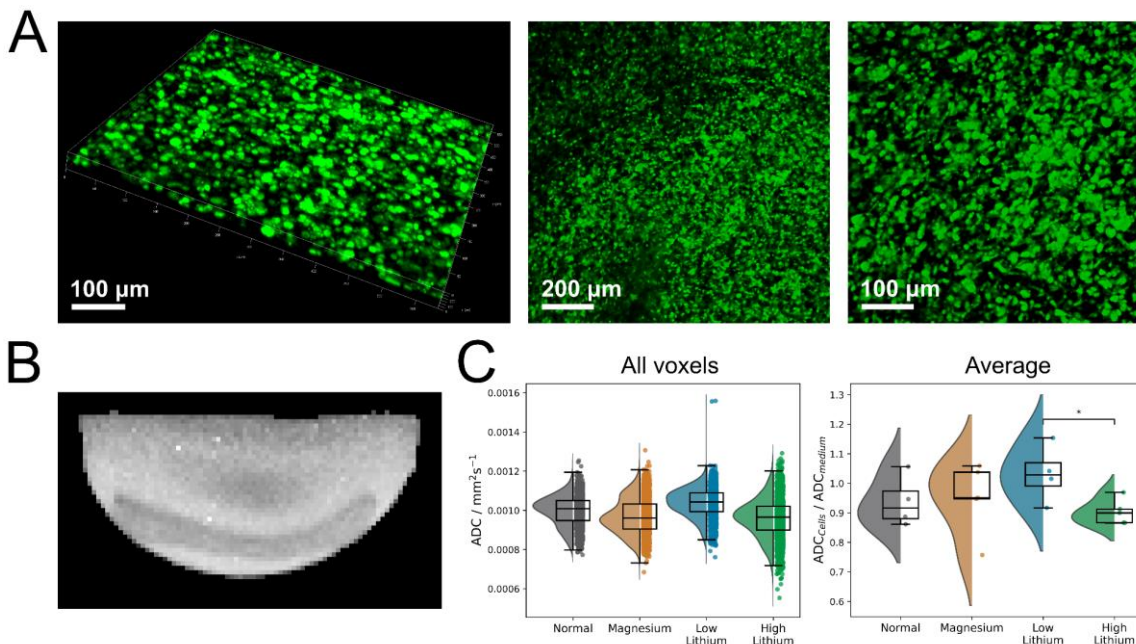
*Figure 5-3: **Imaging 3D astrocyte cell culture.** Confocal laser scanning microscopy images of the 3D astrocyte cell culture showed a homogenous distribution of astrocytes (A). The apparent diffusion coefficient maps allowed for clear delineation of the astrocyte hydrogel from the medium (B). We observed a tendency towards increased diffusivity in astrocytes in low lithium medium (C).*

ANOVA analysis did not show a significant effect ($F_{(3,14)}=1.6$, $p=0.24$) and there were no statistical differences between normal, magnesium, and low lithium.

5.3.4 Good spectral quality could be achieved in 10 minutes

We acquired a 1-hour time series of spectra from the hydrogel, Fig. 5-4A. The data was averaged either as 10-minute independent bins or 2-minute moving averages with 2 Hz line broadening to achieve a sufficient signal-to-noise ratio (SNR) for good quality fitting with LCModel, Fig. 5-4B. To investigate temporal changes over the 1-hour time series, we performed a 2-minute moving average analysis with a sliding window approach and 30 second gap between spectra.

The astrocytes in the four different medium types gave visually similar spectra, Fig. 5-4C. We note that the fit quality was comparable between the 2-minute moving average and 10-minute binning, Fig. 5-4D-E. For the 10-minute average, the Otsu threshold for the coefficient of determination was 0.70 and for the mean absolute error was 3.6, Fig. 5-4E. The relatively high coefficient of determination showed that LCModel can reliably quantify
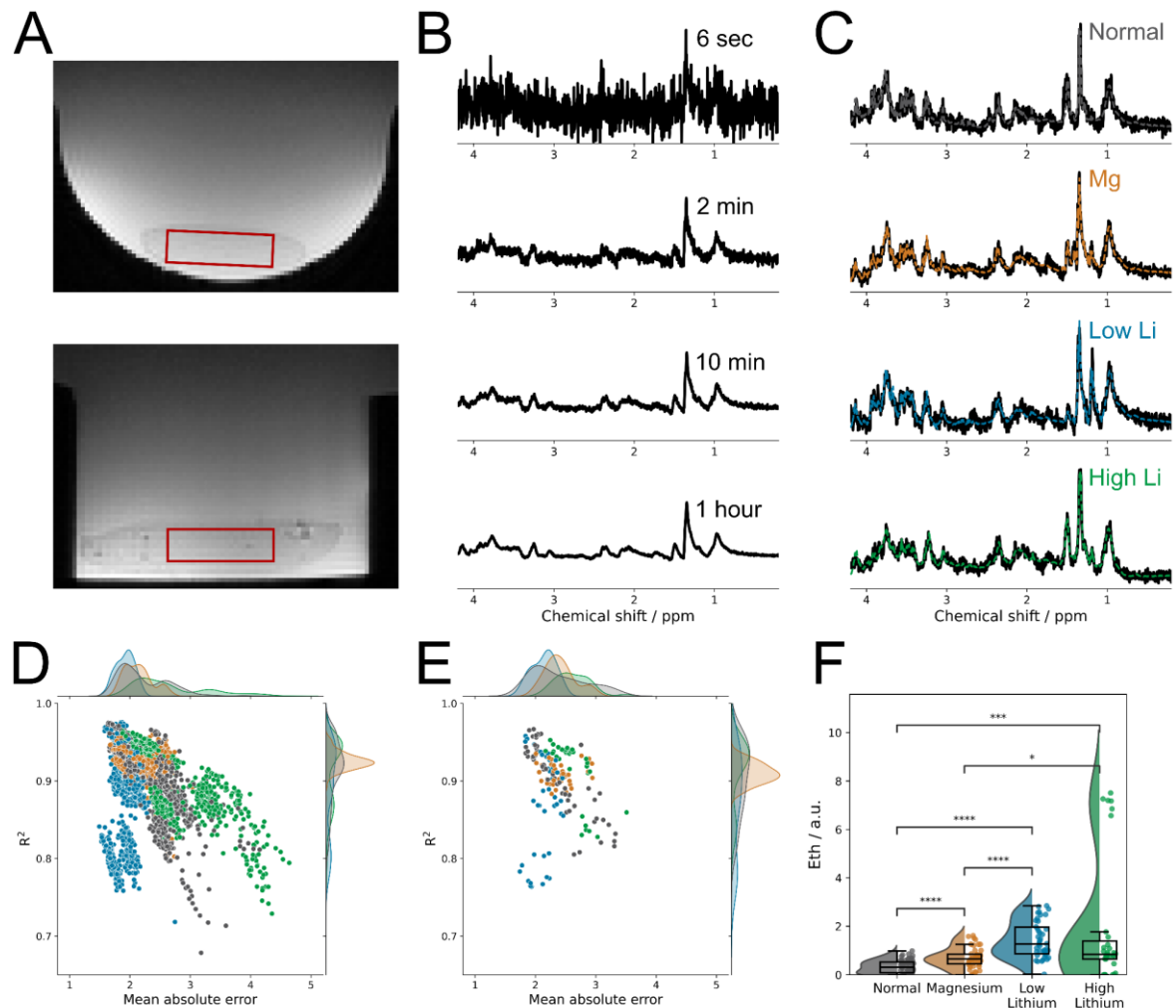
Figure 5-4: **Quality control of spectra acquired from astrocyte hydrogels.** Spectra were acquired from a 5×1.5×5 voxel, which was positioned using T2-weighted images (A). For the moving average spectra, we chose 2-minute windows that were spaced by 30 seconds, whereas 10-minute binning of spectra gave sufficient SNR for metabolic analysis (B). Astrocytes in different cell culture media showed comparable spectra (C). We found that both the 2-minute moving average with 2 Hz line broadening (D) and 10-minute binning (E) yielded high coefficients of determination (R^2) and low mean absolute error of the fitting. Ethanol in the spectra were the result of the cleaning process (F). The six outliers in the high lithium group are from the same 1-hour time series.

the spectra with adequate accuracy. Furthermore, the results indicate that using both the coefficient of determination and mean absolute error may serve as useful quality control parameters to compare spectra within a time series as well as define exclusion criteria in a minimally biased manner.

The concentration of ethanol was higher in lithium-containing media, Fig. 5-4F. One-way ANOVA analysis and post-hoc t-tests for ethanol and all other metabolites discussed can be found in the supplementary information for Chapter 5. However, in table 5-1, a summary of the direction of change for each metabolite as a function of medium is shown.

5.3.5 Lithium-specific changes in astrocyte metabolism

Myo-inositol decreased in astrocytes in low lithium medium – opposite the effect in astrocytes in high lithium medium, Fig. 5-5A. Glycine was increased in astrocytes in all medium types compared to astrocytes in normal medium, Fig. 5-5B. Interestingly, we observed a decrease in phosphocreatine in the astrocytes exposed to the low lithium medium, but an increase in astrocytes exposed to high lithium medium, Fig. 5-5C. The latter observation was also observed in mice (chapter 2).

Astrocytes in high lithium medium showed increased glutamate, contrary to astrocytes in low lithium medium, Fig. 5-5D. Astrocytes in both low and high lithium medium showed a tendency towards decreased glutamine, Fig. 5-5E. The total glutamate and glutamine concentration was decreased in astrocytes in low lithium medium and increased in astrocytes in high lithium medium, Fig. 5-5F.

We observed increased lactate levels in astrocytes in high lithium medium, Fig. 5-6A. We note that the lactate concentration increased steadily, as expected, over the course of the 1-hour measurement, Fig. 5-6B. Glucose concentrations showed large variations; however, the overall tendency was decreased glucose in low lithium astrocytes and increased glucose in high lithium astrocytes, Fig. 5-6C. We note that the time-curve, Fig. 5-6D, showed little systematic change in glucose levels over the course of the 1-hour time series.

5.4 DISCUSSION:

5.4.1 Improving the bioreactor and incubator

While the bioreactor and incubator allowed for the measurement of 3D cell cultures in an MRI system with reasonably stable conditions, a few improvements could be made to the current setup.

We note that the bioreactor was designed to fit on top of a mouse brain radiofrequency coil. However, having designated radiofrequency coils for 3D cell culture experiments would allow for more flexibility in the design of the bioreactor as well as potentially higher SNR. The connections to the bioreactor were airtight, but not watertight. Consequently, the bioreactor was wrapped in the water pipes rather than the water flowing through as intended. To eliminate this problem, we have since created a bioreactor, which uses Luer taper for the connections. Luer taper is also used for syringes, thereby making substance application easier. We note that in the current study, medium was exchanged using syringes – as constant flow was not required. However, for future studies multiple day experiments, a connection between the bioreactor and a larger medium reservoir via a small pump may

Table 5-1: **The impact of medium type on astrocyte metabolism**. *The table depicts the change of the metabolite concentration in astrocytes as a function of medium relative to astrocytes in normal medium. All changes are given as increase, decrease, or left blank (no change observed). Astrocytes in low lithium medium showed decreased myo-inositol (Ins), phosphocreatine (PCr), glutamate (Glu), glutamate plus glutamine (Glu+Gln), and glucose (Glc) opposite the effect of astrocytes in high lithium medium. Glycine (Gly) was increased in astrocytes in all three media. Astrocytes in Metabolites in bold were showed a between group effect on one-way ANOVA analysis. Note that we did not observe an effect of medium on glutamine (Gln) and lactate (Lac).*

Metabolite	Magnesium	Low lithium	High lithium
Ins		**Decrease**	
Gly	**Increase**	**Increase**	**Increase**
PCr		**Decrease**	
Glu		**Decrease**	**Increase**
Gln		**Decrease**	**Decrease**
Glu+Gln	**Decrease**	**Decrease**	
Lac			**Increase**
Glc	**Increase**		**Increase**

be required. When using a pump, the overflow reservoir will serve to allow for multiple whole-volume medium exchanges before the setup needs to be removed from the MRI system. Measuring the pH of the system and regulating the CO_2 concentration accordingly, may be done by connecting the bioreactor to a flow-through cuvette and estimating the pH using ultraviolet-visible spectroscopy – based on the absorption of phenol red. In addition, the creation of a small circulating loop for the medium with a flow cell and ultraviolet-visible spectroscopy may provide optimal cell conditions for longer durations and allow for a larger medium volume. The larger medium volume would provide enough nutrients to allow for longer scan durations.

For the incubator function optimally, a more advanced heating system is required, in this study we used a heating pad below the incubator. It is foreseeable that better temperature control can be achieved using a feedback controller and small heating elements. In addition, the air circulation fans used for the incubator did not produce a high flow rate, which meant that a constant inflow of air and CO_2 was supplied to the incubator. Using larger, more powerful, fans would improve this and reduce the CO_2 usage of the incubator. Additionally, for the incubator to simultaneously serve as an incubator and gas-mixer, one can create a 3D printed insert, which does not require the whole incubator to be opened between scans.

5.4.2 Diffusion MRI showed changes contrary to in vivo findings

The ADC changes related to lithium could warrant further investigation. We note that the ANOVA analysis was not significant, although this is likely the result of low sample size. Measuring ADC changes as a function of lithium concentration, would require spanning the range 0-2.5 mM at smaller intervals to observe therapeutically relevant dose-dependent changes. In the current study, the increased diffusivity in the low lithium condition is interesting as the Li concentration is comparable to the upper range of the therapeutic window (0.4-1.2 mM)[9]. However, *in vivo* studies on mice (chapter 6) and rats[208] have found decreased ADC following lithium treatment, contrary to these findings. We note that *in vivo* experiments observe the additive effects of multiple cell types, whereas this study only looks at astrocytes. *In vivo* measurements have shown that glial activation may be associated with increased diffusivity[209,210].
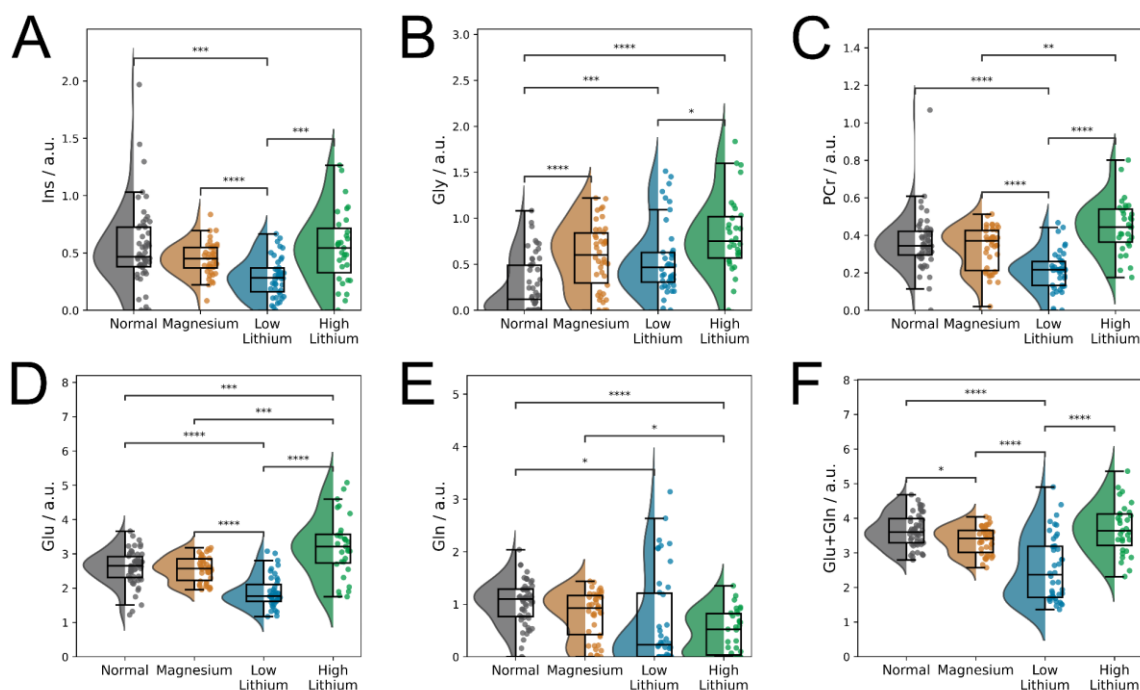
*Figure 5-5: **Astrocytes showed lithium-dependent metabolic differences.** Astrocytes in low lithium medium had decreased myo-inositol and a tendency toward increased glycine (A-B) whereas high lithium medium yielded an increase in both myo-inositol and glycine. Phosphocreatine was decreased in low lithium medium and increased in high lithium medium (C). Astrocyte glutamate (D) was decreased at low lithium levels and increased at high lithium; however, glutamine was decreased in both conditions (E). This led to a decrease in the total glutamate and glutamine (F) for the low lithium group, but an increase for the high lithium group.*

5.4.3 Good spectral quality, but ethanol retention in bioreactor

The spectra had good spectral quality, although it was significantly worse than that obtained on an NMR instrument[197]. Despite good spectral quality, we observed that individual spectra had too low SNR for analysis. As such, the direct interpretation of single spectra was not feasible and an analysis using either 10-minute averages or two-minute sliding windows was required, thereby decreasing the temporal resolution.

We did observe increased ethanol in astrocytes in lithium-containing medium. This is likely the result of cleaning the setup prior to measurement. The six spectra from the high lithium group with high ethanol are from the same time series, Fig. 5-4F. Increased ethanol often comes from ethanol retention in the 3D-printed materials following cleaning. We found that thorough cleaning of the setup with water, rather than ethanol, and then treatment with ultraviolet light for an hour can greatly reduce the ethanol concentration while minimizing the risk of contamination.

5.4.4 Concentration specific effects of lithium on metabolism

We found that the effect of lithium on metabolism was dose-dependent – notably that while myo-inositol, phosphocreatine, glutamate, lactate, and glucose were decreased in astrocytes in low lithium medium, these five metabolites were increased in astrocytes in high lithium medium. The decreased glucose in astrocytes in low lithium is of interest and could suggest higher metabolism in astrocytes in low lithium medium compared to the other conditions. In an *in vivo* study in lithium-fed mice (chapter 6), we found a weak increase in phosphocreatine following lithium treatment (comparable to low lithium), but decreased
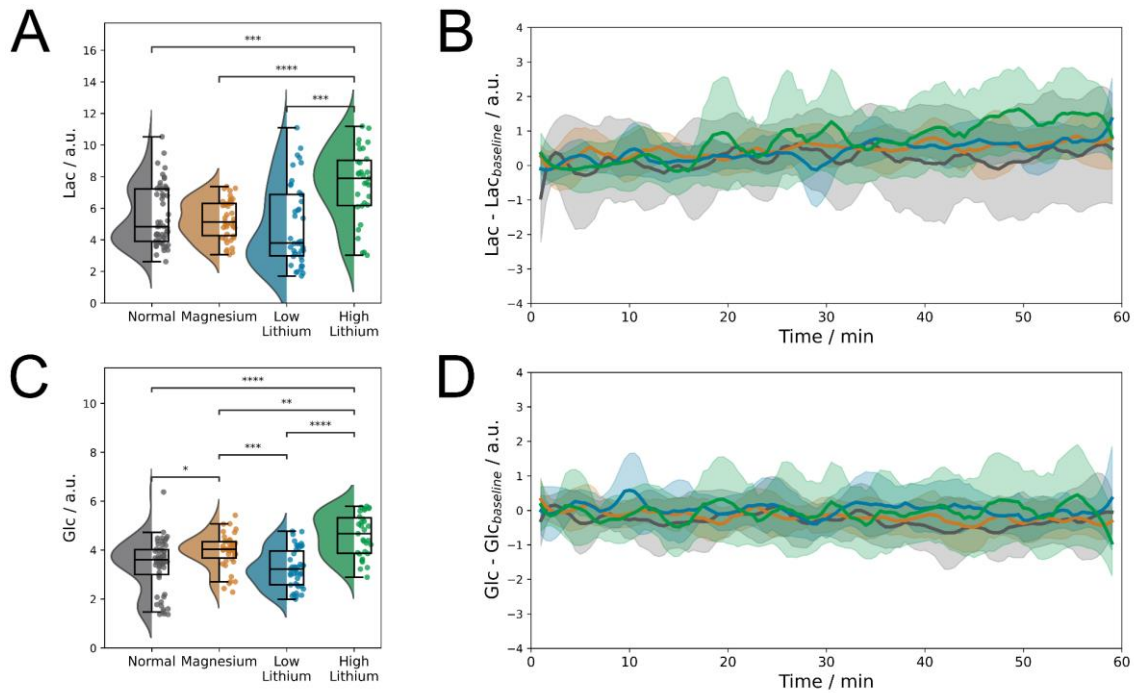
*Figure 5-6: **Time-resolved moving-average spectra.** We found increased lactate in astrocytes in high lithium medium (A). All four media had increased lactate as a function of time (B). The glucose concentration was lower in the low lithium group than the other groups and higher in the high lithium group (C). We did not observe large changes in glucose over the 1-hour time series (D).*

glutamate-to-glutamine ratio – contrary to the finding presented here, Fig. 5-5D-F. Decreased myo-inositol was expected and in line with the myo-inositol depletion hypothesis of lithium treatment[67,95,206]. We note that this effect has not been unanimously been observed in human and rodent studies[70,96,211,212] and was also not present in the high lithium group. Comparable to our results from astrocytes in low lithium medium, Fig. 5-5A-B, it is believed that following the start of lithium administration the myo-inositol decrease is accompanied by a glycine increase[70,213]. Myo-inositol and glycine have similar spectra in the chemical shift range (4.2-0.2 ppm) that is conventionally analyzed, which means accurate distinction and quantification is difficult and subject to high variability.

Increased lactate as a function of time is to be expected, Fig. 5-6B, due to anaerobic metabolism. However, it is of note that we observed no significant difference in LDH between cell cultures in a traditional incubator and the bioreactor. This suggests that the production of lactate observed via MRS is comparable to the expected production in a conventional incubator. Astrocytes in high lithium medium produced increased lactate compared with the other groups, Fig. 5-6A. Interestingly, cells in this medium also showed higher LDH activity. We did not observe systematic decreases in glucose as a function of time, Fig. 5-6D. The time series was only 1 hour on cells in low glucose medium, which makes it likely that the differences were below our detection limit. Future experiments will investigate whether the rate of glycolysis is different between the conditions.

5.4.5 Limitations

While the setup could be kept at constant temperature for the spectroscopy measurements, the gas mixing led to large inter cell culture variability due to insufficient circulation of air between the setup and incubator. As we did not have a direct measure of the pH in real-time, it was difficult to adjust the CO_2 and air partial pressures. Furthermore, due to the high

humidity in the incubator, the CO_2 sensor broke – thus adjustments could only be based on flow rate and the O_2 sensor. It would therefore be ideal to have the gas mixture flow through the CO_2 and O_2 sensors before reaching the incubator or add a heat and moisture exchange filter between the sensors and the incubator, thereby minimizing humidity damage to the sensors.

The low sample size of the study – 20 unique hydrogels – means that the results should be seen as preliminary and not definitive. The metabolite comparison was performed with six spectra from a single hydrogel time series and twelve spectra when combining the time series. Due to the small sample size the spectra were treated as independent for post-hoc testing. We note that this assumption does not necessarily hold; however, a repeated-measures, one-way ANOVA would not be meaningful for the current sample size.

Furthermore, the time series were likely too short to observe metabolic-rate differences due to the high volume of medium outside the cell cultures. However, metabolic differences between the different cell culture conditions could be observed. It is unclear whether the metabolic changes observed in the astrocytes exposed to lithium are transferable to the *in vivo* situation as our study only considered mono-culture rather than cell cultures with multiple cell types.

5.4.6 Conclusion

In this explorative study, we provide – to our knowledge – the first evidence for studying 3D cell culture metabolism in an MRI system. We have shown that MRI and MRS from 3D cell cultures using a home-built incubator and bioreactor was feasible. Astrocytes in low lithium medium had increased ADC and metabolic changes that differed from astrocytes in normal and high lithium medium. These provide early indications of astrocytes being sensitive to the lithium concentration. Previous work showed that metabolism could be studied in an NMR scanner using fibroblasts[197]; however, here we combine a bioreactor and incubator with an MRI system to achieve images of 3D cell cultures using MRI. While challenges persist – low SNR, lack of specialized RF coils, and low accessibility to the cell cultures – our results illustrate that it is feasible to study cell cultures in an MRI system.

5.5 METHODS:

5.5.1 Bioreactor:

The 3D-printed bioreactor was designed to allow for MRI and MRS of cell cultures using radiofrequency coils designed for mouse brains, Fig. 5-2A-B. The bioreactor was printed on a 3BL stereolithography printer (Formlabs Inc., Ohio, USA) using BioMed Clear (Formlabs Inc.) biocompatible resin. The bioreactor was fitted with lids for both the overflow reservoir and main chamber – these were printed in polylactic acid (PLA) on an i3 MK3S+ 3D printer (both from Prusa Research, Prague, Czech Republic). The two lids were wrapped in parafilm (Amcor, Zürich, Switzerland) to ensure an airtight fit. The 3D models are provided in the supplementary material, here the bioreactor can also be found with fittings made for Luer taper.

5.5.2 Incubator:

The incubator was used for gas-mixing and constant gas flow to the bioreactor. The components and circuit diagram of the incubator are shown schematically in Fig. 5-2C-D. The incubator was built around a small Arduino Uno Rev3 (Arduino, Turin, Italy) with components installed for monitoring CO_2, O_2, humidity, and temperature. We used an EXPLORIR-WX-20 CO_2-sensor (Gas Sensing Solutions, Cumbernauld, UK) and an I_2C O_2-sensor (DFRobot SEN0322, Zhiwei Robotics Corp., Shanghai, China). The humidity and temperature were measured using a combined DHT22 sensor (AZ-Delivery Vertriebs GmbH, Deggendorf, Deutschland). Two 30-mm mini-fans (MakerHawk) were used to circulate the air. 3D-printed holders were made for each component and glued to the lid of a 3-liter plastic box. Junctions between sensors and 3D-prints were made airtight using parafilm.

5.5.3 Extract preparation from Mg/Mg-Li thin films

Freestanding Mg, Mg-1.6wt%Li and Mg-9.5wt%Li thin films were fabricated by UV lithography and magnetron sputtering (University of Kiel, Germany). The fabrication process and material characterization are published in detail [https://doi.org/10.1038/s41598-023-39493-9]. The dimensions of the thin films used in this study were 10 x 10 mm and 20 µm thickness. The thin films were cleaned by submerging them in n-hexane and acetone for 20 minutes each. Following this, the thin films were placed in pure ethanol for 3 minutes and sterilized by submerging them in 70% ethanol for 20 minutes. The thin films were allowed to dry under a sterile atmosphere at room temperature. Once dry, they were transferred to Dulbecco's modified Eagle's medium (DMEM, low glucose, 21885025, Thermo Fisher, Germany) supplemented with 10% fetal bovine serum (FBS, S0615, Merck, Germany) and 1% antibiotics (15140122, Thermo Fisher, Germany) (final concentrations were 100 U/mL penicillin and 100 µg/mL streptomycin).

The extraction ratio was 1 mL medium/film and the incubation was carried out under a 5 % CO_2 atmosphere at 37 °C and 96% relative humidity. After 72 h, the supernatant was collected and fresh medium was added for a second round of extraction. The supernatants from each thin film type were pooled, sterile filtered (0.2 µm) and stored at 4 °C until use. The Mg^{2+} and Li^+ concentrations were measured by flame atomic absorption spectroscopy (240 AA, Agilent Technologies, Germany) in a 1% nitric acid matrix with a minimum of 1:250 dilution (see supplementary information). Right before the cell culture experiment, the extracts were diluted using DMEM (low glucose) + 10% FBS + 1% antibiotics such that all three extracts contained 10 mM Mg and the Li concentration corresponded to the thin film composition.

5.5.4 Astrocyte cell culture

Immortalized human astrocytes were purchased from Innoprot (P10251-IM, Innoprot, Spain) and cultured in DMEM (high glucose, 31966047, Thermo Fisher, Germany) + 10% FBS + 1% antibiotics, henceforth referred to as growth medium. To have a large cell yield for seeding in the hydrogels, the cells were grown in Corning® CellSTACK® (CLS3268, Merck, Germany) under a 5 % CO_2 atmosphere at 37 °C and 96% relative humidity.

5.5.5 Seeding astrocytes in collagen hydrogels

The immortalized human astrocytes cells were detached by trypsinization using trypsin-EDTA (0.05%, 25300104, Thermo Fisher, Germany) and counted using a hemocytometer. Collagen Type I (rat tail, 5 mg/mL, ibidi, Germany) was neutralized using 1 M NaOH and mixed with 10x minimum essential medium (MEM, 21430020, Thermo Fisher, Germany) and 7.5% $NaHCO_3$ as per manufacturer instructions (see supplementary information for exact volumes). For each gel, cell suspension containing 10 million cells in growth medium was added to the neutralized collagen, resulting in a final collagen type I concentration of 3 mg/mL. The gels were cast in a 4-well chamber slide (0.5 mL/well, 94.6140.402, Sarstedt, Germany) and allowed to solidify for 30 minutes under cell culture conditions. The solidified gels were then transferred to a 6-well plate (1 gel/well) containing 5 mL/well of growth medium. After 6 h, the medium was changed to the Mg/Mg-Li extract in which the gel would be measured the following day.

5.5.6 Imaging astrocytes in collagen hydrogels

Immortalized human astrocytes cells were incubated with 10 μM of CellTracker™ Green (CMFDA dye, C2925, Thermo Fisher, Germany) in serum-free DMEM (high glucose) for 30 minutes under cell culture conditions. Then, the cells were seeded into collagen hydrogels as previously described and incubated overnight. The gels were imaged using a confocal laser scanning microscope (Leica DM6000 CS, Leica, Germany).

5.5.7 Lactate dehydrogenase (LDH) assay

To evaluate the effects of MR measurements in the bioreactor on the cell health, LDH released into the supernatant from the gels was used a marker of cell death. The Cytotoxicity Detection Kit[PLUS] (4744926001, Merck, Germany) was used to measure the LDH activity as per the manufacturer instructions and the absorbance measurements were acquired using a plate reader (Victor[3]V multilabel plate reader, PerkinElmer, Germany). LDH levels were quantified using an absorbance measurement. The measurement was compared a standard absorbance curve of L-LDH standard (10127230001, Merck, Germany).

5.5.8 Magnetic resonance hardware:

The experiments were performed on a 9.4T MRI system with a 30-cm horizontal bore (BioSpec 94/30; ParaVision 6.0.1, Bruker Biospin MRI GmbH, Ettlingen, Germany). The scanner was fitted with a 12-cm gradient system insert (BGA-12; Bruker BioSpin MRI GmbH, Ettlingen, Germany). ^{1}H MRI and MRS was performed using the combination of an 86-mm resonator and 4-channel receive-only mouse brain radiofrequency coil (Bruker BioSpin MRI GmbH, Ettlingen, Germany). ^{7}Li MRI and MRS was performed using a dual-resonance (^{1}H/[7]Li) transmit-receive RF coil (RAPID Biomedical GmbH, Rimpar, Germany).

5.5.9 Magnetic resonance experiments:

Diffusion MRI, Fig. 5-3B, was acquired with a diffusion echo-planar imaging (EPI) sequence with the following diffusion parameters: 8 b-values (250, 500, 750, 1000, 1500, 2000, 2500, 3000 mm^2/s), 6 diffusion directions, 3 ms gradient duration, and 12.5 ms diffusion time. The EPI sequence has the following acquisition parameters: TR|TE = 2000|25 ms, 4 segments,

0.2×0.2 mm^2 in-plane resolution, 128×128 matrix size, 0.5-mm slice thickness, 0.3-mm slice gap, 18 slices, 3 repetitions, and 21:12 min total scan time.

Prior to MRS, structural MRI was acquired as T2-weighted images with a 2D rapid acquisition with relaxation enhancement (RARE) sequence in two orientations (axial and coronal). The parameters of the RARE sequences were: RARE-factor 4, 40 ms effective echo time (TE), 2800 ms repetition time (TR), 0.2×0.2 mm^2 in-plane resolution, 128×128 matrix size, 0.5-mm slice thickness, 0.3-mm slice gap, 18 slices, and 1:30 min total acquisition time, Fig. 5-4A.

For MRS, the voxel was positioned using the structural MRI scans to maximize the proportion of hydrogel in the voxel, Fig. 5-4A in red. Two different MRS protocols were measured during each experiment: first a single spectrum and second a time series. The single spectrum was acquired using a stimulated echo acquisition mode (STEAM) sequence with parameters: 6000 ms TR, 10 ms TE, 10 ms mixing time, 5×1.5×5 mm^3 voxel size, 32 averages, and 1:36 min scan time. The single spectrum was used to ensure adequate shim and water suppression. The time series was acquired with a similar STEAM sequence with parameters: 6000 ms TR, 10 ms TE, 10 ms mixing time, 5×1.5×5 mm^3 voxel size, 1 average, 600 repetitions, and 1 hr total scan time, sample spectra shown in Fig. 5-4B-C.

5.5.10   Diffusion MRI analysis:

Diffusion MRI images were converted from DICOM to NIfTI using dcm2niix[214]. NIfTI images were denoised (*nlmeans*, DIPY) and analyzed using a standard diffusion tensor imaging (DTI) model in python using the package DIPY[215].

5.5.11   Spectroscopy analysis:

Each spectrum in a time series was phase corrected with the phase correction calculated for average spectrum of the time series. For visualization purposes, we averaged the data in 2-minute and 60-minute bins.

To compare the difference in metabolism between groups, we averaged spectra in 10-minute bins – six bins per time series. Prior to group analysis spectra with spurious echoes were removed using visual inspection. Spectra with low fit quality were removed using an Otsu threshold applied to both the coefficient of determination and mean absolute error.

To look at the time curve of the cell cultures, we performed a moving average analysis. Spectra were averaged in 2-minute sliding windows with a 30 second gap. In order to reduce the background noise, line broadening of 2 Hz was applied. In the 2-minute moving average analysis only spectra with spurious echoes were removed, as both the coefficient of determination and mean absolute error are directly related to the line broadening. The average time curve for each condition was smoothed using a Savitzky-Golay filter (width 11, order 3) to minimize the effect of inaccurate LCModel fits on the time curve.

LCModel of the time series data was analyzed using the reference scan acquired prior to the time series as a reference. All LCModel soft constraints were removed and, due to the low creatine signal, the spectra were referenced to the residual water peak.

5.5.12   Statistical analysis:

For diffusion MRI, we compared the mean diffusivity of the hydrogel divided by the mean diffusivity of the medium for each culture. The groups were compared using independent t-tests – due to the small sample size (n=5 per group) no correction for multiple comparisons was conducted.

For MRS, the metabolite concentration of the six 10-min spectra from each 1-hour time series were averaged and a one-way ANOVA was performed, details in in the supplementary information for Chapter 5. Post-hoc testing was performed assuming that the six 10-min spectra from each 1-hour time series were independent. Post-hoc testing between different medium-types was performed using two-tailed t-tests for metabolites where a one-way ANOVA (medium type) was significant. The two-tailed t-tests were Bonferroni corrected for the number of tests (n=6).

5.6 DATA AVAILABILITY:

Every component of the bioreactor and incubator has been uploaded as STL files on GitHub (https://github.com/Tor-R-Memhave/Cell-Culture). In addition to the components, the 3D model of the MRI system (Fig. 5-1) and the lid with components (Fig. 5-2C) are included as HTML files. The Arduino code for calibration and monitoring are available on GitHub.

5.7 AUTHOR CONTRIBUTIONS:

All authors contributed to the conceptualization and design of the study. E.Q., R.W., and S.B. supervised the study. L.H. and K.B. performed the benchwork. K.B. and T.R.M. performed the data acquisition. T.R.M. conducted the formal analysis and data visualization. T.R.M. wrote the first draft of the manuscript. All authors commented on previous versions of the manuscript and have read and approved its final version.

6

LITHIUM TREATMENT IN MICE

Establishing a magnetic resonance-based profile of lithium treatment in healthy, wild-type mice

Tor Rasmus Memhave[1,2,3], Susann Boretius[1,2,3]

[1]Functional Imaging Laboratory, German Primate Center, Leibniz Institute for Primate Research, Göttingen, Germany

[2]Georg-August Universität Göttingen, Göttingen, Germany

[3]International Max Planck Research School for Neurosciences, Göttingen, Germany

Own contributions:

- Conceptualization
- Data acquisition
    - o Mouse handling
    - o Mouse scoring
    - o *In vivo* magnetic resonance imaging and spectroscopy
- Data analysis
- Data interpretation
- Data visualization
- Writing

6.1 ABSTRACT:

Lithium is the frontline treatment for bipolar disorder and given to more than 50% of bipolar disorder patients. However, lithium treatment has two major challenges: only ~30% of patients are perfect responders and the mood-regulatory mode of action is incompletely understood. Due to the side effects of lithium treatment, non-ideal responders are at risk of developing potentially severe renal complications without improvement of symptoms. In human patients, distinguishing bipolar disorder and lithium treatment effects is challenging, which complicates early detection of positive or negative treatment response. In this study, we aimed to establish a magnetic resonance (MR) based profile of acute lithium treatment thereby establishing MR-detectable biomarkers of lithium treatment. We fed twenty mice either a high lithium (n=8), low lithium (n=4), or a placebo diet (n=8) for 3-4 weeks. We acquired multi-nuclear MR imaging (^{1}H MRI) and MR spectroscopy (^{1}H, ^{7}Li, ^{31}P MRS) at baseline and after three weeks on lithium-enriched/placebo diet. In week 4, ^{7}Li MRS was acquired from the mice on a lithium-enriched diet to estimate the lithium concentration in the brain. ^{7}Li MRS showed that brain lithium concentrations were within the therapeutic window. Mice on a high lithium diet had a brain concentration of 0.9±0.1 mM and mice on a low lithium diet had a brain concentration of 0.4±0.1 mM. We did not observe significant changes in ^{31}P MRS – although there was a tendency toward increased phosphocreatine. ^{1}H MRS showed increased osmolyte concentrations and decreased neuronal markers (N-acetylaspartate and glutamate-to-glutamine ratio). Anatomical MRI showed no change in total brain or cerebrospinal fluid volume. Diffusion MRI showed decreased apparent diffusion coefficient and increase neurite density index in cortex, corpus callosum, and hippocampus in mice on a high lithium diet. Our results suggest that the acute phase of lithium treatment might easily be mistaken for hypernatremia or neurodegeneration, but that when taken together they point at a potential change in cell activity or population. The changes occur across three distinct brain regions in both grey and white matter, which we cautiously interpret as a sign of increased astrocyte activity and density. We used MR techniques to establish a profile of lithium treatment in healthy, wild-type mice, which must be interpreted carefully, but may provide the first MR-detectable biomarkers of lithium treatment.

6.2 INTRODUCTION:

As a frontline treatment for bipolar disorder for over half a century, lithium treatment remains important today. Recent data from Sweden shows that roughly half of bipolar patients receive lithium treatment[10]. Despite the success of lithium treatment, the mechanism of action is still incompletely understood.

Studies have shown multiple cellular targets of lithium treatment including enzymes such as glycogen synthase kinase 3[74] and inositol-1 monophosphatase (IMPase)[66,67], both of which have magnesium sites that are vulnerable to magnesium-to-lithium exchange[65]. IMPase inhibition leads to decreased myo-inositol (Ins) and interruption of the phosphoinositide cycle[61]. These findings illustrate the complex mechanisms of lithium treatment; however, many studies have focused on the effect of lithium at the cellular level. As such, they cannot account for the complexity of lithium treatment on the systems level.

MRI and MRS allow for noninvasive measurements of brain structure, function, and metabolism at the systems level. Many studies on human bipolar disorder patients have been conducted, showing various effects related to lithium treatment. Most notably studies have shown changes in N-acetylaspartate (NAA), glutamate (Glu), and Ins. NAA was initially shown to increase following chronic lithium treatment in bipolar patients[90], although later studies were unable to confirm these findings[68,97–100]. Furthermore, administration of lithium to healthy subjects showed no difference in the brain metabolic profile[68]. Early studies on lithium showed that Glu and glutamine (Gln) decreased in basal ganglia following lithium treatment[71]; however, a more recent study showed increased Glu in the anterior cingulate cortex of bipolar disorder patients[97]. Such discrepancies have been linked to a dose-dependency of lithium on Glu levels with lower dosages leading to decreased Glu and high dosages to increased Glu[51]. Increased Ins have been described in remitters following lithium treatment and after chronic lithium treatment[97,100], although the Ins levels have been shown to fluctuate in cortex[216]. These studies highlight a fundamental challenge, namely, that it is nearly impossible to distinguish the drug from the disease in humans. The genetic variability of humans and different brain regions studied have led to largely inconclusive and difficult to reproduce results.

As lithium is distributed heterogeneously in the human brain[115,124,128], it is reasonable to assume that the effect of lithium varies between different brain regions. In rats, a heterogeneous distribution of lithium in the brain have been shown *ex vivo*[116] and in our recent work we showed a non-homogeneous distribution of lithium *in vivo* in the mouse brain (chapter 2). It is worth noting that while research on rats has been conducted[217,218], to the best of our knowledge no *in vivo* mouse study has been conducted showing the effect of lithium on the healthy brain.

The aim of this study is to understand the MR-based profile of acute lithium treatment in the healthy mouse brain. Lithium was given to mice in lithium-enriched chow to mimic the oral administration in bipolar disorder patients. We acquired ^{7}Li MRS to estimate the lithium concentrations in the brain and ^{31}P MRS to investigate whether lithium treatment influenced the energy metabolism in the brain. We acquired ^{1}H MRS from three different brain regions – cortex, corpus callosum, and hippocampus – as well as structural and diffusion ^{1}H MRI.

6.3 METHODS:

6.3.1 Animals:

Experiments were approved by the local ethics committee (Animal Welfare Service, Lower Saxony State Office for Consumer Protection and Food Safety, license-number 33.19-42502-04-20/3365). 20 adult male C57BL6/N mice were fed either a diet-enriched with 0.3% Li_2CO_3 (w/w, n=8), 0.2% Li_2CO_3 (n=4), 0.3% Na_2CO_3 (n=4), or normal chow (n=4) for four weeks. The two lithium naïve groups were combined for statistical tests. The mice are therefore effectively divided into three groups based on their diet: high lithium (0.3% Li_2CO_3), low lithium (0.2% Li_2CO_3), and placebo. Food and water were provided *ad libitum*. If the daily water consumption increased by more than 300% compared to baseline, a second water bottle with diluted saline solution was provided. The mice were single housed. Nesting data was acquired from 10 adult female C57BL6/N mice on a high lithium diet from a previous study (chapter 2).

In week 0, 3, and 4, the mice underwent MR examination. In week 0 and 3, ^{1}H MRI, ^{1}H MRS, and ^{31}P MRS was measured. In week 4, ^{7}Li MRS was measured. For each MR examination, anesthesia was induced with ketamine (MEDISTAR, Serumwerk Bernburg Tiergesundheit GmbH, Bernburg, Germany) and medetomidine (Dorbene Vet, Zoetis Inc., Parsippany, New Jersey, USA). The mice were then intubated and subsequently artificially ventilated (animal respirator, advanced 4601-2, TSE Systems GmbH, Bad Homburg, Germany). Anesthesia was maintained with isoflurane. The breathing rate and temperature (rectal thermometer) were continuously monitored. At the end of the MR examination, medetomidine was antagonized by atipamezole (Atipzole, Provident Pharmaceuticals, Prodivet Pharmaceuticals sa/nv, Eynatten, Belgium).

Following the final MR examination, the mice were given an overdose and perfused by first phosphate buffered saline and then 4% paraformaldehyde (Carl Roth GmbH, Karlsruhe, Germany). For each mouse, the brain, heart, and kidneys were collected.

6.3.2 Magnetic resonance acquisition:

6.3.2.1 Hardware:
MR examinations were performed on a 94/30 Bruker Biospec MRI system: 9.4T, 30-cm horizontal bore, BGA12 gradient system, and ParaVision 6.0.1 (Bruker BioSpin MRI GmbH, Ettlingen, Germany). For ^{1}H MRI and MRS, an 86-cm resonator and 4-channel, receive-only mouse head radiofrequency coil was used (Bruker). Dual-tuned (^{1}H/^{7}Li and ^{1}H/^{31}P), transmit-receive, 17-cm (inner diameter) surface radiofrequency coils (RAPID Biomedical GmbH, Rimpar, Germany) were used for ^{7}Li and ^{31}P MRS.

6.3.2.2 Spectroscopy:
^{7}Li MRS was acquired using an image-selected *in vivo* spectroscopy (ISIS) sequence with parameters: repetition time (TR) = 40s, 90° excitation flip angle, 256 data points, 10000 Hz acquisition bandwidth, 6×5×8 mm^3 voxel size (whole brain), 2 averages, and 10.7 min acquisition time.

^{31}P MRS was acquired using an ISIS sequence with parameters: TR = 3s, 512 data points, 7000 Hz acquisition bandwidth, 6×5×8 mm^3 voxel size (whole brain), 100 averages, and 40 min acquisition time.

^{1}H MRS from three brain regions – cortex, corpus callosum, and hippocampus – was acquired using a stimulated echo acquisition mode (STEAM) sequence with the following parameters: chemical shift selective (CHESS) water suppression, map shimming (linewidth water <20 Hz), TR|echo time (TE)|mixing time = 6000|10|10 ms, flip angle 78.7°, 5000 Hz acquisition bandwidth, 2048 data points, and 128 averages. The voxel size was 3.9×0.7×3.2 mm^3 (8.7 µl) for cortex, 3.9×0.7×1.7 mm^3 (4.6 µl) for corpus callosum, and 5.9×1×1.9 mm^3 (11 µl) for hippocampus. The voxels are visualized in Fig. 6-4A with one spectrum from each voxel shown in Fig. 6-4B.

6.3.2.3 Imaging:
Anatomical MRI was measured using a magnetization transfer (MT) FLASH sequence with the following parameters: TR|TE = 15.1|3.4 ms, 5° flip angle, MT pulse (3.5 ms, 3000 Hz offset, 135° flip angle), 100×100×100 µm^3 resolution, 192×192×192 matrix size, 100 kHz bandwidth, 2 averages, and 18.6 min acquisition time.

Diffusion MRI was acquired using a diffusion-weighted echo-planer imaging sequence with the following parameters: number of segments = 4, TR|TE = 2000/21.5 ms, 30 diffusion directions, 2 b-values per diffusion direction (1000 s/mm^2, 2000 s/mm^2), 5 b=0 s/mm^2 images, gradient duration/separation 2.5/12.5 ms, 100×100 μm^2 in-plane resolution, 128×128 matrix size, 500 μm slice thickness, 150 μm slice gap, 18 slices, 333 kHz bandwidth, 1 average, and 8.7 min acquisition time.

6.3.3 Data analysis:

6.3.3.1 Spectroscopy:

^{7}Li spectra were opened as Bruker 2dseq files in MATLAB and analyzed using Lorentzian fitting in python with the scipy toolbox *optimize.*

^{31}P spectra were opened as Bruker fid files in MATLAB and converted to text files. They were preprocessed and analyzed in python. Spectral preprocessing was done using the nmrglue library[184]. Spectral preprocessing included the following steps: removing the digital filter, zero-filling to 4096 points, 20 Hz line broadening, and automatic phase correction using the "peak minima" method in nmrglue. Spectra were corrected for scaling using the Bruker reco file. A two-stage polynomial baseline correction was applied to each spectrum. Spectra were fit to a 10-peak Lorentzian model with three variables per peak – integral, linewidth, and chemical shift – using the scipy toolbox *optimize.* The signal-to-noise ratio (SNR) was calculated by dividing the difference between the maximum signal (S_{max}) and the mean of the noise (N_{mean}) with the root mean square of the residuals (r_i), equation 6-1.

$$\text{SNR} = \frac{S_{max} - N_{mean}}{\sqrt{\frac{1}{n}\sum_i r_i}}$$

equation 6-1

The pH was calculated using the chemical shift, $δ$, between phosphocreatine (PCr) and inorganic phosphate (P$_i$) using equation 6-2. As the chemical shift of PCr is defined as 0 ppm, we can write the equation using only the chemical shift of inorganic phosphate[219,220].

$$p\text{H} = 6.73 + \log_{10}\left(\frac{\delta_{\text{P}_i} - 3.275}{5.685 - \delta_{\text{P}_i}}\right)$$

equation 6-2

The pMg, concentration of free magnesium, was calculated using the chemical shift between PCr and the phosphate in the β-position on adenosine triphosphate (βATP) using equation 6-3[220,221].

$$p\text{Mg} = 4.24 + \log_{10}\left(\frac{\delta_{\beta\text{ATP}} + 18.58}{-15.74 - \delta_{\beta\text{ATP}}}\right)$$

equation 6-3

^{1}H MRS spectra were converted from Bruker fid into LC Model RAW files using a home-built script. The spectra were preprocessed using nmrglue[184]. Preprocessing included digital filter removal and zero filling. Spectra were analyzed using LC Model[25]. The results are given in mM.

6.3.3.2 Imaging:

MRI images were exported from ParaVision in the DICOM format and converted to NIfTI (Neuroimaging Informatics Technology Initiative; http://nifti.nimh.nih.gov) with dcm2niix (https://www.nitrc.org/plugins/mwiki/index.php/dcm2nii:MainPage).

Structural MRI was analyzed using a home-built template. The study template was created from the 40 MT MRI acquisitions using rigid registration and *buildtemplateparallel* from the Advanced Normalization Tools (ANTs[222]) (http://stnava.github.io/ANTs/). The individual MRI acquisitions were first N4 biased field corrected and then non-linearly registered (using a symmetric normalization method)[222] to the study template using ANTs. An MT MRI atlas was created by modifying the Dorr-Steadman-Ulman-Richards-Qiu-Egan (DSURQE) atlas[223–226]. The DSURQE atlas was down-sampled to 100-µm isotropic resolution and registered to the MT MRI template. Labels were corrected using a stereotaxic atlas[227]. The total brain and cerebrospinal fluid volume was calculated using a brain and cerebrospinal fluid mask.

Diffusion MRI was analyzed using nipype[228], dipy[215], and dmipy[229] libraries. Bruker 2dseq images were converted to NIfTI using the nipype function *Bru2*. The NIfTI images were denoised using the dipy function *patch2self*[230]. Using dipy, a diffusion tensor model (DTI) was fitted, which calculated: fractional anisotropy (FA), axial diffusivity, radial diffusivity, and apparent diffusion coefficient (ADC) maps. Using dmipy, a neurite orientation dispersion and density imaging (NODDI) model with Bingham diffusion was fitted[36,39]. Beta fraction and orientation dispersion were used as markers for neuronal morphology[39]. The intracellular and extracellular fraction was used to calculate a neurite density index (NDI). For both diffusion MRI methods, we defined three regions of interest were defined to match the ^{1}H MRS voxels: cortex, corpus callosum, and hippocampus. The median was calculated from each region of interest.

6.3.4 Statistics:

To discern aging and treatment effects, we performed two-way ANOVA (scan week and diet) tests using *statsmodels* in python. Post-hoc significance tests were performed between groups using t-tests, *scipy stats* in python. For each group, the difference between a metabolite's concentration in baseline and week 3 was used for significance testing.

6.4 RESULTS:

6.4.1 Lithium-enriched diets led to increased water consumption:

Health monitoring, in the form of daily scoring, was conducted to ensure animal welfare. The mice did not show outward signs of discomfort except for increased water consumption. The water consumption increased by 828% in mice on a high lithium diet and 212% in mice on a low lithium diet, Fig. 6-1A-B. Mice on a placebo diet did not have increased water consumption, Fig. 6-1A-B. The drinking consumption exceeded 300% in all mice on a high lithium diet and one-of-four mice on a low lithium diet. A weight-loss of 13±4% was observed in mice on a high lithium diet whereas low lithium (weight-loss of 4±6%) and mice on a placebo diet (weight-gain of 4±6%) did not show systematic weight changes.

The nest building of five cages of female mice on a high lithium diet were measured weekly, Fig. 6-1C. They were scored by one blind reviewer. We did not observe systematic changes in nesting behavior (p=0.72, one-way ANOVA); however, the polyuria did increase the wetness of the bedding.
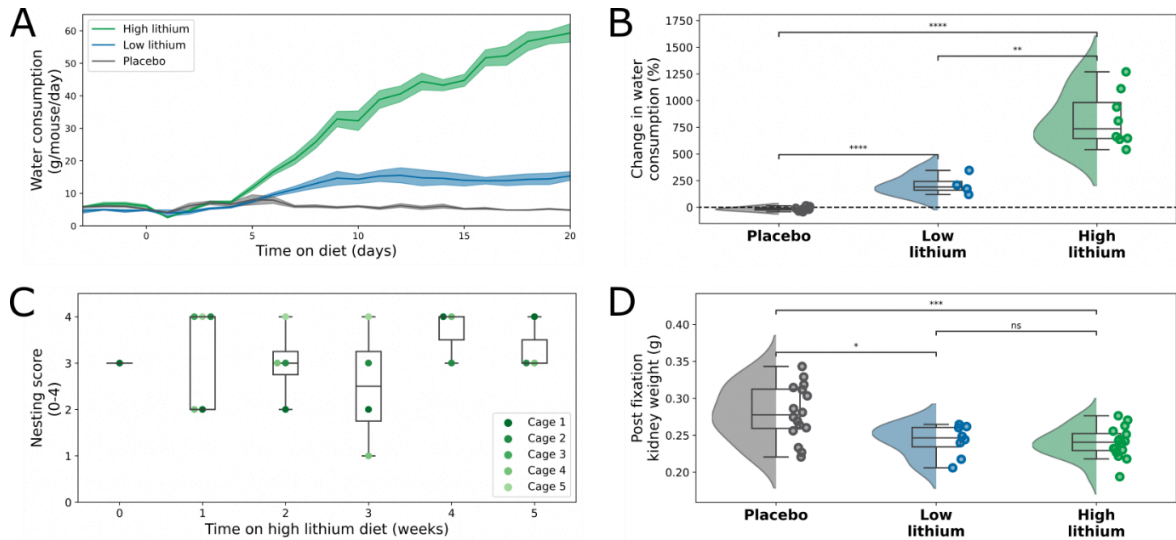
*Figure 6-1: **High lithium diet led to increased water consumption and decreased kidney weight.** Daily water consumption increased in all animals on a lithium-enriched diet (A). Mice on a low lithium diet had 212% and mice on a high lithium diet had 828% increase in water consumption by the end of the third week on a lithium-enriched diet (B). Despite increased water consumption and subsequent polyuria, we observed no systematic change in nesting behavior (C). The polyuria induced by a lithium-enriched diet led to decreased kidney weight in high and mice on a low lithium diet (D).*

In conclusion, the behavior suggests that although the mice develop severe polyuria, no adverse cognitive effects or signs of discomfort was observed in mice during lithium treatment.

6.4.2 Post fixation kidney weight was decreased in all mice on a lithium-enriched diet.

The kidney weight of mice on a high and low lithium diet was lower than for mice on a placebo diet, Fig. 6-1D. A high lithium diet led to a 15% decrease in kidney weight ($p < 0.001$) compared to mice on a placebo diet. Mice on a low lithium diet had a 14% decrease in kidney weight compared with mice on a placebo diet ($p = 0.01$). A decreased kidney weight may be an early sign of fibrosis and/or necrosis in mice on a lithium-enriched diet.

6.4.3 Mice on a lithium-enriched diet showed a dose-dependent uptake in the brain

As expected, *in vivo* ^{7}Li MRS of mice on a high lithium diet showed increased SNR (13.9 vs. 5.8) and the Lorentzian fit had a higher coefficient of determination (0.61 vs. 0.21) compared with mice on a low lithium diet, Fig. 6-2A-B. The linewidth did not vary between groups (0.47 vs. 0.45).
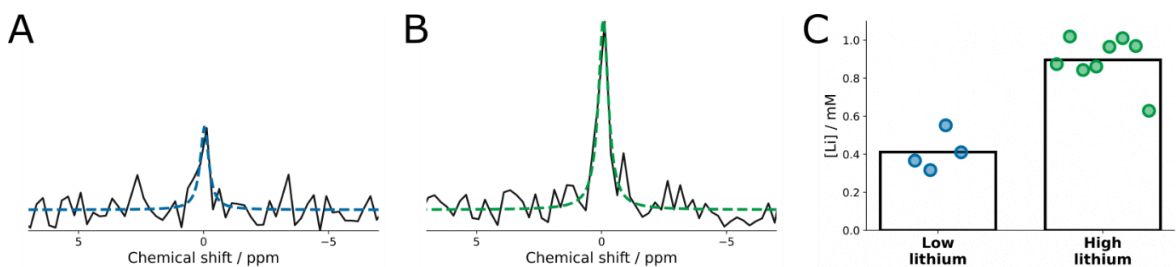
*Figure 6-2: **Lithium uptake in the brain was dose-dependent.** [7]Li spectra were acquired from whole-brain voxels. Mice on a low lithium diet (A) had lower area under the curve than mice on a high lithium diet (B). Using phantom measurements, we estimated that the lithium concentration in the brain was 0.4 mM for mice on a low lithium diet and 0.9 mM for mice on a high lithium diet (C).*

We observed a dose-dependent uptake of lithium in the brain using ^{7}Li MRS, Fig. 6-2C. Mice on a high lithium diet had increased brain lithium compared with mice on a low lithium diet. Using the area under the curve of the central peak in the [7]Li spectra, we estimated that the brain lithium concentration was 0.90±0.12 mM in mice on a high lithium diet and 0.41±0.09 mM in mice on a low lithium diet. The concentration ratio between groups was 2.3 compared with a 1.5 dosage ratio. This suggests a non-linear uptake of lithium in the mouse brain.

6.4.4 Phosphorus spectroscopy showed tendencies toward increased high phosphocreatine

In vivo ^{31}P MRS showed no systematic differences in quality assurance parameters between groups (SNR, linewidth, and coefficient of determination). Bonferroni-corrected, group-wise t-test of each parameter showed no difference between groups.

^{31}P MRS metabolites were normalized to the total phosphate content. Two-way ANOVA analysis of the metabolite concentrations as a function of scan week and diet showed no effects, Table 6-1. All post-hoc tests were performed between placebo and lithium groups on the difference between baseline and week 3, Fig. 6-3B-C, Fig. 6-3E-F, and Fig. 6-3H.

There was no change in the total ATP concentration between groups. The phosphomonoester (PME) to phosphodiester (PDE) ratio, a marker associated with
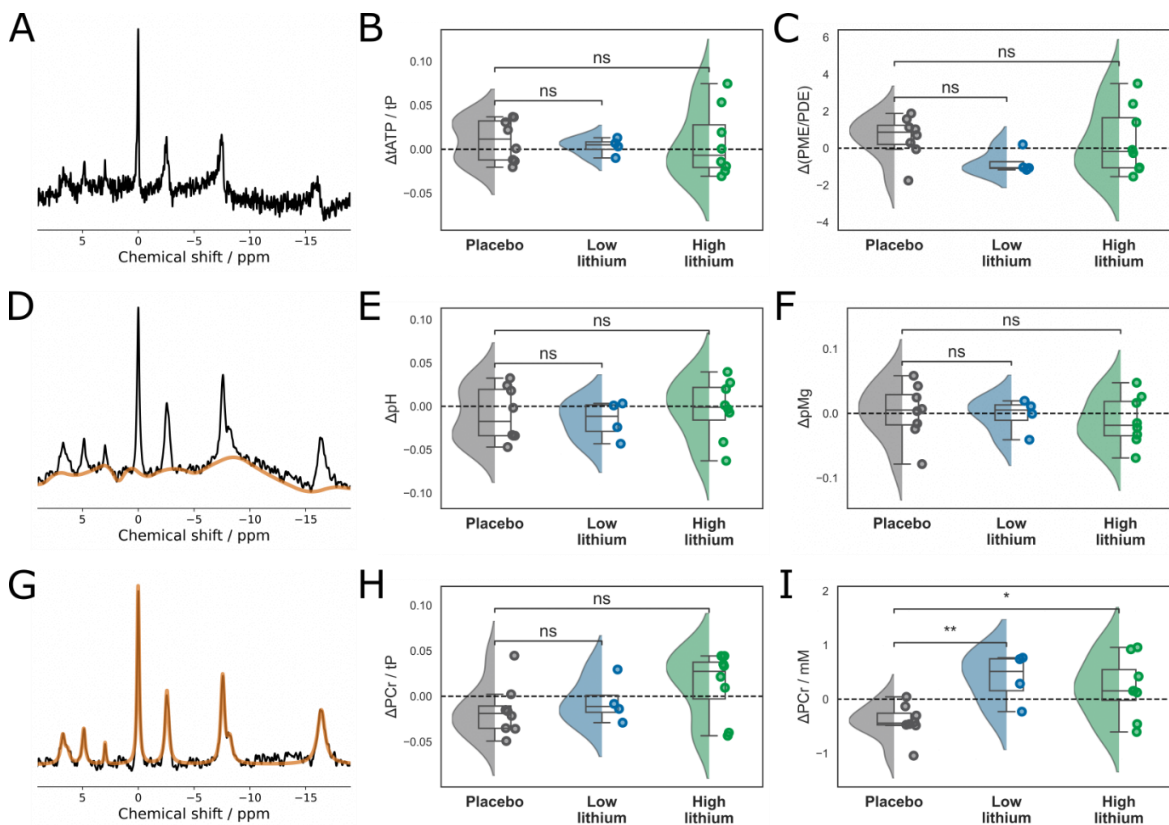
Figure 6-3: ^{31}P MRS showed a tendency of increased PCr. In vivo ^{31}P spectra were acquired from whole brain voxels. The raw spectra (A) were line broadened, phase-corrected, and baseline corrected (D). Quantification was done on baseline-corrected spectra with a 10-peak model (G). The change in total ATP (B) and ratio of phosphomonesters to phosphodiesters (PME/PDE) (C) were not significantly difference between mice on a placebo and a high lithium diet. We did not observe changes in the pH (E) or free magnesium concentration (pMg) (F). We saw a tendency towards increased phosphocreatine (PCr) (H), which we confirmed using the average of the PCr concentration in cortex, corpus callosum, and hippocampus measured by ^{1}H MRS (I).

Table 6-1: Two-way ANOVA (scan week and diet) of 31P MRS did not show significant effect of a high lithium compared to placebo diet.

Two-way ANOVA (scan week, diet), p-value interaction								
Metabolite	tPE	tPC	Pi	PME/PDE	PCr	yATP	aATP	NAD	bATP
p-value	0.59	0.51	0.33	0.78	0.10	0.63	0.61	0.19	0.96

membrane turnover, was not significantly changed in mice on a lithium diet, Fig. 6-3C. However, there is a tendency of a decreased PME/PDE ratio in mice on a lithium diet, which would be interesting to study further as decreased PME/PDE has previously been reported in patients with bipolar disorder[231]. We did not observe changes in pH or pMg, Fig. 6-3E-F. We saw a tendency towards increased PCr (p=0.10), Fig. 6-3H, which we confirmed using proton spectroscopy, Fig. 6-3I. Using the mean PCr concentration – calculated from ^{1}H MRS – from cortex, corpus callosum, and hippocampus, we found increased PCr in the brain of mice on a high lithium diet (p = 0.01).

6.4.5 In vivo proton spectroscopy showed metabolic changes amongst key metabolites:

In vivo ^{1}H MRS was acquired from three different brain regions: cortex, corpus callosum, and hippocampus, Fig. 6-4. *In vivo* ^{1}H MRS showed no major systematic difference in SNR, linewidth, or coefficient of determination of the fit between groups. Bonferroni-corrected, group-wise t-tests of each parameter showed three differences between groups. There was lower SNR in corpus callosum of week 3 compared with week 0 in mice on a low lithium diet. The coefficient of determination was higher in the hippocampus in week 0 of high and mice on a low lithium diet compared with week 3 of mice on a placebo diet. SNR is calculated by LC Model and given as an integer; as such small discrepancies are expected. The difference in coefficient of determination of the fit between mice on a high lithium diet in week 0 and week 3 mice on a placebo diet is 0.009 or ~1% and is therefore likely the result of small sample size.

^{1}H MRS can be used to detect metabolic changes in the mouse brain. We investigated the change in five key metabolites after the first three weeks of lithium treatment: Ins, Tau, total NAA (tNAA), Glu/Gln, and the total creatine (tCr) concentration. tNAA was defined as the sum of NAA and NAA-glutamate. tCr was defined as the sum of Cr, PCr, and Cr2 (downfield Cr peak). To discern the effect of a lithium-enriched diet from inter-measurement variability, we did a two-way ANOVA, Table 6-2. Post-hoc testing between placebo and lithium groups was performed on the difference between baseline and week 3, Fig. 6-4C-G.

Ins, a biomarker associated with glial cells, was increased by 39% in cortex (p=0.02, n=8). The neuronal marker tNAA was decreased by 11% in corpus callosum (p=0.009) and 10% in hippocampus (p=0.01). The Glu/Gln, glutamate being a neurotransmitter and glutamine synthesize in astrocytes, was decreased by 16% in hippocampus (p=0.05). The tCr was unchanged each of the three brain regions, suggesting that the observed changes were not due to a systematic shift in concentration.

Due to the small sample size, some metabolites, which were significant in pair-wise t-tests, were not significant using the conservative statistical tests described above. However, three

Table 6-2: Two-way ANOVA (scan week and diet) of ^{1}H MRS showed significant changes in myo-inositol (Ins), taurine (Tau), and N-acetylaspartate (NAA).

Two-way ANOVA (week, diet), p-value interaction			
Metabolite	Cortex	Corpus callosum	Hippocampus
Ins	**0.01**	**0.02**	0.45
Tau	**0.04**	0.28	0.59
NAA	0.32	**0.02**	**0.01**
Glu/Gln	0.28	0.89	0.08
tCr	0.83	0.85	0.82

Table 6-3: Two-way ANOVA (scan week and diet) of the parameters derived from the two diffusion MRI analyses: DTI and NODDI. †Parameters derived from DTI analysis; ‡parameters derived from NODDI analysis.

Two-way ANOVA (scan week, diet), p-value interaction			
Modality	Cortex	Corpus callosum	Hippocampus
ADC†	**0.01**	**0.003**	**0.02**
FA†	0.81	0.73	0.47
NDI‡	**0.02**	**0.009**	**0.03**
Beta fraction‡	0.28	0.97	0.34
Orientation dispersion‡	0.45	0.48	0.83

tendencies were observed. We verified the following tendencies using a two-sided, one sample t-test of the change between week 0 and week 3 in mice on a high lithium diet against the mean change of the mice on a placebo diet. Ins was increased in corpus callosum by 26% (p=0.03). The osmolyte Tau was increased by 9% in cortex (p=0.04). Glu/Gln was decreased by 14% in cortex (p=0.04).

The increase of osmolytes, Ins and Tau, and decreased on neuron specific markers, Glu and tNAA, could suggest increased glial cells relative to neurons.

6.4.6 Total brain and cerebrospinal fluid volume was unchanged in all mice

Using our study atlas, we observed no change in the total brain volume (p=0.84, two-way ANOVA, scan week and diet interaction) and cerebrospinal fluid volume (p=0.44, two-way ANOVA, scan week and diet interaction) in mice on a lithium-enriched diet.

6.4.7 Diffusivity decreased and neurite density increased in cortex, corpus callosum, and hippocampus

The diffusion data was analyzed using two different models – DTI and NODDI. We looked at diffusive changes in the three regions we also acquired spectroscopy from: cortex, corpus callosum, and hippocampus. For both the DTI and NODDI, we drew conservative regions
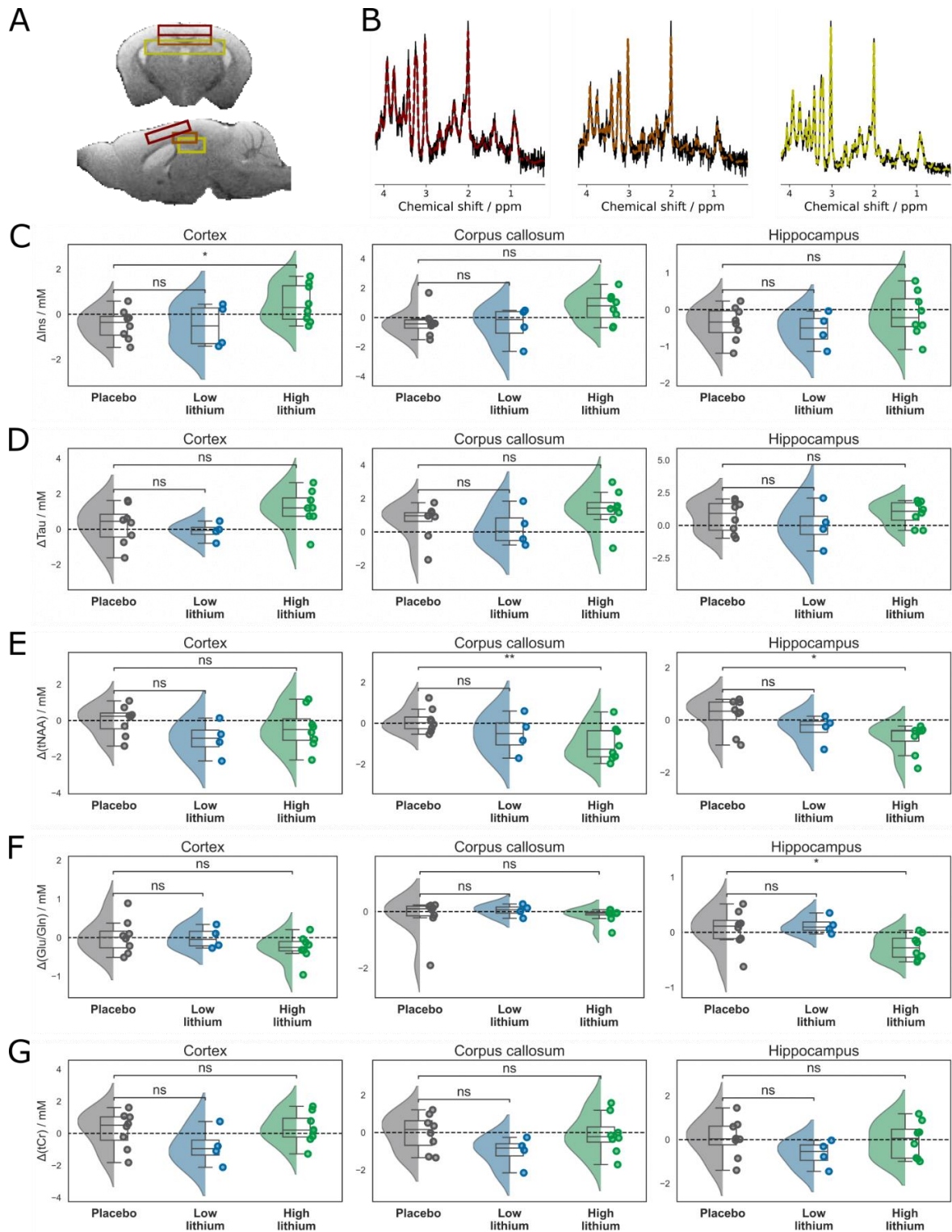
Figure 6-4: ¹H MRS showed increased myo-inositol (Ins) and decreased N-acetylaspartate (NAA) in mice on a high lithium diet. *¹H MRS was acquired from cortex, corpus callosum, and hippocampus (voxels in A, spectra in B). Ins was increased in cortex (C). The change in taurine did not significantly differ between mice on a high lithium and placebo diet (Tau in D). NAA was decreased in corpus callosum and hippocampus in mice on a high lithium diet compared with placebo (E). Hippocampal glutamate-to-glutamine ratio (Glu/Gln in F), was decreased in mice on a high lithium diet. We did not observe changes in total creatine (tCr in G).*

of interest – Fig. 6-5A and 6-5C, respectively. To discern the effect of a lithium-enriched diet from inter-measurement variability, we did a two-way ANOVA, table 6-3. Post-hoc testing

between placebo and lithium groups was performed on the difference between baseline and week 3, Fig. 6-5B and 6-5D.

The DTI analysis showed decreased ADC in mice on a high lithium diet across the three brain regions. The ADC was decreased by 4% in cortex (p=0.005), 5% in corpus callosum (p=0.004), and 4% in hippocampus (p=0.01). We did not observe changes in FA in response to a lithium-enriched diet.

Using the NODDI model, we observed increased NDI across the three brain regions for mice on a high lithium diet. The NDI was increased by 6% in cortex (p=0.01), 7% in corpus callosum (p=0.007), and 6% in hippocampus (p=0.02). We did not observed changes in beta fraction or orientation dispersion.

The two diffusion models yield complementary findings. The decreased ADC and increased NDI suggest that the diffusion changes are related to brain microstructure.

6.5 DISCUSSION:

6.5.1 Are the mice healthy?

The mice were kept in standard animal housing with food and water *ad libetum*. However, this fact does not constitute a healthy mouse, it is therefore important to assess what is meant by healthy. Here, the definition is used to describe a mouse that does not show clinical signs of distress, lithium poisoning, or anhedonia. From our experiments, we have three different measures that can be used to assess welfare: drinking behavior, nest-building behavior, and daily scoring.

The increase in water consumption was expected and seen across all mice on a lithium diet. Increased thirst and urination are common side effects of lithium treatment in humans and rodents[22,232,233]. However, the induction of early-stage nephrogenic diabetes insipidus via a lithium-enriched diet should not be likened with kidney failure and associated problems. In rats, it has been shown that lithium treatment of rats causes reversable kidney changes[234]. The dosing of 0.3% Li_2CO_2 (w/w) is not expected to give blood concentrations larger than 1.2 mM – the upper limit of the acute therapeutic range[9]. While the increased water consumption and subsequent polyuria is expected to cause damage to the kidneys, as seen by decreased kidney weight, we did not observed signs of end-stage renal disease.

Nest-building data was complicated by the polyuria of the animals, which led to wetter nests in general. However, in all mice we observed an attempt to build a nest and no significant reduction in nest-building as function of time on a lithium-enriched diet, Fig. 6-1C. Nest-building was used as an indirect test for anhedonia. However, the nest-building paradigm was insufficient to distinguish the behavioral difference between the mice and was only used to ensure that the mice did not suffer from severe lithium poisoning.

The daily scoring and monitoring of the animals showed no systematic cognitive or behavioral deficits resulting from lithium treatment – aside from increased water consumption. The weighing of the mice before the MR examinations showed that mice on a high lithium diet had decreased body weight between the first and last examination (13%).

It is our opinion that while lithium treatment does result in higher water consumption and the development of polyuria that mice on a lithium-enriched diet did not exhibit signs of distress.
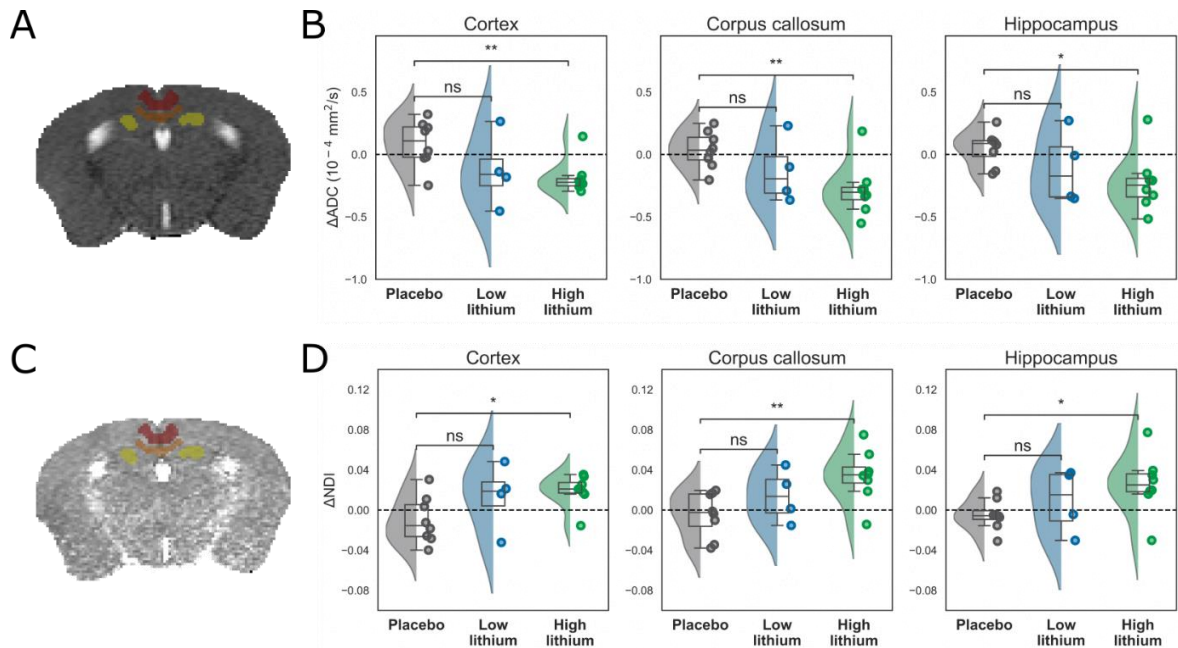
Figure 6-5: ***Mice on a high lithium diet had decreased apparent diffusion coefficient (ADC) and increased neurite density index (NDI).*** *Diffusion MRI was analyzed using two models: DTI (A-B) and NODDI (C-D). From DTI, we analyzed ADC in cortex, corpus callosum, and hippocampus (A). The ADC decreased in all three regions of interest for mice on a high lithium diet (B). Using NODDI (regions of interest in C), we observed increased NDI in all three regions of interest in mice on a high lithium diet (D).*

We note that no standardized behavioral testing was used in the study. This limitation manifests itself in two major components: first, we are unable to test whether the overall activity of the mice play a role in the MR data and second, we cannot state whether the behavior is comparable between groups and/or cages. The interpretation of mouse welfare was therefore limited to simplified health metrics and daily monitoring.

6.5.2 Distinguishing lithium treatment and disease pathology

An increase in Ins is commonly observed in neurodegenerative disorders and has been associated with microglial activation. An interpretation supported by increased Ins correlating with amyloid pathology in Alzheimer's disease[235,236] and thereby increased microglia. However, Ins is not microglial specific, but rather a marker of increased glial cells in the volume of interest. ^{1}H MRS of lithium-treated, adolescent, bipolar disorder patients has previously shown that lithium does not affect Ins levels in the brain[216], contrary to our findings.

Increased cortical Tau concentrations following lithium treatment are complex to interpret, due to the many proposed functions of Tau in the brain. As a semi-essential, sulfur-containing amino acid, the proposed functions of Tau range from mechanisms from neuroprotection to regulation of gene expression[237]. The high Tau concentrations in the rodent brain highlight two other important functions as a calcium regulator[238] and osmolyte[239]. Tau has been linked to cognitive dysfunction and shows decreased concentrations with advanced age in mice[240]. However, Tau concentrations may vary between different cell types, it is well known that the concentration of taurine in astrocytes may exceed 50 mM in mice, in stark contrast to the roughly 1 mM in the extracellular space[241]. A cautious, but interesting interpretation is that increased Tau may be related to an increased astrocyte content.

Traditionally thought of as a marker of neuronal health, the functions of NAA are many and still heavily debated. Unique to the central nervous system, NAA is synthesized from aspartate and acetyl-CoA in neurons[170]. We observed decreased NAA in both corpus callosum and hippocampus. Earlier studies in humans have shown both increased and decreased NAA resulting from lithium treatment of adolescents with bipolar disorder[99,242]. Lithium has been shown to decrease NAA in both a rat model of Canavan disease[243] and human children with Canavan disease[94]. It should be noted that for Canavan disease the NAA levels are highly elevated, which was not the case in healthy mice. However, our data support the hypothesis that lithium may decrease NAA levels. Cross-sectional and longitudinal studies of lithium treatment in human bipolar patients have observed mixed effects on NAA[244]. In the human studies, the treatment and illness are difficult to disentangle; however, in our study, healthy, wild-type mice were placed on a lithium-enriched diet, so the decreased NAA is interpreted as a direct sign of treatment.

With diffusion MRI, we observed decreased ADC in cortex, corpus callosum, and hippocampus – the regions also studied in ^{1}H MRS. Observing decreased ADC across multiple brain regions has often been loss of neurons, commonly observed in mouse models of Alzheimer's or Parkinson's disease[245,246]. However, we do not observe accompanying changes in beta fraction (NODDI), FA (DTI), or orientation dispersion (NODDI). The total brain volume and cerebrospinal fluid volume did not change either. The lack of these common comorbidities of decreased diffusivity in neurodegeneration suggest that an alternative hypothesis is required.

We therefore investigated the NDI, a marker of the amount of axons and dendrites in the voxel[247]. We found increased NDI in cortex, corpus callosum, and hippocampus, which would further support discarding the neurodegeneration interpretation. NDI does not solely correlate with neural density, but also myelin density, especially in cortex[247–249]. The change in NDI in hippocampus likely results from NDI also being sensitive to unmyelinated fibers[249]. As such, decreased ADC and increased NDI could be seen as indication that a change in cell population occurs.

Glu is an important neurotransmitter, which has been associated with a wide range of illnesses. Glu/Gln should therefore be interpreted as an indirect marker of the glutamate turnover, which has been linked to neural plasticity[250]. Observing an increased Glu/Gln ratio suggest that lithium increases the glutamate turnover rate, which may result from increased astrocyte activity. For completion, we also looked that the ratio of the sum of Glu and γ-aminobutyric acid (GABA) to Gln – [Glu+GABA]/Gln – as an indirect measure of the astrocyte turnover rate – both glutamate and GABA are converted to glutamine in astrocytes[251]. We found decreased [Glu+GABA]/Gln in the hippocampus of mice on a high lithium diet (placebo vs. high lithium t-test, p=0.009; two-way ANOVA, scan week and diet intersection p=0.03, Fig. S-3), supporting the hypothesis of increased astrocytic activity. We note that increased Glx (Glu+Gln+GABA) is commonly observed in bipolar disorder[252]. In the manic state Glu/Gln is frequently elevated; however, this may in part be explained by a decreased number of glial cells in bipolar disorder patients[252,253].

Mice on a high lithium diet had increased PCr. A metabolite important for energy homeostasis, PCr is converted to ATP when there is high-energy demand. tCr is a common internal reference, although it should be used with care[157,254]. In humans, tCr does not

change significantly with age or time of day[255,256]. In bipolar disorder decreased tCr and PCr have been reported in bipolar disorder patients both undergoing treatment and medication free[257–260]. This highlights the issue of disentangling the illness from the treatment. It is worth noting that non-lithium medicated bipolar disorder patients have decreased PCr compared to unmedicated bipolar disorder patients[261].

Importantly, tCr was unchanged throughout the experiments. This is an important indicator that edema or other effects of hypernatremia were not present. Edema and hypernatremia may lead to systematic quantification errors, due to increased water content; however, as we observed both increases and decreases in metabolite concentrations, this is unlikely.

We observed decreased post fixation kidney weight, but no signs of urine retention (indicator of kidney failure). The whole brain and cerebrospinal fluid volumes were unchanged. Combining these measures, we suggest that the observed effects of a high lithium diet in healthy, wild-type mice are biomarkers of lithium treatment and not the result of edema or kidney failure.

6.5.3 Lithium administration in healthy human subjects and wild-type rodents

Metabolic changes associated with lithium treatment have been extensively studied in bipolar disorder patients; however, distinguishing the effect of lithium and bipolar disorder has proven difficult. However, a few studies have attempted to look at the profile of lithium treatment in either healthy volunteers or rodents.

6.5.3.1 Lithium treatment in healthy human subjects:

Despite the inositol depletion hypothesis being a proposed mechanism of action of lithium treatment, studies have not reached a consensus on the effect of lithium treatment on Ins in the brain. ^{1}H MRS studies have shown a mixture of no change and decrease in Ins[68–71]. A likely explanation for this lack of consensus is the difficulty in quantifying Ins, especially at low fields, due to its proximity to water and other high concentration metabolites. However, these studies still contradict the Ins increase observed here. Human Ins concentrations are also ~2-fold higher than in mice, which may hint at Ins playing a different role in the two species. In humans, while early studies found increased NAA following lithium administration, more recent work has found no significant changes following lithium treatment[68,71,90]. Glu/Gln was decreased in mice following a lithium-enriched diet, whereas in healthy humans lithium increased Glu/Gln[71].

6.5.3.2 Lithium administration in wild-type rodents:

Ex vivo NMR studies of rat brain extracts have shown decreased Ins after two and four weeks of lithium administration[217], contrary to our findings. In two studies, O'Donnell *et al.* looked at key brain metabolites following 15 days of lithium administration in rats[96,218]. The experiments were conducted on *ex vivo* brain homogenates using NMR. In the first study, NAA was decreased, which we also observed, but Ins and tCr were also decreased – contrary to our findings[96]. In the second study, they observed decreased aspartate, Glu, and Tau[218]. We did not observe significant changes in aspartate. In contrast, we observed increased Tau in our study. Here, it should be noted that high-performance liquid chromatography samples of brain homogenates did not show significantly decreased

Tau[218]. Decreased Glu may be comparable to our finding of a decreased Glu/Gln. Although it has also been suggested that Glu concentrations change in a dose dependent manner[58].

6.5.4 Establishing an MR-based profile of lithium treatment in mice

The aim of this study was to provide the community with unique markers of lithium treatment in wild-type mice. The MR-based profile of lithium treatment was observed in mice on a high lithium diet and showed an increase in cortical osmolytes – Ins and Tau, decreased NAA and Glu/Gln in hippocampus. We observed decreased ADC and increased NDI in cortex, corpus callosum, and hippocampus. However, we did not observe changes in total brain volume or cerebrospinal fluid volume.

6.5.5 A drug as complex as the illness it treats

While the data presented here shows similarities to neurodegenerative phenotypes observed in mice – decreased NAA, increased osmolytes, and Gln – we would like to offer an alternative hypothesis, an increased glial activity. The neurodegenerative phenotype is often associated with microglial activation, which ultimately results in severe symptoms; however, in our mice we did not observe clinical symptoms such as tremor and anhedonia. The mice on a lithium diet showed a large increase in water consumption, but no behavioral abnormalities. Early, mild symptoms of kidney damage are not anticipated to manifest themselves in brain metabolism, although it is well known that hypernatremia will lead to increased Ins (and other osmolytes)[168,262,263]. However, lithium-fed mice are unlikely to have hypernatremia, due to constant water availability and large urine production. We did not observe total brain or cerebrospinal fluid volume changes, which makes edema unlikely.

Future experiments are needed to verify the observed changes. Our experiments provide evidence for metabolic changes occurring in the acute phase of lithium treatment. In future studies, the addition of brain histology and *ex vivo* kidney MRI would help to validate the observed changes and distinguish whether lithium treatment causes changes in cell population, microglial activation, hypernatremia, or a combination of these.

6.5.6 Limitations:

The current study focused on the acute treatment of lithium in mice. As such, the observed changes are likely to mimic the start of lithium treatment rather than chronic long-term lithium treatment. This distinction is important for interpreting the results. Here, we present potential early biomarkers of lithium treatment.

We only acquired data from healthy, wild-type mice. The biomarkers of lithium treatment and the corresponding MR-based profile were based on lithium in the healthy brain – it is unknown if lithium affects brain metabolism different in bipolar disorder patients.

The nomenclature of spectroscopy voxels should be clarified. ^{1}H MRS was acquired from large voxels, Fig. 6-4A-B, so they were named based on the brain region at their center (e.g. the corpus callosum voxel is larger along the superior-inferior axis than the corpus callosum thickness).

Finally, the ^{31}P MRS analysis yields similar, but not identical results based on the preprocessing steps prior to curve fitting. The impact of line broadening, phase correction algorithm, baseline correction, and curve fitting start points on the spectral quantification

are detailed in the supplementary information. Most notably, the chemical shift of βATP was strongly dependent on the analysis method.

6.6 CONCLUSION:

We have described the MR-based profile of a lithium-enriched diet on healthy, wild-type mice. Most notably mice showed dose-dependent lithium uptake as well as spectroscopic and diffusive changes that suggest a change in cell activity and/or population. The mice were clinically healthy with no detectable behavioral symptoms of discomfort, despite increased water consumption and decreased *ex vivo* kidney weight. We have illustrated that there are MR detectable biomarkers of the acute phase of lithium treatment in mice, which may help to disentangle bipolar disorder from its most successful treatment.

6.7 ACKNOWLEDGEMENTS:

6.8 AUTHOR CONTRIBUTIONS:

All authors contributed to the conceptualization and design of the study. S.B. supervised the study. T.R.M. and S.B. performed data acquisition. T.R.M. conducted the formal analysis, data visualization, and wrote the first draft of the manuscript. All authors commented on previous versions of the manuscript and have read and approved its final version.

7

GENERAL DISCUSSION

In this thesis, I have investigated the mechanism of action and *in vivo* distribution of lithium using magnetic resonance imaging (MRI) and spectroscopy (MRS). This is an alternative approach to answer the elusive question of lithium's mechanism of action, which has intrigued scientists since John Cade first found lithium effective against manic depression – the name for bipolar disorder at the time. Since lithium has many targets in the brain, I opted to develop lithium-7 MRI with the aim of visualizing the distribution of lithium in the brain. Alongside lithium-7 MRI, I acquired structural and diffusion MRI to better understand the impact of lithium on the healthy brain in the early phase of lithium treatment. To investigate early metabolic biomarkers of lithium treatment, I acquired MRS from astrocytes in a lithium-containing medium and the mouse brain *in vivo*. Combing these approaches, I found indications of what lithium treatment may look like during the early phase with the ultimate goal of translating this into a profile of a positive treatment response. However, despite this progress towards understanding the mechanism of action of lithium, I have not found a definitive answer.

In the following sections, I will discuss four important questions in the context of lithium treatment. I have provided evidence for a non-homogeneous distribution of lithium in the mouse brain, but which mechanisms give rise to these regional variations in lithium concentration. In chapter 5-6, I showed that lithium alters metabolism in astrocyte cell cultures and mice on a lithium-enriched diet, thereby characterizing an MR-based profile of lithium treatment, but an important question remains, "why does lithium only help some bipolar patients?" In this thesis, I have developed methods for studying the lithium distribution in the mouse brain. In section 7.3, I will discuss the technical aspects of lithium imaging with the aim of improving the resolution to $1 \times 1 \times 1$ mm^3 – sufficient for accurate visualization of the lithium distribution in the mouse brain. Finally, another area of interest in this regard is to understand whether the different properties of lithium-6 and lithium-7, result in an isotope effect on treatment.

7.1 WHAT DRIVES THE HETEROGENEOUS DISTRIBUTION OF LITHIUM IN THE BRAIN?

To understand lithium-7 treatment, we must first understand whether the heterogeneous distribution of lithium in the brain originates from the initial uptake of lithium from the blood or is dictated by lithium retention in certain regions. While progress has been made towards

answering the question of lithium-7 uptake kinetics and distribution in the brain, thorough answers only exist for the former. The distribution of lithium in the brain is still largely unexplained and has shown large variance between subjects in humans[115,128] and, as presented in the thesis, in mice. The problem may be broken down into two separate parts the lithium uptake distribution and the lithium equilibrium distribution.

Understanding the lithium uptake distribution is essential to discern whether all regions of the brain receive the same amount of lithium from the blood. In rats, a heterogenous distribution of lithium in the brain can be observed following an *intraperitoneal* injection of lithium chloride[129]. While the study found low concentrations in the cerebellum (comparable with results in chapter 2), it should be noted that most of the lithium ended in the muscle tissue below the brain. With this in mind, this question is likely to be best addressed in rodents, where lithium naïve animals may receive *intravenous* injections or follow a feeding regime with lithium-7 MRI on consecutive days. Here, it should be noted that lithium-6, due to long T1 relaxation time and an ability to be hyperpolarized[264], may be the preferred option for the *intravenous* application. Van Heeswijk et al. showed that it may be possible to image the distribution of lithium uptake using hyperpolarized lithium-6; however, they were limited by their radiofrequency coil not having full brain coverage[264].

The lithium equilibrium distribution in the brain will continue to be of interest in large-scale human studies. Here, I foresee that cohorts of bipolar patients will shed light on the variation of lithium distributions in humans as well as whether there is a link between lithium distribution and successful treatment. Studies in bipolar disorder patients[115] and *ex vivo* mice[132] have shown increased lithium in the hippocampus. In bipolar disorder patients, it is well established that there are large inter-individual differences in the lithium equilibrium distribution[115,124,128]; however, as of yet there is no definitive indicator of successful treatment based on the lithium equilibrium distribution in the brain. In this regard, understanding distribution differences between wild-type and transgenic mice might provide insights into how lithium treatment works. Specifically, some transgenic mouse-models of bipolar disorder (and mania) are ideal responders to lithium treatment[265,266], others are not[267]. The difference between the lithium equilibrium distribution in the brain of lithium responding and non-responding mice may provide explanations for the observations seen in humans. Furthermore, as mice are scanned under anesthesia, it is feasible to increase the measurement duration. MR examinations in mice can therefore include lithium-7 imaging as well as proton MRI and MRS. Such investigations may pinpoint treatment efficacy, which may in turn provide insights into MR-detectable biomarkers of successful lithium treatment.

7.2 WHY DOES LITHIUM ONLY HELP SOME BIPOLAR PATIENTS?

It remains unclear how to predict ideal lithium response. I have provided a few insights that could potentially be translated into research tools. Specifically, the cautious interpretation that during the early stages of lithium treatment a change in the cell population and/or activity occurs. Specifically, I have observed that astrocytes show dose-dependent changes in metabolism (chapter 5). Diffusion MRI of mice on a high lithium diet (chapter 6) showed decreased apparent diffusion coefficients and increased neurite density index. Alongside our MRS observation of increased in glial markers – myo-inositol and glutamine, the initial MR-based profile of lithium treatment in mice is indicative of an increased number of

astrocytes. Astrocytes are known to be increased in rats following lithium treatment[268]. Recently, targeting astrocytes in bipolar disorder – where they are depleted – has become a prominent route for drug development[205,269]. My findings support this idea; however, further experimentation is required to separate the contribution of different types of glia to the MR-based profile of lithium treatment.

There are only few MR-detectable markers of neurogenesis, most notably a peak at 1.28 ppm in proton MRS[270]. Although the broad peak at 1.28 ppm was originally believed to originate exclusively from neural stem cells[270], it has since been described that it is more directly related to apoptosis[271]. However, this 1.28 ppm peak is not easily observed and is not detectable in my mouse spectra. Furthermore, any conclusion drawn from the current MR-based profile of lithium treatment must be verified by histology. In chapter 2, I observed that lithium would gradually diffuse from our fixed mouse brains into the surrounding solution. Due to this wash-out of lithium, I kept the mouse brains out of solution after the final MR examination in chapter 6. However, this meant that histology was not possible. I am currently testing the hypothesis that the increased glial markers in MR-based profile of lithium treatment is mediated by astrocytes using microglia-depleted mice on a lithium-enriched diet. In this study, histology will be performed after the final MR examination. Microglia-depleted mice will serve as an interesting model for discerning whether the changes observed in this thesis are mediated by astrocytes – as hypothesized.

7.3 HOW CAN WE ACQUIRE LITHIUM IMAGING AT (SUB)-MILLIMETER RESOLUTION?

In this thesis, I have improved the spatial resolution of lithium-7 MRI from $2\times2\times4$ mm^3 (reported by Stout et al.[116]) to $2\times2\times3$ mm^3 (25% smaller), while shortening the measurement protocol from 36 hours to 4 hours (3-fold lower expected signal-to-noise ratio [SNR]). This was primarily possible due to improved sampling of the k-space, due to the rapid acquisition using spiral-encoding. However, $2\times2\times3$ mm^3 is still insufficient for an accurate, region-specific characterization of the *in vivo* distribution in mice. In this regard, achieving sub-millimeter or 1-mm isotropic voxels would be ideal. In order to do this, the SNR would need to be increased at least 10-fold. I propose that this may be possible using the following three improvements. First and foremost, a cryogenic lithium-7 RF coil would improve the SNR roughly three-fold. Although this would allow a significant improvement, it is also the most expensive solution to improve the SNR. The second improvement would be to switch from a spiral-encoding to a radial encoding with a balanced steady-state free precession (bSSFP) sequence. The radial-encoding will allow for fast imaging with every acquisition passing through the center of the k-space (improving the SNR), which in turn would also allow for potential motion correction. Furthermore, the radial bSSFP is less sensitive to inhomogeneity artifacts than the Cartesian bSSFP employed in this thesis (standard encoding scheme). Finally, one could use more advanced reconstruction methods, such as compressed sensing. Used for improving the speed or SNR of an acquisition, compressed sensing relies on the data being reconstructed using only parts of the k-space and optimizing these chosen points in an iterative manner[272]. Using this approach, it would be possible to (theoretically) improve the SNR about four-fold[273]. Combining these approaches would potentially allow lithium-7 MRI at 1-mm isotropic voxels at therapeutic concentrations. Additionally, lithium-6 may be an interesting avenue for understanding the lithium uptake

distribution, when combined with hyperpolarization[264]. However, lithium-6 MRI would require both a new RF coil and hyperpolarization equipment, both of which cannot be readily (or cheaply) attained.

7.4 DO LITHIUM ISOTOPES HAVE AN EFFECT ON TREATMENT?

Finally, I have investigated the treatment with natural lithium, which is predominantly lithium-7; however, it is known that lithium-6 and lithium-7 have different diffusion properties[40]. Furthermore, experiments on rodents suggest that lithium-6 and lithium-7 may have different effects[42,274]. Leading to lithium-6 being taken up faster[41], in higher quantity[275], and having side effects in a larger percentage of mice[43]. Further investigation of the equilibrium distribution of the two isotopes as well as their brain concentrations at equivalent dose may provide insights into whether there is an isotope-specific treatment effect.

7.5 CONCLUDING REMARKS

Despite more than 50 years of clinical usage, lithium treatment remains an interesting puzzle for science. The third smallest element having a fundamental effect on brain structure, diffusion, and metabolism is remarkable. In this thesis, I have attempted to tackle the problem of an absence of detectable biomarkers of lithium treatment. In the first half of the thesis, I focused on developing novel imaging techniques that allow for the direct detection of lithium-7 in the mouse brain. In the process, I developed a cost-efficient, open-source radiofrequency coil for the detection of lithium-7. The final part of method development in this thesis (chapter 4) focused on describing LCModel fitting and developing an open-source toolbox for simulating spectra from different species. The developed lithium-7 MRI protocol will be used in future studies on genetically modified mice to better understand the non-homogeneous lithium equilibrium distribution in the mouse brain. In the final two chapters of this thesis, I looked for detectable biomarkers of lithium treatment in astrocytes and mice on a lithium-enriched diet. While this thesis does not uncover the mechanism of action of lithium, it does provide insights into the distribution in the mouse brain as well as associated early metabolic and diffusive changes, which may serve as potential biomarkers for lithium treatment.

APPENDIX

Measuring Lithium wash-out:
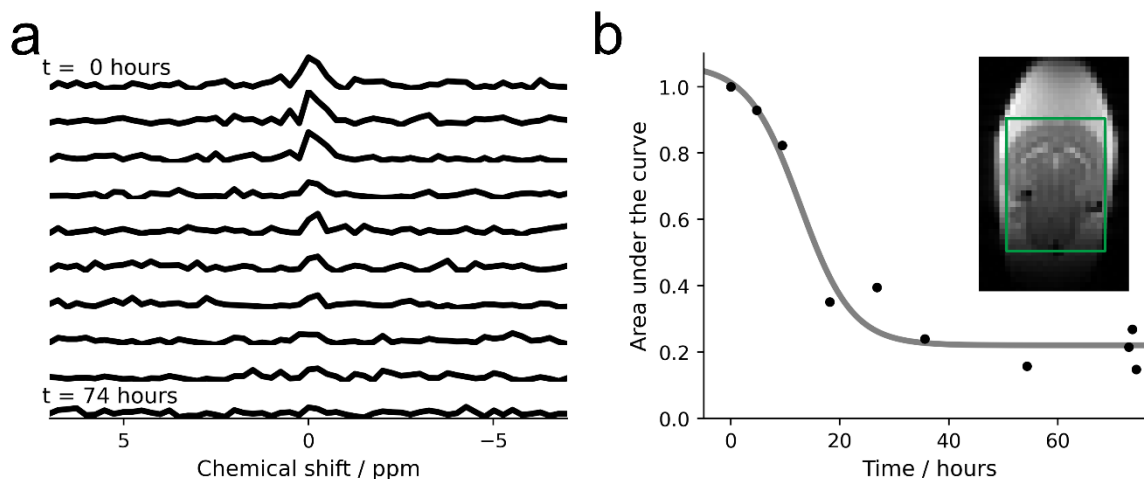
*Figure S-1: **Lithium wash-out after PFA fixation.** (a) Localized (green box in b) ^{7}Li spectra of the isolated brain in PFA solution were continuously acquired over 74 hours. (b) The normalized area under the curve illustrates the lithium wash-out with an inflexion point at 12.7 hours and reaching a steady state after ~27 hours.*

Fitting parameters weekly ^{7}Li spectra:

Table S-1: Fitting parameters of the weekly in vivo ^{7}Li spectra. The fitting parameters of the ^{7}Li spectra of animal 1 and 2 (group 2) are given for each week of treatment. Due to technical problems, no measurements were possible in week 2 of treatment.

Week	Animal 1			Animal 2		
	AUC	Chemical shift / ppm	FWHM / ppm	AUC / a.u.	Chemical shift / ppm	FWHM / ppm
1	4.80	0.13	0.58	3.53	0.15	0.52
2	-	-	-	-	-	-
3	4.63	0.08	0.59	4.01	0.09	0.64
4	4.47	0.10	0.61	3.08	0.12	0.57
5	3.56	0.07	0.59	3.02	0.14	0.54

AUC = area under the curve, FWHM = full-width at half-maximum of the fitted Lorentzian curve

Measuring T1 *in vivo*:
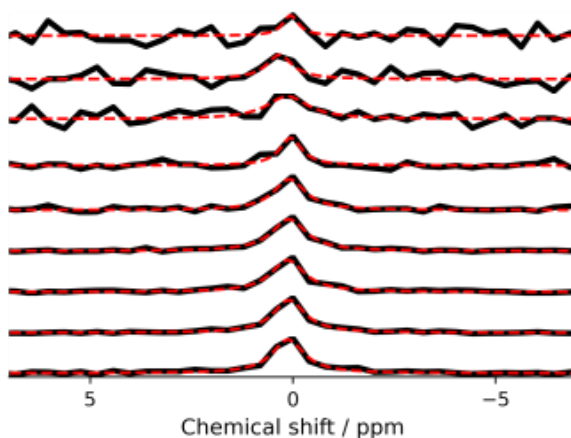
*Figure S-2: **Lorentzian fits of the mean ⁷Li spectra at each TR with the y-axis scaled individually**. The fitting parameters are given in table S2. The ⁷Li spectra of the T1 measurement are plotted using the same y-axis across all repetition times, B. The repetition time increases down the figure.*

Table S-2: In vivo T1 measurement of lithium-7. The fitting parameters of the normalized Lorentzian curves. The area under the curve has been normalized such that the area at TR = 40000 ms is 1. The full-width half-maximum was, as expected, larger in the non-localized spectra than in the localized spectra.

Repetition time / ms	Normalized area under the curve	Chemical shift / ppm	Full-width half-maximum / ppm
250	0.03	0.05	0.46
500	0.08	0.33	0.77
750	0.12	0.13	1.24
1000	0.15	0.05	0.66
2500	0.44	0.08	0.95
5000	0.64	0.09	1.03
10000	0.88	0.12	1.00
20000	0.98	0.09	0.95
40000	1.00	0.12	0.95

SUPPLEMENTARY INFORMATION FOR CHAPTER 4:

Table S-3: The metabolite concentration for key metabolites in mice, rats, marmosets, macaques, and humans are given. The average and standard deviation of the concentration of each metabolite (in mM) is given for each species. Metabolites: Ala: alanine; Asp: aspartate; Cr: creatine; -CrCH2: negative creatine peak; GABA: γ-aminobutyric acid; Glc: glucose; Gln: glutamine; GSH: glutathione; Glu: glutamate; GPC: glycerophosphocholine; Ins: myo-inositol; Lac: lactate; NAA: N-acetylaspartate; NAAG: N-acetylaspartylglutamate; PCh: phosphocholine; PCr: phosphocreatine; Scyllo: scyllo-inositol; Tau: taurine.

Metabolite	Mouse	Rat	Marmoset	Macaque	Human
Ala	0.79±0.25	0.43±0.14	0.41±0.38	0.02±0.03	0.02±0.03
Asp	3.61±0.50	3.09±0.28	4.18±0.79	1.88±0.65	1.36±0.33
Cr	8.58±0.53	4.82±1.45	6.59±2.48	3.17±0.49	2.90±0.17
-CrCH2	3.20±0.50	1.55±0.39	1.78±0.55	0.02±0.05	0.04±0.10
GABA	1.58±0.18	0.93±0.25	1.17±0.29	1.74±0.50	1.99±0.20
Glc	8.56±0.92	2.47±0.56	0.80±0.73	1.10±0.68	0.74±0.38
Gln	4.39±0.51	3.24±0.28	3.96±0.51	2.47±0.51	0.95±0.14
GSH	0.95±0.19	0.79±0.23	1.30±0.37	2.57±0.24	1.66±0.20
Glu	8.75±0.56	10.23±0.41	9.98±0.76	10.14±0.78	7.62±0.57
GPC	1.21±0.20	0.83±0.05	1.00±0.26	1.04±0.25	1.02±0.27
Ins	2.60±0.64	2.86±0.30	6.55±0.77	6.40±0.47	4.45±0.37
Lac	0.01±0.02	0.00±0.00	0.03±0.05	0.07±0.12	0.38±0.16
NAA	8.47±0.52	8.74±0.39	9.25±0.33	8.28±0.51	9.16±0.58
NAAG	0.17±0.15	0.0±0.0	0.42±0.30	1.04±0.44	1.03±0.21
PCh	1.23±0.15	0.71±0.15	0.75±0.40	0.09±0.22	0.09±0.21
PCr	1.67±0.63	1.95±0.59	1.83±0.44	5.51±0.43	3.67±0.34
Scyllo	0.01±0.01	0.0±0.0	0.18±0.06	0.23±0.06	0.11±0.06
Tau	9.38±0.41	3.27±0.53	2.62±0.30	0.65±0.13	0.95±0.10

Table S-4: One-way ANOVA tests (species) were performed for eight metabolites that differed between the five species. Post-hoc testing was performed at a significance of p=0.05 with multiple comparisons corrections (n=10). Significant differences are shown in bold. Metabolites: Ins: myo-inositol; tNAA: total N-acetylaspartate; Tau: taurine; GPC+PCh: glycerophosphocholine plus phosphocholine; GABA: γ-aminobutyric acid; Glu+Gln: glutamate plus glutamine; Glc: glucose; tCr: total creatine.

Species		Ins (F=72.8, p<0.001)		tNAA (F=12.2, p<0.001)	
		t-statistic	p-value	t-statistic	p-value
mouse	rat	-0.9	1	-0.4	1
mouse	marmoset	-9.7	**<0.0001**	-3.9	**0.002**
mouse	macaque	-11.7	**<0.0001**	-3.3	0.01
mouse	human	-6.1	**0.0001**	-5	**0.0003**
rat	marmoset	-11	**<0.0001**	-3.7	**0.003**
rat	macaque	-15.4	**<0.0001**	-3	0.01
rat	human	-8.1	**<0.0001**	-4.8	**0.0004**
marmoset	macaque	0.4	1	1.5	1
marmoset	human	6	**0.0001**	-1.6	1
macaque	human	7.9	**<0.0001**	-3.1	0.01
		Tau (F=661.7, p<0.001)		**GPC + PCh (F=119.8, p<0.001)**	
		t-statistic	p-value	t-statistic	p-value
mouse	rat	22.3	**<0.0001**	13.3	**<0.0001**
mouse	marmoset	32.7	**<0.0001**	7.8	**<0.0001**
mouse	macaque	50.1	**<0.0001**	21.5	**<0.0001**
mouse	human	49.4	**<0.0001**	20.8	**<0.0001**
rat	marmoset	2.6	0.02	-2.6	0.02
rat	macaque	11.7	**<0.0001**	7.2	**<0.0001**
rat	human	10.5	**<0.0001**	7.1	**<0.0001**
marmoset	macaque	14.7	**<0.0001**	7.8	**<0.0001**
marmoset	human	12.9	**<0.0001**	7.8	**<0.0001**
macaque	human	-4.6	**0.0006**	0.3	1
		GABA (F=11.9, p<0.001)		**Glu + Gln (F=44.3, p<0.001)**	
		t-statistic	p-value	t-statistic	p-value
mouse	rat	5.2	**0.0002**	-1.2	1
mouse	marmoset	3	0.01	-1.8	0.09
mouse	macaque	-0.8	1	1	1
mouse	human	-3.8	**0.003**	13.6	**<0.0001**
rat	marmoset	-1.5	1	-1.1	1
rat	macaque	-3.6	**0.004**	1.7	1
rat	human	-8.2	**<0.0001**	15.1	**<0.0001**
marmoset	macaque	-2.4	0.03	2.2	0.05
marmoset	human	-5.8	**0.0001**	11.5	**<0.0001**
macaque	human	-1.1	1	7.4	**<0.0001**
		Glc (F=144.5, p<0.001)		**tCr (F=109.3, p<0.001)**	
		t-statistic	p-value	t-statistic	p-value
mouse	rat	13.8	**<0.0001**	8.9	**<0.0001**
mouse	marmoset	16.2	**<0.0001**	1.1	1
mouse	macaque	16	**<0.0001**	7.1	**<0.0001**
mouse	human	19.2	**<0.0001**	16.2	**<0.0001**
rat	marmoset	4.4	**0.0008**	-9.5	**<0.0001**
rat	macaque	3.8	**0.003**	-2.1	0.05
rat	human	6.2	**<0.0001**	9.4	**<0.0001**
marmoset	macaque	-0.8	1	7.4	**<0.0001**
marmoset	human	0.2	1	18.5	**<0.0001**
macaque	human	1.1	1	11.4	**<0.0001**

SUPPLEMENTARY INFORMATION FOR CHAPTER 5:

ANOVA analysis results are shown for the nine metabolites discussed in chapter 5. Post-hoc testing was performed on all spectra within each group and multiple comparisons corrected for number of tests, n=6.

Ethanol (F(3,25)=2.4, p=0.09)

Medium		t-statistic	p-value
Normal	Mg	-5.2	**<0.0001**
Normal	Low Li	-10.1	**<0.0001**
Normal	High Li	-4.5	**0.0001**
Mg	Low Li	-5.6	**<0.0001**
Mg	High Li	-3.0	**0.02**
Low Li	High Li	-1.2	1

Myo-inositol (F(3,25)=3.1, p=0.04)

Medium		t-statistic	p-value
Normal	Mg	1.8	0.45
Normal	Low Li	4.4	**0.0002**
Normal	High Li	-0.02	1
Mg	Low Li	4.6	**<0.0001**
Mg	High Li	-1.9	0.38
Low Li	High Li	-4.6	**0.0001**

Glycine (F(3,25)=5.2, p=0.007)

Medium		t-statistic	p-value
Normal	Mg	-4.9	**<0.0001**
Normal	Low Li	-4.2	**0.0003**
Normal	High Li	-7.3	**<0.0001**
Mg	Low Li	0.4	1
Mg	High Li	-2.6	0.06
Low Li	High Li	-2.8	**0.04**

Phosphocreatine (F(3,25)=8.3, p=0.0005)

Medium		t-statistic	p-value
Normal	Mg	1.0	1
Normal	Low Li	5.6	**<0.0001**
Normal	High Li	-2.7	0.06
Mg	Low Li	5.0	**<0.0001**
Mg	High Li	-3.8	**0.002**
Low Li	High Li	-8.2	**<0.0001**

Glutamate (F(3,25)=6.1, p=0.003)

Medium		t-statistic	p-value
Normal	Mg	0.5	1
Normal	Low Li	7.1	**<0.0001**
Normal	High Li	-4.0	**0.0006**
Mg	Low Li	7.3	**<0.0001**
Mg	High Li	-4.3	**0.0003**
Low Li	High Li	-8.2	**<0.0001**

Glutamine (F(3,25)=1.7, p=0.20)

Medium		t-statistic	p-value
Normal	Mg	2.6	0.07
Normal	Low Li	2.7	**0.04**
Normal	High Li	6.0	**<0.001**
Mg	Low Li	1.0	1
Mg	High Li	3.2	**0.01**
Low Li	High Li	1.0	1

Glutamate + Glutamine (F(3,25)=4.6, p=0.01)

Medium		t-statistic	p-value
Normal	Mg	3.0	**0.02**
Normal	Low Li	7.3	**<0.0001**
Normal	High Li	-0.4	1
Mg	Low Li	5.1	**<0.0001**
Mg	High Li	-2.5	0.09
Low Li	High Li	-5.6	**<0.0001**

Lactate (F(3,25)=1.6, p=0.21)

Medium		t-statistic	p-value
Normal	Mg	0.7	1
Normal	Low Li	1.3	1
Normal	High Li	-4.3	**0.0003**
Mg	Low Li	0.8	1
Mg	High Li	-5.3	**<0.0001**
Low Li	High Li	-4.4	**0.0002**

Glucose (F(3,25)=3.3, p=0.04)

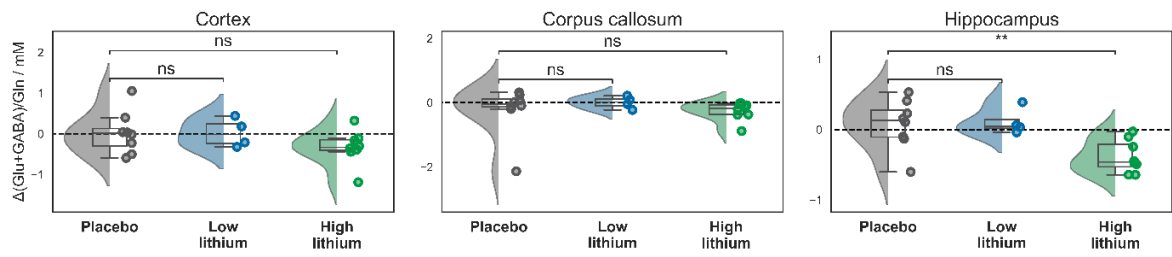| Medium		t-statistic	p-value
Normal	Mg	-2.9	0.02
Normal	Low Li	0.6	1
Normal	High Li	-5.4	<0.0001
Mg	Low Li	4.2	0.0004
Mg	High Li	-3.5	0.005
Low Li	High Li	-6.9	<0.0001

SUPPLEMENTARY INFORMATION FOR CHAPTER 6:

Figure S-3: ***Hippocampal (Glu+GABA)/Gln decreased in mice on a high lithium diet.*** *Decreased (Glu+GABA)/Gln may be interpreted as an indication of higher astrocyte activity or a change in cell population.*

REFERENCES

1. Schioldann, J., and Berrios, G. (2020). 'Insanity in Classical Antiquity', by JL Heiberg (1913). History of Psychiatry.

2. Sani, G., Kotzalidis, G., and Girardi, P. (2017). EDITORIAL: "The Faces of Mania: The Legacy of Athanasios Koukopoulos." CN *15*, 334–337. 10.2174/1570159X1503170228185225.

3. Gerdtz, J. (1994). Mental Illness and the Roman Physician: The Legacy of Soranus of Ephesus. PS *45*, 485–487. 10.1176/ps.45.5.485.

4. Berzelius, J.J. (1817). Ein neue mineralische's Alkali und ein neues Metall. Journal für Chemie und Physik *21*, 44–48.

5. Lange, C. (1895). Om periodiske Depressionstilstande og deres Patogenese : Foredrag holdt i Medicinsk Selskab den 19. Januar 1886 2nd ed. (Jacob Lund).

6. Lange, F. (1894). De vigtigste Sindssygdomsgrupper i kort Omrids. (Gyldendalske Boghandels Forlag).

7. Schou, M. (1992). The first psychiatric use of lithium. Br J Psychiatry *161*, 279–280. 10.1192/bjp.161.2.279.

8. Cade, J.F.J. (1949). Lithium salts in the treatment of psychotic excitement. The Medical journal of Australia *2*, 349–352. 10.1080/j.1440-1614.1999.06241.x.

9. Nolen, W.A., Licht, R.W., Young, A.H., Malhi, G.S., Tohen, M., Vieta, E., Kupka, R.W., Zarate, C., Nielsen, R.E., Baldessarini, R.J., et al. (2019). What is the optimal serum level for lithium in the maintenance treatment of bipolar disorder? A systematic review and recommendations from the ISBD/IGSLI Task Force on treatment with lithium. Bipolar Disorders *21*, 394–409. 10.1111/bdi.12805.

10. Sköld, M., Rolstad, S., Joas, E., Kardell, M., Pålsson, E., Goodwin, G.M., and Landén, M. (2021). Regional lithium prescription rates and recurrence in bipolar disorder. Int J Bipolar Disord *9*, 18. 10.1186/s40345-021-00223-7.

11. Kasper, S. (2003). Issues in the treatment of bipolar disorder. European Neuropsychopharmacology *13*, 37–42. 10.1016/S0924-977X(03)00076-2.

12. Oswald, P., Souery, D., Kasper, S., Lecrubier, Y., Montgomery, S., Wyckaert, S., Zohar, J., and Mendlewicz, J. (2007). Current issues in bipolar disorder: A critical review. European Neuropsychopharmacology *17*, 687–695. 10.1016/j.euroneuro.2007.03.006.

13. Clothier, J., Swann, A.C., and Freeman, T. (1992). Dysphoric Mania. Journal of Clinical Psychopharmacology *12*.

14. Grande, I., Berk, M., Birmaher, B., and Vieta, E. (2016). Bipolar disorder. The Lancet *387*, 1561–1572. 10.1016/S0140-6736(15)00241-X.

15. Alonso, J., Petukhova, M., Vilagut, G., Chatterji, S., Heeringa, S., Üstün, T.B., Alhamzawi, A.O., Viana, M.C., Angermeyer, M., Bromet, E., et al. (2011). Days out of role due to common physical and mental conditions: results from the WHO World Mental Health surveys. Molecular Psychiatry *16*, 1234–1246. 10.1038/mp.2010.101.

References

16. Grunze, H. (2015). Bipolar Disorder. In Neurobiology of Brain Disorders, pp. 655–673. 10.1016/b978-0-12-398270-4.00040-9.

17. Merikangas, K.R., Jin, R., He, J.-P., Kessler, R.C., Lee, S., Sampson, N.A., Viana, M.C., Andrade, L.H., Hu, C., Karam, E.G., et al. (2011). Prevalence and Correlates of Bipolar Spectrum Disorder in the World Mental Health Survey Initiative. Arch Gen Psychiatry *68*, 241. 10.1001/archgenpsychiatry.2011.12.

18. Ekman, M., Granström, O., Omérov, S., Jacob, J., and Landén, M. (2013). The societal cost of bipolar disorder in Sweden. Soc Psychiatry Psychiatr Epidemiol *48*, 1601–1610. 10.1007/s00127-013-0724-9.

19. Statistisches Bundesamt (2020). Krankheitskosten: Deutschland (ICD-10). https://www-genesis.destatis.de/ https://www-genesis.destatis.de/.

20. Alda, M. (2015). Lithium in the treatment of bipolar disorder: pharmacology and pharmacogenetics. Mol Psychiatry *20*, 661–670. 10.1038/mp.2015.4.

21. Alda, M. (2017). Who are excellent lithium responders and why do they matter? World Psychiatry *16*, 319–320. 10.1002/wps.20462.

22. Alsady, M., Baumgarten, R., Deen, P.M.T., and de Groot, T. (2016). Lithium in the Kidney: Friend and Foe? Journal of the American Society of Nephrology *27*, 1587–1595. 10.1681/ASN.2015080907.

23. Bockenhauer, D., and Bichet, D.G. (2015). Pathophysiology, diagnosis and management of nephrogenic diabetes insipidus. Nat Rev Nephrol *11*, 576–588. 10.1038/nrneph.2015.89.

24. Chokhawala, K., Lee, S., and Saadabadi, A. (2022). Lithium. In StatPearls (StatPearls Publishing).

25. Provencher, S.W. (1993). Estimation of metabolite concentrations from localized in vivo proton NMR spectra. Magnetic Resonance in Medicine *30*, 672–679. 10.1002/mrm.1910300604.

26. Frahm, J., Merboldt, K.-D., and Hänicke, W. (1987). Localized proton spectroscopy using stimulated echoes. Journal of Magnetic Resonance (1969) *72*, 502–508. 10.1016/0022-2364(87)90154-5.

27. Bottomley, P.A. (1987). Spatial Localization in NMR Spectroscopy in Vivo. Annals of the New York Academy of Sciences *508*, 333–348. 10.1111/j.1749-6632.1987.tb32915.x.

28. Moonen, C.T.W., Kienlin, M.V., Van Zijl, P.C.M., Cohen, J., Gillen, J., Daly, P., and Wolf, G. (1989). Comparison of single-shot localization methods (steam and press) for In vivo proton NMR spectroscopy. NMR in Biomedicine *2*, 201–208. 10.1002/nbm.1940020506.

29. Ernst, T., Kreis, R., and Ross, B.D. (1993). Absolute Quantitation of Water and Metabolites in the Human Brain. I. Compartments and Water. Journal of Magnetic Resonance, Series B *102*, 1–8. 10.1006/jmrb.1993.1055.

30. Frahm, J., Bruhn, H., Gyngell, M.L., Merboldt, K.D., Hänicke, W., and Sauter, R. (1989). Localized high-resolution proton NMR spectroscopy using stimulated echoes: Initial

applications to human brainin vivo. Magn. Reson. Med. *9*, 79–93. 10.1002/mrm.1910090110.

31. Haase, A., Frahm, J., Hanicke, W., and Matthaei, D. (1985). ^{1}H NMR chemical shift selective (CHESS) imaging. Phys. Med. Biol. *30*, 341–344. 10.1088/0031-9155/30/4/008.

32. Ordidge, R.J., Connelly, A., and Lohman, J.A.B. (1986). Image-selected in Vivo spectroscopy (ISIS). A new technique for spatially selective nmr spectroscopy. Journal of Magnetic Resonance *66*, 283–294. 10.1016/0022-2364(86)90031-4.

33. Wolff, S.D., and Balaban, R.S. (1989). Magnetization transfer contrast (MTC) and tissue water proton relaxation in vivo. Magnetic Resonance in Med *10*, 135–144. 10.1002/mrm.1910100113.

34. Basser, P.J., Mattiello, J., and LeBihan, D. (1994). MR diffusion tensor spectroscopy and imaging. Biophysical Journal *66*, 259–267. 10.1016/S0006-3495(94)80775-1.

35. Basser, P.J., Mattiello, J., and Lebihan, D. (1994). Estimation of the Effective Self-Diffusion Tensor from the NMR Spin Echo. Journal of Magnetic Resonance, Series B *103*, 247–254. 10.1006/jmrb.1994.1037.

36. Zhang, H., Schneider, T., Wheeler-Kingshott, C.A., and Alexander, D.C. (2012). NODDI: Practical in vivo neurite orientation dispersion and density imaging of the human brain. NeuroImage *61*, 1000–1016. 10.1016/j.neuroimage.2012.03.072.

37. Stejskal, E.O., and Tanner, J.E. (1965). Spin Diffusion Measurements: Spin Echoes in the Presence of a Time-Dependent Field Gradient. The Journal of Chemical Physics *42*, 288–292. 10.1063/1.1695690.

38. Basser, P.J., and Pierpaoli, C. (1996). Microstructural and Physiological Features of Tissues Elucidated by Quantitative-Diffusion-Tensor MRI. Journal of Magnetic Resonance, Series B *111*, 209–219. 10.1006/jmrb.1996.0086.

39. Tariq, M., Schneider, T., Alexander, D.C., Gandini Wheeler-Kingshott, C.A., and Zhang, H. (2016). Bingham–NODDI: Mapping anisotropic orientation dispersion of neurites using diffusion MRI. NeuroImage *133*, 207–223. 10.1016/j.neuroimage.2016.01.046.

40. Renshaw, P.F. (1987). A diffusional contribution to lithium isotope effects. Biological Psychiatry *22*, 73–78. 10.1016/0006-3223(87)90132-6.

41. Lieberman, K.W., Alexander, G.J., and Stokes, P. (1979). Dissimilar effects of lithium isotopes on motility in rats. Pharmacology Biochemistry and Behavior *10*, 933–935. 10.1016/0091-3057(79)90070-4.

42. Sechzer, J.A., Lieberman, K.W., Alexander, G.J., Weidman, D., and Stokes, P.E. (1986). Aberrant parenting and delayed offspring development in rats exposed to lithium. Biological Psychiatry *21*, 1258–1266. https://doi.org/10.1016/0006-3223(86)90308-2.

43. Alexander, G.J., Lieberman, K.W., Okamoto, M., Stokes, P.E., and Triana, E. (1982). Lithium toxicology: Effect of isotopic composition on lethality and behavior. Pharmacology Biochemistry and Behavior *16*, 801–804. 10.1016/0091-3057(82)90238-6.

References

44. Sherman, W.R., Munsell, L.Y., and Wong, Y.-H.H. (1984). Differential Uptake of Lithium Isotopes by Rat Cerebral Cortex and Its Effect on Inositol Phosphate Metabolism. J Neurochem *42*, 880–882. 10.1111/j.1471-4159.1984.tb02765.x.

45. Yatham, L.N., Kennedy, S.H., Parikh, S.V., Schaffer, A., Bond, D.J., Frey, B.N., Sharma, V., Goldstein, B.I., Rej, S., Beaulieu, S., et al. (2018). Canadian Network for Mood and Anxiety Treatments (CANMAT) and International Society for Bipolar Disorders (ISBD) 2018 guidelines for the management of patients with bipolar disorder. Bipolar Disorders *20*, 97–170. 10.1111/bdi.12609.

46. Malhi, G.S., Tanious, M., Das, P., Coulston, C.M., and Berk, M. (2013). Potential Mechanisms of Action of Lithium in Bipolar Disorder. CNS Drugs *27*, 135–153. 10.1007/s40263-013-0039-0.

47. Michael, N., Erfurth, A., Ohrmann, P., Gössling, M., Arolt, V., Heindel, W., and Pfleiderer, B. (2003). Acute mania is accompanied by elevated glutamate/glutamine levels within the left dorsolateral prefrontal cortex. Psychopharmacology *168*, 344–346. 10.1007/s00213-003-1440-z.

48. Nonaka, S., Hough, C.J., and Chuang, D.-M. (1998). Chronic lithium treatment robustly protects neurons in the central nervous system against excitotoxicity by inhibiting N-methyl-d-aspartate receptor-mediated calcium influx. Proc. Natl. Acad. Sci. U.S.A. *95*, 2642–2647. 10.1073/pnas.95.5.2642.

49. Dixon, J.F., and Hokin, L.E. (1998). Lithium acutely inhibits and chronically up-regulates and stabilizes glutamate uptake by presynaptic nerve endings in mouse cerebral cortex. Proceedings of the National Academy of Sciences of the United States of America *95*, 8363–8368. 10.1073/pnas.95.14.8363.

50. Hashimoto, R., Hough, C., Nakazawa, T., Yamamoto, T., and Chuang, D. (2002). Lithium protection against glutamate excitotoxicity in rat cerebral cortical neurons: involvement of NMDA receptor inhibition possibly by decreasing NR2B tyrosine phosphorylation. Journal of Neurochemistry *80*, 589–597. 10.1046/j.0022-3042.2001.00728.x.

51. Zanetti, M.V., Otaduy, M.C., de Sousa, R.T., Gattaz, W.F., Busatto, G.F., Leite, C.C., and Machado-Vieira, R. (2015). Bimodal Effect of Lithium Plasma Levels on Hippocampal Glutamate Concentrations in Bipolar II Depression: A Pilot Study. International Journal of Neuropsychopharmacology *18*. 10.1093/ijnp/pyu058.

52. Ghasemi, M., and Dehpour, A.R. (2011). The NMDA receptor/nitric oxide pathway: a target for the therapeutic and toxic effects of lithium. Trends in Pharmacological Sciences *32*, 420–434. 10.1016/j.tips.2011.03.006.

53. Berk, M., Dodd, S., Kauer-Sant'Anna, M., Malhi, G.S., Bourin, M., Kapczinski, F., and Norman, T. (2007). Dopamine dysregulation syndrome: implications for a dopamine hypothesis of bipolar disorder. Acta Psychiatr Scand *116*, 41–49. 10.1111/j.1600-0447.2007.01058.x.

54. Ferrie, L., Young, A.H., and McQuade, R. (2005). Effect of chronic lithium and withdrawal from chronic lithium on presynaptic dopamine function in the rat. J Psychopharmacol *19*, 229–234. 10.1177/0269881105051525.

55. Gambarana, C., Ghiglieri, O., Masi, F., Scheggi, S., Tagliamonte, A., and De Montis, M.G. (1999). The effects of long-term administration of rubidium or lithium on reactivity

to stress and on dopamine output in the nucleus accumbens in rats. Brain Research *826*, 200–209. 10.1016/S0006-8993(99)01286-X.

56. Wegener, G., Bandpey, Z., Heiberg, I.L., Mørk, A., and Rosenberg, R. (2003). Increased extracellular serotonin level in rat hippocampus induced by chronic citalopram is augmented by subchronic lithium: neurochemical and behavioural studies in the rat. Psychopharmacology *166*, 188–194. 10.1007/s00213-002-1341-6.

57. Hide, I., and Yamawaki, S. (1989). Inactivation of presynaptic 5-HT autoreceptors by lithium in rat hippocampus. Neuroscience Letters *107*, 323–326. 10.1016/0304-3940(89)90839-2.

58. Antonelli, T., Ferioli, V., Lo Gallo, G., Tomasini, M.C., Fernandez, M., O'Connor, W.T., Glennon, J.C., Tanganelli, S., and Ferraro, L. (2000). Differential effects of acute and short-term lithium administration on dialysate glutamate and GABA levels in the frontal cortex of the conscious rat. Synapse *38*, 355–362. 10.1002/1098-2396(20001201)38:3<355::AID-SYN15>3.0.CO;2-E.

59. Vargas, C., Tannhauser, M., and Barros, H.M.T. (1998). Dissimilar Effects of Lithium and Valproic Acid on GABA and Glutamine Concentrations in Rat Cerebrospinal Fluid. General Pharmacology: The Vascular System *30*, 601–604. 10.1016/S0306-3623(97)00328-5.

60. Ahluwalia, P., Grewaal, D.S., and Singhal, R.L. (1981). Brain gabaergic and dopaminergic systems following lithium treatment and withdrawal. Progress in Neuro-Psychopharmacology *5*, 527–530. 10.1016/0364-7722(81)90040-0.

61. Harwood, A.J. (2005). Lithium and bipolar mood disorder: the inositol-depletion hypothesis revisited. Mol Psychiatry *10*, 117–126. 10.1038/sj.mp.4001618.

62. Kolczynska, K., Loza-Valdes, A., Hawro, I., and Sumara, G. (2020). Diacylglycerol-evoked activation of PKC and PKD isoforms in regulation of glucose and lipid metabolism: a review. Lipids Health Dis *19*, 113. 10.1186/s12944-020-01286-8.

63. Goode, N., Hughes, K., Woodgett, J.R., and Parker, P.J. (1992). Differential regulation of glycogen synthase kinase-3 beta by protein kinase C isotypes. Journal of Biological Chemistry *267*, 16878–16882. 10.1016/S0021-9258(18)41866-2.

64. Pandey, M.K., and DeGrado, T.R. (2016). Glycogen Synthase Kinase-3 (GSK-3)-Targeted Therapy and Imaging. Theranostics *6*, 571–593. 10.7150/thno.14334.

65. Dudev, T., and Lim, C. (2011). Competition between Li+ and Mg2+ in metalloproteins. Implications for lithium therapy. Journal of the American Chemical Society *133*, 9506–9515. 10.1021/ja201985s.

66. Allison, J.H., and Stewart, M.A. (1971). Reduced Brain Inositol in Lithium-treated Rats. Nature New Biology *233*, 267–268. 10.1038/newbio233267a0.

67. Allison, J.H., Blisner, M.E., Holland, W.H., Hipps, P.P., and Sherman, W.R. (1976). Increased brain myo-inositol 1-phosphate in lithium-treated rats. Biochemical and Biophysical Research Communications *71*, 664–670. 10.1016/0006-291X(76)90839-1.

68. Brambilla, P., Stanley, J.A., Sassi, R.B., Nicoletti, M.A., Mallinger, A.G., Keshavan, M.S., and Soares, J.C. (2004). 1H MRS Study of Dorsolateral Prefrontal Cortex in Healthy Individuals before and after Lithium Administration. Neuropsychopharmacol *29*, 1918–1924. 10.1038/sj.npp.1300520.

References

69. Silverstone, P.H., Rotzinger, S., Pukhovsky, A., and Hanstock, C.C. (1999). Effects of lithium and amphetamine on inositol metabolism in the human brain as measured by 1H and 31P MRS. Biological Psychiatry *46*, 1634–1641. 10.1016/S0006-3223(99)00076-1.

70. Silverstone, P.H., Hanstock, C.C., Fabian, J., Staab, R., and Allen, P.S. (1996). Chronic lithium does not alter human myo-inositol or phosphomonoester concentrations as measured by 1H and 31P MRS. Biological Psychiatry *40*, 235–246. 10.1016/0006-3223(95)00382-7.

71. Shibuya-Tayoshi, S., Tayoshi, S., Sumitani, S., Ueno, S., Harada, M., and Ohmori, T. (2008). Lithium effects on brain glutamatergic and GABAergic systems of healthy volunteers as measured by proton magnetic resonance spectroscopy. Progress in Neuro-Psychopharmacology and Biological Psychiatry *32*, 249–256. 10.1016/j.pnpbp.2007.08.015.

72. Manji, H.K., Etcheberrigaray, R., Chen, G., and Olds, J.L. (1993). Lithium Decreases Membrane-Associated Protein Kinase C in Hippocampus: Selectivity for the α Isozyme. Journal of Neurochemistry *61*, 2303–2310. 10.1111/j.1471-4159.1993.tb07474.x.

73. Manji, H.K., and Chen, G. (2002). PKC, MAP kinases and the bcl-2 family of proteins as long-term targets for mood stabilizers. Mol Psychiatry *7*, S46–S56. 10.1038/sj.mp.4001018.

74. Klein, P.S., and Melton, D.A. (1996). A molecular mechanism for the effect of lithium on development. Proceedings of the National Academy of Sciences of the United States of America *93*, 8455–8459. 10.1073/pnas.93.16.8455.

75. Tajes, M., Yeste-Velasco, M., Zhu, X., Chou, S.P., Smith, M.A., Pallàs, M., Camins, A., and Casadesús, G. (2009). Activation of Akt by lithium: Pro-survival pathways in aging. Mechanisms of Ageing and Development *130*, 253–261. 10.1016/j.mad.2008.12.006.

76. Sarkar, S., Krishna, G., Imarisio, S., Saiki, S., O'Kane, C.J., and Rubinsztein, D.C. (2008). A rational mechanism for combination treatment of Huntington's disease using lithium and rapamycin. Human Molecular Genetics *17*, 170–178. 10.1093/hmg/ddm294.

77. Böer, U., Eglins, J., Krause, D., Schnell, S., Schöfl, C., and Knepel, W. (2007). Enhancement by lithium of cAMP-induced CRE/CREB-directed gene transcription conferred by TORC on the CREB basic leucine zipper domain. Biochemical Journal *408*, 69–77. 10.1042/BJ20070796.

78. Quiroz, J.A., Machado-Vieira, R., Zarate, Jr., C.A., and Manji, H.K. (2010). Novel Insights into Lithium's Mechanism of Action: Neurotrophic and Neuroprotective Effects. Neuropsychobiology *62*, 50–60. 10.1159/000314310.

79. Huang, E.J., and Reichardt, L.F. (2001). Neurotrophins: Roles in Neuronal Development and Function. Annu. Rev. Neurosci. *24*, 677–736. 10.1146/annurev.neuro.24.1.677.

80. Miranda, M., Morici, J.F., Zanoni, M.B., and Bekinschtein, P. (2019). Brain-Derived Neurotrophic Factor: A Key Molecule for Memory in the Healthy and the Pathological Brain. Front. Cell. Neurosci. *13*, 363. 10.3389/fncel.2019.00363.

81. Chiou, Y.-J., and Huang, T.-L. (2019). Brain-derived neurotrophic factor (BDNF) and bipolar disorder. Psychiatry Research *274*, 395–399. 10.1016/j.psychres.2019.02.051.

References

82. Grande, I., Fries, G.R., Kunz, M., and Kapczinski, F. (2010). The Role of BDNF as a Mediator of Neuroplasticity in Bipolar Disorder. Psychiatry Investig *7*, 243. 10.4306/pi.2010.7.4.243.

83. Post, R.M. (2007). Role of BDNF in bipolar and unipolar disorder: Clinical and theoretical implications. Journal of Psychiatric Research *41*, 979–990. 10.1016/j.jpsychires.2006.09.009.

84. Schmidt, H.D., Banasr, M., and Duman, R.S. (2008). Future antidepressant targets: neurotrophic factors and related signaling cascades. Drug Discovery Today: Therapeutic Strategies *5*, 151–156. 10.1016/j.ddstr.2008.10.003.

85. Vaux, D.L., Cory, S., and Adams, J.M. (1988). Bcl-2 gene promotes haemopoietic cell survival and cooperates with c-myc to immortalize pre-B cells. Nature *335*, 440–442. 10.1038/335440a0.

86. Tsujimoto, Y. (1989). Overexpression of the human BCL-2 gene product results in growth enhancement of Epstein-Barr virus-immortalized B cells. Proc. Natl. Acad. Sci. U.S.A. *86*, 1958–1962. 10.1073/pnas.86.6.1958.

87. Hardwick, J.M., and Soane, L. (2013). Multiple Functions of BCL-2 Family Proteins. Cold Spring Harbor Perspectives in Biology *5*, a008722–a008722. 10.1101/cshperspect.a008722.

88. Karlnoski, R., Wilcock, D., Dickey, C., Ronan, V., Gordon, M.N., Zhang, W., Morgan, D., and Taglialatela, G. (2007). Up-regulation of Bcl-2 in APP transgenic mice is associated with neuroprotection. Neurobiology of Disease *25*, 179–188. 10.1016/j.nbd.2006.09.007.

89. Offen, D., Beart, P.M., Cheung, N.S., Pascoe, C.J., Hochman, A., Gorodin, S., Melamed, E., Bernard, R., and Bernard, O. (1998). Transgenic mice expressing human Bcl-2 in their neurons are resistant to 6-hydroxydopamine and 1-methyl-4-phenyl-1,2,3,6- tetrahydropyridine neurotoxicity. Proc. Natl. Acad. Sci. U.S.A. *95*, 5789–5794. 10.1073/pnas.95.10.5789.

90. Moore, G.J., Bebchuk, J.M., Hasanat, K., Chen, G., Seraji-Bozorgzad, N., Wilds, I.B., Faulk, M.W., Koch, S., Glitz, D.A., Jolkovsky, L., et al. (2000). Lithium increases N-acetyl-aspartate in the human brain: In vivo evidence in support of bcl-2's neurotrophic effects? Biological Psychiatry *48*, 1–8. 10.1016/S0006-3223(00)00252-3.

91. Silverstone, P.H., Wu, R.H., O'Donnell, T., Ulrich, M., Asghar, S.J., and Hanstock, C.C. (2003). Chronic treatment with lithium, but not sodium valproate, increases cortical N-acetyl-aspartate concentrations in euthymic bipolar patients: International Clinical Psychopharmacology *18*, 73–79. 10.1097/00004850-200303000-00002.

92. Sassi, R.B., Brambilla, P., Hatch, J.P., Nicoletti, M.A., Mallinger, A.G., Frank, E., Kupfer, D.J., Keshavan, M.S., and Soares, J.C. (2004). Reduced left anterior cingulate volumes in untreated bipolar patients. Biological Psychiatry *56*, 467–475. 10.1016/j.biopsych.2004.07.005.

93. Bearden, C.E., Thompson, P.M., Dalwani, M., Hayashi, K.M., Lee, A.D., Nicoletti, M., Trakhtenbroit, M., Glahn, D.C., Brambilla, P., Sassi, R.B., et al. (2007). Greater Cortical Gray Matter Density in Lithium-Treated Patients with Bipolar Disorder. Biological Psychiatry *62*, 7–16. 10.1016/j.biopsych.2006.10.027.

References

94. Assadi, M., Janson, C., Wang, D.-J., Goldfarb, O., Suri, N., Bilaniuk, L., and Leone, P. (2010). Lithium citrate reduces excessive intra-cerebral N-acetyl aspartate in Canavan disease. European Journal of Paediatric Neurology *14*, 354–359. 10.1016/j.ejpn.2009.11.006.

95. Hallcher, L.M., and Sherman, W.R. (1980). The effects of lithium ion and other agents on the activity of myo-inositol-1-phosphatase from bovine brain. Journal of Biological Chemistry *255*, 10896–10901. 10.1016/S0021-9258(19)70391-3.

96. O'Donnell, T., Rotzinger, S., Nakashima, T.T., Hanstock, C.C., Ulrich, M., and Silverstone, P.H. (2000). Chronic lithium and sodium valproate both decrease the concentration of myo-inositol and increase the concentration of inositol monophosphates in rat brain. Brain Research *880*, 84–91. 10.1016/S0006-8993(00)02797-9.

97. Machado-Vieira, R., Gattaz, W.F., Zanetti, M.V., De Sousa, R.T., Carvalho, A.F., Soeiro-de-Souza, M.G., Leite, C.C., and Otaduy, M.C. (2015). A Longitudinal (6-week) 3T 1H-MRS Study on the Effects of Lithium Treatment on Anterior Cingulate Cortex Metabolites in Bipolar Depression. European Neuropsychopharmacology *25*, 2311–2317. 10.1016/j.euroneuro.2015.08.023.

98. Kato, T., Hamakawa, H., Shioiri, T., Murashita, J., Takahashi, Y., Takahashi, S., and Inubushi, T. (1996). Choline-containing compounds detected by proton magnetic resonance spectroscopy in the basal ganglia in bipolar disorder. J Psychiatry Neurosci *21*, 248–254.

99. Brambilla, P., Stanley, J.A., Nicoletti, M.A., Sassi, R.B., Mallinger, A.G., Frank, E., Kupfer, D., Keshavan, M.S., and Soares, J.C. (2005). 1H magnetic resonance spectroscopy investigation of the dorsolateral prefrontal cortex in bipolar disorder patients. Journal of Affective Disorders *86*, 61–67. 10.1016/j.jad.2004.12.008.

100. Friedman, S.D., Dager, S.R., Parow, A., Hirashima, F., Demopulos, C., Stoll, A.L., Lyoo, I.K., Dunner, D.L., and Renshaw, P.F. (2004). Lithium and valproic acid treatment effects on brain chemistry in bipolar disorder. Biological Psychiatry *56*, 340–348. 10.1016/j.biopsych.2004.06.012.

101. Renshaw, P.F., Haselgrove, J.C., Bolinger, L., Chance, B., and Leigh, J.S. (1986). Relaxation and imaging of lithium in vivo. Magnetic Resonance Imaging *4*, 193–198. 10.1016/0730-725X(86)91058-1.

102. Renshaw, P.F., Haselgrove, J.C., Leigh, J.S., and Chance, B. (1985). In Vivo Nuclear Magnetic Resonance Imaging of Lithium. Magnetic Resonance in Medicine *2*, 512–516. 10.1002/mrm.1910020512.

103. Ramaprasad, S., Newton, J.E.O., Cardwell, D., Fowler, A.H., and Komoroski, R.A. (1992). In vivo 7Li NMR imaging and localized spectroscopy of rat brain. Magnetic Resonance in Medicine *25*, 308–318. 10.1002/mrm.1910250209.

104. Komoroski, R.A., Newton, J.E.O., Sprigg, J.R., Cardwell, D., Mohanakrishnan, P., and Karson, C.N. (1993). In vivo 7Li nuclear magnetic resonance study of lithium pharmacokinetics and chemical shift imaging in psychiatric patients. Psychiatry Research: Neuroimaging *50*, 67–76. 10.1016/0925-4927(93)90011-6.

References

105.   Gonzalez, R.G., Guimaraes, A.R., Sachs, G.S., Rosenbaum, J.F., Garwood, M., and Renshaw, P.F. (1993). Measurement of human brain lithium in vivo by MR spectroscopy. American Journal of Neuroradiology *14*, 1027–1037.

106.   Kushnir, T., Itzchak, Y., Valevski, A., Lask, M., Modai, I., and Navon, G. (1993). Relaxation times and concentrations of 7Li in the brain of patients receiving Lithium therapy. NMR in Biomedicine *6*, 39–42. 10.1002/nbm.1940060107.

107.   Riedl, U., Barocka, A., Kolem, H., Demling, J., Kaschka, W.P., Schelp, R., Stemmler, M., and Ebert, D. (1997). Duration of lithium treatment and brain lithium concentration in patients with unipolar and schizoaffective disorder - A study with magnetic resonance spectroscopy. Biological Psychiatry *41*, 844–850. 10.1016/S0006-3223(96)00330-7.

108.   Girard, F., Suhara, T., Sassa, T., Okubo, Y., Obata, T., Ikehira, H., Sudo, Y., Koga, M., Yoshioka, H., and Yoshida, K. (2001). 7Li 2D CSI of human brain on a clinical scanner. Magma: Magnetic Resonance Materials in Physics, Biology, and Medicine *13*, 1–7. 10.1007/BF02668644.

109.   Ramaprasad, S. (2004). Lithium spectroscopic imaging of rat brain at therapeutic doses. Magnetic Resonance Imaging *22*, 727–734. 10.1016/j.mri.2004.01.063.

110.   Komoroski, R.A., and Pearce, J.M. (2004). Localized 7Li MR spectroscopy and spin relaxation in rat brain in vivo. Magnetic Resonance in Medicine *52*, 164–168. 10.1002/mrm.20112.

111.   Komoroski, R.A., and Pearce, J.M. (2008). Estimating intracellular lithium in brain in vivo by localized 7Li magnetic resonance spectroscopy. Magnetic Resonance in Medicine *60*, 21–26. 10.1002/mrm.21613.

112.   Forester, B.P., Finn, C.T., Berlow, Y.A., Wardrop, M., Renshaw, P.F., and Moore, C.M. (2008). Brain lithium, N-acetyl aspartate and myo-inositol levels in older adults with bipolar disorder treated with lithium: A lithium-7 and proton magnetic resonance spectroscopy study. Bipolar Disorders *10*, 691–700. 10.1111/j.1399-5618.2008.00627.x.

113.   Smith, F.E., Cousins, D.A., Thelwall, P.E., Ferrier, I.N., and Blamire, A.M. (2011). Quantitative lithium magnetic resonance spectroscopy in the normal human brain on a 3 T clinical scanner. Magnetic Resonance in Medicine *66*, 945–949. 10.1002/mrm.22923.

114.   Komoroski, R.A., Lindquist, D.M., and Pearce, J.M. (2013). Lithium compartmentation in brain by 7Li MRS: Effect of total lithium concentration. NMR in Biomedicine *26*, 1152–1157. 10.1002/nbm.2929.

115.   Stout, J., Hozer, F., Coste, A., Mauconduit, F., Djebrani-Oussedik, N., Sarrazin, S., Poupon, J., Meyrel, M., Romanzetti, S., Etain, B., et al. (2020). Accumulation of Lithium in the Hippocampus of Patients With Bipolar Disorder: A Lithium-7 Magnetic Resonance Imaging Study at 7 Tesla. Biological Psychiatry *88*, 1–8. 10.1016/j.biopsych.2020.02.1181.

116.   Stout, J., Hanak, A.S., Chevillard, L., Djemaï, B., Risède, P., Giacomini, E., Poupon, J., Barrière, D.A., Bellivier, F., Mégarbane, B., et al. (2017). Investigation of lithium distribution in the rat brain ex vivo using lithium-7 magnetic resonance spectroscopy and imaging at 17.2 T. NMR in Biomedicine *30*, e3770. 10.1002/nbm.3770.

117. Pearce, J.M., Lyon, M., and Komoroski, R.A. (2004). Localized 7Li MR spectroscopy: In vivo brain and serum concentrations in the rat. Magnetic Resonance in Medicine *52*, 1087–1092. 10.1002/mrm.20250.

118. Renshaw, P.F., and Wicklund, S. (1988). In vivo measurement of lithium in humans by nuclear magnetic resonance spectroscopy. Biological Psychiatry *23*, 465–475. 10.1016/0006-3223(88)90018-2.

119. Komoroski, R.A., Newton, J.E.O., Walker, E., Cardwell, D., Jagannathan, N.R., Ramaprasad, S., and Sprig, J. (1990). In Vivo NMR spectroscopy of lithium-7 in humans. Magnetic Resonance in Medicine *15*, 347–356. 10.1002/mrm.1910150302.

120. Kato, T., Takahashi, S., and Inubushi, T. (1992). Brain lithium concentration by 7Li- and 1H-magnetic resonance spectroscopy in bipolar disorder. Psychiatry Research: Neuroimaging *45*, 53–63. 10.1016/0925-4927(92)90013-T.

121. Plenge, P., Stensgaard, A., Jensen, H.V., Thomsen, C., Mellerup, E.T., and Henriksen, O. (1994). 24-Hour lithium concentration in human brain studied by Li-7 magnetic resonance spectroscopy. Biological Psychiatry *36*, 511–516. 10.1016/0006-3223(94)90614-9.

122. Komoroski, R.A. (2005). Biomedical applications of 7Li NMR. NMR in Biomedicine *18*, 67–73. 10.1002/nbm.914.

123. Hamburger-Bar, R., Robert, M., Newman, M., and Belmaker, R.H. (1986). Interstrain correlation between behavioural effects of lithium and effects on cortical cyclic AMP. Pharmacology Biochemistry and Behavior *24*, 9–13. 10.1016/0091-3057(86)90036-5.

124. Lee, J.-H., Adler, C., Norris, M., Chu, W.-J., Fugate, E.M., Strakowski, S.M., and Komoroski, R.A. (2012). 4-T 7Li 3D MR spectroscopy imaging in the brains of bipolar disorder subjects. Magnetic Resonance in Medicine *68*, 363–368. 10.1002/mrm.24361.

125. Sachs, G.S., Renshaw, P.F., Lafer, B., Stoll, A.L., Guimarães, A.R., Rosenbaum, J.F., and Gonzalez, R.G. (1995). Variability of brain lithium levels during maintenance treatment: A magnetic resonance spectroscopy study. Biological Psychiatry *38*, 422–428. 10.1016/0006-3223(94)00324-V.

126. Moore, C.M., Demopulos, C.M., Henry, M.E., Steingard, R.J., Zamvil, L., Katic, A., Breeze, J.L., Moore, J.E.C., Cohen, B.M., and Renshaw, P.F. (2002). Brain-to-serum lithium ratio and age: An in vivo magnetic resonance spectroscopy study. American Journal of Psychiatry *159*, 1240–1242. 10.1176/appi.ajp.159.7.1240.

127. Kato, T., Inubushi, T., and Takahashi, S. (1994). Relationship of lithium concentrations in the brain measured by lithium-7 magnetic resonance spectroscopy to treatment response in mania. Journal of Clinical Psychopharmacology *14*, 330–335. 10.1097/00004714-199410000-00007.

128. Smith, F.E., Thelwall, P.E., Necus, J., Flowers, C.J., Blamire, A.M., and Cousins, D.A. (2018). 3D 7Li magnetic resonance imaging of brain lithium distribution in bipolar disorder. Molecular Psychiatry *23*, 2184–2191. 10.1038/s41380-018-0016-6.

129. Ramaprasad, S., Ripp, E., Pi, J., and Lyon, M. (2005). Pharmacokinetics of lithium in rat brain regions by spectroscopic imaging. Magnetic Resonance Imaging *23*, 859–863. 10.1016/j.mri.2005.07.007.

References

130. Spirtes, M.A. (1976). Lithium levels in monkey and human brain after chronic, therapeutic, oral dosage. Pharmacology Biochemistry and Behavior *5*, 143–147. 10.1016/0091-3057(76)90030-7.

131. Francis, R. (1970). LITHIUM DISTRIBUTION IN THE BRAINS OF TWO MANIC PATIENTS. The Lancet *296*, 523–524. 10.1016/S0140-6736(70)90144-3.

132. Zanni, G., Michno, W., Di Martino, E., Tjärnlund-Wolf, A., Pettersson, J., Mason, C.E., Hellspong, G., Blomgren, K., and Hanrieder, J. (2017). Lithium accumulates in neurogenic brain regions as revealed by high resolution ion imaging. Scientific Reports *7*, 1–12. 10.1038/srep40726.

133. Komoroski, R.A., Pearce, J.M., and Newton, J.E.O. (1998). Lithium visibility in rat brain and muscle in vivo by 7Li NMR imaging. Journal of magnetic resonance (San Diego, Calif. : 1997) *133*, 98–103. 10.1006/jmre.1998.1435.

134. Komoroski, R.A., Pearce, J.M., and Newton, J.E.O. (1997). The distribution of lithium in rat brain and muscle in vivo by 7Li NMR imaging. Magnetic Resonance in Medicine *38*, 275–278. 10.1002/mrm.1910380217.

135. Bertholf, R.L., Savory, M.G., Winborne, K.H., Hundley, J.C., Plummer, G.M., and Savory, J. (1988). Lithium determined in serum with an ion-selective electrode. Clinical Chemistry *34*, 1500–1502. 10.1093/clinchem/34.7.1500.

136. Schou, M. (1958). Lithium Studies. 1. Toxicity. Acta Pharmacologica et Toxicologica *15*, 70–84. 10.1111/j.1600-0773.1958.tb00287.x.

137. Schou, M. (1958). Lithium Studies. 3. Distribution between Serum and Tissues. Acta Pharmacologica et Toxicologica *15*, 115–124. 10.1111/j.1600-0773.1958.tb00290.x.

138. Blijenberg, B.G., and Leijnse, B. (1968). The determination of lithium in serum by atomic absorption spectroscopy and flame emission spectroscopy. Clinica Chimica Acta *19*, 97–99. 10.1016/0009-8981(68)90193-9.

139. Thellier, M., Heurteaux, C., and Wissocq, J. (1980). Quantitative study of the distribution of lithium in the mouse brain for various doses of lithium given to the animal. Brain Research *199*, 175–196. 10.1016/0006-8993(80)90239-5.

140. Heurteaux, C., Ripoll, C., Ouznadji, S., Ouznadji, H., Wissocq, J.-C., and Thellier, M. (1991). Lithium transport in the mouse brain. Brain Research *547*, 123–129. 10.1016/0006-8993(91)90582-G.

141. Schoepfer, J., Gernhäuser, R., Lichtinger, S., Stöver, A., Bendel, M., Delbridge, C., Widmann, T., Winkler, S., and Graw, M. (2021). Position sensitive measurement of trace lithium in the brain with NIK (neutron-induced coincidence method) in suicide. Sci Rep *11*, 6823. 10.1038/s41598-021-86377-x.

142. Schrauzer, G.N. (2002). Lithium: Occurrence, Dietary Intakes, Nutritional Essentiality. Journal of the American College of Nutrition *21*, 14–21. 10.1080/07315724.2002.10719188.

143. Filippini, T., Tancredi, S., Malagoli, C., Malavolti, M., Bargellini, A., Vescovi, L., Nicolini, F., and Vinceti, M. (2020). Dietary Estimated Intake of Trace Elements: Risk Assessment in an Italian Population. Exposure and Health *12*, 641–655. 10.1007/s12403-019-00324-w.

References

144.   Liaugaudaite, V., Mickuviene, N., Raskauskiene, N., Naginiene, R., and Sher, L. (2017). Lithium levels in the public drinking water supply and risk of suicide: A pilot study. Journal of Trace Elements in Medicine and Biology *43*, 197–201. 10.1016/j.jtemb.2017.03.009.

145.   O'Donnell, K.C., and Gould, T.D. (2007). The behavioral actions of lithium in rodent models: leads to develop novel therapeutics. Neuroscience and biobehavioral reviews *31*, 932–962. 10.1016/j.neubiorev.2007.04.002.

146.   Forester, B.P., Streeter, C.C., Berlow, Y.A., Tian, H., Wardrop, M., Finn, C.T., Harper, D., Renshaw, P.F., and Moore, C.M. (2009). Brain lithium levels and effects on cognition and mood in geriatric bipolar disorder: a lithium-7 magnetic resonance spectroscopy study. The American Journal of Geriatric Psychiatry *17*, 13–23. 10.1097/JGP.0b013e318172b3d0.

147.   Ernst, R.R., and Anderson, W.A. (1966). Application of Fourier Transform Spectroscopy to Magnetic Resonance. The Review of Scientific Instruments *37*, 93–102. 10.1063/1.1719961.

148.   Otsu, N. (1979). A Threshold Selection Method from Gray-Level Histograms. IEEE Transactions on Systems, Man, and Cybernetics *9*, 62–66. 10.1109/TSMC.1979.4310076.

149.   Lai, M., Lanz, B., Poitry-Yamate, C., Romero, J.F., Berset, C.M., Cudalbu, C., and Gruetter, R. (2018). In vivo 13 C MRS in the mouse brain at 14.1 Tesla and metabolic flux quantification under infusion of [1,6- 13 C 2]glucose. Journal of Cerebral Blood Flow & Metabolism *38*, 1701–1714. 10.1177/0271678X17734101.

150.   Santos-Díaz, A., and Noseworthy, M.D. (2020). Phosphorus magnetic resonance spectroscopy and imaging (31P-MRS/MRSI) as a window to brain and muscle metabolism: A review of the methods. Biomedical Signal Processing and Control *60*, 101967. 10.1016/j.bspc.2020.101967.

151.   Doty, F.D., Entzminger, G., Kulkarni, J., Pamarthy, K., and Staab, J.P. (2007). Radio frequency coil technology for small-animal MRI. NMR in Biomedicine *20*, 304–325. 10.1002/nbm.1149.

152.   Villarino, M.B. (2005). Ramanujan's Perimeter of an Ellipse.

153.   Urone, P.P., Hinrichs, R., Dirks, K., and Sharma, M. (2016). College Physics (OpenStax CNX).

154.   Seeber, D.A., Jevtic, J., and Menon, A. (2004). Floating shield current suppression trap. Concepts in Magnetic Resonance *21B*, 26–31. 10.1002/cmr.b.20008.

155.   Stollberger, R., and Wach, P. (1996). Imaging of the active B1 field in vivo. Magnetic Resonance in Medicine *35*, 246–251. 10.1002/mrm.1910350217.

156.   Öz, G., Deelchand, D.K., Wijnen, J.P., Mlynárik, V., Xin, L., Mekle, R., Noeske, R., Scheenen, T.W.J., Tkáč, I., Andronesi, O., et al. (2021). Advanced single voxel 1 H magnetic resonance spectroscopy techniques in humans: Experts' consensus recommendations. NMR in Biomedicine *34*, 1–18. 10.1002/nbm.4236.

157.   Lanz, B., Abaei, A., Braissant, O., Choi, I., Cudalbu, C., Henry, P., Gruetter, R., Kara, F., Kantarci, K., Lee, P., et al. (2021). Magnetic resonance spectroscopy in the

rodent brain: Experts' consensus recommendations. NMR in Biomedicine *34*, 1–20. 10.1002/nbm.4325.

158.   Kreis, R., Boer, V., Choi, I., Cudalbu, C., Graaf, R.A., Gasparovic, C., Heerschap, A., Krššák, M., Lanz, B., Maudsley, A.A., et al. (2021). Terminology and concepts for the characterization of in vivo MR spectroscopy methods and MR spectra: Background and experts' consensus recommendations. NMR in Biomedicine *34*, 1–34. 10.1002/nbm.4347.

159.   Lin, A., Andronesi, O., Bogner, W., Choi, I., Coello, E., Cudalbu, C., Juchem, C., Kemp, G.J., Kreis, R., Krššák, M., et al. (2021). Minimum Reporting Standards for in vivo Magnetic Resonance Spectroscopy (MRSinMRS): Experts' consensus recommendations. NMR in Biomedicine *34*, 1–18. 10.1002/nbm.4484.

160.   Near, J., Harris, A.D., Juchem, C., Kreis, R., Marjańska, M., Öz, G., Slotboom, J., Wilson, M., and Gasparovic, C. (2021). Preprocessing, analysis and quantification in single-voxel magnetic resonance spectroscopy: experts' consensus recommendations. NMR in Biomedicine *34*, 1–23. 10.1002/nbm.4257.

161.   Cudalbu, C., Cavassila, S., Rabeson, H., Van Ormondt, D., and Graveron-Demilly, D. (2008). Influence of measured and simulated basis sets on metabolite concentration estimates: METABOLITE CONCENTRATION USING MEASURED AND SIMULATED BASIS SETS. NMR Biomed. *21*, 627–636. 10.1002/nbm.1234.

162.   De Graaf, A.A., and Bovée, W.M.M.J. (1990). Improved quantification of in vivo 1H NMR spectra by optimization of signal acquisition and processing and by incorporation of prior knowledge into the spectral fitting. Magn. Reson. Med. *15*, 305–319. 10.1002/mrm.1910150212.

163.   Clarke, W.T., Stagg, C.J., and Jbabdi, S. (2021). FSL-MRS: An end-to-end spectroscopy analysis package. Magnetic Resonance in Medicine *85*, 2950–2964. 10.1002/mrm.28630.

164.   Stefan, D., Cesare, F.D., Andrasescu, A., Popa, E., Lazariev, A., Vescovo, E., Strbak, O., Williams, S., Starcuk, Z., Cabanas, M., et al. (2009). Quantitation of magnetic resonance spectroscopy signals: the jMRUI software package. Meas. Sci. Technol. *20*, 104035. 10.1088/0957-0233/20/10/104035.

165.   Wilson, M., Reynolds, G., Kauppinen, R.A., Arvanitis, T.N., and Peet, A.C. (2011). A constrained least-squares approach to the automated quantitation of in vivo [1] H magnetic resonance spectroscopy data: Automated Quantitation of In Vivo [1] H MRS Data. Magn. Reson. Med. *65*, 1–12. 10.1002/mrm.22579.

166.   Soher, B.J., Semanchuk, P., Todd, D., Ji, X., Deelchand, D., Joers, J., Oz, G., and Young, K. (2023). Vespa: Integrated applications for RF pulse design, spectral simulation and MRS data analysis. Magnetic Resonance in Med *90*, 823–838. 10.1002/mrm.29686.

167.   Marjańska, M., Deelchand, D.K., Kreis, R., Alger, J.R., Bolan, P.J., Borbath, T., Boumezbeur, F., Fernandes, C.C., Coello, E., Nagraja, B.H., et al. (2022). Results and interpretation of a fitting challenge for MR spectroscopy set up by the MRS study group of ISMRM. Magnetic Resonance in Medicine *87*, 11–32. 10.1002/mrm.28942.

References

168. Thurston, J.H., Sherman, W.R., Hauhart, R.E., and Kloepper, R.F. (1989). myo-Inositol: A Newly Identified Nonnitrogenous Osmoregulatory Molecule in Mammalian Brain. Pediatr Res *26*, 482–485. 10.1203/00006450-198911000-00024.

169. Brand, A., Richter-Landsberg, C., and Leibfritz, D. (1993). Multinuclear NMR Studies on the Energy Metabolism of Glial and Neuronal Cells. Developmental Neuroscience *15*, 289–298. 10.1159/000111347.

170. Moffett, J., Ross, B., Arun, P., Madhavarao, C., and Namboodiri, A. (2007). N-Acetylaspartate in the CNS: From neurodiagnostics to neurobiology. Progress in Neurobiology *81*, 89–131. 10.1016/j.pneurobio.2006.12.003.

171. Veen, J.W.V.D., and Shen, J. (2013). Regional difference in GABA levels between medial prefrontal and occipital cortices: Regional Difference in GABA Levels. J. Magn. Reson. Imaging *38*, 745–750. 10.1002/jmri.24009.

172. Boretius, S., Tammer, R., Michaelis, T., Brockmöller, J., and Frahm, J. (2013). Halogenated volatile anesthetics alter brain metabolism as revealed by proton magnetic resonance spectroscopy of mice in vivo. NeuroImage *69*, 244–255. 10.1016/j.neuroimage.2012.12.020.

173. Kreis, R., and Boesch, C. (2003). Bad Spectra Can Be Better Than Good Spectra. In Proceedings of the ISMRM.

174. Wijtenburg, S.A., and Knight-Scott, J. (2009). The Impact of SNR on the Reliability of LCModel and QUEST Quantitation in 1H-MRS. In Proceedings of the ISMRM, p. 2401.

175. Helms, G. (1999). Analysis of 1.5 Tesla proton MR spectra of human brain using LCModel and an imported basis set. Magnetic Resonance Imaging *17*, 1211–1218. 10.1016/S0730-725X(99)00058-2.

176. Mlynarik, V., Gambarota, G., Xin, L., and Gruetter, R. (2007). Precision of Metabolite Concentrations Obtained by LCModel as a Function of the Signal-To-Noise Ratio in Rodent Brain. In Proceedings of the Joint Annual Meeting ISMRM-ESMRMB, p. 3173.

177. Kanowski, M., Kaufmann, J., Braun, J., Bernarding, J., and Tempelmann, C. (2004). Quantitation of simulated short echo time1H human brain spectra by LCModel and AMARES. Magn. Reson. Med. *51*, 904–912. 10.1002/mrm.20063.

178. Craven, A.R., Bhattacharyya, P.K., Clarke, W.T., Dydak, U., Edden, R.A.E., Ersland, L., Mandal, P.K., Mikkelsen, M., Murdoch, J.B., Near, J., et al. (2022). Comparison of seven modelling algorithms for γ-aminobutyric acid–edited proton magnetic resonance spectroscopy. NMR in Biomedicine *35*, e4702. 10.1002/nbm.4702.

179. Zhang, Y., and Shen, J. (2020). Effects of noise and linewidth on in vivo analysis of glutamate at 3 T. Journal of Magnetic Resonance *314*, 106732. 10.1016/j.jmr.2020.106732.

180. Mosconi, E., Sima, D.M., Osorio Garcia, M.I., Fontanella, M., Fiorini, S., Van Huffel, S., and Marzola, P. (2014). Different quantification algorithms may lead to different results: a comparison using proton MRS lipid signals: DIFFERENT QUANTIFICATION ALGORITHMS MAY LEAD TO DIFFERENT RESULTS. NMR Biomed. *27*, 431–443. 10.1002/nbm.3079.

References

181. Near, J. (2014). Investigating the effect of spectral linewidth on metabolite measurement bias in short-TE MRS. In Proceedings of the ISMRM, p. 2915.

182. Simpson, R., Devenyi, G.A., Jezzard, P., Hennessy, T.J., and Near, J. (2017). Advanced processing and simulation of MRS data using the FID appliance (FID-A)—An open source, MATLAB-based toolkit. Magnetic Resonance in Medicine *77*, 23–33. 10.1002/mrm.26091.

183. Gajdošík, M., Landheer, K., Swanberg, K.M., and Juchem, C. (2021). INSPECTOR: free software for magnetic resonance spectroscopy data inspection, processing, simulation and analysis. Scientific Reports *11*, 2094. 10.1038/s41598-021-81193-9.

184. Helmus, J.J., and Jaroniec, C.P. (2013). Nmrglue: an open source Python package for the analysis of multidimensional NMR data. J Biomol NMR *55*, 355–367. 10.1007/s10858-013-9718-x.

185. Oeltzschner, G., Zöllner, H.J., Hui, S.C.N., Mikkelsen, M., Saleh, M.G., Tapper, S., and Edden, R.A.E. (2020). Osprey: Open-source processing, reconstruction & estimation of magnetic resonance spectroscopy data. Journal of Neuroscience Methods *343*, 108827. 10.1016/j.jneumeth.2020.108827.

186. Genovese, G., Deelchand, D.K., Terpstra, M., and Marjańska, M. (2023). Quantification of GABA concentration measured noninvasively in the human posterior cingulate cortex with 7 T ultra-short-TE MR spectroscopy. Magnetic Resonance in Med *89*, 886–897. 10.1002/mrm.29514.

187. Beckonert, O., Keun, H.C., Ebbels, T.M.D., Bundy, J., Holmes, E., Lindon, J.C., and Nicholson, J.K. (2007). Metabolic profiling, metabolomic and metabonomic procedures for NMR spectroscopy of urine, plasma, serum and tissue extracts. Nat Protoc *2*, 2692–2703. 10.1038/nprot.2007.376.

188. Moco, S. (2022). Studying Metabolism by NMR-Based Metabolomics. Front. Mol. Biosci. *9*, 882487. 10.3389/fmolb.2022.882487.

189. Nagana Gowda, G.A., and Raftery, D. (2021). NMR-Based Metabolomics. In Cancer Metabolomics Advances in Experimental Medicine and Biology., S. Hu, ed. (Springer International Publishing), pp. 19–37. 10.1007/978-3-030-51652-9_2.

190. Griffin, J.L., Bollard, M., Nicholson, J.K., and Bhakoo, K. (2002). Spectral profiles of cultured neuronal and glial cells derived from HRMAS1H NMR spectroscopy. NMR Biomed. *15*, 375–384. 10.1002/nbm.792.

191. Duarte, I.F., Lamego, I., Marques, J., Marques, M.P.M., Blaise, B.J., and Gil, A.M. (2010). Nuclear Magnetic Resonance (NMR) Study of the Effect of Cisplatin on the Metabolic Profile of MG-63 Osteosarcoma Cells. J. Proteome Res. *9*, 5877–5886. 10.1021/pr100635n.

192. Smith, M.J., Marshall, C.B., Theillet, F.-X., Binolfi, A., Selenko, P., and Ikura, M. (2015). Real-time NMR monitoring of biological activities in complex physiological environments. Current Opinion in Structural Biology *32*, 39–47. 10.1016/j.sbi.2015.02.003.

193. Yilmaz, A., and Utz, M. (2016). Characterisation of oxygen permeation into a microfluidic device for cell culture by in situ NMR spectroscopy. Lab Chip *16*, 2079–2085. 10.1039/C6LC00396F.

References

194.   Tabatabaei Anaraki, M., Dutta Majumdar, R., Wagner, N., Soong, R., Kovacevic, V., Reiner, E.J., Bhavsar, S.P., Ortiz Almirall, X., Lane, D., Simpson, M.J., et al. (2018). Development and Application of a Low-Volume Flow System for Solution-State in Vivo NMR. Anal. Chem. *90*, 7912–7921. 10.1021/acs.analchem.8b00370.

195.   Ackerman, J.J.H., Bore, P.J., Gadian, D.G., Grove, T.H., and Radda, G.K. (1980). N.m.r. studies of metabolism in perfused organs. Phil. Trans. R. Soc. Lond. B, 425–436. 10.1098/rstb.1980.0059.

196.   Kalfe, A., Telfah, A., Lambert, J., and Hergenröder, R. (2015). Looking into Living Cell Systems: Planar Waveguide Microfluidic NMR Detector for *in Vitro* Metabolomics of Tumor Spheroids. Anal. Chem. *87*, 7402–7410. 10.1021/acs.analchem.5b01603.

197.   Hertig, D., Maddah, S., Memedovski, R., Kurth, S., Moreno, A., Pennestri, M., Felser, A., Nuoffer, J.-M., and Vermathen, P. (2021). Live monitoring of cellular metabolism and mitochondrial respiration in 3D cell culture system using NMR spectroscopy. The Analyst *146*, 4326–4339. 10.1039/D1AN00041A.

198.   Mancuso, A., Fernandez, E.J., Blanch, H.W., and Clark, D.S. (1990). A Nuclear Magnetic Resonance Technique for Determining Hybridoma Cell Concentration in Hollow Fiber Bioreactors. Nat Biotechnol *8*, 1282–1285. 10.1038/nbt1290-1282.

199.   Vinci, M., Gowan, S., Boxall, F., Patterson, L., Zimmermann, M., Court, W., Lomas, C., Mendiola, M., Hardisson, D., and Eccles, S.A. (2012). Advances in establishment and analysis of three-dimensional tumor spheroid-based functional assays for target validation and drug evaluation. BMC Biol *10*, 29. 10.1186/1741-7007-10-29.

200.   Pampaloni, F., Reynaud, E.G., and Stelzer, E.H.K. (2007). The third dimension bridges the gap between cell culture and live tissue. Nat Rev Mol Cell Biol *8*, 839–845. 10.1038/nrm2236.

201.   Monteiro, M.V., Gaspar, V.M., Ferreira, L.P., and Mano, J.F. (2020). Hydrogel 3D in vitro tumor models for screening cell aggregation mediated drug response. Biomaterials Science *8*, 1855–1864. 10.1039/C9BM02075F.

202.   Kim, J.B., Stein, R., and O'Hare, M.J. (2004). Three-dimensional in vitro tissue culture models of breast cancer — a review. Breast Cancer Res Treat *85*, 281–291. 10.1023/B:BREA.0000025418.88785.2b.

203.   Ravi, M., Paramesh, V., Kaviya, S.R., Anuradha, E., and Solomon, F.D.P. (2015). 3D Cell Culture Systems: Advantages and Applications: 3D CELL CULTURE SYSTEMS. J. Cell. Physiol *230*, 16–26. 10.1002/jcp.24683.

204.   Bayraktar, O.A., Fuentealba, L.C., Alvarez-Buylla, A., and Rowitch, D.H. (2015). Astrocyte Development and Heterogeneity. Cold Spring Harb Perspect Biol *7*, a020362. 10.1101/cshperspect.a020362.

205.   Rivera, A.D., and Butt, A.M. (2019). Astrocytes are direct cellular targets of lithium treatment: novel roles for lysyl oxidase and peroxisome-proliferator activated receptor-γ as astroglial targets of lithium. Translational Psychiatry *9*, 211. 10.1038/s41398-019-0542-2.

206.   Atack, J.R. (1996). Inositol monophosphatase, the putative therapeutic target for lithium. Brain Research Reviews.

References

207. Sherman, W.R., Leavitt, A.L., Honchar, M.P., Hallcher, L.M., and Phillips, B.E. (1981). Evidence that Lithium Alters Phosphoinositide Metabolism: Chronic Administration Elevates Primarily d-myo-Inositol-1-Phosphate in Cerebral Cortex of the Rat. J Neurochem *36*, 1947–1951. 10.1111/j.1471-4159.1981.tb10819.x.

208. Zhang, D., Wang, F., Zhai, X., Li, X.-H., and He, X.-J. (2018). Lithium promotes recovery of neurological function after spinal cord injury by inducing autophagy. Neural Regen Res *13*, 2191. 10.4103/1673-5374.241473.

209. Garcia-Hernandez, R., Cerdán Cerdá, A., Trouve Carpena, A., Drakesmith, M., Koller, K., Jones, D.K., Canals, S., and De Santis, S. (2022). Mapping microglia and astrocyte activation in vivo using diffusion MRI. Sci. Adv. *8*, eabq2923. 10.1126/sciadv.abq2923.

210. Debaker, C., Djemai, B., Ciobanu, L., Tsurugizawa, T., and Le Bihan, D. (2020). Diffusion MRI reveals in vivo and non-invasively changes in astrocyte function induced by an aquaporin-4 inhibitor. PLoS ONE *15*, e0229702. 10.1371/journal.pone.0229702.

211. Silverstone, P.H., and McGrath, B.M. (2009). Lithium and valproate and their possible effects on the myo-inositol second messenger system in healthy volunteers and bipolar patients. International Review of Psychiatry *21*, 414–423. 10.1080/09540260902962214.

212. Kofman, O., and Belmaker, R.H. (1993). Biochemical, behavioral, and clinical studies of the role of inositol in lithium treatment and depression. Biological Psychiatry *34*, 839–852. 10.1016/0006-3223(93)90052-F.

213. Hirvonen, M.-R., and Savolainen, K. (1991). Lithium-induced decrease of brain inositol and increase of brain inositol-1-phosphate is transient. Neurochem Res *16*, 905–911. 10.1007/BF00965540.

214. Li, X., Morgan, P.S., Ashburner, J., Smith, J., and Rorden, C. (2016). The first step for neuroimaging data analysis: DICOM to NIfTI conversion. Journal of Neuroscience Methods *264*, 47–56. 10.1016/j.jneumeth.2016.03.001.

215. Garyfallidis, E., Brett, M., Amirbekian, B., Rokem, A., van der Walt, S., Descoteaux, M., Nimmo-Smith, I., and Dipy Contributors (2014). Dipy, a library for the analysis of diffusion MRI data. Front. Neuroinform. *8*. 10.3389/fninf.2014.00008.

216. Patel, N.C., DelBello, M.P., Cecil, K.M., Adler, C.M., Bryan, H.S., Stanford, K.E., and Strakowski, S.M. (2006). Lithium Treatment Effects on Myo-Inositol in Adolescents with Bipolar Depression. Biological Psychiatry *60*, 998–1004. 10.1016/j.biopsych.2006.07.029.

217. McGrath, B.M., Greenshaw, A.J., McKay, R., Slupsky, C.M., and Silverstone, P.H. (2006). Lithium alters regional rat brain myo-inositol at 2 and 4 weeks: an ex-vivo magnetic resonance spectroscopy study at 18.8 T. NeuroReport *17*, 1323–1326. 10.1097/01.wnr.0000230501.40349.41.

218. O'Donnell, T., Rotzinger, S., Ulrich, M., Hanstock, C.C., Nakashima, T.T., and Silverstone, P.H. (2003). Effects of chronic lithium and sodium valproate on concentrations of brain amino acids. European Neuropsychopharmacology *13*, 220–227. 10.1016/S0924-977X(03)00070-1.

References

219.   Ren, J., Sherry, A.D., and Malloy, C.R. (2015). (31)P-MRS of healthy human brain: ATP synthesis, metabolite concentrations, pH, and T1 relaxation times. NMR in Biomedicine *28*, 1455–1462. 10.1002/nbm.3384.

220.   Skupienski, R., Do, K.Q., and Xin, L. (2020). In vivo 31P magnetic resonance spectroscopy study of mouse cerebral NAD content and redox state during neurodevelopment. Sci Rep *10*, 15623. 10.1038/s41598-020-72492-8.

221.   Iotti, S., Frassineti, C., Alderighi, L., Sabatini, A., Vacca, A., and Barbiroli, B. (1996). In Vivo Assessment of Free Magnesium Concentration in Human Brain by 31P MRS. A New Calibration Curve Based on a Mathematical Algorithm. NMR Biomed. *9*, 24–32. 10.1002/(SICI)1099-1492(199602)9:1<24::AID-NBM392>3.0.CO;2-B.

222.   Avants, B., Epstein, C., Grossman, M., and Gee, J. (2008). Symmetric diffeomorphic image registration with cross-correlation: Evaluating automated labeling of elderly and neurodegenerative brain. Medical Image Analysis *12*, 26–41. 10.1016/j.media.2007.06.004.

223.   Dorr, A.E., Lerch, J.P., Spring, S., Kabani, N., and Henkelman, R.M. (2008). High resolution three-dimensional brain atlas using an average magnetic resonance image of 40 adult C57Bl/6J mice. NeuroImage *42*, 60–69. 10.1016/j.neuroimage.2008.03.037.

224.   Richards, K., Watson, C., Buckley, R.F., Kurniawan, N.D., Yang, Z., Keller, M.D., Beare, R., Bartlett, P.F., Egan, G.F., Galloway, G.J., et al. (2011). Segmentation of the mouse hippocampal formation in magnetic resonance images. NeuroImage *58*, 732–740. 10.1016/j.neuroimage.2011.06.025.

225.   Ullmann, J.F.P., Watson, C., Janke, A.L., Kurniawan, N.D., and Reutens, D.C. (2013). A segmentation protocol and MRI atlas of the C57BL/6J mouse neocortex. NeuroImage *78*, 196–203. 10.1016/j.neuroimage.2013.04.008.

226.   Steadman, P.E., Ellegood, J., Szulc, K.U., Turnbull, D.H., Joyner, A.L., Henkelman, R.M., and Lerch, J.P. (2014). Genetic Effects on Cerebellar Structure Across Mouse Models of Autism Using a Magnetic Resonance Imaging Atlas: MRI of genetic mouse model's cerebellum. Autism Res *7*, 124–137. 10.1002/aur.1344.

227.   Franklin, K.B.J., and Paxinos, G. (2008). The mouse brain in stereotaxic coordinates Compact 3. ed. (Elsevier Academic Press).

228.   Gorgolewski, K., Burns, C.D., Madison, C., Clark, D., Halchenko, Y.O., Waskom, M.L., and Ghosh, S.S. (2011). Nipype: A Flexible, Lightweight and Extensible Neuroimaging Data Processing Framework in Python. Front. Neuroinform. *5*. 10.3389/fninf.2011.00013.

229.   Fick, R.H.J., Wassermann, D., and Deriche, R. (2019). The Dmipy Toolbox: Diffusion MRI Multi-Compartment Modeling and Microstructure Recovery Made Easy. Front. Neuroinform. *13*, 64. 10.3389/fninf.2019.00064.

230.   Fadnavis, S., Batson, J., and Garyfallidis, E. (2020). Patch2Self: Denoising Diffusion MRI with Self-Supervised Learning. Preprint at arXiv.

231.   Shi, X.F., Carlson, P.J., Sung, Y.H., Fiedler, K.K., Forrest, L.N., Hellem, T.L., Huber, R.S., Kim, S.E., Zuo, C., Jeong, E.K., et al. (2015). Decreased brain PME/PDE ratio in bipolar disorder: A preliminary 31P magnetic resonance spectroscopy study. Bipolar Disorders *17*, 743–752. 10.1111/bdi.12339.

References

232.   De Groot, T., Doornebal, J., Christensen, B.M., Cockx, S., Sinke, A.P., Baumgarten, R., Bedford, J.J., Walker, R.J., Wetzels, J.F.M., and Deen, P.M.T. (2017). Lithium-induced NDI: Acetazolamide reduces polyuria but does not improve urine concentrating ability. American Journal of Physiology - Renal Physiology *313*, F669–F676. 10.1152/ajprenal.00147.2017.

233.   Smith, D.F., and Amdisen, A. (1983). Central Effects of Lithium in Rats: Lithium Levels, Body Weight and Water Intake. Acta Pharmacologica et Toxicologica *52*, 81–85. 10.1111/j.1600-0773.1983.tb03407.x.

234.   Trepiccione, F., Capasso, G., Nielsen, S., and Christensen, B.M. (2013). Evaluation of cellular plasticity in the collecting duct during recovery from lithium-induced nephrogenic diabetes insipidus. American Journal of Physiology-Renal Physiology *305*, F919–F929. 10.1152/ajprenal.00152.2012.

235.   Voevodskaya, O., Sundgren, P.C., Strandberg, O., Zetterberg, H., Minthon, L., Blennow, K., Wahlund, L.-O., Westman, E., Hansson, O., and For the Swedish BioFINDER study group (2016). Myo-inositol changes precede amyloid pathology and relate to *APOE* genotype in Alzheimer disease. Neurology *86*, 1754–1761. 10.1212/WNL.0000000000002672.

236.   Nedelska, Z., Przybelski, S.A., Lesnick, T.G., Schwarz, C.G., Lowe, V.J., Machulda, M.M., Kremers, W.K., Mielke, M.M., Roberts, R.O., Boeve, B.F., et al. (2017). 1 H-MRS metabolites and rate of β-amyloid accumulation on serial PET in clinically normal adults. Neurology *89*, 1391–1399. 10.1212/WNL.0000000000004421.

237.   Jakaria, M., Azam, S., Haque, M.E., Jo, S.-H., Uddin, M.S., Kim, I.-S., and Choi, D.-K. (2019). Taurine and its analogs in neurological disorders: Focus on therapeutic potential and molecular mechanisms. Redox Biology *24*, 101223. 10.1016/j.redox.2019.101223.

238.   Foos, T.M., and Wu, J.-Y. (2002). The Role of Taurine in the Central Nervous System and the Modulation of Intracellular Calcium Homeostasis. Neurochemical Research *27*, 21–26. 10.1023/A:1014890219513.

239.   Thurston, J.H., Hauhart, R.E., and Dirgo, J.A. (1980). Taurine: A role in osmotic regulation of mammalian brain and possible clinical significance. Life Sciences *26*, 1561–1568. 10.1016/0024-3205(80)90358-6.

240.   Zhu, M., Akimana, C., Wang, E., and Ng, C.K. (2019). 1H-MRS Quantitation of Age-Dependent Taurine Changes in Mouse Brain. Mol Imaging Biol *21*, 812–817. 10.1007/s11307-019-01333-6.

241.   Walz, W., and Allen, A.F. (1987). Evaluation of the osmoregulatory function of taurine in brain cells. Exp Brain Res *68*. 10.1007/BF00248794.

242.   Patel, N.C., DelBello, M.P., Cecil, K.M., Stanford, K.E., Adler, C.M., and Strakowski, S.M. (2008). Temporal Change in *N* -Acetyl-Aspartate Concentrations in Adolescents with Bipolar Depression Treated with Lithium. Journal of Child and Adolescent Psychopharmacology *18*, 132–139. 10.1089/cap.2007.0088.

243.   Janson, C.G., Assadi, M., Francis, J., Bilaniuk, L., Shera, D., and Leone, P. (2005). Lithium Citrate for Canavan Disease. Pediatric Neurology *33*, 235–243. 10.1016/j.pediatrneurol.2005.04.015.

References

244. Szulc, A., Wiedlocha, M., Waszkiewicz, N., Galińska-Skok, B., Marcinowicz, P., Gierus, J., and Mosiolek, A. (2018). Proton magnetic resonance spectroscopy changes after lithium treatment. Systematic review. Psychiatry Research - Neuroimaging *273*, 1–8. 10.1016/j.pscychresns.2018.01.001.

245. Cong, L., Muir, E.R., Chen, C., Qian, Y., Liu, J., Biju, K.C., Clark, R.A., Li, S., and Duong, T.Q. (2016). Multimodal MRI Evaluation of the MitoPark Mouse Model of Parkinson's Disease. PLoS ONE *11*, e0151884. 10.1371/journal.pone.0151884.

246. Mueggler, T., Meyer-Luehmann, M., Rausch, M., Staufenbiel, M., Jucker, M., and Rudin, M. (2004). Restricted diffusion in the brain of transgenic mice with cerebral amyloidosis. Eur J Neurosci *20*, 811–817. 10.1111/j.1460-9568.2004.03534.x.

247. Grussu, F., Schneider, T., Tur, C., Yates, R.L., Tachrount, M., Ianuş, A., Yiannakas, M.C., Newcombe, J., Zhang, H., Alexander, D.C., et al. (2017). Neurite dispersion: a new marker of multiple sclerosis spinal cord pathology? Ann Clin Transl Neurol *4*, 663–679. 10.1002/acn3.445.

248. Jespersen, S.N., Bjarkam, C.R., Nyengaard, J.R., Chakravarty, M.M., Hansen, B., Vosegaard, T., Østergaard, L., Yablonskiy, D., Nielsen, N.Chr., and Vestergaard-Poulsen, P. (2010). Neurite density from magnetic resonance diffusion measurements at ultrahigh field: Comparison with light microscopy and electron microscopy. NeuroImage *49*, 205–216. 10.1016/j.neuroimage.2009.08.053.

249. Fukutomi, H., Glasser, M.F., Zhang, H., Autio, J.A., Coalson, T.S., Okada, T., Togashi, K., Van Essen, D.C., and Hayashi, T. (2018). Neurite imaging reveals microstructural variations in human cerebral cortical gray matter. NeuroImage *182*, 488–499. 10.1016/j.neuroimage.2018.02.017.

250. Brennan, B.P., Hudson, J.I., Jensen, J.E., McCarthy, J., Roberts, J.L., Prescot, A.P., Cohen, B.M., Pope, H.G., Renshaw, P.F., and Öngür, D. (2010). Rapid Enhancement of Glutamatergic Neurotransmission in Bipolar Depression Following Treatment with Riluzole. Neuropsychopharmacol *35*, 834–846. 10.1038/npp.2009.191.

251. Walls, A.B., Waagepetersen, H.S., Bak, L.K., Schousboe, A., and Sonnewald, U. (2015). The Glutamine–Glutamate/GABA Cycle: Function, Regional Differences in Glutamate and GABA Production and Effects of Interference with GABA Metabolism. Neurochem Res *40*, 402–409. 10.1007/s11064-014-1473-1.

252. Yüksel, C., and Öngür, D. (2010). Magnetic Resonance Spectroscopy Studies of Glutamate-Related Abnormalities in Mood Disorders. Biological Psychiatry *68*, 785–794. 10.1016/j.biopsych.2010.06.016.

253. Öngür, D., Drevets, W.C., and Price, J.L. (1998). Glial reduction in the subgenual prefrontal cortex in mood disorders. Proc. Natl. Acad. Sci. U.S.A. *95*, 13290–13295. 10.1073/pnas.95.22.13290.

254. Rackayova, V., Cudalbu, C., Pouwels, P.J.W., and Braissant, O. (2017). Creatine in the central nervous system: From magnetic resonance spectroscopy to creatine deficiencies. Analytical Biochemistry *529*, 144–157. 10.1016/j.ab.2016.11.007.

255. Saunders, D.E., Howe, F.A., Van Den Boogaart, A., Griffiths, J.R., and Brown, M.M. (1999). Aging of the adult human brain: In vivo quantitation of metabolite content with proton magnetic resonance spectroscopy. J. Magn. Reson. Imaging *9*, 711–716. 10.1002/(SICI)1522-2586(199905)9:5<711::AID-JMRI14>3.0.CO;2-3.

256.   Soreni, N., Noseworthy, M.D., Cormier, T., Oakden, W.K., Bells, S., and Schachar, R. (2006). Intraindividual variability of striatal 1H-MRS brain metabolite measurements at 3 T. Magnetic Resonance Imaging *24*, 187–194. 10.1016/j.mri.2005.10.027.

257.   Frey, B.N., Stanley, J.A., Nery, F.G., Serap Monkul, E., Nicoletti, M.A., Chen, H.-H., Hatch, J.P., Caetano, S.C., Ortiz, O., Kapczinski, F., et al. (2007). Abnormal cellular energy and phospholipid metabolism in the left dorsolateral prefrontal cortex of medication-free individuals with bipolar disorder: an in vivo [1] H MRS study. Bipolar Disorders *9*, 119–127. 10.1111/j.1399-5618.2007.00454.x.

258.   Hamakawa, H., Kato, T., Shioiri, T., Inubushi, T., and Kato, N. (1999). Quantitative proton magnetic resonance spectroscopy of the bilateral frontal lobes in patients with bipolar disorder. Psychol. Med. *29*, 639–644. 10.1017/S0033291799008442.

259.   Kato, T., Shioiri, T., Murashita, J., Hamakawa, H., Takahashi, Y., Inubushi, T., and Takahashi, S. (1995). Lateralized abnormality of high energy phosphate metabolism in the frontal lobes of patients with bipolar disorder detected by phase-encoded [31] P-MRS. Psychol. Med. *25*, 557–566. 10.1017/S003329170003347X.

260.   Kato, T., Takahashi, S., Shioiri, T., Murashita, J., Hamakawa, H., and Inubushi, T. (1994). Reduction of brain phosphocreatine in bipolar II disorder detected by phosphorus-31 magnetic resonance spectroscopy. Journal of Affective Disorders *31*, 125–133. 10.1016/0165-0327(94)90116-3.

261.   Shi, X.-F., Kondo, D.G., Sung, Y.-H., Hellem, T.L., Fiedler, K.K., Jeong, E.-K., Huber, R.S., and Renshaw, P.F. (2012). Frontal lobe bioenergetic metabolism in depressed adolescents with bipolar disorder: a phosphorus-31 magnetic resonance spectroscopy study: 31P-MRS adolescent bipolar disorder. Bipolar Disorders *14*, 607–617. 10.1111/j.1399-5618.2012.01040.x.

262.   Häussinger, D., Laubenberger, J., Vom Dahl, S., Ernst, T., Bayer, S., Langer, M., Gerok, W., and Hennig, J. (1994). Proton magnetic resonance spectroscopy studies on human brain Myo-inositol in hypo-osmolarity and hepatic encephalopathy. Gastroenterology *107*, 1475–1480. 10.1016/0016-5085(94)90552-5.

263.   Bothwell, J.H., Rae, C., Dixon, R.M., Styles, P., and Bhakoo, K.K. (2001). Hypo-osmotic swelling-activated release of organic osmolytes in brain slices: implications for brain oedema in vivo: Organic osmolyte decrease in brain slices. Journal of Neurochemistry *77*, 1632–1640. 10.1046/j.1471-4159.2001.00403.x.

264.   Van Heeswijk, R.B., Uffmann, K., Comment, A., Kurdzesau, F., Perazzolo, C., Cudalbu, C., Jannin, S., Konter, J.A., Hautle, P., Van Den Brandt, B., et al. (2009). Hyperpolarized lithium-6 as a sensor of nanomolar contrast agents. Magnetic Resonance in Medicine *61*, 1489–1493. 10.1002/mrm.21952.

265.   Kristensen, M., Nierenberg, A.A., and Østergaard, S.D. (2018). Face and predictive validity of the ClockΔ19 mouse as an animal model for bipolar disorder: a systematic review. Mol Psychiatry *23*, 70–80. 10.1038/mp.2017.192.

266.   Leussis, M.P., Berry-Scott, E.M., Saito, M., Jhuang, H., de Haan, G., Alkan, O., Luce, C.J., Madison, J.M., Sklar, P., Serre, T., et al. (2013). The ANK3 Bipolar Disorder Gene Regulates Psychiatric-Related Behaviors That Are Modulated by Lithium and Stress. Biological Psychiatry *73*, 683–690. 10.1016/j.biopsych.2012.10.016.

References

267. Van Enkhuizen, J., Milienne-Petiot, M., Geyer, M.A., and Young, J.W. (2015). Modeling bipolar disorder in mice by increasing acetylcholine or dopamine: chronic lithium treats most, but not all features. Psychopharmacology *232*, 3455–3467. 10.1007/s00213-015-4000-4.

268. Rocha, E., Achaval, M., Santos, P., and Rodnight, R. (1998). Lithium treatment causes gliosis and modifies the morphology of hippocampal astrocytes in rats. NeuroReport *9*, 3971–3974. 10.1097/00001756-199812010-00037.

269. Peng, L., Li, B., and Verkhratsky, A. (2016). Targeting astrocytes in bipolar disorder. Expert Review of Neurotherapeutics *16*, 649–657. 10.1586/14737175.2016.1171144.

270. Manganas, L.N., Zhang, X., Li, Y., Hazel, R.D., Smith, S.D., Wagshul, M.E., Henn, F., Benveniste, H., Djurić, P.M., Enikolopov, G., et al. (2007). Magnetic Resonance Spectroscopy Identifies Neural Progenitor Cells in the Live Human Brain. Science *318*, 980–985. 10.1126/science.1147851.

271. Loewenbrück, K.F., Fuchs, B., Hermann, A., Brandt, M., Werner, A., Kirsch, M., Schwarz, S., Schwarz, J., Schiller, J., and Storch, A. (2011). Proton MR Spectroscopy of Neural Stem Cells: Does the Proton-NMR Peak at 1.28 ppm Function As a Biomarker for Cell Type or State? Rejuvenation Research *14*, 371–381. 10.1089/rej.2010.1102.

272. Lustig, M., Donoho, D., and Pauly, J.M. (2007). Sparse MRI: The application of compressed sensing for rapid MR imaging. Magnetic Resonance in Med *58*, 1182–1195. 10.1002/mrm.21391.

273. Liang, S., Dresselaers, T., Louchami, K., Zhu, C., Liu, Y., and Himmelreich, U. (2017). Comparison of different compressed sensing algorithms for low SNR [19] F MRI applications—Imaging of transplanted pancreatic islets and cells labeled with perfluorocarbons. NMR in Biomedicine *30*, e3776. 10.1002/nbm.3776.

274. Ettenberg, A., Ayala, K., Krug, J.T., Collins, L., Mayes, M.S., and Fisher, M.P.A. (2020). Differential effects of lithium isotopes in a ketamine-induced hyperactivity model of mania. Pharmacology Biochemistry and Behavior *190*, 172875. 10.1016/j.pbb.2020.172875.

275. Stokes, P.E., Okamoto, M., Lieberman, K.W., Alexander, G., and Triana, E. (1982). Stable isotopes of lithium: in vivo differential distribution between plasma and cerebrospinal fluid. Biological Psychiatry *17*, 413–421.

ACKNOWLEDGEMENTS